Synthesis, Characterisation and Biological Activity of Silicon Nanoparticles Functionalised by Anticancer Compounds

Mehrnaz Behray

School of Chemistry

University of East Anglia

Norwich, United Kingdom

2016

A thesis submitted in fulfilment of the requirements for the degree of Doctor of Philosophy of the University of East Anglia.

© This copy of the thesis has been supplied on condition that anyone who consults it is understood to recognise that its copyright rests with the author and that use of any information derived there from must be in accordance with current UK Copyright Law. In addition, any quotation or extract must include full attribution.

Declaration

I declare that the research contained in this thesis, submitted for the degree of Doctor of Philosophy, is original, except where due reference is made to other authors, and has not previously been submitted by me for a degree at this or any other universities.

Mehrnaz Behray

Acknowledgements

I would first like to express my deepest gratitude to my beloved parents, Maryam Minapour and Mehdi Behray for their endless support and encouragement. All I have accomplished in my life is a result of their inspirational love and boundless generosity. Without their tremendous moral and financial support, I would never be able to arrive at this point. I'd also like to thank my lovely sister, Mahtab, who has always supported me during this journey.

I would convey my sincere appreciation to my supervisor, Dr Yimin Chao, for his support and guidance throughout my PhD. I am grateful to him for giving me the opportunity to work within this field of research. I would also like to thank Dr Andrew Mayes, for his excellent guidance, advice and valuable discussions as my secondary supervisor and providing me with the necessary laboratory facilities and instrumentations during my research at UEA.

My warmest gratitude goes to Mrs and Mr Eslamian for their continuous support, love and encouragement from the beginning I came to the UK. I am truly blessed to have them as such supportive family friends; helping me like my own parents.

I am extremely grateful to my friend, Carl Webster, for his generous help, suggestions and comments in every step of this project. I owe him a great deal for various training and foundational knowledge he gave me, and also being prepared for any questions relating to the biomedical section of my project. His assistance in proof reading this work is very much appreciated. I am most fortunate to have him as such a supportive friend.

I would like to express my special appreciation and thanks to Dr Christopher May for his continuous help, encouragement and being my supportive best friend. I'm very grateful for the time he spent to help me with proof reading and general comments.

Many special thanks to Dr Qi Wang for such a lovely and true friendship and for her help assisting me in my work both practically and scientifically. I greatly appreciate her generosity in providing me with the laboratory facilities, which made my work possible. Her presence assured me that I would never go off-track in my research for too long.

In addition, I wish to thank all my colleagues from Dr Chao's research group. I'm very thankful to my friends, Ting Li and Tiezheng Bian for their support, advice, and kindness throughout my research, which have been always a great source of motivation for me. A very special thanks goes to Dr Shane Ashby, not only for many valuable discussions but also for his

great friendship. I would also like to acknowledge Dr Jayshree Ahire for the training she gave me during the first year of my PhD.

Many thanks to Dr Wafa Al-Jamal and Sara Pereira for an excellent collaboration cumulating in our publication. Their support and valuable advice provided me with a better understanding of the scientific approach and lab work throughout the biomedical studies of my project. I wish to appreciate Dr Yongping Bao's research group in providing me with the necessary cell lines and drugs.

I also wish to thank my dearest friends Dr Sonia Tariq and Dr Abdirahman Saeed for their endless help, friendship and being the best companions I could ask for all the way through my PhD.

I would like to thank members of Professor Andrew Cammidge's group for kindly providing me with the laboratory instrumentations. I'm also grateful to Dr Isabelle Chambrier for her advice and useful discussions.

Lastly, I would like to thank all the collaborators at MAX-IV laboratory for the synchrotron FTIR Microspectroscopy experiments, NEXUS for the XPS data as well as the groups supervised by Prof Xixiang Zhang from King Abdullah University and Dr Satheesh Krishnamurthy from The Open University for the TEM images.

This thesis is dedicated to my dearest parents

Maryam Minapour and Mehdi Behray

Abstract

Silicon Nanoparticles (SiNPs) are non-toxic materials particularly suitable for various biomedical applications. They exhibit unique optical properties for use in bioimaging and diagnostic applications. To exploit these aspects, this thesis explores the synthesis, characterisation and biological activity of SiNPs functionalised by anticancer compounds.

Thiourea-based compounds have been shown to represent one of the most promising classes of anticancer agents due to their strong inhibitory activity against Epidermal Growth Factor Receptor (EGFR), overexpression of which is observed in common types of cancer cells. Conjugation of thiourea compounds in nanosystems presents one potential approach to target such cells. In this thesis, successful synthesis of novel thiourea-functionalised SiNPs was undertaken and their physiochemical properties were investigated by photoluminescence emission and elemental analysis. *In vitro* cytotoxicity assay was employed to evaluate the effect of SiNPs. Confocal microscopy images demonstrate SiNP internalisation and flow cytometry data confirms receptor-mediated targeting in cancer cells.

Isothiocyanates (ITCs) can prevent the onset of carcinogenesis and act as chemopreventive compounds. ITC-functionalised SiNPs were synthesised using two different methods, initiated from two different types of SiNPs. The surface chemistry of these particles were characterised and their optical properties examined to assess both synthesis approaches. The samples produced from the precursor Br SiNPs exhibit strong photoluminescence and therefore are suitable for uptake studies. The cytotoxicity of ITC SiNPs was evaluated by MTT and their internalisation confirmed using confocal microscopy and flow cytometry assay.

Synchrotron-based FTIR microspectroscopy was used as a novel approach to investigate ITC SiNP cell internalisation. Spectral comparison between treated and control cells shows the effect of ITCs, leading to an increase both in protein level in the nuclei, and also in the chance of apoptosis, which increases phospholipid contents.

Considering the obtained results, such multifunctional nanosystems have the potential to be applied for further diagnostic and therapeutic applications.

Table of contents

Chapter 2: Methods and Materials

Chapter 4: Synthesis and Characterisation of Isothiocyanate-functionalised Silicon Nanoparticles

Chapter 6: Conclusions and Future Prospects

List of Figures

List of Schemes

List of Tables

List of Abbreviations

AFM	Atomic Force Microscopy
AITC	Allyl Isothiocyanate
APTES	3-Aminopropyl Trimethoxysilane
ARE	Antioxidant Responsive Element
AS	Ascorbate Sodium
ATP	Adenosine Triphosphate
ATR	Attenuated Total Reflectance
Au	Gold
a.u.	Abbreviated Units
BITC	Benzyl Isothiocyanate
Br SiNPs	Bromine terminated Silicon Nanoparticles
CaF_2	Calcium Fluoride
CCV	Clathrin Coated Vesicles
CdSe	Cadmium Selenide
CO_2	Carbon Dioxide
CS_2	Carbon Disulphide
CYP	Cytochrome P450 Enzymes
DAG	1,2-diacylglycerol
DCM	Dichloromethane
DLS	Dynamic Light Scattering
DMSO	Dimethylsulfoxide
DNA	Deoxyribonucleic Acid
EDTA	Ethylenediaminetetraacetic Acid
EDX	Energy Dispersive X-ray Spectroscopy
EGFR	Epidermal Growth Factor Receptor
$EtAlCl_2$	Ethylaluminum Dichloride
EtOAc	Ethyl Acetate
EtOH	Ethanol
Et_3N	Triethylamine
eV	Electron Volt
FBS	Foetal Bovin Serum
FITR	Fourier Transform Infrared Spectroscopy
FPA	Focal Plane Arrays
FSC	Forward Scatter
FWHM	Full Width at Half Maximum
GST	Glutathione S-transferases
H-terminated	Hydrogen-terminated
H_2O_2	Hydrogen Peroxide
HF	Hydrofluoric Acid
HNO_3	Nitric Acid
H_2PtCl_6	Hexachloroplatinic Acid
IC_{50}	Half Maximal Inhibitory Concentration
IP3	1,3,5-triphosphate
ITC	Isothiocyanate
ITC SiNPs	Isothiocyanate terminated Silicon Nanoparticles
ITC SiNPs (Br SiNPs)	ITC SiNPs produced from the precursor Br SiNPs
ITC SiNPs (NH_2 SiNPs)	ITC SiNPs produced from the precursor NH_2 SiNPs
KBr	Potassium Bromide
KSi	Potassium Silicate
LDV	Laser Doppler Velocimetry
$LiAlH_4$	Lithium Aluminium Hydride

MAPK	Mitogen-activated Protein Kinase
$MgSO_4$	Magnesium Sulfate
Mg_2Si	Magnesium Silicide
MTT	3-(4,5-Dimethylthiazol-2-yl)-2,5-Diphenyltetrazolium Bromide
MTV	Multivesicular Bodies
NaCl	Sodium Chloride
NADH	Nicotinamide Adenine Dinucleotide Phosphate Hydrogen
NH_4Cl	Ammonium Chloride
NH_2 SiNPs	Amine terminated Silicon Nanoparticles
NP	Nanoparticle
Nrf2	Nuclear Factor E2-related Factor 2
PBS	Phosphate Buffered Saline
PCS	Photon Correlation Spectroscopy
PdI	Polydispersity Index
PEITC	Phenethyl Isothiocyanate
PET	Positron Emission Tomography
PFA	Paraformaldehyde
PI3K	Phosphatidylinositol 3-kinase
PL	Photoluminescence
PLCγ	Phospholipase Cγ
PKC	Protein Kinase C
P-Si	Porous Silicon
P/S	Penicillin/Streptomycin
Pt	Platinum Catalyst
PTK	Protein Tyrosine Kinase
PTFE	Polytetrafluoroethylene
QD	Quantum Dot
QY	Quantum Yield
RPMI	Roswell Park Memorial Institute medium
RTK	Receptor Tyrosine Kinase
SEM	Scanning Electron Microscopy
SFN	Sulforaphane
Si	Silicon
$SiCl_4$	Silicon Tetrachloride
SiNP	Silicon Nanoparticle
SiO	Silicon Monoxide
SiO_2	Silicon Dioxide
SI-FTIR	Synchrotron Radiation Fourier Transform Infrared Spectroscopy
S/N	Signal to Noise ratio
SSC	Side Scatter
STAT	Signal Transducers and Activators of Transcription
TEM	Transmission Electron Microscopy
TGA	Thermal Gravimetric Analysis
TGF-α	Transforming Growth Factor-α
THF	Tetrahydrofuran
TKI	Tyrosine Kinase Inhibitor
TMB	Tetramethylbenzidine
UV	Ultra Violet
UV-vis	Ultra Violet-Visible
Wt	Weight
XPS	X-ray Photoelectron Spectroscopy

Chapter 1:

Introduction

1. General Background and Concepts

In common conversation, things that are small are synonymous with concepts such as the 'head of a pin'. Reality however, requires imagination orders of magnitude greater, as there are 1,000,000 nm within this minute space. 'Nanometre' is derived from the Greek *nano* meaning 'dwarf', and denotes a factor of 10^{-9}; thus, a nanometre is one billionth of a metre. In this standard unit, the thickness of a human hair is approximately 80,000 nm, while a red blood cell is approximately 7000 nm. Having one or more dimensions of the order of 100 nm or less is considered nanoscale according to British Standards Institution (BSI).[1] The science of materials that possess at least one dimension in the nanoscale is called nanoscience. More precisely, nanoscience is the study of phenomena and manipulation of materials at atomic, molecular and macromolecular scales, where material properties differ significantly from those at a larger scale. Nanoscience is a highly multidisciplinary field which is known to be at the interference between chemistry and physics; between molecules and solids; between quantum mechanics and classical physics and chemistry.[2, 3]

In 1959, Richard Feynman gave a lecture to the American Physical Society which is considered as a first source of inspiration towards the conceptual understanding of nanoscience. His talk was entitled "There is plenty of room at the bottom" in which he laid out some of the consequences of measuring and manipulating materials at nanoscale. Initially he attempted to visualise this by explaining the idea of being able to write the entire 24 volumes of the Encyclopaedia Britannica on the head of a needle; each letter would be 8 nm in diameter, around 32 atoms across.[4] His contribution opened up to a wider audience the concept of the science of the miniature, in a similar way as Einstein in his popularisation of macro-scale physics.

The term "nanotechnology" was itself coined by Tokyo Science University Professor, Norio Taniguchi at a 1974 conference. His original statement remains as the standard definition today: "Nanotechnology mainly consists of the processing of separation, consolidation and deformation of materials by one atom or one molecule".[5] In modern applications the standard definition has expanded to the design, characterisation, production and application of structures, devices and systems by controlling shape and size at nanometre scale.[2] Nanochemistry is then the utilisation of chemistry to make nanoscale building blocks of different size, shape, composition and surface structure, charge and functionality.[6]

According to historical evidence there exist several remarkable examples of what we would now call nanoscience and nanotechnology. One of the earliest cases of this can be observed in "The Roman Lycurgus Cup" related to the 4th century presently in the British Museum (Figure 1.1). The glass of this cup shows unusual optical effects which appears pea-green in daylight (reflected light), whilst appearing wine-red coloured when illuminated with transmitted light from the inside of the vessel. The chemical analysis of the glass of the cup attributed this dichronic colouring to the surface plasmon resonance of the nanocrystals of an alloy of gold and silver and probably copper which are dispersed throughout the glassy matrix of the cup.[7]

Figure 1.1. The Lycurgus Cup under the reflected (left) and transmitted (right) light, Department of Prehistory and Europe, The British Museum.[8]

9th century Abbasid lustre ceramics similarly have a coating that forms a nano-grating which produces a multi-coloured iridescence (Figure 1.2 (a)).[9] Carbon nanotubes were also used unwittingly by 10th century Muslim sword-smiths in their though Damascus blades (Figure 1.2 (b)).[10] Another example is the use of colloidal metal nanoparticles in stained glass windows of ancient European cathedrals. In the Middle Ages, colloidal gold was used to produce bright red and purple colours by artisans. Figure 1.3 (a) shows a stained glass window made by Niccolo da Varallo between 1480 and 1486 in Milan Cathedral. This contains gold nanoparticles which appear red in diameters from 10-100 nm.[11] Moreover, the red and purple colours appear in the Rose window of the Cathedral of Notre Dame (Figure 1.3 (b)) are as a result of the presence of colloidal gold in the window.[12]

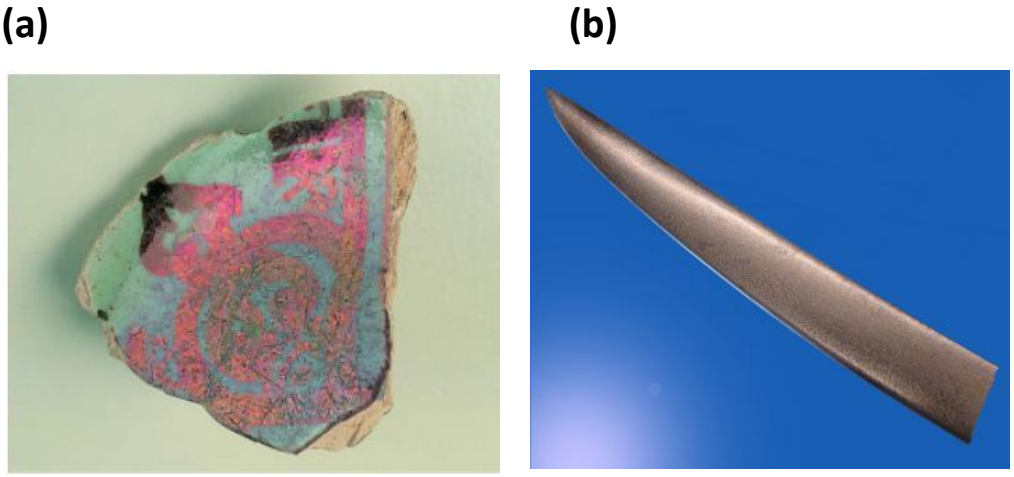

Figure 1.2. A Pottery containing silver and copper nanoclusters excavated from Fustat, Cairo, Egypt (a)[9] and a Damascus sword with the nanotube structure (b).[13]

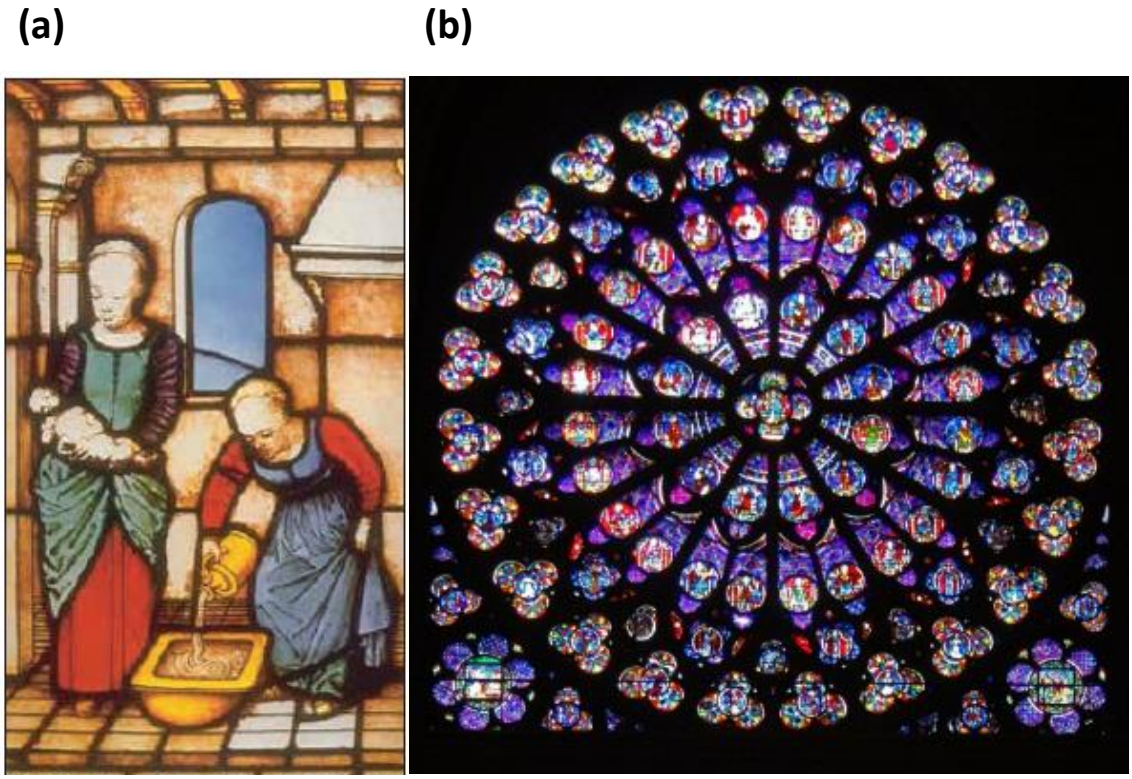

Figure 1.3. The stained Glass window by Niccolo da Varallo at Duomo of Milan (a)[11] and the Gothic stained glass rose window of Notre-Dame de Paris (b) the red colour is due to colloidal gold nanoparticles.[14]

Although the incidental use of nanoscience and nanotechnology is present in historical artefacts, the awareness and the importance of them only existed since the late 1950s. Significant breakthroughs have been made however since the invention of the Scanning Tunnelling Microscope (STM) by Gerd Binnig and Heinrich Rohrer at IBM Zurich in the early

1980s.[15, 16] This innovation allowed the direct observation of nanostructures, previously impossible, and since then nanomaterials have come to be at the forefront of scientific research with potential applications in a wide range of fields from biomedicine to engineering.[17-21]

1.1. Nanomaterials

Nanoscience and nanotechnologies are concerned with producing new or enhanced materials with at least one dimension in nanoscale. These nanomaterials appear in a variety of forms. Some materials such as films or coating surfaces of computer chips are nanoscale in only one dimension and the other two are macroscopic. Nanotubes and nanowires are considered as two-dimensional nanostructures with nanometre scale.[22] Sometimes they might show three dimensions in nanoscale such as nanoparticles and colloids. In some other cases, it is possible to find bulk material which are nanocrystalline materials made of nanometre-size grains such as nanoporous materials which contain features at nanometre.[23]

The surface reactivity and electrical characteristics are fundamental properties of materials which are size dependent and this behaviour is dependent on the ratio of surface atoms to the total number of atoms within the material. For a microstructure material this ratio is zero whereas it is different for nanomaterials. For example, a particle with size of 30 nm has 5% of atoms on its surface, a particle with 10 nm size has 20% of atoms on the surface, and this relationship continues to the situation where half of all atoms are on the surface for a particle with 3 nm size.[24] As a result of the reduced dimensions of nanocrystals, the increase in the surface area per unit mass occurs and thus the chemical and physical properties of nanomaterials is different from those of bulk materials. For example, nanomaterials show much lower melting points and sintering temperatures and they exhibit different catalytic properties and thermal stabilities due to the large fractions of surface atoms and surface energy. The mechanical strength of nanomaterials is normally higher than their bulk counterparts which occurs because of the reduction of crystal defects.[25] Therefore, nanoscale materials exhibit unique optical, electrical, photonic and catalytic properties and as a result they are ideal for use in various applications in nanotechnology.[26]

1.2. Semiconductor Nanoparticles

A nanoparticle (NP) is a cluster of atoms or molecules with three dimensions in nanoscale. There are several sub-categories of NP depending on the nature of the material. For instance, for crystalline materials this is called a nanocrystal and if the material is a semiconductor with three nanoscale dimensions, where the dimensions are of a similar magnitude to the exciton Bohr radius of the material, this is called a quantum dot (QD).[2]

Semiconductor NPs or QDs are of particular interest to the scientific community due to their unique optical, electronic and physical properties which are size dependent. Depending on the material, the size range could be between 2 to 20 nm. In addition to the large surface area to volume ratio and the dominant role of the surface, there is another factor responsible for these unique properties and that is the well-known quantum confinement effect.[27, 28] This has given rise to many potential applications such as optical, electronics, catalysis, and optoelectronics. Therefore by selecting the appropriate synthesis method used to produce QDs it is possible to obtain particles with the desired size, which is the dominant factor determining the underling material properties.[29-31]

1.2.1. Quantum Confinement Effect

The size dependent property of QDs is generally described as the quantum confinement effect, which is considered to be their most significant characteristic feature.[32] This effect is essentially as a result of direct influence of the ultra-small length-scale on the energy band structure. The term "confinement" refers to the motion of electrons moving randomly as this path is restricted in specific energy levels and the word "quantum" refers to the atomic dominion of particles. A simple explanation of this effect uses a model called "The electron in the box" or "potential well".[33] Based on this, the reduction of the size of the box in three dimensions gives rise to discrete energy levels instead of a continues band as in bulk materials. As the particle size decreases, the energy gap between the valence and conduction bands increases (Figure 1.4).[34, 35]

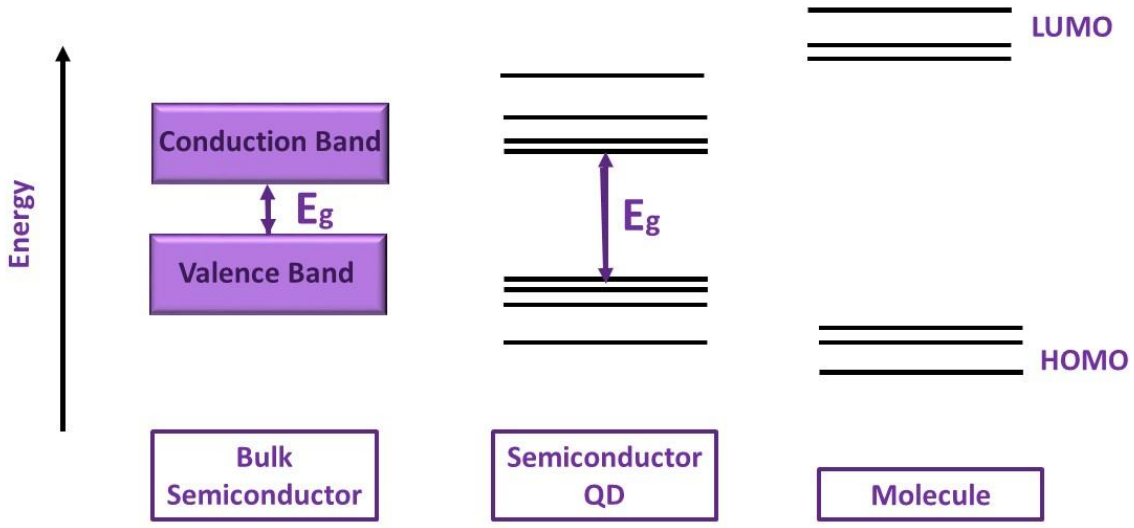

Figure 1.4. Schematic of energy diagrams illustrating the difference between the energy electronic states of bulk semiconductor, semiconductor QDs and molecules, reproduced from O'Farrell *et al*.[27]

This phenomenon can be discussed by the relationship between the position and energy of an electron in both free and confined space. In a bulk semiconductor, the energy or crystal momentum of an electron can be precisely defined whereas the position cannot be defined. However, in a semiconductor NP, as we decrease the size of the particle, we increase the certainty of where the electrons are while the momentum is no longer well defined. In the bulk semiconductor, series of nearby transitions occur with slightly different energies while in the QD the transitions are compressed into a single and intense transition as a result of the quantum confinement. This therefore causes discrete absorption bands and fluorescence in terms of the optical properties of QDs.[34] The electron-hole pair produced as a result of the absorption of a photon, is then delocalised over the interior of the NP and then recombination of the electron and hole leads to the emission of a photon which caused fluorescence. This is only efficient when the size of the QD is smaller than the exciton Bohr radius.[36]

1.3. Silicon Nanoparticles

Among the different types of semiconductor NPs, silicon is a well-known semiconductor material and is of particular interest. SiNPs are heavy metal free in nature and exhibit visible photoluminescence as a result of the quantum confinement effect.[37-40] The size tuneable emission,[41-43] high brightness[44] and high photostability compared to organic dyes,[45] have made SiNPs attractive materials as fluorescent cellular markers. In addition, silicon is abundant and

economical[46] but more importantly silicon has low inherent toxicity which conveniently leads to several applications in the biomedical field. Studies report silicon to be almost ten times safer than cadmium-based counterparts for use in biomedical and bioimaging applications.[47] Unlike other semiconductors, silicon has an indirect band gap that provides significant optical properties due to their very small size (about 4 nm), which is close to the bulk Bohr radius.[43, 48]

The silicon atom that exists on the surface of SiNPs has a different geometry than the bulk lattice structure, due to surface reconstruction. This influences the properties of NPs particularly those with very small size down to 1-2 nm.[49] The surface termination can also impact the photophysical properties of NPs significantly. Considering the monohydride termination, each surface atom has three Si-Si "back-bonds" and one Si-H bond which provides a different set of bonding constrains compared to dihydride termination.[50, 51] SiNPs can therefore be functionalised with different groups which can change the chemical and electronic properties, tailored for specific applications.

1.3.1 Synthetic Strategies for Silicon Nanoparticles

Strategies to synthesise SiNPs, utilising different apparatus and chemical compositions, have advanced significantly during the past 50 years. Through repeated experimentation, two important factors have been understood to control key properties of SiNPs: particle size and surface functionalisation. Both of these can be modified by number of different synthetic strategic methods and preparative conditions applied in the synthesis approach. Several reports (detailed in the following sections) have focussed on developing synthetic strategies to produce stable SiNPs along the lines suggested in the synthesis of SiNPs by Health *et al.* in 1992.[52] This study reported a liquid solution phase techniques for the production of micrometre and submicrometre-sized silicon crystals. The synthesis was based on a reduction of $SiCl_4$ and $RSiCl_3$ in a nonpolar organic solvent.

There are numerous synthesis methods for producing silicon nanocrystals featuring desired characteristics, and are described as either 'top down' or 'bottom up' techniques. Top down techniques are based on the bulk reduction of silicon which produces very small structures from larger material pieces. SiNPs are produced by this method from crystalline silicon by applying an etching procedure to reduce the size of bulk silicon to nanometre sized particles.

These physical processes generally produce limited yields of pure products but can remove contaminants originating from by-products. Using bottom up techniques on the other hand, SiNPs can be constructed by assembly methods; atom by atom, one silicon atom at a time. Self-assembly is one way of achieving this whereby the atoms of molecules arrange themselves into a structure as a result of their specific natural properties. Chemical synthesis of large molecules provides an example of self-assembly. Chemical routes tend to scale up the yields and complete further functionalisation of the surface synchronously, however, they are plagued by impure products.[53] Another bottom up approach is to use tools to move each atom or molecule individually as a positional assembly, however, this method is currently laborious and not suitable for industrial applications despite the fact that it offers great control over construction.[2] The synthesised SiNPs are initially either hydrogen or halogen terminated and thus require further surface passivation in order to prevent oxidation on the surface. This is crucial because oxidation can alter the optical properties of SiNPs as well as increase toxicity levels in biological environments.[54, 55] All of these methods have advantages and disadvantages relating to the surface chemistry, monodispersity, shape, stability and optical properties on SiNPs.

1.3.1.1. Top Down Methods

1.3.1.1.1. Electrochemical Etching

For the first time Canham *et al.* reported that porous silicon can show photoluminescence at room temperature in 1990.[56] They produced mesoporous silicon layers with high porosity and visible red luminescence using the electrochemical and chemical dissolution techniques. Perhaps the most reliable way to produce hydrogen terminated SiNPs is electrochemical etching.[57] This produces SiNPs by breaking up the porous silicon. Utilising the HF in this synthesis method produces a hydrogen terminated surface with very low levels of oxide. Porous silicon can be produced first via electrochemical etching and followed by a fracturing process in a dry solvent, producing hydrogen terminated SiNPs. This method was originally reported by Heinrich *et al.* in 1992.[58] They reported the synthesis of porous silicon by electrochemically etching of n-type or p-type silicon wafers. This was achieved by soaking in a (1:1) solution of HF:EtOH using an electrical potential. This approach was later followed by ultra-sonication of the material to remove the nanostructured silicon from the surface of the wafer. The resultant SiNPs were polydispersed with irregular shapes and showed a visible red luminescence. This method was later optimised by Bley *et al.* in 1996; the sensitivity of the synthesis method was

studied by his research group by investigating factors including the current density, etching time, sonication time and more importantly the effect of HF on the synthesis. They reported how the optical and physical properties of SiNPs can be affected by these parameters.[59] In 1999 Wolkin *et al*. produced SiNPs by electrochemical etching followed by photo-assisted stain etching of p-type Si wafers.[60] Using this method they showed that the photoluminescence of these SiNPs can be tuned from near infrared to ultraviolet by changing the size of NPs. Belomoin *et al.* in 2002 showed that further optimisation of the photoluminescence can be achieved through an improved control on the size of SiNPs. In this study, they optimised the current density and the etching time to obtain SiNPs with different diameters (1.0, 1.67, 2.15 and 2.9 nm) resulting in different colours of luminescence (ultra-bright blue, green, yellow and red) for each specific size.[61] An improved optimisation of this method was reported by Lie *et al.* in 2002 and Chao *et al.* in 2007 showing that a low etching time with high current density can produce SiNPs in a range of 2 to 10 nm.[62-64] This was done by using a 1:1 mixture of 48% aqueous HF and ethanol acting as etching solution and a current density of 210–550 $mAcm^{-2}$ which passed through a silicon wafer in a PTFE cell. The silicon wafers needed to be dry *in vacuo* and later the ultrasonication in a dry solvent produced hydrogen terminated SiNPs.

According to this well-established procedure, many factors including electrolyte composition, silicon dopant type, dopant concentration and etching time may adversely affect the surface morphology and properties of the PSi thin film.[65] The role of EtOH is used to prevent bubbles, which occur during the etching process, from splitting and also to overcome the strong hydrophobic nature of the silicon surface to ensure that pores continue propagating on the surface.[66] As a result, more uniform hydrogen-terminated SiNPs can be generated.

1.3.1.1.2. Reactive Sputtering

In 1998 Furukawa *et al.* reported the use of a reactive sputtering technique to synthesise hydrogen terminate SiNPs. In this method they used a low substrate temperature of approximately 100K and produced SiNPs with a wide optical band gap up to 2.4 eV.[67]

1.3.1.1.3. Annealing of SiO Powders

In 2005 Liu *et al*. showed a new method which involves annealing SiO powders at approximately 700K under ambient conditions. The annealed powder was later etched with 10% HF and the resulting particles were functionalised via hydrosilylation. Although this method is economical, the synthesised SiNPs were rather polydisperse and showed significant amount of oxide on the surface.[68]

1.3.1.1.4. Ball Milling

High energy ball milling is a mechanical technique which is straightforward and industrially scalable.[69] Using this method, silicon particles can be ground down into smaller particles. The size of synthesised nanoparticles produced is rather large in a range of 40 to 800 nm. Therefore, these particles do not show the properties which are normally associated with quantum confinement effects such as photoluminescence. In 2000, Lam *et al*. produced SiNPs with dimensions of about 5 nm by pure mechanical attrition of solid graphite with SiO_2 in a planetary ball miller for 7–10 days followed by annealing at 150 ^{o}C. The resulting NPs were capped with an amorphous oxide layer of silicon about 1 nm in thickness and featured a multi-peak PL spectrum, due to the broad range of particle sizes. Besides the wide size distribution, aggregation was also a serious issue because this led to a complex and uneven shape. As a result of these drawbacks, ball milling methods are rarely used in place of other physical synthetic strategies, despite its convenience and inexpensive nature.[70]

In 2007 Heinz *et al.* showed the synthesis of alkyl-capped SiNPs by this method which exhibited quantum size effects.[71] The obtained crystalline SiNPs showed a PL at 450 nm. Nevertheless, the functionalisation was carried out via oxygen atoms. Therefore, this would affect their optical properties and long term stability for further application.

1.3.1.1.5. Laser Ablation

In 2001, Hata *et al.* reported the use of a self-assembled monolayer of hexanethiol on epitaxial Au (111) surfaces to deposit SiNPs by laser ablation. According to the data obtained from SEM and AFM observations and PL measurements, SiNPs had a round shape structure

and remained stable for at least a couple of months. They found control over the NP size could be obtained by changing the argon ambient pressure.[72]

In 2008, Umezu *et al.* demonstrated the use of laser ablation to synthesise SiNPs. The synthesis was performed by pulsing a laser on a Si single crystal under an inert atmosphere. The crystallinity of particles was shown to be improved by increasing the pressure of inert gas.[73]

A year later Shiharata *et al.* demonstrated the one-pot synthesis of a silicon wafer by the same method using 1-octene to functionalise the resultant SiNPs and produce octyl-teriminated SiNPs. The diameter of the particles was between 1 to 10 nm and the maximum PL emission was centred at 375 nm.[74]

Many researchers prefer to use laser ablation to prepare SiNPs since the particle size is easily adjusted by controlling experimental parameters without requiring additional chemicals. It is straightforward and clean as it is carried out on a bare silicon wafer or immersed in water or polar solvents. However, low production efficiency in this method cannot be ignored.

1.3.1.2. Bottom Up Methods

1.3.1.2.1. Solution Synthesis and Micelle Reduction

Another synthesis method which is chemical based is micelle reduction. This method uses a reducing agent such as $LiAlH_4$ or Mg_2Si for the reduction of silicon based micelles (anhydrous compounds e.g. SiX_4; X = Cl, Br or I). This technique gives more control over the size of the synthesised SiNPs to obtain a narrow size distribution. In 1999 Wilcoxon *et al.* introduced the synthesis of hydrogen terminated SiNPs which retained their crystallite structures down to 4 nm and had a PL in the range of 700–350 nm.[75] This synthesis method was later optimised to functionalise the surface and introduce Si-C mainly via hydrosilylation.[76]

Another type of product which can be obtained by micelle reduction is halide-terminated SiNPs with the use of non-hydride reducing. This field was established by the Kauzlarich *et al.* group in 1996.[77-80] They used various reducing agents such as Mg_2Si, KSi and sodium naphthalide to reduce micelles of $SiCl_4$ in 1, 2-dimethoxyethane and produce chloride-terminated SiNPs. This type of NPs can be used as a reactive template for further

functionalization. For example, they can undergo nucleophillic substitutions with reagents such as primary alcohols and organometallic nucleophiles.

Amine-functionalised SiNPs have been synthesised using micelle reduction by several different research groups. In 2009, Rosso-Vasic *et al.* produced biocompatible NPs which were used for bioimaging in BV2 cells and were quite stable in a range of different pH values and high temperatures up to 120 ^{o}C.[81] Wang *et al.* reported another recent method with facile conditions in 2013.[82] This involved using sodium ascorbate as a reducing agent to reduce 3-aminopropyl trimethoxysilane (APTES) in water at ambient conditions to obtain water soluble amine-functionalised SiNPs which had an average diameter of 1.5 nm.

1.3.1.2.2. Thermolysis and Pyrolysis

A synthesis method involving the decomposition of salines was introduced by Littau *et al*. in 1993 in which they used a high temperature aerosol apparatus to produce small size surface-oxidised SiNPs. These particles were prepared by homogeneous gas-phase nucleation following pyrolysis of dilute disilane in helium. They showed a red photoluminescence and had a crystalline silicon core with 1.2 nm silicon oxide sell around.[83]

A year later Fojtil *et al.* reported a similar synthesis method which was followed by etching the particles in acyclohexane/propan-2-ol suspension with HF. They showed the effect of the solvent polarity on the PL of the particles, since the polar solvents such as alcohol and chloroform partially quenched the PL of the nanoparticle suspension, whereas they did not observed the quenching effect with non-polar solvents such as CCl_4.[84]

Another method for the synthesis of SiNPs involves the decomposition of a liquid precursor and high temperatures (500 ^{o}C), which was reported by Korgl *et al.* in 2001.[85] They demonstrated the decomposition of diphenylsilane using the thermal decomposition to produce SiNPs. Even though the size control was achieved using this technique, the susceptibility of the particle surface to react with solvent borne impurities was considered as a drawback of using the liquid precursor.

The decomposition of both liquid and gas precursors is an attractive method to prepare SiNPs. However the decomposition of gas phase precursors has been more successful.[86] One

of the major drawbacks of using liquid precursors is their high decomposition temperature and the possibility of the particle surface to react with other solvent impurities.

In 2003 Li *et al.* reported the synthesis of SiNPs using a CO_2 laser-induced decomposition of silane as a gaseous precursor molecule.[87] Large quantities of nanoparticles were produced via this method with an average diameter of 5 nm. The PL emission was later established by using HNO_3 leading to chemical oxidation. Later, Swihart *et al.* modified this method to control the size of NPs.[87] They reported that the flow rates and the laser power can affect the size of NPs. This size was further optimised by etching with HF/HNO_3 in water to produce smaller size particles. However, the resultant particles showed some degree of surface oxidation a non-homogeneous surface; thus, the PL was not stable. To remedy this drawback, SiNPs were further etched with 5% HF and thermally hydrosilylated with a series of alkyl- and ester-termination which resulted in a much more stable PL for particles.[88]

Solid precursors have also been reported to be used for the decomposition to prepare SiNPs by Belomoin *et al.* in 2002.[89] Nanoparticles can be synthesised from the pyrolytic decomposition of hydrogen silsesquioxane or other silicon rich oxides by heating at 1000 ^oC in an atmosphere containing 5% H_2 and 95% N_2. Afterward, HF etching must be undertaken to remove silicon oxide.[89, 90]

1.3.2. Strengths and Weaknesses

To summarise, size control of SiNPs prepared by physical methods is simple without requiring the use of chemical reagents. However, it cannot trivially realise scalable production and the obtained NPs require further modification to become stabilised. Using chemical procedures, on the other hand, allows simultaneous control under mild conditions of the synthesis, surface modification as well as the NP diameter. Nevertheless, contamination of residual by-products, such as the reducing agents, can be a complicating factor.

Porous silicon, produced by the electrochemical procedure under certain conditions, is always regarded as the primary material for SiNPs.[91] However, the lack of capability to control particle size, shape and size distribution is a noticeable drawback of etching, which needs a further separation process.

1.3.3. Functionalisation of Silicon Nanoparticles

Hydrogen terminated SiNPs or halogen terminated SiNPs are highly reactive and therefore prone to oxidation under ambient conditions.[92] As surface oxides can alter the optical properties considerably, these types of nanoparticle require further functionalisation in order to passivate the surface, and thus avoid oxidation and agglomeration.

There are different types of surface functionalisation for SiNPs ranging from alkylation reactions by hydrosilylation to radical halogenation. In some cases it is possible to determine the surface passivation prior to the particle synthesis by choosing the specific surfactants in some micelle reduction methods.

Hydrosilylation has been known as one of the most common methods of functionalisation for hydrogen terminated SiNPs. Due to the specific coordination of surface atoms in SiNPs, the covalent Si-C linkage can stabilise the particle surface and avoid oxidation. Hydrosilylation can be undertaken on planar or porous silicon surfaces as one of the methods which can add C=C bonding to the surface of hydrogen or halogen terminated SiNPs. This Si-C linkage can be introduced using different methods such as thermal initiation,[62, 93] photo initiation (with UV[94], or visible light)[95, 96] or using a radical initiator (benzoyl peroxide)[97] and applying different catalysts ($EtAlCl_2$ or H_2PtCl_6)[76]. The resultant NPs will in fact be protected from the surrounding environment by the new functional group which provides electronic stabilisation of the surface. In addition to the improved stability of nanoparticles, hydrosilylation can also alter the solubility of NPs according to polarity of the specific functional group present on the surface of the adding ligand.[98, 99] One of the other advantages of hydrosilylation is that it does not break the Si-Si bond while adding the Si-C on the surface; therefore, the optical properties remain unchanged.[100]

When using a radical initiator for hydrosilylation, normally a source such as heat or light is used to generate radicals for the reaction. This can form a radical site on the silicon surface after reacting with the hydrogen. This radical site will then directly react with an alkene and this trend will terminate by picking up hydrogen from the neighbouring silicon atom (Scheme 1.1).[101] The thermal hydrosilylation is also assumed to follow a similar mechanism as the radical based mechanism. This method normally is done by refluxing for several hours in a solvent containing the desired ligand and hydrogen terminated SiNPs.[62, 63, 78]

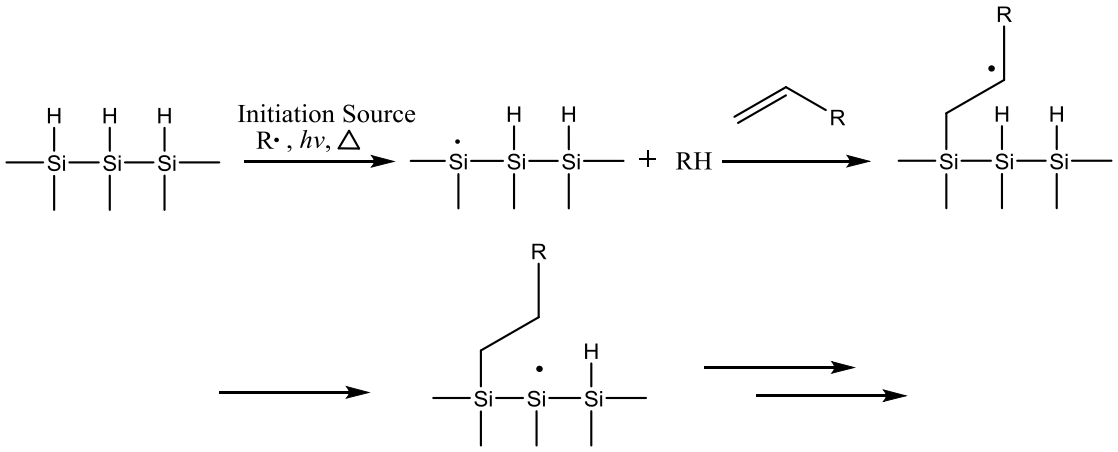

Scheme 1.1. Mechanism of radical-based hydrosilylation.[101]

Another type of hydrosilylation uses the metal catalysis (e.g. H_2PtCl_6 (Speier's catalysts)) to functionalises SiNPs.[102] The proposed mechanism in this case is known to be the Chalk-Harrod mechanism and is shown in Scheme 1.2.[103] The mechanism can be divided into two steps. First, the oxidative addition of a hydrosilane gives a hydridosilyl complex which is coordinated with the functional ligand. This complex then undergoes migratory insertion of the ligand into the Pt-H bond (hydrometallation) to give a new species. Reductive elimination of this species at the end will form the final hydrosilylation product.

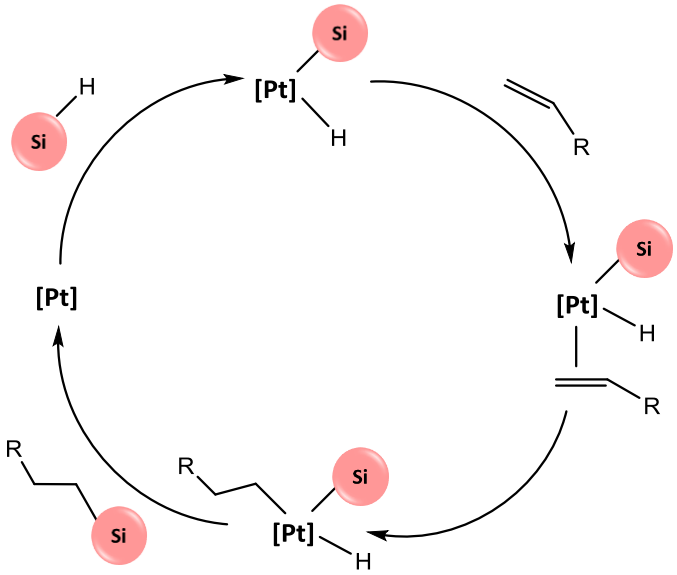

Scheme 1.2. Metal complex catalysed hydrosilylation of SiNPs using Speier's catalysts.

1.4. Biomedical Applications of Semiconductor Quantum Dots

Semiconductor QDs exhibit unique optical and electronic properties such as high quantum yield, size dependent and tuneable fluorescence emission[42, 43, 89] and stability against photobleaching as well as against chemical degradation.[45, 76] These NPs have been investigated for various biomedical applications not only because of their unique optical properties but also owing to their dimensional similarities with biological macromolecules such as proteins and nucleic acids.[27, 104] These characteristics allow them to be used for bioimaging applications as well as drug delivery detection systems. They have several advantages over their organic counterparts in the field of bioimaging. First of all they possess very narrow emission spectra which decreases the chance of spectral overlap and thus increases the possibility of distinguishing multiple fluorophores simultaneously. Moreover, QDs show a very broad excitation spectra which enables the use of single excitation wavelength to excite QDs with different colours.[27] In addition, there is large separation between the excitation and emission wavelength of QDs (the Stokes' shift) which allows the whole emission spectra to be collected.[105] QDs are also brighter than the conventional dyes due to their larger extinction coefficients.[106] They are also more stable to photobleaching for several hours, allowing the collection of images with high contrast and is useful for 3D imaging too where bleaching of fluorophores during the acquisition of successive z-sections is problematic.[106]

Until now, various types of fluorescent QDs with elements of groups II–IV such as CdSe and CdS (with tuneable wavelength emission) have been used as biological probes. However, the use of these materials for biological applications is challenging due to their toxicity. Thus, less toxic or non-toxic materials such as silicon can be suitable candidates to replace cadmium based QDs for biomedical applications.[107]

Silicon has been considered as an extremely biocompatible material due to its low level toxicity. Their applications in drug delivery, cancer cell diagnostics and therapeutics are active fields and of considerable attention of research over recent years.[106, 108, 109]

1.4.1. Cytotoxicity

Toxicity is a critical factor to consider when evaluating the use of nanomaterials for biomedical purposes, especially *in vivo* applications, and as such research into nanotoxicology

is gaining more attention. Exposure to NPs for medical purposes involves intentional contact or administration; thus understanding the properties of nanoparticles and their effect on the body is crucial before any clinical trials or use can occur.

Cytotoxicity is known to be dependent on a number of factors such as the particle size, capping ligand, shape, surface charge and chemistry, dose of NPs, coating bioactivity and processing parameters.[110] Even if NPs do not induce significant alterations in cell physiology, they can produce subtle alterations of function which may affect the quality of data derived from their use. Free radical formation, and interaction of QDs with intracellular components are considered as some of the potential mechanisms responsible for NP cytotoxicity.[111, 112] If NPs show aggregation or morphological variations in the biological media, this can affect the overall cytotoxicity and therefore it is important to check the stability of NPs in biological environments by assessing different parameters such as the hydrodynamic size and the zeta potential of NPs. In this regard, Lin *et al.* investigated the aggregation state in the cell culture media. They studied NPs with two different sizes (15 nm and 46 nm) and observed no difference in terms of the cytotoxic behaviour due to the fact that both NPs reached a similar size after aggregation in the culture medium.[113]

Surface charge is one of the factors which plays a significant role in cytotoxicity. Cationic surfaces have shown to be more cytotoxic than anionic and neutral surfaces.[114] This could be because of the affinity of cationic NPs to the cellular membrane which is negatively charged. Thus, adding a coating to render the surface charge of NPs can greatly affect their toxicity. In addition, the cytotoxicity of NPs is also cell dependent as the conditions of each cell line can be completely different and they can show different interactions with nanomaterials.[115] Therefore, it is crucial to determine the cytotoxicity of each type of NPs for the various potential environments that they may be exposed to before taking any step further towards their actual applications.

One simple cytotoxicity test involves visual inspection of the cells with bright-field microscopy for changes in cellular or nuclear morphology before and after the treatment with NPs.[116] Fiorito *et al.* used this technique to evaluate the cytotoxicity of single-walled carbon nanotubes.[117] However, the majority of cytotoxicity assays used in this field measure cell death using colorimetric techniques. These colorimetric methods can be further categorised into assays that measure mitochondrial activity and plasma membrane integrity.[116] MTT (3-(4,5-dimethylthiazol-2-yl)-2,5-diphenyl tetrazolium bromide) assay is considered as one of the most

widely used methods which measures the activity of the mitochondrial dehydrogenase enzyme.[118] This enzyme cleaves the tetrazolium ring, which only occurs in living cells.[119] MTT salt is pale yellow in solution but produces an insoluble purple formazan product within live cells. Another common method is Trypan blue dye exclusion assay which provides information of cell death by showing dye staining on ruptured cells, whilst live cells remain colourless. The amount of cell death can be determined via light microscopy.[120]

One potential cause of NP toxicity is the occurrence of internal heavy metals (such as Cd and Se) which can gradually leak in the biological environments.[121] As the toxicity of heavy metal ions are known, the release rate and environmental conditions can being measured. Kondoh *et al.* reported that Cd induces apoptosis in HL-60 cells via caspase-9 activation.[122] Furthermore, Shen *et al.* found sodium-selenite induced oxidative stress and apoptosis in HepG2 cells.[123] These findings confirmed the toxicity of both bulk cadmium and selenium *in vitro*. In another work, Derfus *et al.* published data regarding the toxicity of CdSe NPs in hepatocytes as a liver model.[124] They further suggested functionalisation of these QDs with mercaptoacetic acid (MAA) which can make them water soluble and remove cytotoxic effects.[125] In addition, the cellular viability decreased when NPs were initially subjected into air and then functionalised with mercaptoacetic acid which was dose dependent. These findings indicated that oxygen in the air induced the CdSe NPs oxidisation and the consequential release of Cd^{2+} ions which induce cytotoxicity in cells. Cd-induced hepatotoxicity can be explained either by direct or indirect cytotoxic pathways. The direct pathway occurs when Cd^{2+} binds to sulfhydryl groups on the mitochondrial molecules, leading to damage of the mitochondria. The indirect pathway, on the other hand, is assumed to occur via activation of Kupffer cells.[126]

Although, there has been significant breakthroughs published on the cytotoxicity of group II–VI semiconductor NPs, research into the cytotoxicity of SiNPs has not progressed as far. Chin *et al.* investigated the effect of porous silicon on primary hepatocytes under various culture conditions.[127] The viability of cells in all conditions and in the long-term was considerable suggesting no obvious cytotoxicity from porous silicon on cells.

NPs used for imaging and drug delivery applications are often purposely coated with bioconjugates such as DNA, proteins, and antibodies to target specific cells. Despite the fact much of the function of NPs is due to their core structure, the surface coating defines much of their activity in the biological environments.[116] For many types of NPs to be more effective in biological applications, the addition of some type of surface coating is required. This coating

can alter the potential toxicity of the whole system. Since these NPs are intentionally designed to interact with cells, it is vital to ensure that these enhancements are not causing any adverse effects. More specifically, information should be obtained about whether naked or functionalised NPs will undergo any biodegradation in the cellular environment and what cellular responses those degraded NPs might induce. For instance, biodegraded NPs may accumulate within cells and lead to intracellular changes such as disruption of organelle integrity or gene alterations.[116]

Several *in vitro* and *in vivo* studies have demonstrated the low level of toxicity for SiNPs.[128-130] The main factors affecting the toxicity of SiNPs are surface ligands and the NP diameter. The surface functionality of SiNPs on lung and skin cell viability was investigated by Shiohara *et al*.[131] They reported that highly reactive surface groups, like epoxides, were twice as toxic to lung epithelial cells compared with amine or diol surface groups due to the epoxide's ability to cause oxidative stress within the cell. In addition, smaller SiNPs (1.6 nm) have been found to be more toxic than larger NPs (3.9 nm) due to an increased surface area per unit volume.[55] Alsharif *et al.* examined the cytotoxicity of alkyl-capped SiNPs and the intracellular internalisation in human neoplastic and normal primary cells. No clear evidence of cytotoxicity was observed *in vitro* based on their data.[132] Poly acrylic acid and amine coatings on SiNPs are other examples of functionalisation which have been also shown to have not any serious cytotoxic effect up to 200 μg/mL NPs in HepG2 cells.[99, 133] However, this reported data could be time and cell line dependent. Therefore, the nature of the functionalised group can strongly determine the cytotoxic behaviour.

In vivo toxicity studies by Swihart *et al.* performed on two animal models of mice and monkeys, showed that a large dose of SiNPs of up to 200 mg/kg had no adverse effects in terms of blood chemistry, behaviour, and weight.[128] However, pathology work did show a difference between the two animal models, with mice showing adverse effects in the liver.

In order to understand the excretion pathway of SiNPs, Tu *et al*. carried out *in vivo* positron emission tomogorpahy (PET) studies on mice.[129] The data showed that SiNPs are largely removed via renal filtration within minutes to hours after injection, with a very small population residing within the liver for up to several weeks.

1.4.2. Biomedical Applications of Silicon Nanoparticles

Bioimaging applications require nanomaterials with good biocompatibility, low cytotoxicity and stable photoluminescence emission.[134] The stability plays a key role for biomedical applications, and this could be achieved by improving the solubility in water and biological environment in order to avoid the aggregation.[76] Aggregation and precipitation of NPs can interrupt the cell internalisation and also cause cytotoxicity. Moreover, labelling NPs with targeting molecules not only can lead the particles to specific cells for specific purposes but also can make them more hydrophilic and stable and therefore this functionalisation for specific biomedical applications has high utility.[76]

In 2002, Perez *et al.* synthesised nanometric particles from porous silicon film to investigate the growth behaviour of *B. subtilis* and *K. pneumoniae* bacterial strains.[135] The different behaviour that each bacterium presents (grown in a medium containing SiNPs) suggests the idea that these particles can be used as a bacteriological sensor.

Fluorescent SiNPs are regarded as an ideal biological probe due to their low toxicity, substantial quantum yields and photostability.[136] However, most surface ligands of SiNPs (e.g. styrene, alkyl, and octene) are hydrophobic, resulting in poor dispersibility in aqueous media and thus have limited bioapplications as a result. Tremendous effort has been made to address this issue. For example, in 2004, Ruckenstein *et al.* reported the use of red emitting poly (acrylic acid) SiNPs to image CHO cells.[96] These NPs showed strong luminescence after 24 h exposure to UV light whereas a series of organic dyes lost emission after 20 min exposure. Swihart *et al.* also showed that red emitting SiNPs encapsulated within PEG phospholipid micelles could be used for imaging applications in panc-1 cells.[137] The photoluminescence from these NPs was still visible after 2 month and showed good pH stability.

The first use of blue emission for the imaging of HeLa cells was reported by Yamamoto *et al.* in 2005.[76] Blue emitting SiNPs had strong luminescence after 60 min of UV exposure compared to the organic dye which significantly decreased in luminescence over the same time period. Confocal images confirmed that blue emitting SiNPs retained their fluorescence in MCF-7 cells after a 24 h incubation, showing that they are suitable candidates for longer term biological fluorescence imaging.[138]

In 2010, Prasad *at al.* showed the *in vivo* multi-colour imaging of SiNPs conjugate to a protein in mice models with emission ranging from red to NIR.[139] They also developed a class

of red and blue emitting SiNPs conjugated to proteins that allowed immunofluorescent cell imaging of HeLa cells.

1.5. Thiourea as an Epidermal Growth Factor Receptor Inhibitor

1.5.1. EGFR and Its Inhibition in Cancer Therapy

Receptor protein tyrosine kinases play a crucial role in signal transduction pathways which control cell division and differentiation. These receptors exist as inactive monomers which can be dimerised upon binding to their specific extracellular growth factors. After the ligand binding, the tyrosine kinase intercellular domain of the receptor is activated leading to the autophosphorylation of the intracellular domain. This initiates a cascade of downstream signalling events.[140] Many of the growth factor receptor proteins have intracellular domains that function as tyrosine kinases, and thus can effect signalling. The interaction between growth factors and these receptors is a necessary event in normal regulation of cell growth. However, under certain conditions, as a result of overexpression or mutation of the ligand and the receptor, these receptors can become hyper-activated leading to the uncontrolled cell proliferation.[141]

Among various growth factor receptor kinases that have been identified as being important in cancer is the epidermal growth factor receptor (EGFR) kinase, also known as erb-B1 or HER-1. It was discovered by Stanley Cohen from Vanderbilt University, for which he received the 1986 Nobel Prize in Medicine, shared with Rita Levi-Montalcini for their discovery of growth factors.[142, 143] EGFR signalling is important for cell proliferation. It also contributes to multiple processes involve in cancer progression such as angiogenesis, metastatic spread, and the inhibition of apoptosis.[144, 145] EGFR overexpression has been reported in a wide variety of solid human cancers, including lung, colorectal carcinomas, breast, gastric, bladder, ovarian, prostate, head and neck and glioblastomas in which it is generally associated with advanced disease and poor prognosis.[146-148] Over-expression of EGFR has also been linked to other factors such as hormonal therapy, cytotoxic agents and radiotherapy.[148-151]

The critical role of the EGFR in cancer growth has led to an extensive search to find and synthesise potential compounds to inhibit the EGFR signalling pathway; successful targeting the EGFR could represent a significant contribution to cancer therapy. A variety of different

methods are currently being used to target the EGFR. Some of the most promising approaches include monoclonal antibodies in order to prevent the ligand binding and also small molecule inhibitors of the tyrosine kinase enzymatic activity to inhibit autophosphorylation and downstream intracellular signalling. However, the therapeutic efficiency of the existing inhibitors is limited. Hence, identifying new molecules which can through novel strategies inhibit the EGFR, as a prime target for cancer therapy, is an exciting avenue in the development of targeted cancer therapy research.[152]

Zeneca Pharmaceuticals has reported the discovery and optimisation of novel quinazoline-based compounds as anticancer agents.[153, 154] Anilinoquinazoline is a synthetic molecule with low-molecular weight which effectively inhibited EGFR tyrosine kinase *in vitro* and also inhibited the growth of EGF-stimulated KB oral carcinoma cells. Further experiments showed inhibition of autophosphorylation of EGFR in a number of tumour cell lines such as A549 (lung), DU145 (prostate) and HT29 (colorectal).[155, 156]

Other EGFR inhibitors have been reported by Pfizer which are also a quinazoline derivative.[157] This compound showed behaviour that inhibits EGFR tyrosine kinase and also autophosphorylation in DiFi human colon tumour cell line. The inhibitor has indicated selectivity for EGFR, as opposed to other tyrosine kinases studied. The compound can block the cell cycle in phase G1 with significant accumulations of underphosphorylated retinoblastoma protein and the cell cycle inhibitor p27KIP1. This compound has also showed activity against various human tumour xenografts *in vivo*.[158]

An antibody (C225) inhibiting the binding of ligand to EGFR has been shown to significantly inhibit the growth of A431 vulval carcinoma xenografts.[159] It also inhibited EGF-induced receptor activation in prostate carcinoma cells and alone or in conjunction with doxorubicin, inhibited progression of DU145 and PC-3 prostate carcinoma xenografts.[160]

One interesting development has been the conjugation of recombinant human EGF to genistein, a soybean-derived tyrosine kinase inhibitor, giving an EGFR-targeted cytotoxic agent with tyrosine kinase inhibitory activity. This new conjugated compound was 100-fold more potent with EGFR inhibitory activity than unconjugated genistein. This agent initiated rapid apoptosis in MDAMB-231 and BT-20 breast cancer cells at nanomolar concentrations.[161]

1.5.2. EGFR Overexpression in Colorectal Cancer

The role of EGFR has been most thoroughly studied in breast cancer, where it is overexpressed in approximately 25–30% of cases and is associated with a poor prognosis.[142] However, the enhanced activity of EGFR has been found to be associated with tumour progression in several other malignancies including colon. It has been shown that the overexpression of EGFR in colon cancer may be correlated to an advanced stage of the disease or might be a sign of a potential metastatic risk.[162, 163] However, the influence of EGFR expression on survival is controversial and it is not uniformly related to an unfavourable prognosis. According to immunohistochemical methods, used for the detection of EGFR in colorectal cancer, the EGFR overexpression ranges from 25% to 82%[163-167] and this level of expression in colorectal cancer tissue is higher than in surrounding mucosa.[163, 164, 168] In primary cultures of human colorectal carcinomas, EGFR overexpression has also been observed during the tumour progression suggesting an increased sensitivity of colon cancer cells to a mitogenic stimulation.[169]

1.5.3. EGFR Signalling Pathways

The HER/ERBB family consists of four transmembrane receptors, including EGFR (HER1/erbB-1), HER2 (erbB-2/neu), HER3 (erbB-3) and HER4 (erbB-4). The EGFR (HER1/erbB-1) is a protein comprising three major functional domains: an extracellular ligand-binding domain, a short hydrophobic transmembrane domain and an intracellular tyrosine kinase domain.[170]

EGFR signalling is a well-conserved pathway which controls key cellular programmes including survival, proliferation and differentiation both during development and postnatally.[171] The enactment of these diverse cellular programmes requires that receptor signals with adequate strength and duration are generated to produce responses that are either binary, such as cell proliferation, or graded such as cell motility.[164]

Under physiological conditions, specific soluble ligands selectively bind to the extracellular domains of EGFR. Seven genetically distinct ligands have been shown to be capable of binding with EGFR including EGF, transforming growth factor-α (TGF-α), heparin-binding EGF, amphiregulin, betacellulin, epiregulin and neuregulin G2b.[170, 172] The ligand binding to the receptor induces a conformational change of the receptor ectodomain that is followed by

receptor dimerisation as a homodimer or as a heterodimer (with other members). EGFR dimerisation stimulates its intrinsic intracellular protein-tyrosine kinase activity. As a result, autophosphorylation of several tyrosine residues within the COOH-terminal tail of the receptors occurs in the cytoplasm.[173, 174] The autophosphorylation stimulates downstream activation and signalling by several other cytoplasmic proteins that associate with the phosphorylated tyrosines through their own phosphotyrosine-binding SH2 domains. These downstream signalling proteins initiate a cascade of intracellular signalling transduction pathways which lead to DNA synthesis and cell proliferation. The specificity and potency of each intracellular signalling cascades are determined by several factors:

- The specific composition of the activating ligand
- Expression of positive and negative regulators
- Receptor dimer constituents
- Array of proteins that associate with the tyrosine phosphorylated domain of the receptors

1.5.3.1. Ras/Raf/mitogen-activated Protein Kinase Pathway

This pathway is a critically important route which regulates cell proliferation and survival. Following EGFR phosphorylation, the complex formed by proteins Grb2 and Sos binds either directly or through association with the adaptor molecule Shc to specific docking sites on the receptor (Figure 1.5).[175] This interaction leads to a conformational modification of Sos which causes Ras activation (Ras-GDP changes to Ras-GTP). Ras-GTP activates Raf-1 that phosphorylates the mitogen-activated protein kinases (MAPK).[176] Activated MAPKs are imported into the nucleus where they phosphorylate specific transcription factors involved in cell proliferation.[177]

1.5.3.2. Phosphatidylinositol 3-kinase Pathway

This pathway is mainly involved in cell growth, apoptosis resistance, invasion and migration. Phosphatidylinositol 3-kinase (PI3K) is an enzyme composed of a p85 subunit (regulatory), which is responsible for binding to erbB receptor specific docking sites (Figure 1.5). The docking sites for p85 are absent on EGFR, whereas on HER-3 receptors they are

abundant. Instead, the p85 subunit can interact with EGFR through the docking protein Gab-1.[174, 178]

1.5.3.3. Phospholipase Cγ Pathway

Phospholipase Cγ (PLCγ) interacts directly with activated EGFR and hydrolyses phosphatidylinositol 4,5-diphosphate to form inositol 1,3,5-triphosphate (IP3) and 1,2-diacylglycerol (DAG) as depicted in Figure 1.5. IP3 is important for intracellular calcium release and while DAG serves as a direct activator of protein kinase C. Protein kinase C (PKC) activation can result in MAPK and NH_2-terminal kinase activation.[174]

1.5.3.4. Signal Transducers and Activators of the Transcription Pathway

Signal transducers and activators of transcription (STAT) proteins interact with phosphotyrosine docking residues on the EGFR via their SH2 domain. Upon dimerisation, they translocate to the nucleus and induce the expression of specific target genes (Figure 1.5).[179]

1.5.3.5. Src Kinase Pathways

Src plays a critical role in cell proliferation, migration, adhesion, angiogenesis, and immune function.[180] Src is located in the cytosol and activates a series of other proteins including PI3K, and STAT proteins as shown in Figure 1.5.[180] Src serves as a signal transducer and an enhancer of EGFR activation.[181] However, it may also be involved in resistance to EGFR therapies through independent activation or association with other receptors.[174]

1.5.4. Mechanism of Action of EGFR Inhibitors

The most clinically advanced approaches to inhibit EGFR include the use of monoclonal antibodies which act at the EGFR extracellular ligand-binding site of the receptor, and the use of small molecule tyrosine kinase inhibitors (TKIs) which function at the intracellular tyrosine kinase domain of the EGFR. TKIs bind to the intracellular domain, which prevents the tyrosine kinase activation and phosphorylation by competing for the intracellular ATP-binding sites, therefore, this leads to inhibition of EGFR signalling pathways.[182] Gefitinib (Iressa) and

erlotinib (Tarceva) are some of the well-known ATP-competitive EGFR TKIs.[174, 178] In addition to these mentioned clinically approved strategies, other approaches suggest using antisense oligonucleotides and ribozymes in order to block receptor translation.[183]

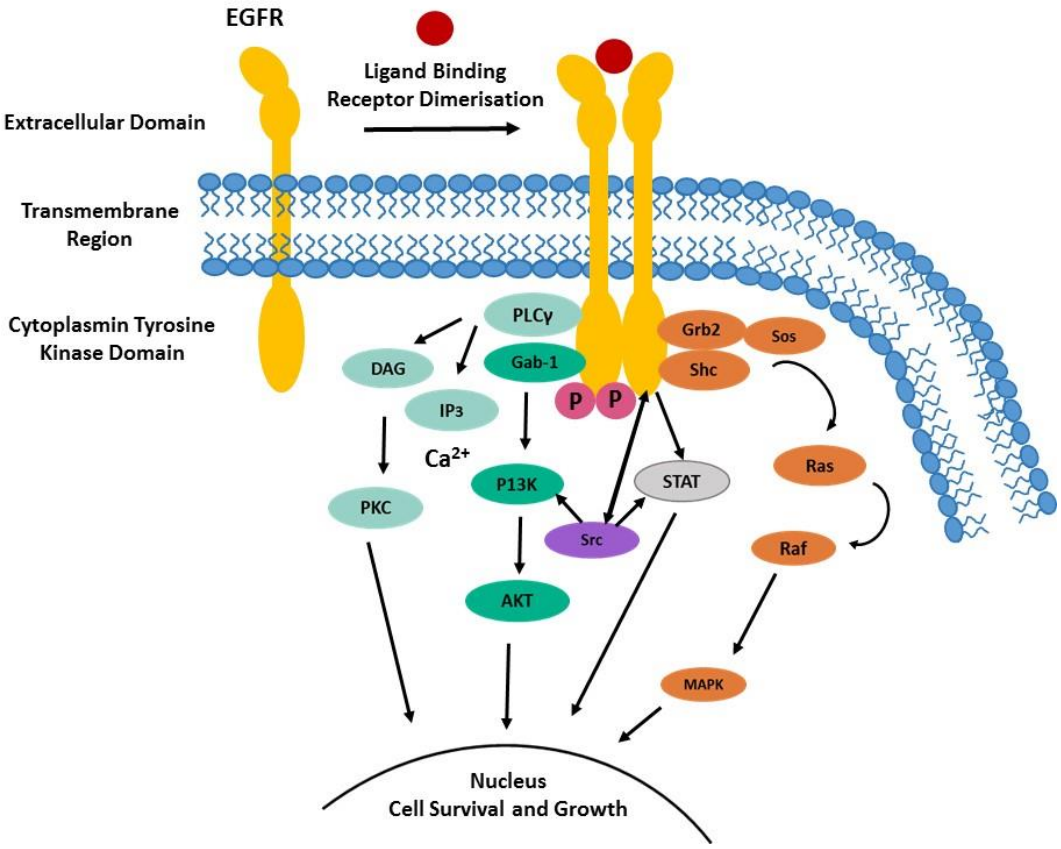

Figure 1.5. Schematic representation of major EGFR signalling pathways.[178, 184, 185]

1.5.5. Thiourea Derivatives as Inhibitors of EGFR

The cytotoxicity and genotoxicity of anticancer drugs for normal cells are major concerns in cancer therapy and increases the risk of inducing secondary malignancy.[186] A sufficient dose of anticancer drug in order to kill cancer cells is normally toxic to normal tissues and cells and leads to several side effects, which limits the efficacy of treatment. In recent years, there has been a concerted effort to discover and develop novel selective antitumour agents, in order to avoid the undesirable side effects of conventional anticancer compounds. In the search to develop drugs with such capabilities, many different aspects of cancer biology have to be taken into consideration.

Among the anticancer drugs discovered in recent years, thiourea derivatives possess potent anticancer properties. Thiourea-based compounds represent one of the most promising classes of anticancer agents which have been shown a wide range of biological activities.[187] These compounds contain a central hydrophilic component and two hydrophobic moieties forming a butterfly-like conformation. The presence of the thiocarbonyl functional group may alter the properties of the compound exposed to it. For example, the hydrophilicity or hydrophobicity as well as electronic properties have the potential to be changed.[188] Thiourea derivatives have demonstrated potential antitumour activity as a result of their inhibitory activity against receptor tyrosine kinases (RTKs), protein tyrosine kinases (PTKs) and nicotinamide adenine dinucleotide phosphate hydrogen (NADH) oxidase.[142, 189]

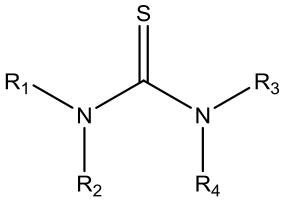

Scheme 1.3. Chemical structure of thiourea derivatives.

In the past two decades many reports have been published on the synthesis of thiourea derivatives and their evaluation as anticancer compounds, mechanism of action as well as the structural activity relationships.[190, 191] In these reports PTKs such as EGFR have been identified as the prime targets of thiourea based chemotherapeutics. Several research groups such as Liu and Jiang *et al.* focused on the antitumour activity of a series of N-substituted-thiourea derivatives which acted as EGFR inhibitors.[192, 193] They reported on the optimisation of anticancer activity through the EGFR role in angiogenesis. Out of the library of forty newly synthesised and bioassayed compounds, four compounds with a pyridine ring in the side chain showed promising inhibitory activity toward human lung adenocarcinoma cell line SPAC1. Two compounds with amine moiety in the side chain showed the most potent tumour anticancer activity toward SPAC1.

Another series of novel N-substituted-N′-phenylthiourea derivative as potential antiproliferative agents have also been reported.[142] By comparison with positive control erlotinib, the compounds showed potent antiproliferative activity for autophosphorylation of EGFR. Assays of different synthesized thiourea compounds against MCF-7 revealed that these thiourea derivatives exhibit significant antiproliferative activity against MCF-7. The

replacement of terminal aryl group with an alkyl group caused a decrease in EGFR inhibitory activity, probably due to a less effective interaction of the alkyl group with the hydrophobic regions. The molecular docking of the most potent thiourea inhibitors into the ATP binding site of EGFR kinase on the binding model was also performed, which demonstrated that thiourea compounds bind effectively to the region with the N–H groups toward the side chain carbonyl group of Leu 768 (amino acid). From this, the external N–H formed a more optimal H-bond interaction, and the hydroxyl group formed a hydrogen bond with amino hydrogen of Gln767.[142]

Zhu *et al*. reported the synthesis of novel thiourea derivatives containing the pyrazole moiety as potent antiproliferative agents for the MCF-7 cell line.[189] Thiourea compounds also displayed a similar characteristic against the MCF-7 breast cancer cell line with IC50 values ranging from 0.08 to 0.71μM. Additionally, these compounds showed inhibited autophosphorylation of EGFR kinases which had IC50 values ranging from 0.07 to 1.36μM. This data was comparable to the positive control erlotinib with IC50 of 0.03 μM.

The important interaction between the thiourea compounds and EGFR can happen through the formation of hydrogen bonds between the thiourea and the carbonyl group of amino acids in the ATP binding site of EGFR.[189, 194] Furthermore, thiourea compounds exhibit several other properties such as antiviral,[195] antibacterial,[187] antimalarial,[196] anti-inflammatory[197] and antifungal (plant growth regulator)[198] properties and thus attract great attention in pharmaceutical industry. Thiourea derivatives have also attracted the attention of synthetic medicinal chemists for developing synthetic methods for the synthesis of these entities with enhanced anticancer activity. Therefore, a thorough detailed investigation into the synthesis more potent thiourea derivatives with EGFR inhibitory properties, as well as their stability under biological conditions, is highly desirable. The importance of such work lies in the possibility that the next generation of thiourea compounds might be more efficacious as anticancer agents when combined with other diagnostic agents.

1.6. Isothiocyanate Compounds for Cancer Therapy

Isothiocyanates (ITCs) are naturally occurring molecules which are formed from glucosinolate (β-thioglucoside N-hydroxysulfates) (GSH) precursors in cruciferous vegetables.[199] GSHs exist as a N-hydroxysulfate with a sulphur linked β–glucose and a variable

side chain containing an alkyl, alkenyl, aromatic, indolyl, or perhaps other moieties (Scheme 1.4).[200] GSHs are usually broken down through hydrolysis catalysed by myrosinase, an enzyme which is released by physical stress such as chewing or chopping of the plant. ITCs are also known as mustard oils and abundant in cruciferous vegetables such as broccoli, Brussel sprouts, watercress, cabbage, horseradish, mustard and cauliflower. ITCs are responsible for the pungent odour and acrid and bitter flavour of condiments such as mustard and horseradish and the biting taste that develops when some cruciferous vegetables are eaten. The term "mustard oil" originates from the flavour of mustard seeds which is mainly due to the presence of abundant quantities of allyl isothiocyanate (AITC).

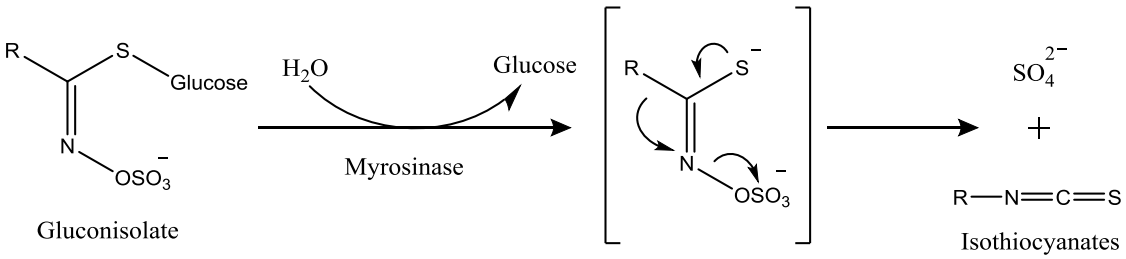

Scheme 1.4. Conversion of glucosinolates to their corresponding isothiocyanates reproduced from Fahey *et al*.[200]

ITCs are reactive compounds with the structure R-N=C=S, where R is an alkyl or aryl group. Their reactivity is contributed particularly with respect to nucleophilic attack at the electron-deficient central carbon atom. Nucleophilic attack of ITCs by thiols forms dithiocarbamates R-N(=S)-SR′ which are unstable under physiological conditions and undergo a reverse reaction, which results in the establishment of an equilibrium as follow:[201, 202]

$$\text{R-N=C=S} + \text{R′SH} \rightleftharpoons \text{RNHC(=S)-SR′}$$

In addition to their characteristic flavours and odours, ITCs have a variety of other important properties such as antibacterial, antifungal, and antiprotozoal actions; the ability to attract or repel insects, the induction of chromosome abnormalities and the inhibition of chemical carcinogenesis. Many of ITCs significantly contribute to the cancer chemopreventive activity of cruciferous vegetables since they reduce activation of carcinogens and increase their detoxification. Some ITCs derived from cruciferous vegetables, such as AITC, sulforaphane (SFN), phenethyl isothiocyanate (PEITC) and benzyl isothiocyanate (BITC), shown in Scheme

1.4, are greatly effective in preventing or reducing the risk of cancer induced by carcinogens in animal models. They have also been recognised to inhibit the growth of various types of cancer cells.[203, 204] The antitumour activity of ITCs happens due to affecting several pathways such as apoptosis, oxidative stress, and cell cycle progression.[201]

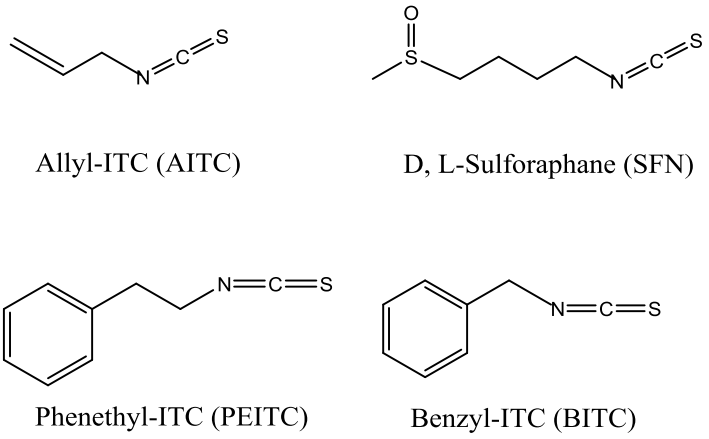

Scheme 1.5. Chemical structures of some ITCs.

1.6.1. Chemopreventive Effects of Isothiocyanates

ITCs can profoundly affect carcinogen metabolism. The ability of ITCs to inhibit chemical carcinogenesis was first documented more than 30 years ago with α-naphthyl isothiocyanate.[205] Interest in these compounds arose from its ability to produce profound proliferative damage in the liver tissue. In long-term feeding experiments this ITC considerably reduced the formation of liver tumours in male Wistar rats in a dose-dependent manner.[206, 207] These findings laid the groundwork for various subsequent studies on the tumour blocking activities of ITCs.

1.6.1.1. Phase II Enzyme Induction

Approximately 20 natural and synthetic ITCs have been shown to block chemically induced carcinogenesis since that time. The anticarcinogenic activities of ITCs have been tested in animal models using various chemical carcinogens such as polycyclic aromatic hydrocarbons and several nitrosamines. Protection is observed in multiple target organs including the lungs, liver, forestomach, small intestine, colon and bladder.[205, 208] The cellular and molecular events affected or regulated by these chemopreventive ITCs include inhibition of Phase I enzymes (e.g. cytochrome P450 enzymes (CYP)), which are involved in the bioactivation of

carcinogens, and induction of Phase II enzymes (e.g. glutathione S-transferases (GST)), responsible in carcinogen detoxification.[209, 210] These enzymes play a critical role in cellular defence against chemical carcinogens and oxidants. Therefore, deficiencies of them lead to increased DNA damage and cancer risk, whereas increased expression of these enzymes, on the other hand, suppresses cancer development.[211] Since ITCs increase the activity of Phase II enzymes but not that of Phase I enzymes, they are referred to as monofunctional inducers.[212] Enhanced expression of most of Phase II genes by ITCs is mediated through the antioxidant responsive element (ARE). Nuclear factor E2-related factor 2 (Nrf2) is a member of the family of transcriptional factors which dimerises and binds to the ARE, resulting in the transcriptional activation of a battery of detoxification and antioxidant proteins.[213] Nrf2 which is sequestered by cytoskeleton-anchored Keap1 protein in the cytoplasm, exists as an inactive form.[214] Following exposure to the extracellular stimuli such as ITCs, Nrf2 is dissociated from Keap1 protein, translocates into the nucleus and binds to the ARE and this leads to the induction of Phase II enzymes (Figure 1.6).

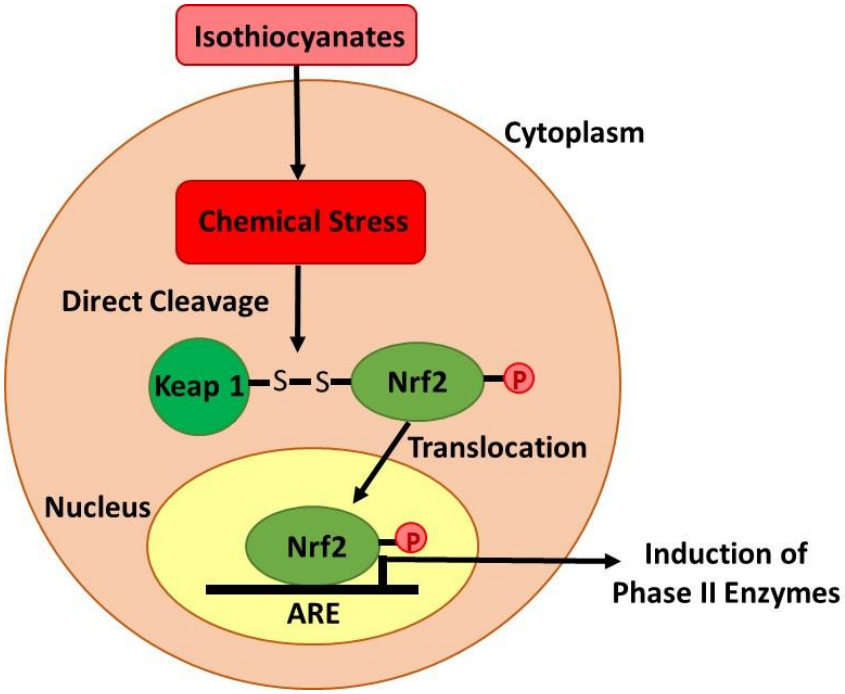

Figure 1.6. Model of the signalling pathways involved in activation of Nrf2 by ITCs to induce Phase II enzymes; reproduced from Keum *et al*.[208]

1.6.1.2. Apoptosis Induction

Apoptosis or programmed cell death is an active process in which dysfunctional cells are removed in order to maintain normal functioning of the tissues. Apoptosis plays an important role as a protective mechanism by eliminating genetically damaged or excess cells that have been improperly induced to divide.[208]

Many reports have demonstrated the induction of apoptosis by ITCs; they exhibit antitumor activity at the post-initiation phase suggesting their additional role in cancer prevention.[205] Mitochondria are damaged by ITC's intracellular metabolites that can accumulate in the cells, and thus mitochondrial damage induced by ITCs leads to apoptosis. Specifically, AITCs are known to inhibit TNF, a protein involved in a type of apoptosis known as extrinsic apoptosis.[215] Another hypothesis in this regard is that, oxidative stress by depletion of intracellular GSH may contribute to subsequent signalling events leading to apoptosis.[208] For instance, depletion of intracellular GSH caused by the treatment with some ITCs such as SFN may play a significant role in the induction of Phase II enzymes as well as apoptotic responses in HepG2 cells.[216] However, this is highly dependent on the amount of SFN added. When the cells are treated with SFN, ARE reporter expression was maximal while no apoptotic responses were observed; however, when the concentration of SFN was increased ARE reporter activity was totally abolished while apoptosis was significantly increased.[216]

1.6.1.3. Induction of Cell Cycle Arrest

When DNA is damaged, cell cycle arrest occurs by activating cellular checkpoints including G1/S or G2/M phase until errors are corrected in the DNA. However, if DNA damage is substantial and irreparable, apoptosis is initiated instead of cell cycle arrest. Therefore, both cell cycle arrest and apoptosis are closely coupled as cellular protective mechanisms which are promising avenues to develop chemopreventive strategies. ITCs have been reported to induce cell cycle arrest possibly by transcriptionally inhibiting cyclin D1 expression in cells, which is a protein required for progression through the G1 phase of the cell cycle.[208]

In general, ITC compounds have many favourable properties that make them attractive for further development as chemopreventive agents for human cancer.[217]

1.6.2. Metabolism of Isothiocyanates

ITCs are metabolised *in vivo* through the mercapturic acid pathway. Initial conjugation of the –N=C=S group with the cysteine thiol of glutathione forms the corresponding conjugates (dithiocarbamates) which are then metabolised sequentially to the cysteinylglycine, cysteine and N-acetylcysteine (NAC) conjugates. These compounds are then excreted and concentrated in the urine.[218]

1.7. Endocytosis Mechanisms

In order to communicate with the biological environment, all different types of cells in the body use the endocytosis process. This process controls the lipid and protein composition of the plasma membrane and is energy-dependant which allows the cell internalisation of ions and biomolecules.[219] More specifically, the internalisation of nutrients and signalling molecules occurs to obtain energy and interact with other cells respectively. In addition, endocytosis is known as the major route in nanomedicine to transport across the cellular membrane. The endocytosis pathways are generally classified into phagocytosis and pinocytosis.

1.7.1. Phagocytosis

Phagocytosis is a special endocytic pathway which is actin-dependent and mainly restricted to professional phagocytes such as macrophages. When phagocytic cells internalise foreign materials (particles larger than 0.5 μm) the phagocytosis pathway is most likely used.[220, 221] NPs which adopt this way of entry into cells need to be recognised by the opsonin firstly, such as immunoglobulin and blood serum proteins. Afterwards, the opsonised NPs bind to the cell surface and interact with the receptor, which will induce the formation of a cup-shaped membrane extension as depicted in Figure1.7.[222] The membrane extensions enclose the NPs and internalise them, which will form phagosomes that have a diameter of 0.5 to 10 μm. At the final stage, the phagosomes move to fuse with lysosomes[223] and the cargo within the phagosomes will be destroyed by acidification and enzymolysis in the lysosomes. Thus, in order to produce desired effects for NPs, they must bypass this route to avoid degradation.[222]

1.7.2. Pinocytosis

Pinocytosis is a major route for the cells to drink fluid and suspensions containing small particles. Based on the proteins involved in the pathways, it is classified to clathrin-dependent endocytosis, caveolae-dependent endocytosis, macropinocytosis and clathrin- and caveolae-independent endocytosis.[222, 224]

1.7.3. Clathrin-dependent Endocytosis

Clathrin-dependent endocytosis is receptor mediated and present in all types of mammalian cells. This type of endocytosis is considered as an important part in cellular entry. Many types of cells use this pathway in order to internalise materials at nanoscale.[221, 225] After NPs interact with receptors on the cell membrane, a kind of cytosolic protein called clathrin-1 polymerises on the cytosolic side of the plasma where the cargo is internalised.[224] After wrapping the NPs inside the cells, the vesicle is pinched off by dynamin (an enzyme responsible for endocytosis) and forms clathrin coated vesicles (CCV) around the internalised material as illustrated in Figure 1.7.[226] CCVs move further inside the cells by using the energy supplied by actin,[227] and the clathrin coat is shed off in the cytosol. The destination of the vesicles is associated with the receptor that NPs' ligands interact with. They can either be transferred to lysosomes for degradation, such as the interaction between low-density lipoprotein particles and LDL receptor, or recycled back to the cell surface, such as when iron-loaded transferrin interact with transferrin receptor.[228]

1.7.4. Caveolae-dependent Endocytosis

Caveolae-dependent endocytosis is another common cellular entry pathway that is receptor mediated. As this pathway could bypass lysosomes, many pathogens including viruses and bacteria select this way to avoid lysosomal degradation.[228] For the same reason, this route is considered to be beneficial for improving both targeting and therapeutic effects. Caveolin is a protein which exists in most cells and plays a dominant role. There are three types of caveolin in mammalian cells: caveolin-3 is muscle specific, while caveolin-1 and -2 are in most non-muscle cells such as endothelial cells and fibroblasts and absent in neurons and leukocytes.[228] NPs or pathogens can bind to the receptors on the plasma membrane and interact with them to

induce the formation of the flask-shaped vesicles, which are then cut off from the membrane by dynamin. Caveolar vesicles require actin to move and transmit within the cell, similar to clathrin-dependent endocytosis. The caveolae vesicles transmit to combine with caveosomes or multivesicular bodies (MTV) which have a neutral pH (Figure 1.7).[229] MTVs containing NPs move along with microtubules towards the endoplasmic reticulum,[230] from which they then can penetrate into the cytosol, and then enter the nuclear envelope via the nuclear pore complex.[222]

Compared to clathrin-dependent endocytosis, this pathway has smaller vesicles and the process takes longer time. The NPs which undertake caveolae-dependent endocytosis, can avoid degradation and enhance the delivery to a target organelle such as endoplasmic reticulum or nucleus, which is significant in terms of the improvement of therapeutic delivery systems.[222]

1.7.5. Macropinocytosis

Macropinocytosis is a non-specific process for the internalisation of surrounding fluids and particles into large vacuoles[228] and commonly defined as a transient clathrin- and caveolin-independent or growth factor-induced endocytosis. This pathway can be found in almost all cells, with few exceptions for example brain microvessel endothelial cells, and is generally begins with external stimulations. The activation of receptor mediates a signalling cascade that causes the formation of membrane ruffles (Figure 1.7). Based on the form of the ruffles, there are different mechanisms of the macropinosomes which get pinched off from the membrane. For example, circular ruffles are cut off by dynamin whereas lamellipodial macropinosomes separated from the membrane is free of dynamin. Depending on the cell type, after separating from the membrane, macropinosomes either move into the cytosol and fuse with lysosomes or travel back to the cell surface of the membrane and release the contents to the extracellular space.[231]

1.7.6. Clathrin- and Caveolae-independent Endocytosis

Clathrin- and caveolae-independent endocytosis is a distinct pathway, which relies on cholesterol and requires specific lipid compositions. Although this pathway is not well understood, dynamins play a dominant role.

When NPs are systemically administered into the body, they are confronted with different types of cells. It is believed that the efficiency of NP endocytosis is dependent on several parameters such as physiochemical properties of NP including size, shape and surface charge and chemistry, as well as cell-specific parameters such as cell type or cell cycle phase.[232] Since NPs have emerged as drug carriers for the treatment of complex diseases, it has become crucial to understand endocytosis mechanisms they overtake.

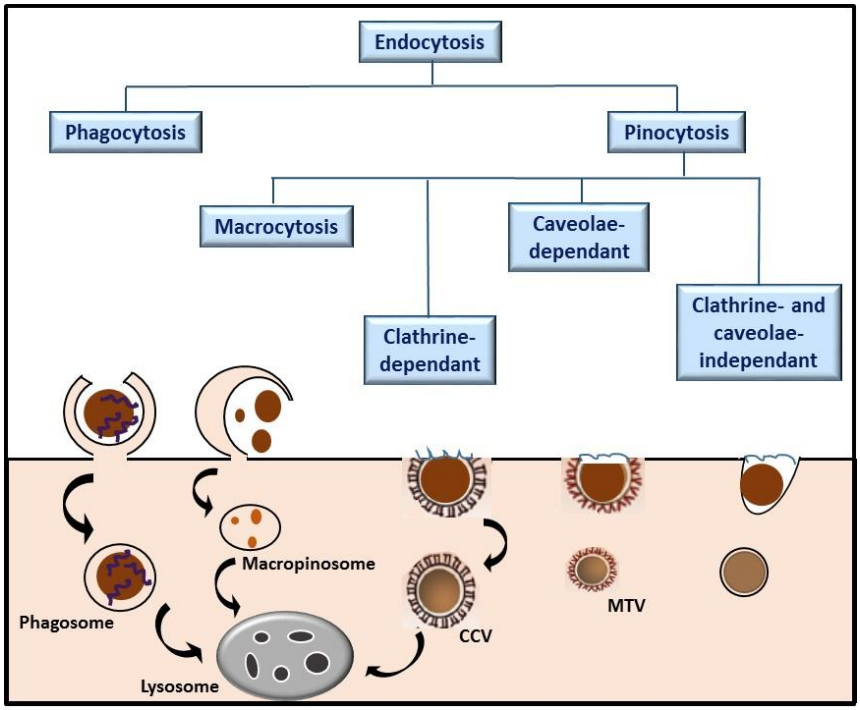

Figure 1.7. NPs internalisation pathways in mammalian cells reproduced from He *et al*.[222]

1.8. Motivation, Aims and Objectives of the Study

Although significant advances have been made in nanomedicine in recent years, one of the remaining key challenges is defining the optimal targeting agents to selectively deliver nano-compounds to cancer tissues. Identifying tumour specific antigens, such as cell surface protein receptors, is the current focus of many research projects, further advancing methods which can recognise cancerous cells among thousands of other normal cells. Therapeutic treatments have been developed to target some of these proteins, and receptor expression is sometimes used as a prognostic indicator. Therefore, compounds such as thiourea derivatives which are known to specifically target these receptors and inhibit their activity can be exploited to improve the targeting properties of therapeutic systems. Moreover, integrating these compounds on the

surface of NPs can increase the functionality of the system. It is well known that SiNPs have a high potential for bioimaging, and thus are known to offer exciting opportunities for design of high performance silicon based nano-agents. This can play a vital role in the efficiency of cell internalisation since the targeting molecule can enhance specific NP–cell surface interactions and increase endocytosis of the NPs. As a result, successful internalisation of NP drug delivery systems, through better targeting, has shown improvements in therapeutic effect.[233-235]

In this thesis, for the first time we report the synthesis of two types of functionalised SiNPs as new multifunctional nanoscale systems. By developing such hybrid NPs, we can exploit the unique optical properties of SiNPs whilst introducing the targeting and therapeutic characteristics of the functional ligands for diagnostic applications. The aims of this thesis are as follows:

- To develop methods of synthesising SiNPs with biologically active ligands.
- To develop functionalised SiNPs with targeting capability on cancerous cells for diagnostic purposes.
- To determine the therapeutic properties of SiNPs functionalised with known anticancer drugs.
- To utilise a range of characterisation methods to evaluate the physiochemical properties of synthesised SiNPs.

To achieve these aims, the following objectives are undertaken:

- To carry out prospective research on the development of hybrid SiNPs, integrating thiourea compounds to develop a diagnostic approach with efficient targeting of cancer cells.
- To explore potential therapeutic properties of functionalised SiNPs, isothiocyanate compounds are conjugated and the resulting effect on cancerous cells evaluated.
- To study and employ the process of hydrosilylation for the synthesis of SiNPs.
- Investigating the structure and physiochemical properties of the synthesised SiNPs using various characterisation techniques and analysis.
- Determining the stabilisation and compatibility of the obtained SiNPs as well as the effect of different synthetic procedures for biomedical applications.
- *In vitro* evaluation of synthesised SiNPs to investigate their potential for further biomedical applications.

- Using a synchrotron FTIR microspectroscopy as a novel technique to investigate the cell internalisation of functionalised SiNPs.

1.9. Thesis Overview

This thesis comprises six chapters dealing with the development and optimisation of methods for the synthesis of stable functionalised SiNPs and their detailed characterisation. The study aims to examine the potential of these synthesised SiNPs for further biomedical applications. A brief description of each chapter is summarised below:

Chapter 1 covers the general introduction for the overall project with the basic concepts and terminology related to nanomaterials, nanoparticles and semiconductor quantum dots. A variety of methods to synthesise SiNPs will be discussed as well as the description of the origin of SiNP luminescence. The concerns and considerations about the cytotoxicity of SiNPs will be explained and a brief overview regarding the biomedical applications of SiNPs. The chemopreventive properties of thiourea and isothiocyanates, used as functional ligands in this project, will be described.

Chapter 2 describes the synthetic procedures for the production of different functionalised SiNPs. Various chemical and physical characterisation techniques used to analyse nanomaterials are discussed. Later on in this chapter, methods for *in vitro* evaluation of the biomedical studies of synthesised SiNPs are discussed.

Chapter 3 describes the preparation of thiourea-functionalised SiNPs using allylamine and sulforaphane, an important anticancer drug, followed by a hydrosilylation reaction on the surface of hydrogen terminated SiNPs. The physiochemical properties of SiNPs were investigated using photoluminescence emission, FTIR, and elemental analysis. The size of NPs was measured by TEM and DLS techniques. The MTT assay was employed to evaluate *in vitro* toxicity in Caco-2 and CCD-841 cells. Confocal microscopy was performed on cells before and after the treatment with NPs to evaluate the cell internalisation and flow cytometry was used to confirm the interaction of synthesised NPs with EGFR on the surfaces of cancer cells. The two different methods, top down and bottom up, were used to synthesise amine-functionalised SiNPs as less cytotoxic nanomaterials to be used as control in biological experiments.

A portion of this chapter has appeared in the following publication:

Behray M, Webster C A, Pereira S, Ghosh P, Krishnamurthy A, Al-Jamal W and Chao Y, Synthesis of Diagnostic Silicon Nanoparticles for Targeted Delivery of Thiourea to Epidermal Growth Factor Receptor-Expressing Cancer Cells, *ACS Applied Materials and Interfaces* **2016,** DOI: 10.1021/acsami.5b12283

Chapter 4 discusses the synthesis of isothiocyanate-functionalised SiNPs obtained from two different precursors using bromine-functionalised SiNPs and amine-functionalised SiNPs. All types of NPs were characterised using FTIR and elemental analysis. The size measurement was performed using TEM and DLS and their optical properties were evaluated by PL and UV-vis spectroscopy. The cytotoxicity of ITC SiNPs was evaluated by MTT and their internalisation was examined using the confocal microscopy and flow cytometry assay.

Chapter 5 demonstrates the use of synchrotron-based FTIR microspectroscopy as a novel approach to investigate the cell internalisation of isothiocyanate-functionalised SiNPs in Caco-2 and CCD-841 cell lines. The spectral comparison of cells treated with NPs and control cells is presented showing the individual spectra from both nuclei and cytoplasm of cells and the variations in the protein and phospholipid contents of cells are monitored. The response of cells to changes in their chemical environment was evaluated using the infrared chemical images obtained from the FPA detector.

1.10. References

1. Institution, B. S., Terminology for nanomaterials. *PAS* **2007,** *136*.

2. Dowling, A.; Clift, R.; Grobert, N.; Hutton, D.; Oliver, R.; O'neill, O.; Pethica, J.; Pidgeon, N.; Porritt, J.; Ryan, J., Nanoscience and nanotechnologies: opportunities and uncertainties. *London: The Royal Society & The Royal Academy of Engineering Report* **2004,** *61*, e64.

3. Behari, J., Principles of nanoscience: An overview. *Indian J Exp Biol* **2010,** *48* (10), 1008-1019.

4. Lindsay, S. M., *Introduction to Nanoscience*. Oxford University Press: United States, New York, **2010.**

5. Guston, D. H., *Encyclopedia of nanoscience and society*. Sage Publications: **2010.**

6. Ludovico Cademartiri, G. A. O., *Concepts of nanochemistry* Wiley-VCH, **2009.**

7. Freestone, I.; Meeks, N.; Sax, M.; Higgitt, C., The Lycurgus cup—a roman nanotechnology. *Gold Bulletin* **2007,** *40* (4), 270-277.

8. Nanotechnology and the Ancient Romans: A Breakthrough 1,600 Years in the Making. http://antiquitynow.org/2014/03/06/nanotechnology-and-the-ancient-romans-a-breakthrough-1600-years-in-the-making/ (accessed 6 March **2014**).

9. Colomban, P.; Truong, C., Non-destructive Raman study of the glazing technique in lustre potteries and faience (9–14th centuries): silver ions, nanoclusters, microstructure and processing. *Journal of Raman Spectroscopy* **2004,** *35* (3), 195-207.

10. Reibold, M.; Paufler, P.; Levin, A.; Kochmann, W.; Pätzke, N.; Meyer, D., Materials: Carbon nanotubes in an ancient Damascus sabre. *Nature* **2006,** *444* (7117), 286-286.

11. Murphy, C. J., Nanocubes and nanoboxes. *Science* **2002,** *298* (5601), 2139-2141.

12. Link, S.; El-Sayed, M. A., Optical properties and ultrafast dynamics of metallic nanocrystals. *Annual review of physical chemistry* **2003,** *54* (1), 331-366.

13. Sanderson, K., Sharpest cut from nanotube sword. *Nature news* **2006**.

14. The Medieval Stained Glass Photographic Archive. http://www.therosewindow.com/pilot/Paris-N-Dame/N-rose-Frame.htm (accessed March **2016**).

15. Baratoff, A.; Binnig, G.; Rohrer, H., Scanning tunneling microscopy of semiconductor surfaces. *Journal of Vacuum Science & Technology B* **1983,** *1* (3), 703-704.

16. Lertsatitthanakorn, C.; Rungsiyopas, M.; Therdyothin, A.; Soponronnarit, S., Performance study of a double-pass thermoelectric solar air collector with flat-plate reflectors. *Journal of electronic materials* **2012,** *41* (6), 999-1003.

17. Singh, R.; Nalwa, H. S., Medical Applications of Nanoparticles in Biological Imaging, Cell Labeling, Antimicrobial Agents, and Anticancer Nanodrugs. *J. Biomed. Nanotechnol.* **2011,** *7* (4), 489-503.

18. Tomasina, J.; Lheureux, S.; Gauduchon, P.; Rault, S.; Malzert-Freon, A., Nanocarriers for the targeted treatment of ovarian cancers. *Biomaterials* **2013,** *34* (4), 1073-1101.

19. Giri, S.; Karakoti, A.; Graham, R. P.; Maguire, J. L.; Reilly, C. M.; Seal, S.; Rattan, R.; Shridhar, V., Nanoceria: A Rare-Earth Nanoparticle as a Novel Anti-Angiogenic Therapeutic Agent in Ovarian Cancer. *PLoS One* **2013,** *8* (1), 13.

20. Tarver, T., Food nanotechnology. *Food Technology-Champaign Then Chicago-* **2006,** *60* (11), 22.

21. Novoselov, K. S.; Geim, A. K.; Morozov, S.; Jiang, D.; Zhang, Y.; Dubonos, S. a.; Grigorieva, I.; Firsov, A., Electric field effect in atomically thin carbon films. *science* **2004,** *306* (5696), 666-669.

22. Guldi, D. M.; Rahman, G.; Prato, M.; Jux, N.; Qin, S.; Ford, W., Single-Wall Carbon Nanotubes as Integrative Building Blocks for Solar-Energy Conversion. *Angewandte Chemie* **2005,** *117* (13), 2051-2054.

23. Xie, Y.; Wilson, W.; Ross, F.; Mucha, J.; Fitzgerald, E.; Macaulay, J.; Harris, T., Luminescence and structural study of porous silicon films. *Journal of applied physics* **1992,** *71* (5), 2403-2407.

24. Giuseppe, A. D., *Metrology and Physical Constants*. IOS Press.

25. Meyers, M. A.; Mishra, A.; Benson, D. J., Mechanical properties of nanocrystalline materials. *Progress in materials science* **2006,** *51* (4), 427-556.

26. Liz-Marzán, L.; Kamat, P., Nanoscale materials. **2003.** Boston: Kluwer Academic Publishers. xv.

27. O'Farrell, N., Silicon nanoparticles: applications in cell biology and medicine. *international Journal of Nanomedicine* **2006,** *1* (4), 451-472.

28. Dal Negro, L.; Pavesi, L.; Pucker, G.; Franzo, G.; Priolo, F., Optical gain in silicon nanocrystals. *Optical Materials* **2001,** *17* (1), 41-44.

29. Semonin, O. E.; Luther, J. M.; Beard, M. C., Quantum dots for next-generation photovoltaics. *Materials today* **2012,** *15* (11), 508-515.

30. Weller, H., Colloidal semiconductor Q-particles: chemistry in the transition region between solid state and molecules. *Angewandte Chemie International Edition in English* **1993,** *32* (1), 41-53.

31. Weller, H., Quantized semiconductor particles: a novel state of matter for materials science. *Advanced Materials* **1993,** *5* (2), 88-95.

32. Woggon, U.; Gaponenko, S.; Langbein, W.; Uhrig, A.; Klingshirn, C., Homogeneous linewidth of confined electron-hole-pair states in II-VI quantum dots. *Physical Review B* **1993,** *47* (7), 3684.

33. Brus, L. E., Electron–electron and electron-hole interactions in small semiconductor crystallites: The size dependence of the lowest excited electronic state. *The Journal of chemical physics* **1984,** *80* (9), 4403-4409.

34. Nirmal, M.; Brus, L., Luminescence photophysics in semiconductor nanocrystals. *Accounts of Chemical Research* **1999,** *32* (5), 407-414.

35. Zorman, B.; Ramakrishna, M. V.; Friesner, R., Quantum confinement effects in CdSe quantum dots. *The Journal of Physical Chemistry* **1995,** *99* (19), 7649-7653.

36. Einevoll, G., Confinement of excitons in quantum dots. *Physical Review B* **1992,** *45* (7), 3410.

37. Chang, H.; Sun, S.-Q., Silicon nanoparticles: Preparation, properties, and applications. *Chinese Physics B* **2014,** *23* (8).

38. Zhang, X.; Neiner, D.; Wang, S.; Louie, A. Y.; Kauzlarich, S. M., A new solution route to hydrogen-terminated silicon nanoparticles: synthesis, functionalization and water stability. *Nanotechnology* **2007,** *18* (9).

39. Dasog, M.; Yang, Z.; Regli, S.; Atkins, T. M.; Faramus, A.; Singh, M. P.; Muthuswamy, E.; Kauzlarich, S. M.; Tilley, R. D.; Veinot, J. G. C., Chemical Insight into the Origin of Red and Blue Photoluminescence Arising from Freestanding Silicon Nanocrystals. *Acs Nano* **2013,** *7* (3), 2676-2685.

40. Ledoux, G.; Guillois, O.; Porterat, D.; Reynaud, C.; Huisken, F.; Kohn, B.; Paillard, V., Photoluminescence properties of silicon nanocrystals as a function of their size. *Physical Review B* **2000,** *62* (23), 15942-15951.

41. Belomoin, G.; Therrien, J.; Smith, A.; Rao, S.; Twesten, R.; Chaieb, S.; Nayfeh, M. H.; Wagner, L.; Mitas, L., Observation of a magic discrete family of ultrabright Si nanoparticles. *Applied Physics Letters* **2002,** *80* (5), 841-843.

42. English, D. S.; Pell, L. E.; Yu, Z. H.; Barbara, P. F.; Korgel, B. A., Size tunable visible luminescence from individual organic monolayer stabilized silicon nanocrystal quantum dots. *Nano Letters* **2002,** *2* (7), 681-685.

43. Schuppler, S.; Friedman, S. L.; Marcus, M. A.; Adler, D. L.; Xie, Y. H.; Ross, F. M.; Chabal, Y. J.; Harris, T. D.; Brus, L. E.; Brown, W. L.; Chaban, E. E.; Szajowski, P. F.; Christman, S. B.; Citrin, P. H., Size, Shape, And Composition Of Luminescent Species In Oxidized Si Nanocrystals And H-Passivated Porous Si. *Physical Review B* **1995,** *52* (7), 4910-4925.

44. Rogozhina, E.; Belomoin, G.; Smith, A.; Abuhassan, L.; Barry, N.; Akcakir, O.; Braun, P. V.; Nayfeh, M. H., Si-N linkage in ultrabright, ultrasmall Si nanoparticles. *Applied Physics Letters* **2001,** *78* (23), 3711-3713.

45. Rosso-Vasic, M.; Spruijt, E.; van Lagen, B.; De Cola, L.; Zuilhof, H., Alkyl-Functionalized Oxide-Free Silicon Nanoparticles: Synthesis and Optical Properties. *Small* **2008,** *4* (10), 1835-1841.

46. Sato, S.; Swihart, M. T., Propionic-acid-terminated silicon nanoparticles: Synthesis and optical characterization. *Chemistry of Materials* **2006,** *18* (17), 4083-4088.

47. Fujioka, K.; Hiruoka, M.; Sato, K.; Manabe, N.; Miyasaka, R.; Hanada, S.; Hoshino, A.; Tilley, R. D.; Manome, Y.; Hirakuri, K.; Yamamoto, K., Luminescent passive-oxidized silicon quantum dots as biological staining labels and their cytotoxicity effects at high concentration. *Nanotechnology* **2008,** *19* (41).

48. Zou, J.; Sanelle, P.; Pettigrew, K. A.; Kauzlarich, S. M., Size and spectroscopy of silicon nanoparticles prepared via reduction of SiCl4. *Journal of Cluster Science* **2006,** *17* (4), 565-578.

49. Mitas, L.; Therrien, J.; Twesten, R.; Belomoin, G.; Nayfeh, M., Effect of surface reconstruction on the structural prototypes of ultrasmall ultrabright Si29 nanoparticles. *Applied Physics Letters* **2001,** *78* (13), 1918-1920.

50. Allan, G.; Delerue, C.; Lannoo, M., Excitons in silicon nanostructures. *Journal of luminescence* **1993,** *57* (1-6), 239-242.

51. Nayfeh, M. H.; Rigakis, N.; Yamani, Z., Photoexcitation of Si-Si surface states in nanocrystallites. *Physical Review B* **1997,** *56* (4), 2079.

52. Heath, J. R., A liquid-solution-phase synthesis of crystalline silicon. *Science* **1992,** *258* (5085), 1131-1133.

53. Huan, C.; Shu-Qing, S., Silicon nanoparticles: Preparation, properties, and applications. *Chinese Physics B* **2014,** *23* (8), 088102.

54. Froner, E.; Adamo, R.; Gaburro, Z.; Margesin, B.; Pavesi, L.; Rigo, A.; Scarpa, M., Luminescence of porous silicon derived nanocrystals dispersed in water: dependence on initial porous silicon oxidation. *Journal of Nanoparticle Research* **2006,** *8* (6), 1071-1074.

55. Bhattacharjee, S.; Rietjens, I. M.; Singh, M. P.; Atkins, T. M.; Purkait, T. K.; Xu, Z.; Regli, S.; Shukaliak, A.; Clark, R. J.; Mitchell, B. S., Cytotoxicity of surface-functionalized silicon and germanium nanoparticles: the dominant role of surface charges. *Nanoscale* **2013,** *5* (11), 4870-4883.

56. Canham, L. T., Silicon quantum wire array fabrication by electrochemical and chemical dissolution of wafers. *Applied Physics Letters* **1990,** *57* (10), 1046-1048.

57. Kang, Z.; Liu, Y.; Lee, S.-T., Small-sized silicon nanoparticles: new nanolights and nanocatalysts. *Nanoscale* **2011,** *3* (3), 777-791.

58. Heinrich, J. L.; Curtis, C. L., Luminescent colloidal silicon suspensions from porous silicon. *Science* **1992,** *255* (5040), 66.

59. Cronin, B.; Germanium, S., In CRC Handbook of Thermoelectrics. CRC Press Boca Raton, FL: **1995.**

60. Wolkin, M.; Jorne, J.; Fauchet, P.; Allan, G.; Delerue, C., Electronic states and luminescence in porous silicon quantum dots: the role of oxygen. *Physical Review Letters* **1999,** *82* (1), 197.

61. Belomoin, G.; Rogozhina, E.; Therrien, J.; Braun, P.; Abuhassan, L.; Nayfeh, M.; Wagner, L.; Mitas, L., Effects of surface termination on the band gap of ultrabright Si 29 nanoparticles: Experiments and computational models. *Physical Review B* **2002,** *65* (19), 193406.

62. Lie, L. H.; Duerdin, M.; Tuite, E. M.; Houlton, A.; Horrocks, B. R., Preparation and characterisation of luminescent alkylated-silicon quantum dots. *Journal of Electroanalytical Chemistry* **2002,** *538*, 183-190.

63. Chao, Y.; Siller, L.; Krishnamurthy, S.; Coxon, P. R.; Bangert, U.; Gass, M.; Kjeldgaard, L.; PatoleO, S. N.; Lie, L. H.; O'Farrell, N.; Alsop, T. A.; Houlton, A.; Horrocks, B. R., Evaporation and deposition of alkyl-capped silicon nanocrystals in ultrahigh vacuum. *Nature Nanotechnology* **2007,** *2* (8), 486-489.

64. Chao, Y.; Wang, Q.; Pietzsch, A.; Hennies, F.; Ni, H., Soft X-ray induced oxidation on acrylic acid grafted luminescent silicon quantum dots in ultrahigh vacuum. *Physica Status Solidi a-Applications and Materials Science* **2011,** *208* (10), 2424-2429.

65. Bley, R. A.; Kauzlarich, S. M.; Davis, J. E.; Lee, H. W., Characterization of silicon nanoparticles prepared from porous silicon. *Chemistry of materials* **1996,** *8* (8), 1881-1888.

66. Sailor, M. J.; Wu, E. C., Photoluminescence-Based Sensing With Porous Silicon Films, Microparticles, and Nanoparticles. *Advanced Functional Materials* **2009,** *19* (20), 3195-3208.

67. Furukawa, S.; Miyasato, T., Quantum size effects on the optical band gap of microcrystalline Si: H. *Physical Review B* **1988,** *38* (8), 5726.

68. Liu, S.-m.; Sato, S.; Kimura, K., Synthesis of luminescent silicon nanopowders redispersible to various solvents. *Langmuir* **2005,** *21* (14), 6324-6329.

69. Bux, S. K.; Blair, R. G.; Gogna, P. K.; Lee, H.; Chen, G.; Dresselhaus, M. S.; Kaner, R. B.; Fleurial, J. P., Nanostructured bulk silicon as an effective thermoelectric material. *Advanced Functional Materials* **2009,** *19* (15), 2445-2452.

70. Lam, C.; Zhang, Y.; Tang, Y.; Lee, C.; Bello, I.; Lee, S., Large-scale synthesis of ultrafine Si nanoparticles by ball milling. *Journal of crystal growth* **2000,** *220* (4), 466-470.

71. Heintz, A. S.; Fink, M. J.; Mitchell, B. S., Mechanochemical Synthesis of Blue Luminescent Alkyl/Alkenyl-Passivated Silicon Nanoparticles. *Advanced Materials* **2007,** *19* (22), 3984-3988.

72. Hata, K.; Yoshida, S.; Fujita, M.; Yasuda, S.; Makimura, T.; Murakami, K.; Shigekawa, H., Self-assembled monolayer as a template to deposit silicon nanoparticles fabricated by laser ablation. *Journal of Physical Chemistry B* **2001,** *105* (44), 10842-10846.

73. Umezu, I.; Kondo, I.; Sugimura, A., Formation of surface stabilized Si nanocrystal by pulsed laser ablation in hydrogen gas. *Applied Physics A* **2008,** *93* (3), 717-720.

74. Shirahata, N.; Linford, M. R.; Furumi, S.; Pei, L.; Sakka, Y.; Gates, R. J.; Asplund, M. C., Laser-derived one-pot synthesis of silicon nanocrystals terminated with organic monolayers. *Chemical Communications* **2009,** (31), 4684-4686.

75. Wilcoxon, J.; Samara, G.; Provencio, P., Optical and electronic properties of Si nanoclusters synthesized in inverse micelles. *Physical Review B* **1999,** *60* (4), 2704.

76. Warner, J. H.; Hoshino, A.; Yamamoto, K.; Tilley, R., Water-Soluble Photoluminescent Silicon Quantum Dots. *Angewandte Chemie* **2005,** *117* (29), 4626-4630.

77. Baldwin, R. K.; Pettigrew, K. A.; Ratai, E.; Augustine, M. P.; Kauzlarich, S. M., Solution reduction synthesis of surface stabilized silicon nanoparticles. *Chem. Commun.* **2002,** (17), 1822-1823.

78. Baldwin, R. K.; Pettigrew, K. A.; Garno, J. C.; Power, P. P.; Liu, G.-y.; Kauzlarich, S. M., Room temperature solution synthesis of alkyl-capped tetrahedral shaped silicon nanocrystals. *Journal of the American Chemical Society* **2002,** *124* (7), 1150-1151.

79. Pettigrew, K. A.; Liu, Q.; Power, P. P.; Kauzlarich, S. M., Solution synthesis of alkyl- and alkyl/alkoxy-capped silicon nanoparticles via oxidation of Mg2Si. *Chemistry of materials* **2003,** *15* (21), 4005-4011.

80. Neiner, D.; Chiu, H. W.; Kauzlarich, S. M., Low-temperature solution route to macroscopic amounts of hydrogen terminated silicon nanoparticles. *Journal of the American Chemical Society* **2006,** *128* (34), 11016-11017.

81. Rosso-Vasic, M.; Spruijt, E.; Popović, Z.; Overgaag, K.; Van Lagen, B.; Grandidier, B.; Vanmaekelbergh, D.; Domínguez-Gutiérrez, D.; De Cola, L.; Zuilhof, H., Amine-terminated silicon nanoparticles: synthesis, optical properties and their use in bioimaging. *Journal of Materials Chemistry* **2009,** *19* (33), 5926-5933.

82. Wang, J.; Ye, D.-X.; Liang, G.-H.; Chang, J.; Kong, J.-L.; Chen, J.-Y., One-step synthesis of water-dispersible silicon nanoparticles and their use in fluorescence lifetime imaging of living cells. *Journal of Materials Chemistry B* **2014,** *2* (27), 4338-4345.

83. Littau, K.; Szajowski, P.; Muller, A.; Kortan, A.; Brus, L., A luminescent silicon nanocrystal colloid via a high-temperature aerosol reaction. *The Journal of Physical Chemistry* **1993,** *97* (6), 1224-1230.

84. Fojtik, A.; Henglein, A., Luminescent colloidal silicon particles. *Chemical Physics Letters* **1994,** *221* (5-6), 363-367.

85. Holmes, J. D.; Ziegler, K. J.; Doty, R. C.; Pell, L. E.; Johnston, K. P.; Korgel, B. A., Highly luminescent silicon nanocrystals with discrete optical transitions. *Journal of the American Chemical Society* **2001,** *123* (16), 3743-3748.

86. Veinot, J. G., Synthesis, surface functionalization, and properties of freestanding silicon nanocrystals. *Chemical Communications* **2006,** (40), 4160-4168.

87. Li, X.; He, Y.; Talukdar, S. S.; Swihart, M. T., Process for preparing macroscopic quantities of brightly photoluminescent silicon nanoparticles with emission spanning the visible spectrum. *Langmuir* **2003,** *19* (20), 8490-8496.

88. Li, X.; He, Y.; Swihart, M. T., Surface functionalization of silicon nanoparticles produced by laser-driven pyrolysis of silane followed by HF-HNO3 etching. *Langmuir* **2004,** *20* (11), 4720-4727.

89. Belomoin, G.; Therrien, J.; Smith, A.; Rao, S.; Twesten, R.; Chaieb, S.; Nayfeh, M.; Wagner, L.; Mitas, L., Observation of a magic discrete family of ultrabright Si nanoparticles. *Applied Physics Letters* **2002,** *80* (5), 841-843.

90. Kelly, J. A.; Shukaliak, A. M.; Fleischauer, M. D.; Veinot, J. G., Size-dependent reactivity in hydrosilylation of silicon nanocrystals. *Journal of the American Chemical Society* **2011,** *133* (24), 9564-9571.

91. Wilson, W. L.; Szajowski, P.; Brus, L., Quantum confinement in size-selected, surface-oxidized silicon nanocrystals. *SCIENCE-NEW YORK THEN WASHINGTON-* **1993,** *262*, 1242-1242.

92. Lide, D. R., *Handbook of Chemistry and Physics*. CRC Press **2000.**

93. Rogozhina, E. V.; Eckhoff, D. A.; Gratton, E.; Braun, P. V., Carboxyl functionalization of ultrasmall luminescent silicon nanoparticles through thermal hydrosilylation. *Journal of Materials Chemistry* **2006,** *16* (15), 1421-1430.

94. Linford, M. R.; Fenter, P.; Eisenberger, P. M.; Chidsey, C. E., Alkyl monolayers on silicon prepared from 1-alkenes and hydrogen-terminated silicon. *Journal of the American Chemical Society* **1995,** *117* (11), 3145-3155.

95. Hua, F.; Swihart, M. T.; Ruckenstein, E., Efficient surface grafting of luminescent silicon quantum dots by photoinitiated hydrosilylation. *Langmuir* **2005,** *21* (13), 6054-6062.

96. Li, Z.; Ruckenstein, E., Water-soluble poly (acrylic acid) grafted luminescent silicon nanoparticles and their use as fluorescent biological staining labels. *Nano Letters* **2004,** *4* (8), 1463-1467.

97. de Smet, L. C.; Zuilhof, H.; Sudhölter, E. J.; Lie, L. H.; Houlton, A.; Horrocks, B. R., Mechanism of the hydrosilylation reaction of alkenes at porous silicon: experimental and computational deuterium labeling studies. *The Journal of Physical Chemistry B* **2005,** *109* (24), 12020-12031.

98. Wang, Q.; Ni, H.; Pietzsch, A.; Hennies, F.; Bao, Y.; Chao, Y., Synthesis of water-dispersible photoluminescent silicon nanoparticles and their use in biological fluorescent imaging. *Journal of Nanoparticle Research* **2011,** *13* (1), 405-413.

99. Wang, Q.; Bao, Y.; Zhang, X.; Coxon, P. R.; Jayasooriya, U. A.; Chao, Y., Uptake and Toxicity Studies of Poly-Acrylic Acid Functionalized Silicon Nanoparticles in Cultured Mammalian Cells. *Advanced Healthcare Materials* **2012,** *1* (2), 189-198.

100. Stewart, M. P.; Buriak, J. M., New approaches toward the formation of silicon-carbon bonds on porous silicon. *Comments on inorganic chemistry* **2002,** *23* (3), 179-203.

101. Buriak, J. M., Organometallic chemistry on silicon and germanium surfaces. *Chemical reviews* **2002,** *102* (5), 1271-1308.

102. Speier, J. L., Homogeneous catalysis of hydrosilation by transition metals. *Advances in Organometallic Chemistry* **1979,** *17*, 407-447.

103. Chalk, A. J.; Harrod, J., Homogeneous Catalysis. II. The Mechanism of the Hydrosilation of Olefins Catalyzed by Group VIII Metal Complexes1. *Journal of the American Chemical Society* **1965,** *87* (1), 16-21.

104. Thurn, K. T.; Brown, E. M.; Wu, A.; Vogt, S.; Lai, B.; Maser, J.; Paunesku, T.; Woloschak, G. E., Nanoparticles for applications in cellular imaging. *Nanoscale Research Letters* **2007,** *2* (9), 430-441.

105. Jaiswal, J. K.; Goldman, E. R.; Mattoussi, H.; Simon, S. M., Use of quantum dots for live cell imaging. *Nature Methods* **2004,** *1* (1), 73-78.

106. Michalet, X.; Pinaud, F.; Bentolila, L.; Tsay, J.; Doose, S.; Li, J.; Sundaresan, G.; Wu, A.; Gambhir, S.; Weiss, S., Quantum dots for live cells, in vivo imaging, and diagnostics. *science* **2005,** *307* (5709), 538-544.

107. Chinnathambi, S.; Chen, S.; Ganesan, S.; Hanagata, N., Silicon quantum dots for biological applications. *Advanced healthcare materials* **2014,** *3* (1), 10-29.

108. Salata, O. V., Applications of nanoparticles in biology and medicine. *Journal of nanobiotechnology* **2004,** *2* (1), 3.

109. Ghaderi, S.; Ramesh, B.; Seifalian, A. M., Fluorescence nanoparticles "quantum dots" as drug delivery system and their toxicity: a review. *Journal of drug targeting* **2011,** *19* (7), 475-486.

110. Sharifi, S.; Behzadi, S.; Laurent, S.; Forrest, M. L.; Stroeve, P.; Mahmoudi, M., Toxicity of nanomaterials. *Chemical Society Reviews* **2012,** *41* (6), 2323-2343.

111. Fard, J. K.; Jafari, S.; Eghbal, M. A.; Sina, M.; Farajzadeh, D.; Dastmalchi, S.; Haddadi, R.; Brooshghalan, S. E.; Farajniya, S.; Nayebi, A. M., A Review of Molecular Mechanisms Involved in Toxicity of Nanoparticles. **2015**.

112. Sabella, S.; Carney, R. P.; Brunetti, V.; Malvindi, M. A.; Al-Juffali, N.; Vecchio, G.; Janes, S. M.; Bakr, O. M.; Cingolani, R.; Stellacci, F., A general mechanism for intracellular toxicity of metal-containing nanoparticles. *Nanoscale* **2014,** *6* (12), 7052-7061.

113. Lin, W.; Huang, Y.-w.; Zhou, X.-D.; Ma, Y., In vitro toxicity of silica nanoparticles in human lung cancer cells. *Toxicology and applied pharmacology* **2006,** *217* (3), 252-259.

114. Goodman, C. M.; McCusker, C. D.; Yilmaz, T.; Rotello, V. M., Toxicity of gold nanoparticles functionalized with cationic and anionic side chains. *Bioconjugate chemistry* **2004,** *15* (4), 897-900.

115. Pradines, B.; Lievin-Le Moal, V.; Vauthier, C.; Ponchel, G.; Loiseau, P. M.; Bouchemal, K., Cell line-dependent cytotoxicity of poly (isobutylcyanoacrylate) nanoparticles coated with chitosan and thiolated chitosan: Insights from cultured human epithelial HeLa, Caco2/TC7 and HT-29/MTX cells. *International journal of pharmaceutics* **2015,** *491* (1), 17-20.

116. Lewinski, N.; Colvin, V.; Drezek, R., Cytotoxicity of nanoparticles. *small* **2008,** *4* (1), 26-49.

117. Fiorito, S.; Serafino, A.; Andreola, F.; Bernier, P., Effects of fullerenes and single-wall carbon nanotubes on murine and human macrophages. *Carbon* **2006,** *44* (6), 1100-1105.

118. Takahashi, H.; Niidome, Y.; Niidome, T.; Kaneko, K.; Kawasaki, H.; Yamada, S., Modification of gold nanorods using phosphatidylcholine to reduce cytotoxicity. *Langmuir* **2006,** *22* (1), 2-5.

119. Mosmann, T., Rapid colorimetric assay for cellular growth and survival: application to proliferation and cytotoxicity assays. *Journal of immunological methods* **1983,** *65* (1-2), 55-63.

120. Altman, S. A.; Randers, L.; Rao, G., Comparison of trypan blue dye exclusion and fluorometric assays for mammalian cell viability determinations. *Biotechnology progress* **1993,** *9* (6), 671-674.

121. Derfus, A. M.; Chan, W. C.; Bhatia, S. N., Probing the cytotoxicity of semiconductor quantum dots. *Nano letters* **2004,** *4* (1), 11-18.

122. Kondoh, M.; Araragi, S.; Sato, K.; Higashimoto, M.; Takiguchi, M.; Sato, M., Cadmium induces apoptosis partly via caspase-9 activation in HL-60 cells. *Toxicology* **2002,** *170* (1), 111-117.

123. Shen, H. M.; Yang, C. F.; Ong, C. N., Sodium selenite-induced oxidative stress and apoptosis in human hepatoma HepG2 cells. *International Journal of Cancer* **1999,** *81* (5), 820-828.

124. Derfus, A.; Chan, W.; Bhatia, S., Probing the cytotoxicity of CdSe quantum dots with surface modification. *Nano Letters* **2004,** *4* (1), 11-18.

125. Shiohara, A.; Hoshino, A.; Hanaki, K. i.; Suzuki, K.; Yamamoto, K., On the cyto-toxicity caused by quantum dots. *Microbiology and immunology* **2004,** *48* (9), 669-675.

126. Rikans, L. E.; Yamano, T., Mechanisms of cadmium-mediated acute hepatotoxicity. *Journal of biochemical and molecular toxicology* **2000,** *14* (2), 110-117.

127. Chin, V.; Collins, B. E.; Sailor, M. J.; Bhatia, S. N., Compatibility of primary hepatocytes with oxidized nanoporous silicon. *Advanced Materials* **2001,** *13* (24), 1877.

128. Liu, J.; Erogbogbo, F.; Yong, K.-T.; Ye, L.; Liu, J.; Hu, R.; Chen, H.; Hu, Y.; Yang, Y.; Yang, J., Assessing clinical prospects of silicon quantum dots: studies in mice and monkeys. *ACS nano* **2013,** *7* (8), 7303-7310.

129. Tu, C.; Ma, X.; House, A.; Kauzlarich, S. M.; Louie, A. Y., PET imaging and biodistribution of silicon quantum dots in mice. *ACS medicinal chemistry letters* **2011,** *2* (4), 285-288.

130. Fujioka, K.; Hiruoka, M.; Sato, K.; Manabe, N.; Miyasaka, R.; Hanada, S.; Hoshino, A.; Tilley, R. D.; Manome, Y.; Hirakuri, K., Luminescent passive-oxidized silicon quantum

dots as biological staining labels and their cytotoxicity effects at high concentration. *Nanotechnology* **2008,** *19* (41), 415102.

131. Shiohara, A.; Hanada, S.; Prabakar, S.; Fujioka, K.; Lim, T. H.; Yamamoto, K.; Northcote, P. T.; Tilley, R. D., Chemical Reactions on Surface Molecules Attached to Silicon Quantum Dots. *Journal of the American Chemical Society* **2010,** *132* (1), 248-253.

132. Alsharif, N. H.; Berger, C. E.; Varanasi, S. S.; Chao, Y.; Horrocks, B. R.; Datta, H. K., Alkyl-Capped Silicon Nanocrystals Lack Cytotoxicity and have Enhanced Intracellular Accumulation in Malignant Cells via Cholesterol-Dependent Endocytosis. *Small* **2009,** *5* (2), 221-228.

133. Ahire, J. H.; Wang, Q.; Coxon, P. R.; Malhotra, G.; Brydson, R.; Chen, R.; Chao, Y., Highly Luminescent and Nontoxic Amine-Capped Nanoparticles from Porous Silicon: Synthesis and Their Use in Biomedical Imaging. *Acs Applied Materials & Interfaces* **2012,** *4* (6), 3285-3292.

134. McVey, B. F.; Tilley, R. D., Solution synthesis, optical properties, and bioimaging applications of silicon nanocrystals. *Accounts of chemical research* **2014,** *47* (10), 3045-3051.

135. Pérez, L.; Flores, M.; Avalos, J.; San Miguel, L.; Resto, O.; Fonseca, L. In Comparative study of the growth curves of B. subtilis, K. pneumoniae, C. xerosis and E. coli bacteria in medium containing nanometric silicon particles, *MRS Proceedings*, *Cambridge Univ Press*: **2002;** p F3. 6.

136. He, Y.; Fan, C.; Lee, S.-T., Silicon nanostructures for bioapplications. *Nano Today* **2010,** *5* (4), 282-295.

137. Erogbogbo, F.; Yong, K.-T.; Roy, I.; Xu, G.; Prasad, P. N.; Swihart, M. T., Biocompatible luminescent silicon quantum dots for imaging of cancer cells. *Acs Nano* **2008,** *2* (5), 873-878.

138. Shiohara, A.; Prabakar, S.; Faramus, A.; Hsu, C.-Y.; Lai, P.-S.; Northcote, P. T.; Tilley, R. D., Sized controlled synthesis, purification, and cell studies with silicon quantum dots. *Nanoscale* **2011,** *3* (8), 3364-3370.

139. Erogbogbo, F.; Yong, K.-T.; Roy, I.; Hu, R.; Law, W.-C.; Zhao, W.; Ding, H.; Wu, F.; Kumar, R.; Swihart, M. T., In vivo targeted cancer imaging, sentinel lymph node mapping and multi-channel imaging with biocompatible silicon nanocrystals. *ACS nano* **2010,** *5* (1), 413-423.

140. Wells, A., EGF receptor. *The international journal of biochemistry & cell biology* **1999,** *31* (6), 637-643.

141. Hickey, K.; Grehan, D.; Reid, L. M.; O'Briain, S.; Walsh, T. N.; Hennessy, T. P., Expression of epidermal growth factor receptor and proliferating cell nuclear antigen predicts response of esophageal squamous cell carcinoma to chemoradiotherapy. *Cancer* **1994,** *74* (6), 1693-1698.

142. Li, H.-Q.; Yan, T.; Yang, Y.; Shi, L.; Zhou, C.-F.; Zhu, H.-L., Synthesis and structure–activity relationships of N-benzyl-N-(X-2-hydroxybenzyl)-N′-phenylureas and thioureas as antitumor agents. *Bioorganic & medicinal chemistry* **2010,** *18* (1), 305-313.

143. Kumar, V.; Singh Chimni, S., Recent Developments on Thiourea Based Anticancer Chemotherapeutics. *Anti-Cancer Agents in Medicinal Chemistry (Formerly Current Medicinal Chemistry-Anti-Cancer Agents)* **2015,** *15* (2), 163-175.

144. Perry, J. E.; Grossmann, M. E.; Tindall, D. J., Epidermal growth factor induces cyclin D1 in a human prostate cancer cell line. *The Prostate* **1998,** *35* (2), 117-124.

145. Noonberg, S. B.; Benz, C. C., Tyrosine kinase inhibitors targeted to the epidermal growth factor receptor subfamily. *Drugs* **2000,** *59* (4), 753-767.

146. Woodburn, J., The epidermal growth factor receptor and its inhibition in cancer therapy. *Pharmacology & therapeutics* **1999,** *82* (2), 241-250.

147. Sung, T.; Miller, D. C.; Hayes, R. L.; Alonso, M.; Yee, H.; Newcomb, E. W., Preferential inactivation of the p53 tumor suppressor pathway and lack of EGFR amplification distinguish de novo high grade pediatric astrocytomas from de novo adult astrocytomas. *Brain pathology* **2000,** *10* (2), 249-259.

148. Salomon, D. S.; Brandt, R.; Ciardiello, F.; Normanno, N., Epidermal Growth Factor-Related Peptides And Their Receptors In Human Malignancies. *Critical Reviews in Oncology/Hematology* **1995,** *19* (3), 183-232.

149. Nicholson, R.; Gee, J.; Barrow, D.; Pamment, J.; Knowlden, J.; McClelland, R., Endocrine resistance in breast cancer can involve a switch towards EGFR signaling pathways and a gain of sensitivity to an EGFR-selective tyrosine kinase inhibitor, ZD1839. *Clin Cancer Res* **1999,** *5*, 3735S.

150. Akimoto, T.; Hunter, N. R.; Buchmiller, L.; Mason, K.; Ang, K. K.; Milas, L., Inverse relationship between epidermal growth factor receptor expression and radiocurability of murine carcinomas. *Clinical Cancer Research* **1999,** *5* (10), 2884-2890.

151. Chen, Z.; Ke, L.; Yuan, X.; Adler-Storthz, K., Correlation of cisplatin sensitivity with differential alteration of EGFR expression in head and neck cancer cells. *Anticancer research* **1999,** *20* (2A), 899-902.

152. Ciardiello, F.; Tortora, G., A novel approach in the treatment of cancer: targeting the epidermal growth factor receptor. *Clinical Cancer Research* **2001,** *7* (10), 2958-2970.

153. Wakeling, A.; Barker, A.; Davies, D.; Brown, D.; Green, L.; Cartlidge, S.; Woodburn, J., Specific inhibition of epidermal growth factor receptor tyrosine kinase by 4-anilinoquinazolines. *Breast cancer research and treatment* **1996,** *38* (1), 67-73.

154. Ward, W. H.; Cook, P. N.; Slater, A. M.; Davies, D. H.; Holdgate, G. A., Epidermal growth factor receptor tyrosine kinase: investigation of catalytic mechanism, structure-based searching and discovery of a potent inhibitor. *Biochemical pharmacology* **1994,** *48* (4), 659-666.

155. Gibson, K.; Grundy, W.; Godfrey, A.; Woodburn, J.; Ashton, S.; Curry, B.; Scarlett, L.; Barker, A.; Brown, D., Epidermal growth factor receptor tyrosine kinase: Structure-activity relationships and antitumour activity of novel quinazolines. *Bioorganic & Medicinal Chemistry Letters* **1997,** *7* (21), 2723-2728.

156. Woodburn, J.; Barker, A. In 4-anilinoquinazolines-A potential new therapy for major human solid tumours overexpressing the EGF receptor, *British Journal Of Cancer, Stockton Press Houndmills, Basingstoke, Hampshire, England* RG21 6XS: **1996;** pp 33-33.

157. Moyer, J. D.; Barbacci, E. G.; Iwata, K. K.; Arnold, L.; Boman, B.; Cunningham, A.; DiOrio, C.; Doty, J.; Morin, M. J.; Moyer, M. P., Induction of apoptosis and cell cycle arrest by CP-358,774, an inhibitor of epidermal growth factor receptor tyrosine kinase. *Cancer research* **1997,** *57* (21), 4838-4848.

158. Lavelle, F., American Association for Cancer Research 1997: progress and new hope in the fight against cancer. *Expert opinion on investigational drugs* **1997,** *6* (6), 771-775.

159. Goldstein, N. I.; Prewett, M.; Zuklys, K.; Rockwell, P.; Mendelsohn, J., Biological efficacy of a chimeric antibody to the epidermal growth factor receptor in a human tumor xenograft model. *Clinical Cancer Research* **1995,** *1* (11), 1311-1318.

160. Prewett, M.; Rockwell, P.; Rockwell, R.; Giorgio, N. A.; Mendelsohn, J.; Scher, H. I.; Goldstein, N. I., The biologic effects of C225, a chimeric monoclonal antibody to the EGFR, on human prostate carcinoma. *Journal of immunotherapy with emphasis on tumor immunology: official journal of the Society for Biological Therapy* **1996,** *19* (6), 419-427.

161. Uckun, F. M.; Narla, R. K.; Zeren, T.; Yanishevski, Y.; Myers, D. E.; Waurzyniak, B.; Ek, O.; Schneider, E.; Messinger, Y.; Chelstrom, L. M., In vivo toxicity, pharmacokinetics, and anticancer activity of Genistein linked to recombinant human epidermal growth factor. *Clinical Cancer Research* **1998,** *4* (5), 1125-1134.

162. Gross, M.; Zorbas, M.; Danels, Y.; Garcia, R.; Gallick, G.; Olive, M.; Brattain, M.; Boman, B.; Yeoman, L., Cellular growth response to epidermal growth factor in colon carcinoma cells with an amplified epidermal growth factor receptor derived from a familial adenomatous polyposis patient. *Cancer research* **1991,** *51* (5), 1452-1459.

163. Radinsky, R.; Risin, S.; Fan, D.; Dong, Z.; Bielenberg, D.; Bucana, C. D.; Fidler, I. J., Level and function of epidermal growth factor receptor predict the metastatic potential of human colon carcinoma cells. *Clinical Cancer Research* **1995,** *1* (1), 19-31.

164. Yarden, Y.; Sliwkowski, M. X., Untangling the ErbB signalling network. *Nature reviews Molecular cell biology* **2001,** *2* (2), 127-137.

165. Goldstein, N. S.; Armin, M., Epidermal growth factor receptor immunohistochemical reactivity in patients with American Joint Committee on cancer stage IV colon adenocarcinoma. *Cancer* **2001,** *92* (5), 1331-1346.

166. McKay, J.; Murray, L.; Curran, S.; Ross, V.; Clark, C.; Murray, G.; Cassidy, J.; McLeod, H., Evaluation of the epidermal growth factor receptor (EGFR) in colorectal tumours and lymph node metastases. *European journal of cancer* **2002,** *38* (17), 2258-2264.

167. Wan, C.-W.; McKnight, M.; Brattain, D.; Brattain, M.; Yeoman, L., Different epidermal growth factor growth responses and receptor levels in human colon carcinoma cell lines. *Cancer letters* **1988,** *43* (1), 139-143.

168. Cunningham, D.; Humblet, Y.; Siena, S.; Khayat, D.; Bleiberg, H.; Santoro, A.; Bets, D.; Mueser, M.; Harstrick, A.; Verslype, C., Cetuximab monotherapy and cetuximab plus

irinotecan in irinotecan-refractory metastatic colorectal cancer. *New England journal of medicine* **2004,** *351* (4), 337-345.

169. Tong, W.; Ellinger, A.; Sheinin, Y.; Cross, H., Epidermal growth factor receptor expression in primary cultured human colorectal carcinoma cells. *British journal of cancer* **1998,** *77* (11), 1792.

170. Harari, P., Epidermal growth factor receptor inhibition strategies in oncology. *Endocrine-related cancer* **2004,** *11* (4), 689-708.

171. Sibilia, M.; Kroismayr, R.; Lichtenberger, B. M.; Natarajan, A.; Hecking, M.; Holcmann, M., The epidermal growth factor receptor: from development to tumorigenesis. *Differentiation* **2007,** *75* (9), 770-787.

172. Watanabe, T.; Shintani, A.; Nakata, M.; Shing, Y.; Folkman, J.; Igarashi, K.; Sasada, R., Recombinant human betacellulin. Molecular structure, biological activities, and receptor interaction. *Journal of Biological Chemistry* **1994,** *269* (13), 9966-9973.

173. Ono, M.; Kuwano, M., Molecular mechanisms of epidermal growth factor receptor (EGFR) activation and response to gefitinib and other EGFR-targeting drugs. *Clinical Cancer Research* **2006,** *12* (24), 7242-7251.

174. Scaltriti, M.; Baselga, J., The epidermal growth factor receptor pathway: a model for targeted therapy. *Clinical Cancer Research* **2006,** *12* (18), 5268-5272.

175. Lowenstein, E.; Daly, R.; Batzer, A.; Li, W.; Margolis, B.; Lammers, R.; Ullrich, A.; Skolnik, E.; Bar-Sagi, D.; Schlessinger, J., The SH2 and SH3 domain-containing protein GRB2 links receptor tyrosine kinases to ras signaling. *Cell* **1992,** *70* (3), 431-442.

176. Hallberg, B.; Rayter, S. I.; Downward, J., Interaction of Ras and Raf in intact mammalian cells upon extracellular stimulation. *Journal of Biological Chemistry* **1994,** *269* (6), 3913-3916.

177. Hill, C. S.; Treisman, R., Transcriptional regulation by extracellular signals: mechanisms and specificity. *Cell* **1995,** *80* (2), 199-211.

178. Arteaga, C. L.; Engelman, J. A., ERBB receptors: from oncogene discovery to basic science to mechanism-based cancer therapeutics. *Cancer cell* **2014,** *25* (3), 282-303.

179. Haura, E. B.; Turkson, J.; Jove, R., Mechanisms of disease: Insights into the emerging role of signal transducers and activators of transcription in cancer. *Nature clinical practice Oncology* **2005,** *2* (6), 315-324.

180. Summy, J. M.; Gallick, G. E., Treatment for advanced tumors: SRC reclaims center stage. *Clinical Cancer Research* **2006,** *12* (5), 1398-1401.

181. Jorissen, R. N.; Walker, F.; Pouliot, N.; Garrett, T. P.; Ward, C. W.; Burgess, A. W., Epidermal growth factor receptor: mechanisms of activation and signalling. *Experimental cell research* **2003,** *284* (1), 31-53.

182. Ciardiello, F., Epidermal growth factor receptor tyrosine kinase inhibitors as anticancer agents. *Drugs* **2000,** *60* (1), 25-32.

183. Ciardiello, F.; Caputo, R.; Troiani, T.; Borriello, G.; Kandimalla, E. R.; Agrawal, S.; Mendelsohn, J.; Bianco, A. R.; Tortora, G., Antisense oligonucleotides targeting the epidermal growth factor receptor inhibit proliferation, induce apoptosis, and cooperate with cytotoxic drugs in human cancer cell lines. *International journal of cancer* **2001,** *93* (2), 172-178.

184. Avraham, R.; Yarden, Y., Feedback regulation of EGFR signalling: decision making by early and delayed loops. *Nature reviews Molecular cell biology* **2011,** *12* (2), 104-117.

185. Citri, A.; Yarden, Y., EGF–ERBB signalling: towards the systems level. *Nature reviews Molecular cell biology* **2006,** *7* (7), 505-516.

186. Aydemir, N.; Bilaloğlu, R., Genotoxicity of two anticancer drugs, gemcitabine and topotecan, in mouse bone marrow in vivo. *Mutation Research/Genetic Toxicology and Environmental Mutagenesis* **2003,** *537* (1), 43-51.

187. Saeed, S.; Rashid, N.; Jones, P. G.; Ali, M.; Hussain, R., Synthesis, characterization and biological evaluation of some thiourea derivatives bearing benzothiazole moiety as potential antimicrobial and anticancer agents. *European Journal of Medicinal Chemistry* **2010,** *45* (4), 1323-1331.

188. Sacht, C.; Datt, M., Synthesis and characterisation of mixed-ligand platinum (II)–sulfoxide complexes,[PtCl (DMSO)(L)], for potential use as chemotherapeutic agents (HL= N, N-dialkyl-N′-(3-R-benzoyl) thiourea). *Polyhedron* **2000,** *19* (11), 1347-1354.

189. Lv, P.-C.; Li, H.-Q.; Sun, J.; Zhou, Y.; Zhu, H.-L., Synthesis and biological evaluation of pyrazole derivatives containing thiourea skeleton as anticancer agents. *Bioorganic & Medicinal Chemistry* **2010,** *18* (13), 4606-4614.

190. Wissner, A.; Overbeek, E.; Reich, M. F.; Floyd, M. B.; Johnson, B. D.; Mamuya, N.; Rosfjord, E. C.; Discafani, C.; Davis, R.; Shi, X., Synthesis and structure-activity relationships of 6, 7-disubstituted 4-anilinoquinoline-3-carbonitriles. The design of an orally active, irreversible inhibitor of the tyrosine kinase activity of the epidermal growth factor receptor (EGFR) and the human epidermal growth factor receptor-2 (HER-2). *Journal of medicinal chemistry* **2003,** *46* (1), 49-63.

191. Tsou, H.-R.; Mamuya, N.; Johnson, B. D.; Reich, M. F.; Gruber, B. C.; Ye, F.; Nilakantan, R.; Shen, R.; Discafani, C.; DeBlanc, R., 6-Substituted-4-(3-bromophenylamino) quinazolines as putative irreversible inhibitors of the epidermal growth factor receptor (EGFR) and human epidermal growth factor receptor (HER-2) tyrosine kinases with enhanced antitumor activity. *Journal of medicinal chemistry* **2001,** *44* (17), 2719-2734.

192. Li, J.; ZHANG, J.; SHEN, X.; DING, J.; XIONG, B.; XIONG, X. s.; LIU, H.; JIANG, H. l., Design, synthesis and antitumor evaluation of a new series of N-substituted-thiourea derivatives1. *Acta pharmacologica sinica* **2006,** *27* (9), 1259-1271.

193. Xiong, X.; Liu, H.; Fu, L.; Li, L.; Li, J.; Luo, X.; Mei, C., Antitumor activity of a new N-substituted thiourea derivative, an EGFR signaling-targeted inhibitor against a panel of human lung cancer cell lines. *Chemotherapy* **2008,** *54* (6), 463-474.

194. Dai, Y.; Hartandi, K.; Ji, Z.; Ahmed, A. A.; Albert, D. H.; Bauch, J. L.; Bouska, J. J.; Bousquet, P. F.; Cunha, G. A.; Glaser, K. B., Discovery of N-(4-(3-Amino-1 H-indazol-4-yl)

phenyl)-N'-(2-fluoro-5-methylphenyl) urea (ABT-869), a 3-Aminoindazole-Based Orally Active Multitargeted Receptor Tyrosine Kinase Inhibitor. *Journal of medicinal chemistry* **2007,** *50* (7), 1584-1597.

195. Karakuş, S.; Küçükgüzel, Ş. G.; Küçükgüzel, İ.; De Clercq, E.; Pannecouque, C.; Andrei, G.; Snoeck, R.; Şahin, F.; Bayrak, Ö. F., Synthesis, antiviral and anticancer activity of some novel thioureas derivedfrom N-(4-nitro-2-phenoxyphenyl)-methanesulfonamide. *European journal of medicinal chemistry* **2009,** *44* (9), 3591-3595.

196. Krajačić, M. B.; Dumić, M.; Novak, P.; Cindrić, M.; Koštrun, S.; Fajdetić, A.; Alihodžić, S.; Brajša, K.; Kujundžić, N., Discovery of novel ureas and thioureas of 3-decladinosyl-3-hydroxy 15-membered azalides active against efflux-mediated resistant Streptococcus pneumoniae. *Bioorganic & medicinal chemistry letters* **2011,** *21* (2), 853-856.

197. Alagarsamy, V.; Meena, S.; Ramseshu, K.; Solomon, V.; Thirumurugan, K.; Dhanabal, K.; Murugan, M., Synthesis, analgesic, anti-inflammatory, ulcerogenic index and antibacterial activities of novel 2-methylthio-3-substituted-5, 6, 7, 8-tetrahydrobenzo (b) thieno [2, 3-d] pyrimidin-4 (3H)-ones. *European journal of medicinal chemistry* **2006,** *41* (11), 1293-1300.

198. Eweis, M.; Elkholy, S.; Elsabee, M., Antifungal efficacy of chitosan and its thiourea derivatives upon the growth of some sugar-beet pathogens. *International Journal of Biological Macromolecules* **2006,** *38* (1), 1-8.

199. Verhoeven, D. T.; Goldbohm, R. A.; van Poppel, G.; Verhagen, H.; van den Brandt, P. A., Epidemiological studies on brassica vegetables and cancer risk. *Cancer Epidemiology Biomarkers & Prevention* **1996,** *5* (9), 733-748.

200. Fahey, J. W.; Zalcmann, A. T.; Talalay, P., The chemical diversity and distribution of glucosinolates and isothiocyanates among plants. *Phytochemistry* **2001,** *56* (1), 5-51.

201. Wu, X.; Zhou, Q.-h.; Xu, K., Are isothiocyanates potential anti-cancer drugs? *Acta Pharmacologica Sinica* **2009,** *30* (5), 501-512.

202. Shapiro, T. A.; Fahey, J. W.; Wade, K. L.; Stephenson, K. K.; Talalay, P., Human metabolism and excretion of cancer chemoprotective glucosinolates and isothiocyanates of cruciferous vegetables. *Cancer Epidemiology Biomarkers & Prevention* **1998,** *7* (12), 1091-1100.

203. Trachootham, D.; Zhang, H.; Zhang, W.; Feng, L.; Du, M.; Zhou, Y.; Chen, Z.; Pelicano, H.; Plunkett, W.; Wierda, W. G., Effective elimination of fludarabine-resistant CLL cells by PEITC through a redox-mediated mechanism. *Blood* **2008,** *112* (5), 1912-1922.

204. Lee, J. W.; Cho, M. K., Phenethyl isothiocyanate induced apoptosis via down regulation of Bcl-2/XIAP and triggering of the mitochondrial pathway in MCF-7 cells. *Archives of pharmacal research* **2008,** *31* (12), 1604-1612.

205. Zhang, Y.; Talalay, P., Anticarcinogenic activities of organic isothiocyanates: chemistry and mechanisms. *Cancer research* **1994,** *54* (7 Supplement), 1976s-1981s.

206. Sidransky, H.; Ito, N.; Verney, E., Influence of α-naphthyl-isothiocyanate on liver tumorigenesis in rats ingesting ethionine and N-2-fluorenylacetamide. *Journal of the National Cancer Institute* **1966,** *37* (5), 677-686.

207. Sasaki, S., Inhibitory effects by alpha-naphthylisothiocyanate on development of hepatoma in rats treated with 3′-methyl-4-dimethylaminoazobenzene. *J. Nara Med. Assoc* **1963,** *14*, 101-115.

208. Keum, Y.-S.; Jeong, W.-S.; Kong, A. T., Chemoprevention by isothiocyanates and their underlying molecular signaling mechanisms. *Mutation Research/Fundamental and Molecular Mechanisms of Mutagenesis* **2004,** *555* (1), 191-202.

209. Moreno, R. L.; Kent, U. M.; Hodge, K.; Hollenberg, P. F., Inactivation of cytochrome P450 2E1 by benzyl isothiocyanate. *Chemical research in toxicology* **1999,** *12* (7), 582-587.

210. Hwang, E.-S.; Jeffery, E. H., Effects of different processing methods on induction of quinone reductase by dietary broccoli in rats. *Journal of medicinal food* **2004,** *7* (1), 95-99.

211. Kensler, T. W., Chemoprevention by inducers of carcinogen detoxication enzymes. *Environmental Health Perspectives* **1997,** *105* (Suppl 4), 965.

212. Prochaska, H. J.; Talalay, P., Regulatory mechanisms of monofunctional and bifunctional anticarcinogenic enzyme inducers in murine liver. *Cancer Research* **1988,** *48* (17), 4776-4782.

213. Itoh, K.; Chiba, T.; Takahashi, S.; Ishii, T.; Igarashi, K.; Katoh, Y.; Oyake, T.; Hayashi, N.; Satoh, K.; Hatayama, I., An Nrf2/small Maf heterodimer mediates the induction of phase II detoxifying enzyme genes through antioxidant response elements. *Biochemical and biophysical research communications* **1997,** *236* (2), 313-322.

214. Itoh, K.; Wakabayashi, N.; Katoh, Y.; Ishii, T.; Igarashi, K.; Engel, J. D.; Yamamoto, M., Keap1 represses nuclear activation of antioxidant responsive elements by Nrf2 through binding to the amino-terminal Neh2 domain. *Genes & development* **1999,** *13* (1), 76-86.

215. Thejass, P.; Kuttan, G., Allyl isothiocyanate (AITC) and phenyl isothiocyanate (PITC) inhibit tumour-specific angiogenesis by downregulating nitric oxide (NO) and tumour necrosis factor-α (TNF-α) production. *Nitric Oxide* **2007,** *16* (2), 247-257.

216. Kim, B.-R.; Hu, R.; Keum, Y.-S.; Hebbar, V.; Shen, G.; Nair, S. S.; Kong, A. T., Effects of glutathione on antioxidant response element-mediated gene expression and apoptosis elicited by sulforaphane. *Cancer research* **2003,** *63* (21), 7520-7525.

217. Hecht, S. S., Inhibition Of Carcinogenesis By Isothiocyanates. *Drug metabolism reviews* **2000,** *32* (3-4), 395-411.

218. Zhang, Y., Cancer-preventive isothiocyanates: measurement of human exposure and mechanism of action. *Mutation Research/Fundamental and Molecular Mechanisms of Mutagenesis* **2004,** *555* (1), 173-190.

219. Iversen, T.-G.; Skotland, T.; Sandvig, K., Endocytosis and intracellular transport of nanoparticles: present knowledge and need for future studies. *Nano Today* **2011,** *6* (2), 176-185.

220. Young, K. D., The selective value of bacterial shape. *Microbiology and molecular biology reviews* **2006,** *70* (3), 660-703.

221. Oh, N.; Park, J.-H., Endocytosis and exocytosis of nanoparticles in mammalian cells. *Int J Nanomedicine* **2014,** *9* (Suppl 1), 51-63.

222. Kou, L.; Sun, J.; Zhai, Y.; He, Z., The endocytosis and intracellular fate of nanomedicines: Implication for rational design. *Asian Journal of Pharmaceutical Sciences* **2013,** *8* (1), 1-10.

223. Aderem, A.; Underhill, D. M., Mechanisms of phagocytosis in macrophages. *Annual review of immunology* **1999,** *17* (1), 593-623.

224. Rappoport, J. Z., Focusing on clathrin-mediated endocytosis. *Biochemical Journal* **2008,** *412* (3), 415-423.

225. Pelkmans, L.; Kartenbeck, J.; Helenius, A., Caveolar endocytosis of simian virus 40 reveals a new two-step vesicular-transport pathway to the ER. *Nature cell biology* **2001,** *3* (5), 473-483.

226. Pucadyil, T. J.; Schmid, S. L., Conserved functions of membrane active GTPases in coated vesicle formation. *Science* **2009,** *325* (5945), 1217-1220.

227. Doherty, G. J.; McMahon, H. T., Mechanisms of endocytosis. *Annual review of biochemistry* **2009,** *78*, 857-902.

228. Benmerah, A.; Lamaze, C., Clathrin-Coated Pits: Vive La Différence? *Traffic* **2007,** *8* (8), 970-982.

229. Parton, R. G.; Simons, K., The multiple faces of caveolae. *Nature reviews Molecular cell biology* **2007,** *8* (3), 185-194.

230. Pelkmans, L.; Püntener, D.; Helenius, A., Local actin polymerization and dynamin recruitment in SV40-induced internalization of caveolae. *Science* **2002,** *296* (5567), 535-539.

231. Mayor, S.; Pagano, R. E., Pathways of clathrin-independent endocytosis. *Nature reviews Molecular cell biology* **2007,** *8* (8), 603-612.

232. Mahmoudi, M.; Saeedi-Eslami, S. N.; Shokrgozar, M. A.; Azadmanesh, K.; Hassanlou, M.; Kalhor, H. R.; Burtea, C.; Rothen-Rutishauser, B.; Laurent, S.; Sheibani, S., Cell "vision": complementary factor of protein corona in nanotoxicology. *Nanoscale* **2012,** *4* (17), 5461-5468.

233. Byrne, J. D.; Betancourt, T.; Brannon-Peppas, L., Active targeting schemes for nanoparticle systems in cancer therapeutics. *Advanced drug delivery reviews* **2008,** *60* (15), 1615-1626.

234. Davis, M. E.; Chen, Z.; Shin, D. M., Nanoparticle therapeutics: an emerging treatment modality for cancer. *Nature Reviews Drug Discovery* **2008,** *7* (9), 771-782.

235. Cho, K.; Wang, X.; Nie, S.; Shin, D. M., Therapeutic nanoparticles for drug delivery in cancer. *Clinical cancer research* **2008,** *14* (5), 1310-1316.

Chapter 2:

Methods and Materials

2.1. Materials

The following chapter describes the synthesis methods, experimental apparatus and chemicals used in the work presented in the thesis. This includes an overview of the preparation methods used in the synthesis of silicon nanoparticles conjugated by allylamine, allyl bromide, thiourea and isothiocyanate functional groups. Following this, the characterisation techniques, such as chemical analysis, optical and size measurements, and biological methods are provided.

All chemicals were employed without further purification unless specified. The following materials, reagents and solvents have been used in the following work.

Table 2.1. List of chemicals and materials.

Substance	Source	Description
Acetone	Sigma Aldrich	99.5%
Dichloromethane (DCM)	Sigma Aldrich	99%
Dimethylsulfoxide (DMSO)	Fisher Scientific	≥99.9%
Ethanol (EtOH)	Sigma Aldrich	99.8 %
Ethyl Acetate (EtOAc)	Fisher Scientific	99.9%
Hexane	Fisher Scientific	99.9%
Iso-Propanol	Sigma Aldrich	≥99.7%
Tetrahydrofuran (THF)	Fisher Scientific	99.5%, dried by reflux over sodium and benzophenone and collected by distillation
Toluene	Fisher Scientific	99.9 %, dried by reflux over molten sodium and collected by distillation.
Allyl Isothiocyanate (AITC)	Sigma Aldrich	94%, stabilized with 0.01% alpha-tocopherol

3-Amino-1-propene (Allylamine)	Sigma Aldrich	>99%
3-aminopropyl trimethoxysilane (APTES)	Sigma Aldrich	97%
3-Bromo-1-propene (Allyl Bromide)	Sigma Aldrich	99%
Ascorbate Sodium (AS)	Sigma Aldrich	≥98%
Carbon Disulphide (CS_2)	Sigma Aldrich	≥99.9%
Chloroplatinic Acid (H_2PtCl_6)	Sigma Aldrich	8 wt. % in H_2O 0.05M
Dicyandiamide	Sigma Aldrich	99%
Hydrofluoric Acid (HF)	Argos Organics	48% in water
L-Sulforaphane	Toronto Research Chemicals	≥95%
Magnesium Sulphate ($MgSO_4$)	Sigma Aldrich	97%
Potassium Thiocyanate (KSCN)	Sigma Aldrich	≥99%
Triethylamine (Et_3N)	Sigma Aldrich	≥99%
Anti-EGFR Antibody	Abcam	Primary Antibody 0.2 mg/ml, 1:1000
Anti-rabbit IgG, HRP-linked Antibody	Abcam	Secondary Antibody 2 mg/ml BSA, 1:1000
Ammonium Chloride (NH_4Cl)	Sigma Aldrich	50 mM
3-(4,5-dimethylthiazol-yl)-2,5 diphenyltetrazolium bromide (MTT)	Sigma Aldrich	———

Fetal Bovine Serum (FBS)	Fisher Scientific	_____
Hoechst 33342	Sigma Aldrich	2 µg/mL
Hydrogen Peroxide (H_2O_2) TMB stop solution	Fisher Scientific	Peroxide Solution
Hydromount	Vectashield hard, Vector Labs	Non-fluorescing Mounting Media
Janus Green Whole Stain	Fisher Scientific	_____
L-Glutamine	Fisher Scientific	1% , 200mM
Paraformaldehyde (PFA)	Sigma-Aldrich	4% (v/v)
Penicillin/ Streptomycin (P/S)	Fisher Scientific	5000u
Permeabilization buffer	Fisher Scientific	0.5 % Triton X-100 in PBS
Phosphate Buffered Saline (PBS)	Fisher Scientific	_____
Roswell Park Memorial Institute medium (RPMI)	Fisher Scientific	_____
Sodium Chloride (NaCl)	Sigma Aldrich	0.9 %
3,3',5,5'-Tetramethyl benzidine (TMB substrate)	Fisher Scientific	Peroxidase Substrate
Texas Red-X Phalloidin	Life Technologies	6.6 µM
Trypsin/EDTA	Fisher Scientific	0.25%

Silicon Wafer	Compart Technology Ltd	Thickness: 500 µm, one side polished
Calcium Fluoride (CaF_2) substrates	Crystran Limited	13 mm diameter × 1 mm polished window 10 mm diameter × 1 mm polished window
Potassium Bromide (KBr) substrates	Crystran Limited	13 mm diameter × 1 mm polished window

2.2. Synthetic Procedures

As mentioned earlier in the Chapter 1, there are two major methods to synthesise silicon nanoparticles: bulk reduction (top down) and self-assembly (bottom up). The final silicon nanoparticles synthesised throughout this work were mainly based on the top down method and derived from the nanometre-sized structures found within the surface layers of porous silicon. In this project, porous silicon was obtained by electrochemical etching (anodisation) of crystalline silicon. A bottom up method, although not utilised in the biomedical applications presented in this thesis, is also given to show how large-scale synthesis could be undertaken.

2.2.1. Top Down Synthesis of Silicon Nanoparticles

2.2.1.1. Synthesis of Porous Silicon

Electrochemical etching was carried out in a PTFE (Teflon) cell as previously described by Chao *et al.*[1] The boron-doped p-Si (100) wafer (10 Ωcm resistivity, Compart Technology, Peterborough, UK) was cut into square chips (1.25 × 1.25 cm) by a diamond-tipped scribe to adopt the anodisation cell which is circular in cross-section. The silicon chips were rinsed in absolute ethanol and distilled water in order to eliminate the surface impurities and dried under nitrogen flow. Silicon chips were later dipped briefly in 48 wt.% HF to remove the native oxide layer from the surface followed by rinsing with distilled water and then dried under the nitrogen flow. The silicon chip was positioned between the upper and lower plates of the cell chamber while the polished side of the chip was exposed to the electrolyte solution. The silicon chip

was placed on a platinum foil to improve the conductivity. The upper plate contains an open cavity in the centre in order to hold the electrolyte solution and is fitted with a VitonTM O-ring (Polymax LT) to prevent the etching solution from leaking. The cell was later filled with the electrolyte solution that was 1:1 98 wt.% ethanol to 48 wt.% hydrofluoric acid. The silicon chip acts as anode and HF-resistant electrode serves as a cathode. The addition of the ethanol to the electrolyte solution increases the silicon wafer wettability, improving pore penetration and therefore making the porous silicon layer more homogeneous. Furthermore, ethanol assists in the removal of hydrogen gas evolved in the dissolution reaction from the silicon surface and maintain more uniform current density. The cathode was a piece of tungsten wire (0.5 mm in diameter, Goodfellow UK) coiled into a loop to improve the uniformity of the current distribution and the etching was carried out using a constant current source (Keithley Source Meter 2601). The silicon chip was etched at a current density 400 $mAcm^{-2}$ for 5 min. After etching, the H-terminated porous silicon chip was dried under vacuum for at least 2 h to remove residual hydrofluoric acid and was stored under nitrogen flow until use.[2]

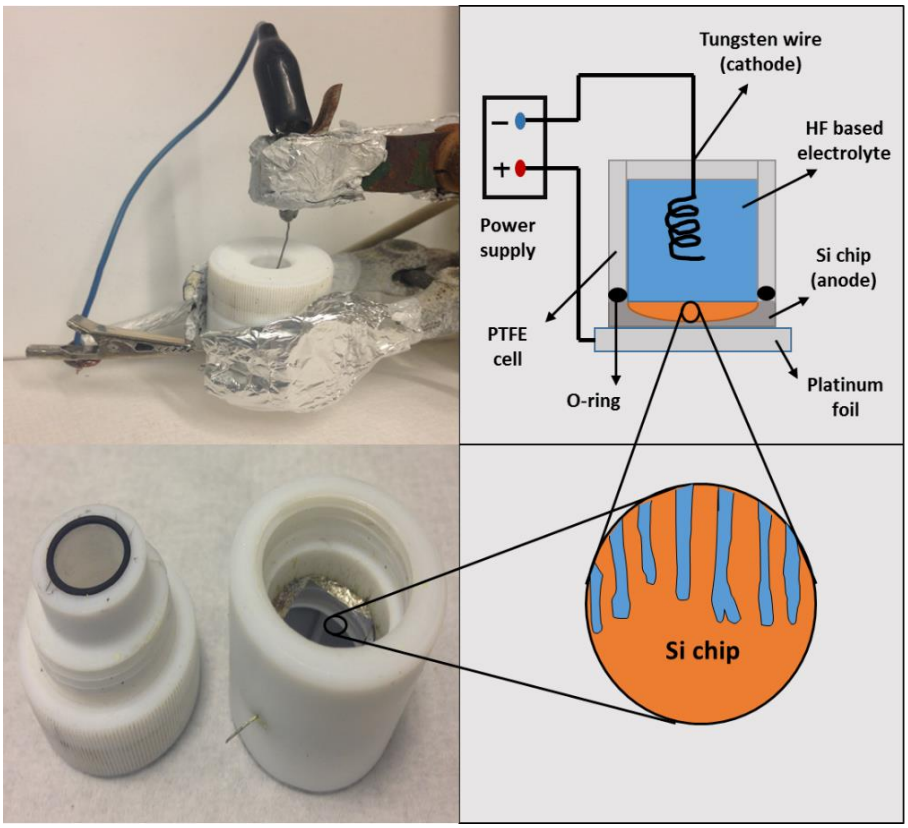

Figure 2.1. Schematic diagram of the synthesis of porous silicon through electrochemical etching. Top right shows the two-electrode electrochemical cell used for etching. Enlarged cross section of porous silicon is shown on bottom right.

$$Si + 4HF_2^- + 2H^+ \rightarrow SiF_6^{2-} + 2HF + 2H_2 \quad \textbf{(Equation 2.1)}$$

2.2.1.2. Synthesis of Amine-functionalised Silicon Nanoparticles

Amine-functionalised silicon nanoparticles were synthesised from H-terminated porous silicon through the hydrosilylation reaction as previously described by Ahire *et al*[3] with some modifications.

Hydrosilylation has been shown as one of the methods to introduce C=C of alkenes to H-terminated silicon surface in order to form Si-C bonding.[4-6] This can be induced through different approaches such as photochemical,[7-9] thermal,[10] UV irradiation[11] and by employing catalysts (normally $EtAlCl_2$ or H_2PtCl_6).[12-14] In this work, the conventional hydrosilylation of alkenes by chloroplatinic acid as catalyst has been applied on the surface of H-terminated silicon nanoparticles.

Amine-functionalised SiNPs were synthesised through a two-step reaction. The first step is the breakup of the nanostructured porous silicon layer to release the silicon nanoparticles and the second step is the functionalisation of the surface of nanoparticles by covalently bonded propylamine.

H-terminated porous silicon, produced from the etching of four chips, was dried in a Schlenk flask under vacuum for 2 h. Chloroplatinic acid solution (H_2PtCl_6 8 wt. % in H_2O, 160 μL, 0.948 mmol, 0.05M) was added to the porous silicon in the presence of iso-propanol (10 mL) as solvent under nitrogen flow. Then allylamine (2 mL, 26.725 mmol) was added to the Schlenk flask followed by 20 min of sonication at room temperature (RT). The reaction mixture was filtered to remove the silicon chips and dried under reduced pressure at 60 ^oC. Heating up to this temperature would evaporate the unreacted allylamine from the product. The product was washed with CH_2Cl_2 (3 × 10 mL) and extracted in water (3 × 5 mL) to remove any by-products as well as the Pt catalyst and then dried under reduced pressure.

Although the amount of the product obtained from the top down methods is batch dependent, the average of 30 mg water soluble amine-functionalised silicon nanoparticles were produced from each reaction.

2.2.1.3. Synthesis of Thiourea-functionalised Silicon Nanoparticles

H-terminated SiNPs were synthesised by galvanostatic anodization of porous silicon layer as reported previously in Section 2.2.1.1.

Thiourea chain was obtained after 6 hrs refluxing of sulforaphane (4 µl, 0.0225 mmol) with 2 equivalent of allylamine (3.37 µl, 0.45 mmol) at RT in dry acetone (5 mL) under N_2. The reaction mixture was dried under reduced pressure.

The product was reacted with dry H-terminated SiNPs obtained from etching of 4 silicon chips for extra 24 hours in ethanol at 35 ^oC. The mixture solution was centrifuged and the solvent was evaporated under the reduced pressure at 60 ^oC. The average of 20 mg of thiourea-functionalized SiNPs was obtained from each batch.

2.2.1.4. Synthesis of Bromine-functionalised Silicon Nanoparticles

H-terminated porous silicon, from etching four chips, were synthesised and dried *in vacou*. Dry toluene (10 mL) was introduce to the reaction mixture followed by sonication for 5 min to dissolve all SiNPs in the solvent. Silicon chips were filtered from the solvent and allyl bromide (2 mL, 23.142 mmol) was added to the reaction mixture. Bromine-functionalised SiNPs were synthesised after refluxing overnight at 65 ^oC. The average of 26 mg bromine-functionalised SiNPs were obtained from each batch.

2.2.1.5. Synthesis of Isothiocyanate-functionalised Silicon Nanoparticles

Two different approaches have been investigated to synthesise isothiocyanate-functionalised SiNPs in this project.

2.2.1.5.1. Use of Amine-functionalised Silicon Nanoparticles as the Precursor

To a mixture of amine-functionalised SiNPs (30 mg) in dry THF (10 mL), CS_2 (2.7 mL, 44.681 mmol) was added dropwise over a period of 20 min while the reaction mixture was cooled with an ice bath. This was followed by stirring the reaction for 3 h. Dicyandiamide (1.5 g, 17.84 mmol) was added followed by more dry THF (10 mL). Next, Et_3N (3 drops) was added

followed by 3 hours stirring at 40 ºC. The solvent was removed and then the compound was extracted in ethyl acetate (3 × 5 mL) and washed with water (3 × 10 mL). The organic layer was dried over magnesium sulphate, filtered and the solvent was removed *in vacuo*. A resultant 28 mg ITC SiNPs was obtained from this procedure.

2.2.1.5.2. Use of Bromine-functionalised Silicon Nanoparticles as the Precursor

A mixture of bromine-functionalised SiNPs (30 mg), Potassium thiocyanate (KSCN) (18 mg, 0.185 mmol) and dry ethanol (10 mL) were placed in a flask, stirred and refluxed at 65 ºC overnight. On completion of the reaction, the mixture was allowed to cool and then the solvent was removed under the reduced pressure. The mixture was extracted into diethyl ether (3 × 10 mL). The organic layer was washed with water (3 × 12 mL), dried over magnesium sulphate and filtered. The filtrate was subjected to a vacuum and produced ~25 mg of the desired isothiocyanate-functionalised SiNPs.

2.2.2. Bottom Up Synthesis of Silicon Nanoparticles

Amine-functionalised SiNPs were synthesised by a method adapted from Wang *et al.*[15] APTES (1 mL, 4.273 mmol) was added to water (4 mL) while stirring. Next, Ascorbate Sodium (AS) (1.25 mL, 10.663 mmol, 0.1 M) was added to the mixture followed by stirring for 20 min. The average of 500 mg water soluble NPs were produced from each reaction.

2.3. Characterisation Techniques

In order to have a better understanding about the characteristics of the synthesised silicon nanoparticles, a variety of experimental techniques were used to explore their properties. This is done to assess the behaviour of these materials for biomedical applications and also allow for the identification of any necessary modifications to the nanocompounds. Furthermore, it is essential to confirm the validity of the synthetic procedures used to prepare nanoparticles through use of different characterisation techniques.

2.3.1. Chemical Analysis

2.3.1.1. Fourier Transform Infrared Spectroscopy (FTIR)

Fourier Transform Infrared Spectroscopy (FTIR) deals with the infrared radiation region of the electromagnetic spectrum which is normally from 4500 cm^{-1} to 500 cm^{-1}. It is a very sensitive instrument for identifying different types of chemical bonds in molecules by producing an infrared absorption spectrum. Each functional group absorbs the radiation at specific frequencies and therefore produces structural information. This is normally unique for each type of molecule and therefore is considered as a molecular fingerprint.

FTIR was used for the identification of specific functionalisation on the surface of SiNPs to confirm the presence of ligands. As nanoparticles that were dispersed in solvents gave weaker signals, all spectra in this work were recorded from powder samples using Attenuated Total Reflection (ATR) FTIR spectroscopy. FTIR Measurements were carried out using a Perkin-Elmer ATR-FTIR spectrometer from the solid sample of SiNPs. The spectra were recorded after 16 scans by correcting the background.

2.3.1.2. X-ray Photoelectron Spectroscopy (XPS)

X-ray photoelectron spectroscopy (XPS) is a quantitative surface analytical technique which is used for chemical analysis. More specifically, XPS measures the elemental composition, empirical formula, chemical and electronic states of the elements that exist within a material. Apart from the surface chemical composition of materials, this method is used to determine the local chemical environment of a given atom.

XPS spectra are obtained by bombarding a material with a beam of X-ray photons under vacuum while simultaneously measuring the kinetic energy and the number of electrons that escape from the top 1 to 10 nm of the material. After the incident X-ray photons interact with the sample, they exchange energy with the inner orbital electrons near the surface of a material and this thus causes ejection of electrons. All electrons, whose binding energy is less than that of the incident X-rays, are ejected from the atom and get detected. This relies on the photoelectric effect. The ejected core electrons have a specific kinetic energy (E_k) that is determined by the following equation:

$$E_k = h\nu - E_b - \Phi \qquad \textbf{(Equation 2.2)}$$

Where E_k is related to the energy of the exciting electron $(h\nu)$ where h represents the Planck constant and ν is the frequency of a photon. The characteristic work function of the material is represented by Φ which is the minimum energy needed to remove an electron from solid and (E_b) is the binding energy of the electron to the atom.[16]

There is a characteristic binding energy for each element that is associated with each core atomic orbital. Thus, each element will give rise to a characteristic set of peaks in the photoelectron spectrum at specific kinetic energies determined by the photon energy and the respective binding energies. Figure 2.2 illustrates the schematic representation of the X-ray photoelectron process.

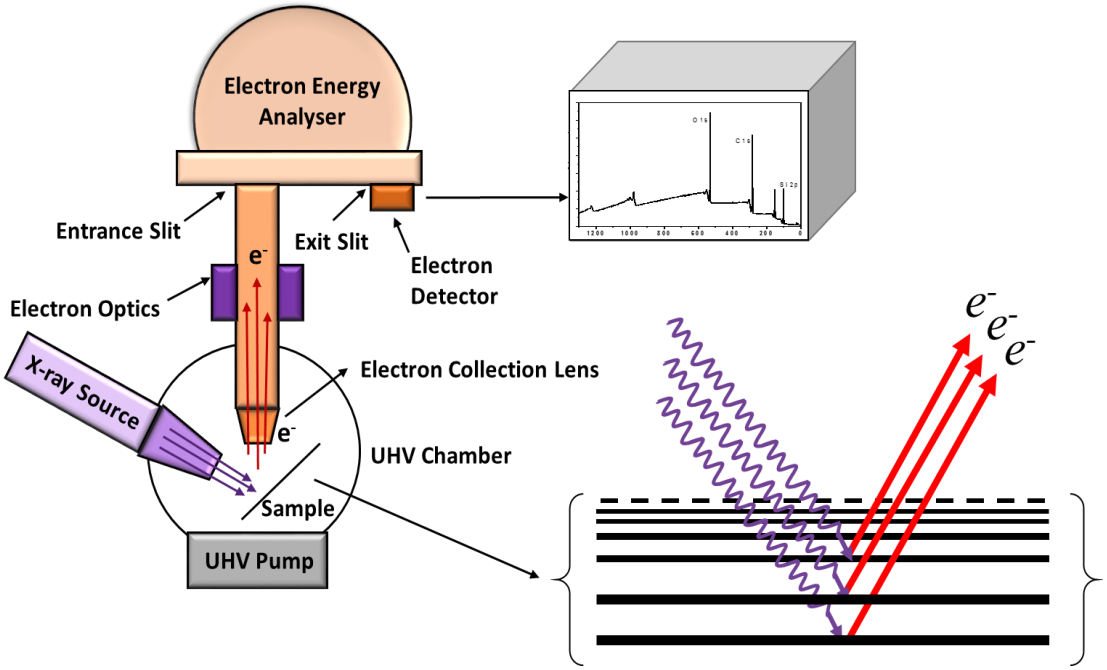

Figure 2.2. Schematic representation of an X-ray photoelectron spectrometer equipped with an X-ray source and a hemispherical analyser showing the basic components of the system and the process occurring during XPS.

XPS measurements were performed on a K-Alpha XPS instrument (Thermo Scientific, East Grinstead, UK) at NEXUS nanolab. A few drops of the concentrated dispersion of SiNPs were drop-cast onto a cleaned gold substrate (10 mm × 10 mm). The film was introduced into a load-

lock attached to an ultra-high vacuum (UHV) chamber in which the typical pressure was maintained below 5×10^{-9} mbar. All spectra were acquired at normal emission with AlKα radiation at 1486.6 eV and a spot size of 400 µm. A pass energy of 200 eV and step size of 0.4 eV was used for the survey spectra and a pass energy of 40 eV and step size of 0.1 eV was used for high resolution spectra. In all photoemission spectra, binding energies (BEs) were referred to the Au 4f7/2 line measured on a gold foil in direct electrical contact with the sample which was found at binding energy of 84 eV. XPS data analysis and peak fitting was performed using CasaXPS software version 2.3.

2.3.1.3. Energy Dispersive X-ray Spectroscopy (EDX)

Energy dispersive X-ray Spectroscopy (EDX) is an analytical technique used in conjugation with Scanning Electron Microscopy (SEM). EDX is used for the elemental analysis or chemical characterisation of a sample. This technique relies on the fundamental principle that each element has a unique atomic structure producing a characteristic set of peaks on a X-ray emission spectrum. Therefore, EDX is based on the interaction of a source of X-ray excitation and the sample analysed. A high-energy beam of charged particles such as electrons or photons, or a beam of X-rays, is focused onto the sample and this will stimulate the emission of X-rays. When the sample is bombarded by the incident beam, electrons are ejected from the inner energy levels of the sample's surface atoms. The resulting electron holes are filled by electrons from a higher-energy state and an X-ray is emitted to balance the energy difference between the two electron states. The energy of the X-rays emitted is characteristic of the energy difference between the two levels and also of the unique atomic structure of the element. Therefore, the elemental composition can be estimated. However, the data obtained from this technique is generally indicative and not particularly sensitive to atomic ratios.[16]

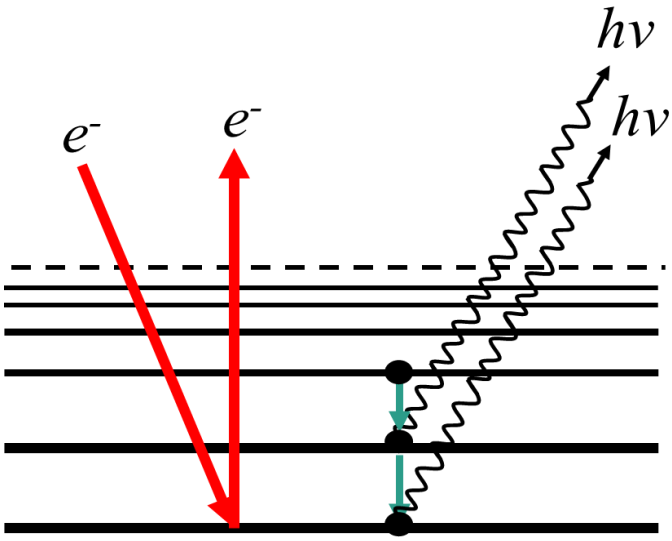

Figure 2.3. Schematic diagram of the process occurring with energy and electrons during EDX.

In this work, the samples were analysed using an EDX sensor attached to a JEOL Scanning Electron Microscope (SEM). Samples in powder form were coated with gold (Au) which was used as the reference. This allowed conduction away from the structure of material when observed under the SEM. Points of interest on the material were identified by SEM and then an individual spectrum was produced for each in turn.

2.3.2. Size and Dispersity Measurement and Surface Charge

2.3.2.1. Transmission Electron Microscopy (TEM)

Transmission electron microscopy (TEM) is an electron based technique used to study materials. TEM is capable of much higher magnifications and has a greater resolution than a light microscope as it can probe the internal structure of the samples providing information about the fine morphological structure details.

In order to avoid the scattering of electrons from the air molecules, the instrument is operated under a high level of vacuum. A beam of electrons transmits through a thin sample and is detected on the other side to form an image. As electrons strongly interact with matter, this gives rise to the ability to use contrast for detection. Dark areas in the images represent regions where electrons do not transmit through, while lighter regions are more electron transparent.[17]

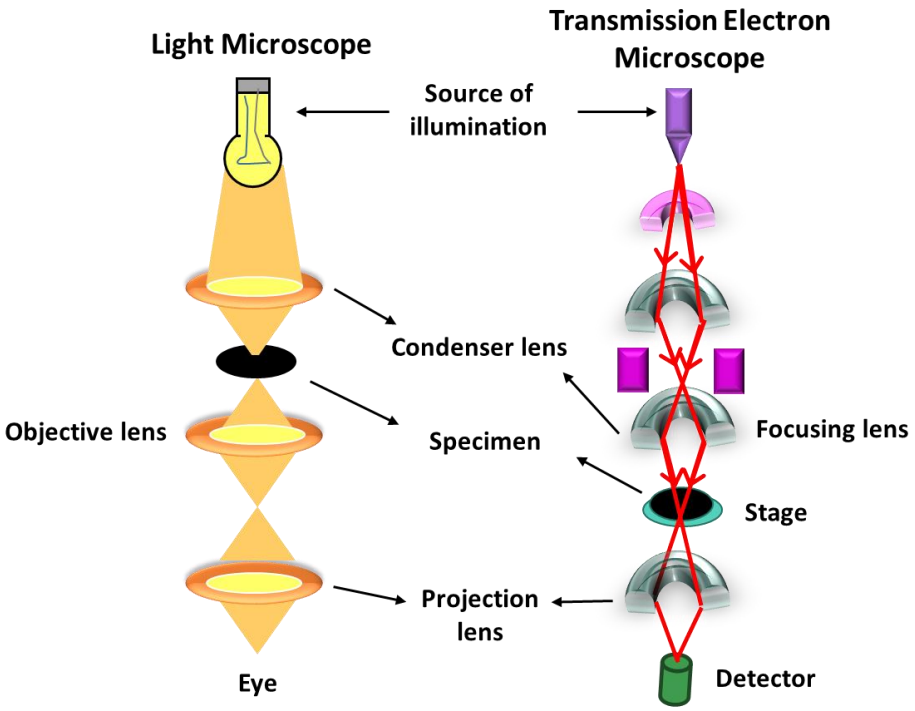

Figure 2.4. Schematic representation of a light and transmission electron microscope with different components showing the optical path through a light microscope and electron beam path through a TEM.

TEM results were used to measure the core particle size in this work as well as to visualise their morphology. Particle size plays a key role in the properties observed in SiNPs. Therefore, it is important to measure the particle size and size distribution of SiNPs. In addition, TEM is able to identify the crystalline structure of the silicon core.

Studies were performed with the JEOL, JEM 2100 microscope running a LaB6 (lanthanum hexaboride crystal) emitter at voltage 200 kV. TEM samples were prepared by drop-casting a dilute suspension of the sample dispersed in an appropriate solvent (according to their solubility) onto a 200 mesh carbon-coated copper grid (Agar Scientific). The grids were dried before the measurement. TEM micrographs were taken at different spots of grids from at least 100 particles from each sample. ImageJ was used to view and analyse the micrographs.

2.3.2.2. Dynamic Light Scattering (DLS)

Dynamic Light Scattering (DLS), which is also known as Photon Correlation Spectroscopy (PCS), is another technique to characterise the size of the nanoparticles typically in the sub-micron region. This technique is capable of particle sizing down to 1 nm diameter. The diameter that is measured in DLS is related to a value that shows how a particle diffuses within a solution and therefore is referred to as a hydrodynamic diameter.

DLS measures the light scattered from a monochromatic light beam such as a laser that passes through a colloidal solution and by analysing the modulation of the scattered light intensity as a function of time. By doing this the hydrodynamic size of particles and particle agglomerates can be determined. DLS works based on the Brownian motions of the particles and relates this to their size. Brownian motion is the movement of particles due to the random collision with the molecules of the liquid that surrounds the particle. An important feature of Brownian motion for DLS is that small particles move quickly and large particles move more slowly. In other words, the larger particles will diffuse slower than smaller particles and the DLS instrument measures the time dependence of the scattered light to generate a correlation function and this can be mathematically linked to a particle size. The velocity of the Brownian motions is defined by the translational diffusion coefficient. Thus, the size of the particle can be calculated by the Stokes- Einstein equation as follow:

$$D_h = \frac{k_B T}{3\pi\eta D_t} \qquad \textbf{(Equation 2.3)}$$

Where D_h is the hydrodynamic diameter, D_t is the translational diffusion coefficient, k_B is Boltzmann's constant, T is absolute temperature and η is the dynamic viscosity.

When DLS sizing data is compared to Transmission Electron Microscopy data, the aggregation state of the particles can be determined. In an unagglomerated suspension, the diameter measured will be similar or slightly larger than the TEM size. If the particles are agglomerated, the DLS measurement is often much larger than the TEM size and can have a high polydispersity index (PdI) which shows the variability in the particle size.

PdI is a measure of the width of the particle size distribution. Polydispersity indices less than 0.1 are typically referred to as monodisperse and can be related to the particle size as the following formula:

$$\boldsymbol{PdI = (\frac{\sigma}{d})^2} \qquad \textbf{(Equation 2.4)}$$

Where $\boldsymbol{\sigma}$ is the standard deviation and $\boldsymbol{d}$ represents the mean diameter.

The hydrodynamic diameter of SiNPs and polydispersity index were determined by DLS measurement with Zetasizer Nano ZS (Malvern Instruments, Malvern, UK) at room temperature, equilibrating samples for 120 seconds prior to the measurement.

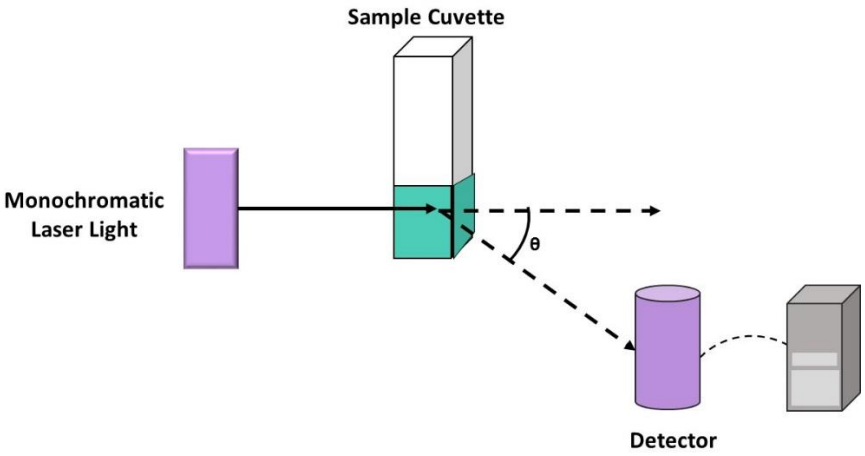

Figure 2.5. Schematic demonstration of a DLS instrument showing different components.[18]

1 mg/mL of SiNP solution was measured in a variety of solvents according to their solubility to assess the stability of the SiNPs under normal and *in vitro* conditions. Size measurements were performed in triplicates and, in order to obtain the diameter of SiNPs as close as possible to real size, ultrasonication and filtration were applied before any measurement. The scattered photons were detected under an angle of 173° and the relative intensity distribution was obtained.

2.3.2.3. Zeta Potential

Zeta potential is a physical property which is displayed by particles in suspension. It can be used to optimise the formulations of suspensions and emulsions. The zeta potential can be used to estimate the long-term stability of compounds, which is necessary for use in biomedical applications.

In an ionic solution, nanoparticles with a certain net charge will have a layer of ions with the corresponding opposite charge which is strongly bound to the surface. This layer is known as the Stern layer. A second layer, called a diffuse outer layer, is comprised of loosely associated ions. These two layers are collectively called the electrical double layer. As the particle moves in the solution, described by Brownian motions or an applied force, a distinction is produced between ions in the diffuse layer that move with the nanoparticle and ions that remain with the bulk dispersant. The electrostatic potential at this "slipping plane" boundary is related to the surface charge of the NP and this is what the zeta potential refers to.

In zeta potential measurements, an electrical field is applied across the sample and the movement of the NPs (electrophoretic mobility) is measured by laser doppler velocimetry (LDV).

In order to calculate the zeta potential, the Henry equation is then used:

$$U_e = \frac{2\,\varepsilon\, z\, f(ka)}{3\eta} \qquad \textbf{(Equation 2.5)}$$

Where, U_e is the electrophoretic mobility, ε is the dielectric constant, z is the zeta potential, $f(ka)$ is the Henry function, a is the particle radius, ka is the ratio of particle radius to double layer thickness (the Debye length) and η represents the absolute zero-shear viscosity of the medium.[19]

Zeta potential of SiNPs was measured using the Zetasizer Nano ZS (Malvern Instruments, Malvern, UK) in water and the measurements were performed in triplicates. Prior to the measurement, ultrasonication and filtration were applied on samples.

2.3.3. Optical Measurements

2.3.3.1. Ultraviolet-Visible Spectroscopy (UV-Vis)

Ultraviolet–visible spectroscopy (UV-Vis) refers to the absorption spectroscopy in the ultraviolet-visible region of electromagnetic spectrum. This technique uses the light in the visible and adjacent (near-UV and near-infrared) ranges. The absorption in the visible range normally affects the colour of the chemicals involved in the sample being analysed. In this spectral region, molecules undergo electronic transitions and the absorption measures transitions from the ground state to the excited state.[20]

A beam of light from a visible or/and UV light source is separated into its component wavelengths by a prism or diffraction grating. Each monochromatic beam is split into two equal intensity beams by a half-mirrored device. The sample beam passes through a cuvette containing the sample being analysed and the other beam, which is the reference, passes through another cuvette containing only the dispersing solvent. The intensity of these beams is measured by electronic detectors and then compared to each other. The ultraviolet region scanned is normally from 200 to 400 nm and the visible regions from 400 to 800 nm.

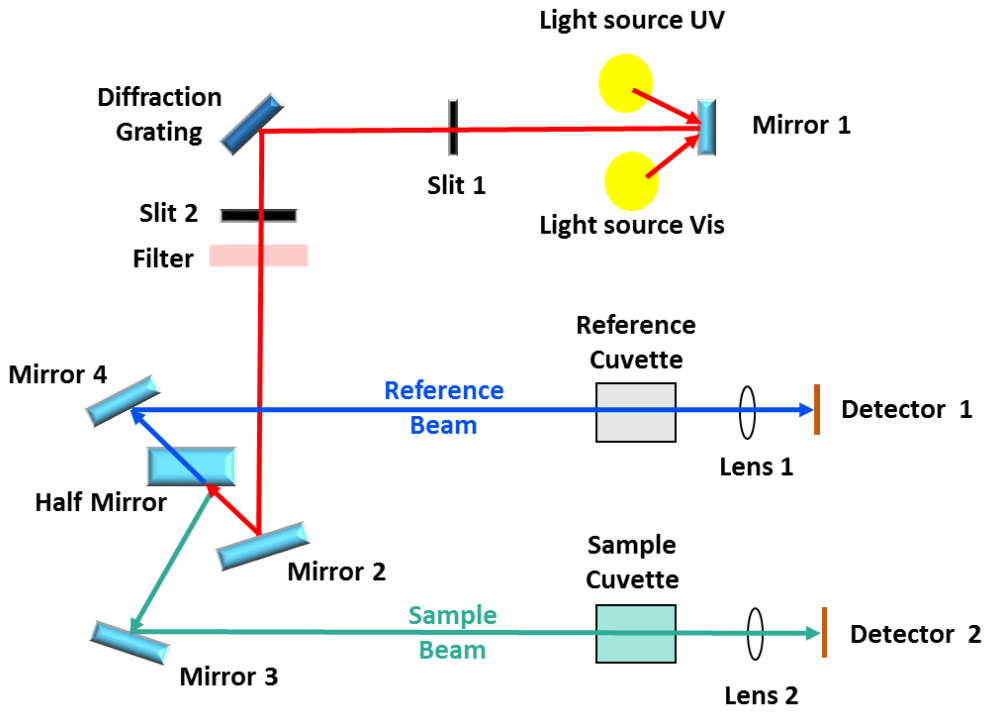

Figure 2.6. A diagram of a typical UV-Vis spectrometer with different components. The sample beam (in green) passes through a cuvette containing the sample dispersed in a solvent and the reference beam (in blue) passes through an identical cuvette containing only the dispersing solvent.[21]

The absorbance of UV-Vis light is related to the concentration of the sample based on the Beer-Lambert Law as follows:

$$A = \varepsilon l c \qquad \textbf{(Equation 2.6)}$$

Where A represents the absorbance, ε is the molar absorptivity, l is the path length of the sample and c is the concentration of the sample.

UV-Vis spectroscopy was used to identify the maximum absorbance of SiNPs. In SiNPs, this is normally seen as a shoulder on the spectrum since SiNPs scatter shorter wavelengths. Therefore, as the spectrum moves towards 200 nm, the absorbance increases due to greater scattering.

The measurement was performed on SiNPs dispersed in suitable solvents. The UV-Vis absorption spectra were recorded by a Perkin-Elmer 35 UV-Vis double-beam spectrometer in a quartz cuvette (10×10 mm). The scan range was over a 200 to 700 nm at a rate of 900 nm/min and the spectra were corrected by subtracting the background contribution from the dispersing solvent.

2.3.3.2. Photoluminescence Spectroscopy (PL)

Photoluminescence spectroscopy (PL) is a method for probing the electronic structure of materials and is considered to be non-contact and non-destructive. Light is directed onto a sample, where it is absorbed and where a process called photo-excitation can occur. The photo-excitation process causes the electrons in a material to jump to a higher electronic state. As it relaxes, the electrons return to a lower energy level through the release of energy in the form of photons. The emission of light or luminescence through this process is photoluminescence or PL.

Photoluminescence is a key property of quantum dots such as SiNPs. This technique can be used to measure the emission wavelength of SiNPs and the optimum excitation wavelength. This data is useful in terms of designing the imaging experiments using these NPs.

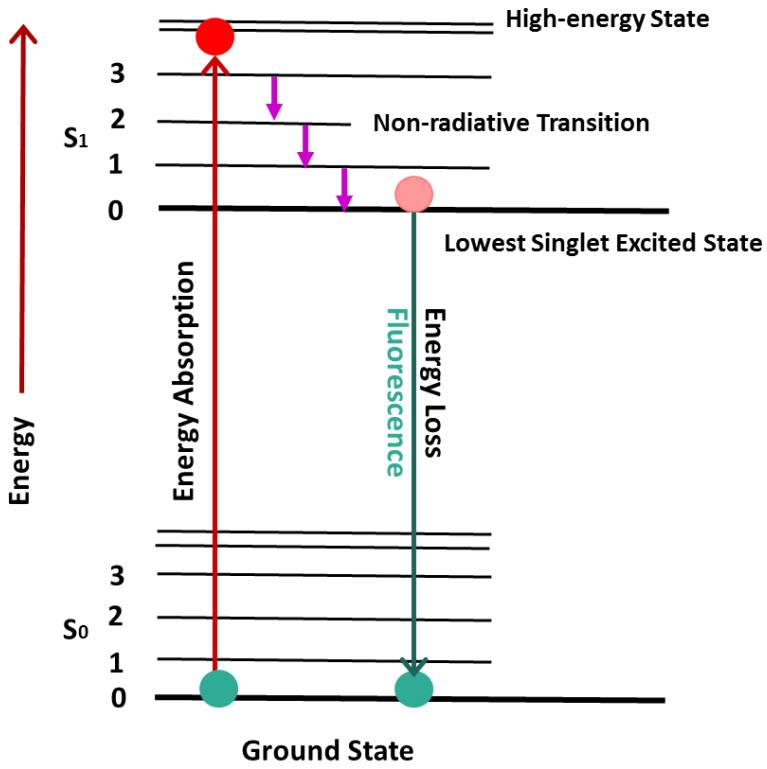

Figure 2.7. Schematic representation of an energy diagram known as Jablonski diagram explaining the fluorescence process. Green circles represent the normal energy level of the fluorophore and red circles depict the maximum energy level.[22]

The PL spectra were collected using a Perkin Elmer LS55 spectrometer for SiNPs dissolved in a suitable solvent in a quartz cuvette (10×10 mm). The excitation and emission slit widths set at 10 nm. The emission spectra were corrected by the background spectra which was from the pure solvent emission under the same condition.

2.3.3.3. Quantum Yield (QY)

The fluorescence QY is the ratio of the number of photons absorbed to the number of photos emitted through fluorescence. In other words, the QY shows the probability of the excited state being deactivated by fluorescence rather than by other, non-radiative mechanisms.

There are two different approaches to calculate the QY: absolute and relative. The measurements of the absolute QY require sophisticated instrumentation. It is easier, therefore, to determine the relative QY of a fluorophore by comparison to a reference fluorophore with a well-known QY.

There are two different methods for assessing relative QYs: a single-point and a comparative method.[23] Single-point uses only one emission value for the sample and one for the standard to calculate the QY of the unknown sample. By using this method, the QY is calculated using the integrated emission intensities from a single sample and reference pair with identical concentrations. The QY is calculated as in Equation 2.7.

$$Q = Q_R \frac{I}{I_R} \frac{A_R}{A} \frac{\eta^2}{\eta_R^2} \qquad \textbf{(Equation 2.7)}$$

Where Q is the quantum yield, I represents the integrated intensity, η is the refractive index of the solvent and A is the absorbance. The subscript R refers to the standard fluorophore with a known quantum yield.

Even though measuring the QY using this method is fast, it is not always reliable due to the inaccurate measurement of the fluorophore's absorbance. A more reliable method for recording QY is the comparative method of Williams *et al*.[24] which involves the use of multiple well-characterised standard samples with known QY values. Solutions of the standard and test samples with identical absorbance can be assumed to be absorbing the same number of photons at the same excitation wavelength. Thus, a simple ratio of the integrated fluorescence intensities of the two solutions, under identical conditions, will yield the ratio of the QY values. As QY for the standard sample is known, QY for the test sample can be calculated.

In this work, QY was calculated to estimate the quantum efficiency of SiNPs which is particularly important for imaging applications. Solutions with absorbance between 0.1 and 0.01 were prepared and the QY obtained by calculating the gradient of the line generated by plotting the integrated fluorescence intensity against the absorption for various concentrations of fluorophore. The QY can be calculated using Equation 2.8.

$$Q = Q_R \left(\frac{Grad}{Grad_R}\right)\left(\frac{\eta^2}{\eta_R^2}\right) \qquad \textbf{(Equation 2.8)}$$

Where Q is the quantum yield, and η is the refractive index of the solvent. Grad is the gradient from the plot of integrated fluorescence intensity *vs.* absorbance. The subscript R refers to the reference fluorophore of a known QY. In this study Quinine sulphate (Q_R =0.546 in 0.5M H_2SO_4) was used as reference.

2.3.4. Thermal Gravimetric Analysis (TGA) and Differential Scanning Calorimetry (DSC)

Thermal gravimetric analysis (TGA) and differential scanning calorimetry (DSC) are useful techniques to measure the thermal stability of materials in addition to the ligand coverage of SiNPs.

TGA is a technique that can show the weight change caused by the chemical of physical processes as a function of temperature or time in a controlled atmosphere. The weight change of materials can happen due to the decomposition, oxidation or dehydration of samples.

DSC provides an indication of the nature of the process under observation. This technique shows the typical transitions and phase changes when a material is subjected to continuous heating.

TGA and DSC analysis was performed using a Mettler-Toledo TGA-DSC1. The powder sample of SiNPs (approx. 1.5 mg) was placed in a 40 µL aluminium pan and measurements were taken while heating the sample between the specified temperature limits. The background measurements were performed from heating an empty pan within the same temperature range.

2.4. Biological Studies

2.4.1. Culture of Cell Lines

Two mammalian cell lines including Caco-2 (human colorectal adenocarcinoma) and CCD-841 (human normal colon epithelial) were used in this study. Both cell lines were a kind gift from Dr Yongping Bao (Norwich Medical School, UK).

Cell lines were cultured in Roswell Park Memorial Institute medium (RPMI) supplemented with 10% Fetal Bovine Serum (FBS). The media contained 1% Penicillin/ Streptomycin (P/S, 5000u) and 1% L-Glutamine (200mM).

Both cell lines are adherent cell lines which grow *in vitro* until they have covered the available surface area or the medium nutrients are depleted. At this point the cells should be subcultured in order to prevent cell death. When cells reached 70-80% confluence, the old medium was removed and cells were washed three times by pre-warmed Phosphate Buffered Saline (PBS). Cells were detached from the culture flask surface by adding 2mL

Trypsin/EDTA (0.25%) and incubated at 37 ºC for 5-10 min. Trypsin was then neutralised by adding 5 mL fresh medium. Later, cells were centrifuged and re-suspended in a fresh medium. Cells were maintained at 37 ºC in a humidified atmosphere containing 5% CO_2. The medium was changed every two-three days and cells were checked under microscope.

2.4.2. *In Vitro* Cytotoxicity Studies by Colourimetric MTT Assay

In vitro cytotoxicity of synthesised SiNPs was assessed by standard MTT [3-(4,5-dimethylthiazol-2-yl)- 2,5-diphenyltetrazolium bromide] bioassay in cancerous and normal cells.[25] This can evaluate the influence of samples on cell proliferation. MTT measures the mitochondrial activity of cells using tetrazolium salts which act as mitochondrial dehydrogenase enzymes and cleave the tetrazolium ring. This only occurs in living cells.

Initially, Caco-2 and CCD-841 cells were seeded in a 96-well culture plate (Applied Biosystems) at a seeding density of 4.5×10^4 cells per well and allowed to attach overnight at 37 ºC. After which the media was removed and replaced with a range of different concentrations of SiNPs suspension in media for various time points according to the table 2.2. At the end of these periods, the medium was removed and 10 μL of MTT (Sigma-Aldrich) solution (5mg/mL in sterile water) mixed with 100 μL fresh medium was added to each well including controls for determination of living cells.

After four hours incubation at 37 ºC, the medium was removed and formazan was solubilised in dimethylsulfoxide (DMSO). The absorbance was recorded by a microplate reader (BMG Labtech Polar Star Optima) at the wavelength of 570 nm. The percentage of mean cell viability was calculated from a minimum of triplicate wells normalised to untreated control cells. All experiments were repeated at least three different occasions and experimental error given as a standard deviation.

Table 2.2. List of different experimental conditions used for MTT assays.

Chapter	NPs	Concentration (µg/mL)	Incubation Time (h)	Cell Line
3	NH_2 SiNPs (top down)	5, 10, 20, 50, 100	24, 48	Caco-2 CCD-841
3	NH_2 SiNPs (bottom up)	5, 10, 20, 50, 100	24, 48	Caco-2 CCD-841
3	Thiourea SiNPs NH_2 SiNPs (top down, control)	5, 10, 20, 50,100, 200, 500, 1000, 1200, 1500	24, 72	Caco-2 CCD-841
4	ITC SiNPs (P Br SiNPs) NH_2 SiNPs (top down, control)	5, 10, 15, 20, 30, 50, 70	24, 48	Caco-2 CCD-841
4	ITC SiNPs (P NH_2 SiNPs) NH_2 SiNPs (top down, control)	5, 10, 15, 20, 30, 50, 70	24, 48	Caco-2 CCD-841

2.4.3. Cellular Uptake Studies

2.4.3.1. Bioimaging

2.4.3.1.1. Microscope Slide Preparation and Cell Staining

Caco-2 cells were seeded on a 12 well plate with a sterile ø 18 mm borosilicate glass cover slip at a density of 1×10^5 cells per well and were allowed to attach overnight at 37 ^{o}C. Cells were grown on cover slips until approximately 70% confluent. The growth medium was then removed and 100 µg/mL of SiNPs were added on top of the cells (Control was also made at the same time). Cells were incubated with thiourea functionalised SiNPs for 2 and 4 h and ITC SiNPs for 6 and 12 h at 37°C.

After these time periods, cells were washed three times with PBS and fixed by 4% (v/v) paraformaldehyde (PFA) in FBS solution for 20 min at room temperature. After washing three times with PBS, 200 µL of NH_4Cl (50 mM) was added to each well for 20 min to quench the effect of fixing agent. The solution was then removed and the cells were washed three times with PBS. Nuclei were stained with Hoechst 33342 (2 µg/mL) in PBS for 5 min. Followed by three times PBS washing, Texas Red-X Phalloidin (6.6 µM) was employed for actin staining. All cover slips were washed with PBS three times and then with autoclaved water. A drop of mounting media (~10 µL) was added on top of the microscope slide. The cover slips were turned upside down on top of the mounting media and then sealed with nail varnish. The slide was then dried in the fridge for approx. 30 min before use.

2.4.3.1.2. Confocal Laser Scanning Microscopy

Confocal imaging is an optical imaging technique that produces highly detailed images and is used for an increased optical resolution and contrast of images over conventional microscopes. This is achieved by adding a spatial pinhole at the confocal plane of the lens to eliminate out of focus light.[26] In addition to allowing improved observation of fine details, this technique enables the reconstruction of three-dimensional (3D) structure of a specimen by assembling a series of thin slices taken along the vertical axis.

Confocal microscopy can overcome the limitations of wide-field fluorescence microscopes. In these conventional microscopes, the sample is flooded evenly in light from a source. Thus, all parts of the sample being analysed are excited at the same time and the resulting

fluorescence is detected. A confocal microscope, on the other hand, uses point illumination and a pinhole in an optically conjugate plane in front of the detector in order to eliminate the out of focus signal. A spot of a minimum size in the specimen is illuminated and an image formed by scanning the specimen.

Figure 2.8 shows the internal mechanism of a confocal microscope. First, the laser light is directed by a dichroic mirror towards a pair of rotating mirrors which scan the light over the *x* and *y* plane. The light then passes through the microscope objective and excites the sample. The fluorescent light from the sample passes back through the objective, followed by the same set of rotating mirrors used to scan the sample. After that, the light passes through the dichroic mirror through a pinhole placed in the confocal plane of the sample. Next, the pinhole rejects all out-of-focus light arriving from the sample. Finally, the light that emerges from the pinhole is measured by a detector.[27]

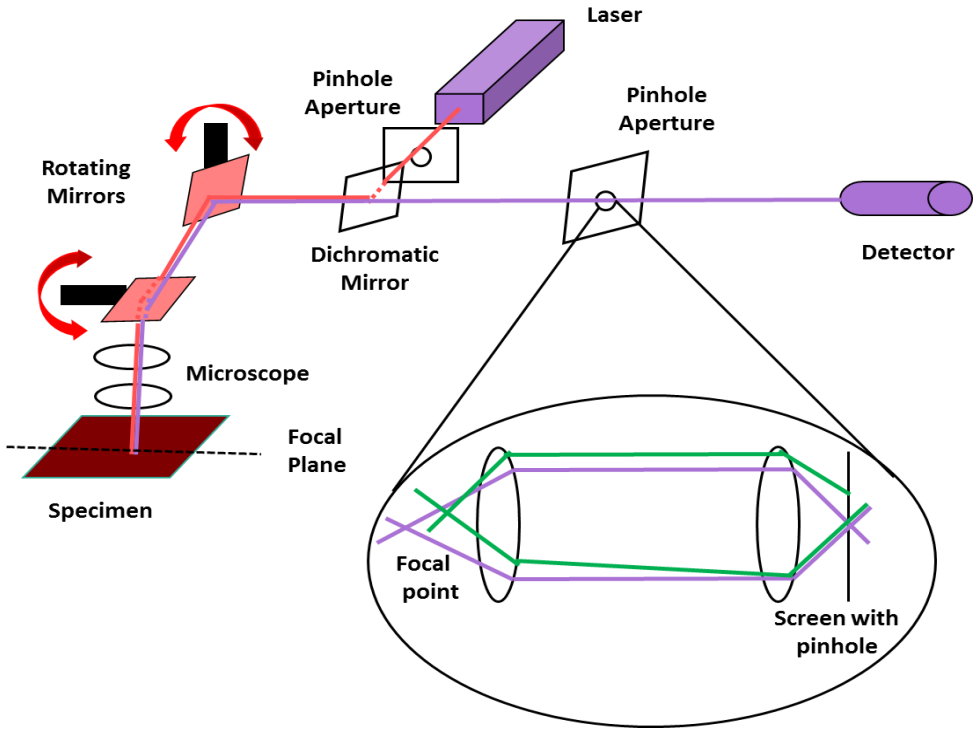

Figure 2.8. Schematic diagram of a conventional confocal microscope reproduce from Prasad *et al*.[27] The light passes through a diachronic mirror followed by two rotating mirrors in x and y directions. Then, the light excites the specimen. The fluorescence light from the sample passes through the same components and then directed to the pinhole which lies in the back focal plane of the sample and rejects most of out of focus light. The light that emerges from the pinhole is measured by a detector. The inset shows the light from the focal point that reaches the screen is allowed through and the light away from the focal point is mostly rejected.

Laser scanning confocal microscopy was performed on a Zeiss LSM510 META confocal microscope using a 63× oil immersion objective lens for imaging. SiNPs were excited using a 488 nm laser beams. Hoechst was excited using a 364 nm laser and Phalloidin imaging was performed using 543 nm excitation wavelength.

The same microscope was used to image cells in multi-track mode. Z-series images were collected with stepper motor. ImagePro software was used to process the images.

2.4.3.2. Flow Cytometry

Flow cytometry is a laser-based technology that allows simultaneous multi-parametric analysis such as cell counting, cell sorting, biomarker detection and protein engineering. This can happen by suspending cells in a stream of fluid and passing them by an electronic detection apparatus. This technique is able to measure the light scattering and fluorescence from biological cells as well as particles. Individual cells with fluorophore labels can be characterised by flow cytometry and provide semi quantitative information about the cellular uptake of NPs.[28, 29]

The optical system in flow cytometry comprises several lasers which illuminate the particles present in the stream as they pass through and scatter light from the laser. Any fluorescent molecules on the particle can be detected by various lenses. The light scattered from up to six or more fluorescence molecules is determined from two different angles. Optical filters and beam splitters then direct the light signals to the relevant detectors, which emit electronic signals proportional to the signals that hit them. Data can then be collected on each particle or event and the characteristics of those events or particles are determined based on their fluorescent and light scattering properties. The size of the cells can be measured using forward scatter and the granularity of cells by side scatter (Figure 2.9)

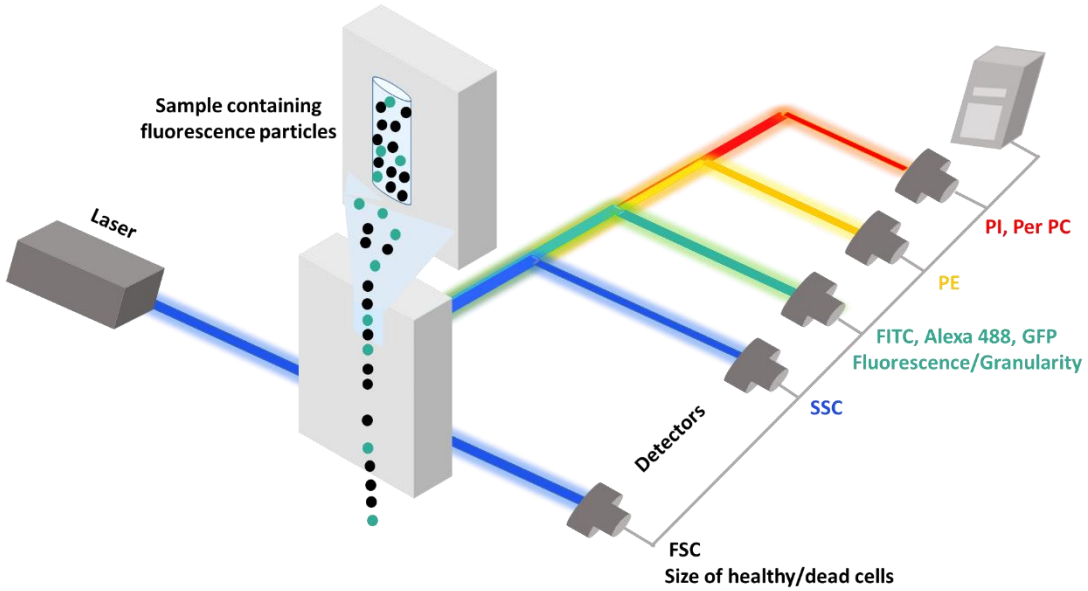

Figure 2.9. Schematic representation of a flow cytometer with different lasers. The sample containing cells with fluorescence molecules is injected in the middle of a fluid sheeth and funnelled to give a single line of ordered cells. The cells are passed through a laser beam that measures the forward scatter (FSC) and side scatter (SSC).[30]

Fluorescence-activated cell sorting (FACS) is a specialised type of flow cytometry which provides a method for sorting a heterogeneous mixture of biological cells into two or more containers. Each cell is analysed one at a time, based upon their specific light scattering and fluorescent characteristics. FACS is a useful scientific instrument since it provides fast, objective and quantitative recording of fluorescent signals from individual cells as well as physical separation of cells of particular interest. The cell suspension is entrained in the centre of a narrow, rapidly flowing stream of liquid. The flow is arranged based on the relative diameter of cells so that there is a large separation between cells. A vibrating mechanism causes the stream of cells to break into individual droplets. One cell per droplet is analysed by this system. The flow passes through a fluorescence measuring station where the fluorescent character of each cell of interest is measured. An electrical charging ring is placed where the stream breaks into droplets. A charge is placed on the ring based on the immediately prior fluorescence intensity measurement, and the opposite charge is trapped on the droplet as it breaks from the stream. The charged droplets then fall through an electrostatic deflection system that diverts droplets into containers based upon their charge.[31]

Caco-2 and CCD-841 cells were seeded on 24 well plates at a density of 5×10^4 cells per well and incubated at 37 ^{o}C overnight. The attached cells were subsequently washed with PBS

and exposed to a range of different concentrations of SiNPs for various time points according to table 2.3. The cells were trypsinised and then washed three times with PBS followed by centrifugation at 1200 rpm for 5 min after each washing. Finally, the cells were fixed with 4% (v/v) PFA in FBS for 20 min and washed again with PBS. Prior to the flow cytometric measurement, the cells were re-suspended in a buffer of 5 % (v/v) FBS in PBS. The uptake of NPs was examined in 10,000 gated cells by detecting SiNPs fluorescence using FL1 channel detector under the excitation wavelength at 488 nm and a BD FACS Calibur (BD Bioscience). Measurements were performed in triplicate (with different sets of NPs) and data was analysed with CellQuest Pro® software (BD Biosciences) and presented as median ± SD.

Table 2.3. List of different parameters examined in flow cytometric analysis.

Chapter	NPs	Concentration (µg/mL)	Incubation time	T (°C)	Cell line
3	Thiourea SiNPs	**10, 20, 50, 100**	30 min, 4 h	37	Caco-2
3	NH_2 SiNPs (control)	**10, 20, 50, 100**	30 min, 4 h	37	Caco-2
3	Thiourea SiNPs	100	**30 min, 1, 4, 6, 8 h**	37	Caco-2
					CCD-841
3	NH_2 SiNPs (control)	100	**30 min, 1, 4, 6, 8 h**	37	Caco-2
					CCD-841
4	ITC SiNPs	**20 and 80**	**6, 12, 24, 48 h**	37	Caco-2
4	ITC SiNPs	80	6, 12, 24 h	**4, 37**	Caco-2

2.4.4. ELISA Assay

The enzyme-linked immunosorbent assay (ELISA) is a test that benefits using antibodies and colour change to identify an analyte, usually an antigen, in a sample.

Antigens from the sample are attached to a surface. Then, a specific antibody is added to the surface so it can bind to the antigen. The secondary antibody, which is linked to an enzyme, is added and attach to the primary antibody. Finally, a substance containing the enzyme's substrate is added. The subsequent reaction produces detectable signal, most commonly as a colour change in the substrate, which correlates to the amount of analyte present in the original sample.[32]

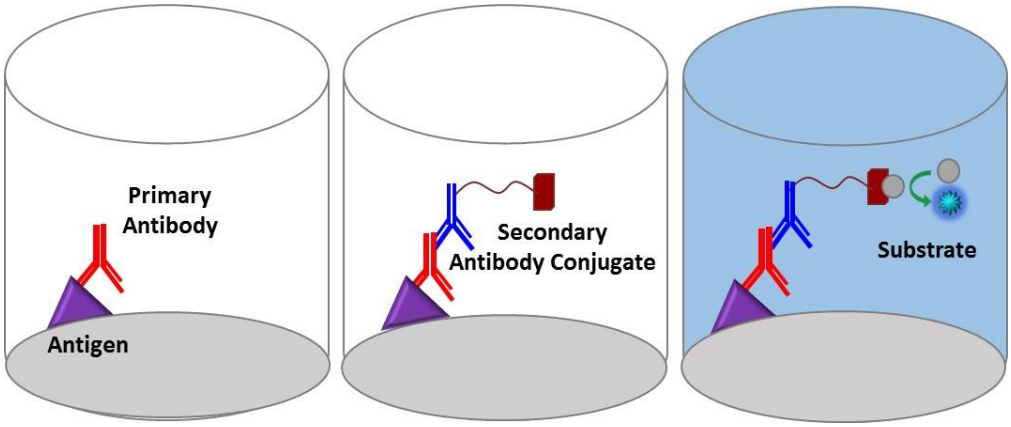

Figure 2.10. Schematic representation of an indirect ELISA assay. Unknown amount of antigen is coated to the well and it is incubated with dilutions of antibodies. The antigen bound antibody is then recognized by the secondary antibody linked to the enzyme. A colorimetric substrate is used to measure the level of antibody.

Caco-2 cells were seeded on a 96 well plate at a seeding density of 5×10^4 cells per well and incubated overnight at 37 ^{o}C. Thiourea and amine capped SiNPs were added at a range of different concentrations from 10 to 100 µg/mL for 4 h. The media was then removed and 100 µL of 4 % (v/v) PFA was added to each well for 15 minutes to fix the cells. Cells were washed twice with 100 µL tris-buffered saline (TBS). Permeabilization buffer (100 µL, 0.5 % Triton X) was added and incubated for 15 minutes at room temperature. Followed by another TBS washing, NH_4Cl (100 µL) as the quenching solution was added. Then blocking buffer (10 % (v/v) FBS in PBS) was added and incubated for 30 minutes. The primary antibody (Anti-EGFR antibody, 0.2 mg/ml, 1:1000) was added to each well and incubated overnight at 4 ^{o}C. The day after, the primary antibody solution was removed and the plate was washed three times with

the wash buffer. The secondary antibody (anti-rabbit IgG, HRP-linked antibody, 2 mg/ml BSA, 1:1000) was added and incubated for 30 minutes at room temperature. Finally 3,3',5,5'-Tetramethylbenzidine (TMB) substrate (100 µL per well) was added to each well and incubated at room temperature and protected from light. The TMB stop solution (100 µL per well) was added after 15 minutes when the blue colour was achieved and the absorbance was measured at 450 nm using a microplate reader (BMG Labtech Polar Star Optima) within 30 minutes of stopping the reaction.

Before the whole cell staining, the plate was emptied and washed twice with ultrapure water. Janus Green Whole Stain (100 µL per well, 0.3%) was added to each well and incubated for 5 minutes at room temperature. All excess stain was removed followed by 3-5 times washing with ultrapure water (200 µL per well). The Elution buffer (100 µL per well) was added and the absorbance was measured at 615 nm after 10 minutes incubation at room temperature.

2.5. Synchrotron-based Fourier Transform Infrared Microspectroscopy Techniques

A synchrotron is an electron storage ring that produces intense broadband light from X-rays through microwaves. Synchrotron radiation is the light emitted by relativistic electrons in high-energy accelerators along a circular trajectory. Infrared beamlines collect synchrotron light from bending magnets in the electron storage ring. This light extends from X-rays down through the infrared spectral range, and acts as a source for a number of biologically relevant measurement techniques. This is particularly important for the infrared where the high source brightness enables microspectroscopy to be performed at the unprecedented resolution of just a few microns. This size scale is appropriate for investigating the variations in individual cells and therefore has a great advantage over other techniques since biological cells and tissues are extremely complex structures that vary widely in composition.[33]

Infrared microspectroscopy is a quantitative analytical and non-destructive technique. The IR microscope beamlines are designed around an excitation system that collects ~40 mr from the storage ring. The extraction of the synchrotron light from the storage ring is commonly done with a combination of gold or aluminium coated plane and toroid/ellipsoid or spherical mirrors. The infrared light is focused through an infrared-transparent window, such as KBr and CaF_2, which separates the ultrahigh vacuum (UHV) conditions of the storage ring and the rough

vacuum of the IR beamline. The IR transparent windows isolate the beamline vacuum from the ambient pressure of the microscope. The beam is then re-collimated and directed into the IR microscope. Although IR light passes easily through water vapour and carbon dioxide (CO_2), it is highly absorbed by air, thus IR microscopes are typically purged with dry nitrogen or dry air.[34, 35]

Synchrotron measurements in this work were performed at D7 beamline (MAX-IV laboratory, Lund, Sweden).

2.5.1. Sample Preparation

Free standing SiNPs were added on top of KBr substrates for analysis.

Caco-2 and CCD-841 cell lines were used for synchrotron measurements. Cells were seeded on CaF_2 IR optical substrates for the measurements, which were placed in 12 well plates, at a density 5×10^4 cells per well. All substrates were cleaned with 70% ethanol before being used for cell culture. After 24 h incubation, the media was removed and cells were washed three times with PBS. Then 50 µg/mL of ITC SiNPs were added to the cells and incubated for 6 h according to table 2.4. At the end of this time period, the growth medium was removed and cells were washed three times with PBS and then NaCl (0.9 %) and fixed with 4% PFA in PBS for 30 min. Then substrates were washed with distilled water and dried under ambient conditions. They were stored in the fridge before analysis under IR microscope.[35]

2.5.2. Synchrotron FTIR Microspectroscopy

The IR microspectroscopy measurements were performed on a Bruker IFS66V FTIR spectrometer coupled to a Hyperion 3000 infrared microscope using synchroton radiation at MAX-IV laboratory. The microscope was operated in transmission mode with a 10×10 µm^2 aperture using a ×15 objective and a condenser along with a single element, 100×100 µm^2 MCT detector. This arrangement gives a visible magnification of ×115 for the video camera in the microscope used to locate relevant structures in the samples. The data acquisition was performed using OPUS software (Bruker) version 7. The spectra selection for data treatment was based on eliminating those with very weak absorbance (poor S/N ratio). About 100 spectra

were analysed on each substrate for each cell line. Spectra were obtained by co-addition of 256 scans at a spectral resolution of 4 cm^{-1}.

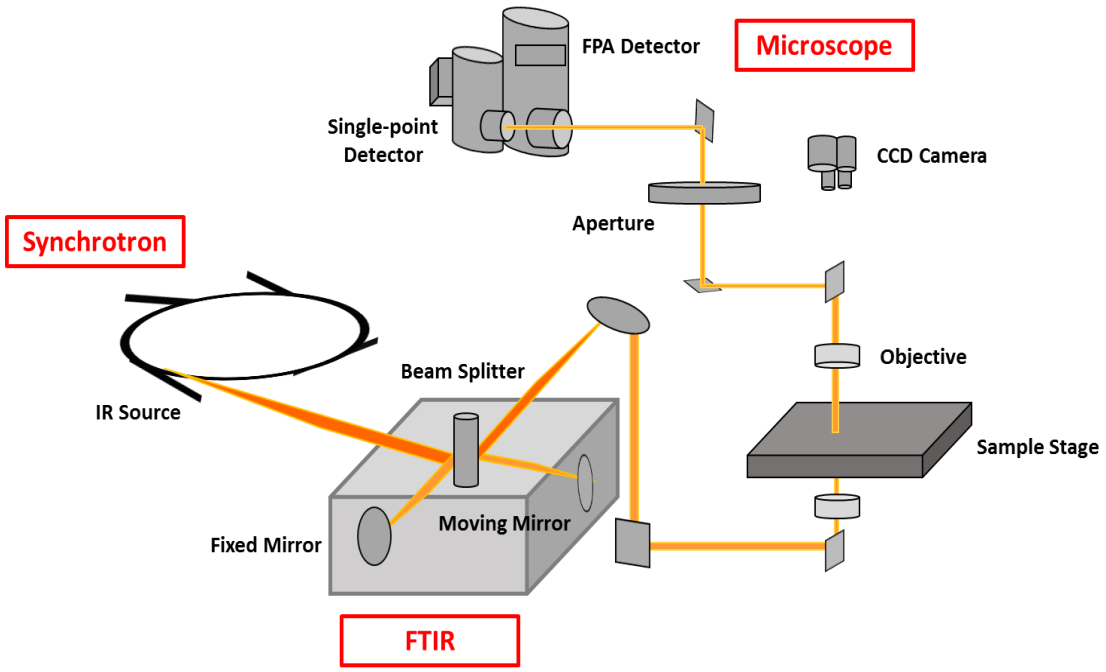

Figure 2.11. Schematic representation of a synchrotron FTIR microspectroscope reproduced from Bhargava.[36]

2.5.3. FTIR Imaging Using Focal Plane Arrays Detector (FPA)

A conventional globar was used as light source for the FTIR imaging spectra in transmission mode. Optical and FTIR images were performed with the same microscope and spectrometer and a 128 × 128 FPA detector with individual dimension of detectors 40 × 40 μm^2; Bruker Optik, Ettlingen, Germany. In order to minimise the atmospheric variations and ensure optimum spectral acquisition, N_2 was performed on both spectrometer and microscope. As the transmission mode uses a 15× objective this gives a sample area of 340 × 340 μm^2 for each image. This enables the visualisation of the structure and quantitative spectral characterisation with the necessary signal to noise ratio. Spectral images were obtained by co-addition of 128 scans at a spectral resolution of 8 cm^{-1}. After recording the spectra, images were performed using the integrated intensities of selected spectral areas characteristic of either protein or phospholipid constituents and colour codes were used to determine the distribution of the examined constituent.

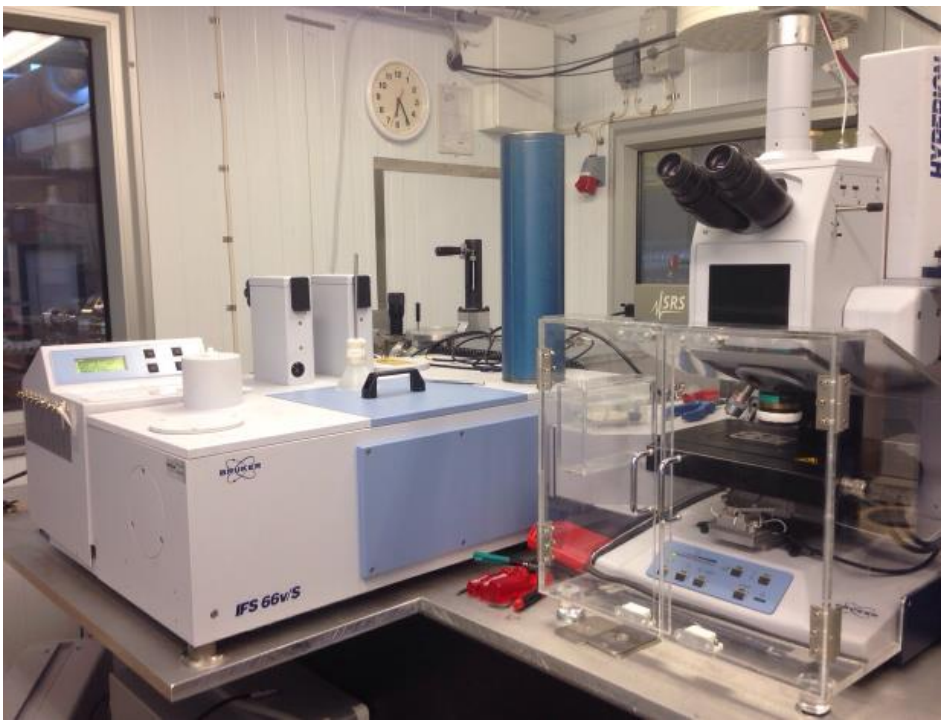

Figure 2.12. Photograph of the synchrotron FTIR microspectroscopy facility at MAX-IV laboratory, Lund.

Table 2.4. List of different parameters examined in FTIR synchrotron microspectroscopy and imaging.

NPs	Concentration	Incubation Time (h)	Cell Line	Substrate
ITC SiNPs (P Br SiNPs) NH_2 SiNPs	50 µg/mL	6	Caco-2 CCD-841	CaF_2
ITC SiNPs (P Br SiNPs) ITC SiNPs (P NH_2 SiNPs) Br SiNPs NH_2 SiNPs	5 mg	–	Free standing material	KBr

2.6. Statistics

Statistical methods throughout this study are represented as mean ± SEM taken over a minimum of three independent experiments. Statistical significance was measured by two-way-ANOVA followed by a Bonferroni post-test using GraphPad Prism version 5.03 for Windows, GraphPad Software, San Diego California, USA.

2.7. References

1. Chao, Y.; Siller, L.; Krishnamurthy, S.; Coxon, P. R.; Bangert, U.; Gass, M.; Kjeldgaard, L.; PatoleO, S. N.; Lie, L. H.; O'Farrell, N.; Alsop, T. A.; Houlton, A.; Horrocks, B. R., Evaporation and deposition of alkyl-capped silicon nanocrystals in ultrahigh vacuum. *Nature Nanotechnology* **2007,** *2* (8), 486-489.

2. Wang, Q.; Ni, H.; Pietzsch, A.; Hennies, F.; Bao, Y.; Chao, Y., Synthesis of water-dispersible photoluminescent silicon nanoparticles and their use in biological fluorescent imaging. *Journal of Nanoparticle Research* **2011,** *13* (1), 405-413.

3. Ahire, J. H.; Wang, Q.; Coxon, P. R.; Malhotra, G.; Brydson, R.; Chen, R.; Chao, Y., Highly Luminescent and Nontoxic Amine-Capped Nanoparticles from Porous Silicon: Synthesis and Their Use in Biomedical Imaging. *Acs Applied Materials & Interfaces* **2012,** *4* (6), 3285-3292.

4. Linford, M. R.; Chidsey, C. E. D., Alkyl monolayers covalently bonded to silicon surfaces. *Journal of the American Chemical Society* **1993,** *115* (26), 12631-12632.

5. Linford, M. R.; Fenter, P.; Eisenberger, P. M.; Chidsey, C. E. D., Alkyl monolayers on silicon prepared from 1-alkenes and hydrogen-terminated silicon. *Journal of the American Chemical Society* **1995,** *117* (11), 3145-3155.

6. Bateman, J. E.; Eagling, R. D.; Worrall, D. R.; Horrocks, B. R.; Houlton, A., Alkylation of porous silicon by direct reaction with alkenes and alkynes. *Angewandte Chemie-International Edition* **1998,** *37* (19), 2683-2685.

7. Effenberger, F.; Gotz, G.; Bidlingmaier, B.; Wezstein, M., Photoactivated preparation and patterning of self-assembled monolayers with 1-alkenes and aldehydes on silicon hydride surfaces. *Angewandte Chemie-International Edition* **1998,** *37* (18), 2462-2464.

8. Cicero, R. L.; Linford, M. R.; Chidsey, C. E. D., Photoreactivity of unsaturated compounds with hydrogen-terminated silicon(111). *Langmuir* **2000,** *16* (13), 5688-5695.

9. Stewart, M. P.; Buriak, J. M., Exciton-mediated hydrosilylation on photoluminescent nanocrystalline silicon. *Journal of the American Chemical Society* **2001,** *123* (32), 7821-7830.

10. Sung, M. M.; Kluth, G. J.; Yauw, O. W.; Maboudian, R., Thermal behavior of alkyl monolayers on silicon surfaces. *Langmuir* **1997,** *13* (23), 6164-6168.

11. Wayner, D. D. M.; Wolkow, R. A., Organic modification of hydrogen terminated silicon surfaces. *J. Chem. Soc.-Perkin Trans. 2* **2002,** (1), 23-34.

12. Zazzera, L. A.; Evans, J. F.; Deruelle, M.; Tirrell, M.; Kessel, C. R.; McKeown, P., Bonding organic molecules to hydrogen-terminated silicon wafers. *Journal of the Electrochemical Society* **1997,** *144* (6), 2184-2189.

13. Buriak, J. M., Organometallic chemistry on silicon surfaces: formation of functional monolayers bound through Si-C bonds. *Chemical Communications* **1999,** (12), 1051-1060.

14. Schmeltzer, J. M.; Porter, L. A.; Stewart, M. P.; Buriak, J. M., Hydride abstraction initiated hydrosilylation of terminal alkenes and alkynes on porous silicon. *Langmuir* **2002,** *18* (8), 2971-2974.

15. Wang, J.; Ye, D.-X.; Liang, G.-H.; Chang, J.; Kong, J.-L.; Chen, J.-Y., One-step synthesis of water-dispersible silicon nanoparticles and their use in fluorescence lifetime imaging of living cells. *Journal of Materials Chemistry B* **2014,** *2* (27), 4338-4345.

16. Hobarr H. Willard, L. L. M., Jr..; John A. Dean, a. F. A. S., Jr.,; Belmon, W., Instrumental methods of analysis. *Journal of Chemical Education* **1988,** *66* (1), 64.

17. Keyse, R. J. G.-R., A. J.; Goodhew, P. J.; Lorimer, G. W., , *Introduction To Scanning Transmission Electron Microscopy.* Spinger-Verlag: New York, **1998.**

18. Hiemenz, P., *Principles of colloid and surface chemistry, 2nd Ed*. Marcel Dekker: New York, **1986.**

19. Zeta Potential Electrophoresis http://www.escubed.co.uk/sites/default/files/zeta_potential_(an011)_elecrophoresis.pdf.

20. Skoog, D. A. H., F. James; Crouch, Stanley R. . Belmont, , *Principles of Instrumental Analysis (6th ed.)*. Thomson Brooks: CA, **2007.**

21. Characterization'of'crystallizing'solutions. http://lafactoria.lec.csic.es/mcc/attachments/article/40/100385-CharctXSol.pdf.

22. Jaboski, A., Efficiency of Anti-Stokes Fluorescence in Dyes. *Nature* **1993,** (131), 839-840.

23. Lakowicz, J. R., *Principles of Fluorescence Spectroscopy*. Plenum Publ, **1999**.

24. Williams, A. T. R.; Winfield, S. A.; Miller, J. N., Relative fluorescence quantum yields using a computer-controlled luminescence spectrometer. *Analyst* **1983,** *108* (1290), 1067-1071.

25. Berridge, M. V.; Tan, A. S., Characterisation of the cellular reduction of 3-(4,5-Dimethylthiazol-2-YL)-2,5-Diphenyltetrazolium Bromide (MTT) *Archives of Biochemistry and Biophysics* **1993,** *303* (2), 474-482.

26. Pawley, J. B., *Handbook of Biological Confocal Microscopy (3rd ed.).* Springer: Berlin, **2006.**

27. Prasad, V.; Semwogerere, D.; Weeks, E. R., Confocal microscopy of colloids. *J. Phys.-Condes. Matter* **2007,** *19* (11), 25.

28. Kumar, A.; Pandey, A. K.; Singh, S. S.; Shanker, R.; Dhawan, A., A Flow Cytometric Method to Assess Nanoparticle Uptake in Bacteria. *Cytometry Part A* **2011,** *79A* (9), 707-712.

29. Zucker, R. M.; Massaro, E. J.; Sanders, K. M.; Degn, L. L.; Boyes, W. K., Detection of TiO2 Nanoparticles in Cells by Flow Cytometry. *Cytometry Part A* **2010,** *77A* (7), 677-685.

30. Sabban, S. Development of an in vitro model system for studying the interaction of Equus caballus lgE with its high-affinity Fc receptor. The University of Sheffield, Sheffield, **2011.**

31. Julius, M. H.; Masuda, T.; Herzenbe.La, Demonstration that Antigen-Binding Cells are Precursors of Antibody-Producing Cells After Purification With A Fluorescence-Activated Cell Sorter. *Proceedings of the National Academy of Sciences of the United States of America* **1972,** *69* (7), 1934-&.

32. Yalow, R. S.; Berson, S. A., Immunoassay of endogenous plasma insulin in man. *Journal of Clinical Investigation* **1960,** *39* (7), 1157-1175.

33. Miller, L. M.; Dumas, P., Chemical imaging of biological tissue with synchrotron infrared light. *Biochimica Et Biophysica Acta-Biomembranes* **2006,** *1758* (7), 846-857.

34. Miller, L. M.; Smith, G. D.; Carr, G. L., Synchrotron-based biological microspectroscopy: From the mid-infrared through the far-infrared regimes. *Journal of Biological Physics* **2003,** *29* (2-3), 219-230.

35. Wehbe, K.; Filik, J.; Frogley, M. D.; Cinque, G., The effect of optical substrates on micro-FTIR analysis of single mammalian cells. *Analytical and bioanalytical chemistry* **2013,** *405* (4), 1311-24.

36. Bhargava, R., Infrared Spectroscopic Imaging: The Next Generation. *Applied Spectroscopy* **2012,** *66* (10), 1091-1120.

Chapter 3:
Synthesis and Characterisation of Thiourea-functionalised Silicon Nanoparticles for Inhibiting EGFR

3.1. Overview

Conventional cancer chemotherapies have been associated with serious systemic toxicities and dose-limiting side effects that restrict their clinical application.[1] Targeted therapeutics on the other hand, by being more selective, can potentially minimise the side effects of these anticancer agents by avoiding healthy cells.[2, 3] In efforts to develop targeted anticancer drugs, it is essential to consider many different aspects of molecular biology, such as the interactions with cell surface receptors.[4, 5] RTKs have been identified as major contributors in numerous signal transduction pathways and are implicated in cell proliferation.[6, 7] EGFR is one of the most important RTKs and plays a key role in a wide diversity of biological processes, including cell proliferation, metastasis, and angiogenesis.[8-10] Although EGFR is involved in various physiological processes, and as such is expressed in non-malignant tissues, this tyrosine kinase has been shown to be over-expressed in tumours of epithelial origin such as colon, breast, ovarian, lung, and prostate cancer.[11, 12] Consequently, EGFR overexpression in cancerous tissue presents an attractive target for compounds with inhibitory activity.

Among the anticancer drugs discovered in recent years, thiourea compounds have shown potent anticancer properties owing to their strong inhibitory activity against RTKs, PTKs, and NADH oxidase, which are all active in the process of tumorigenesis.[10, 11, 13] EGFR, as one of the important PTKs, is known to be overexpressed in many types of cancer cells. This receptor has also been identified as the prime target of thiourea based chemotherapeutics.

In this chapter we report the synthesis of thiourea-functionalised SiNPs as a new multifunctional nanoscale system. By developing such hybrid nanoparticles, we can exploit the unique optical properties of SiNPs whilst introducing the functionalities of the thiourea ligand for diagnostic applications. We herein report the synthesis and *in vitro* evaluation of the toxicity and targeting activity of thiourea-functionalised SiNPs. This approach investigates the ability of thiourea to target EGFR overexpression in cancer cells whilst taking advantage of the intrinsic photoluminescence properties of SiNPs, without the need for any fluorescent tags.

First, we demonstrate the synthesis and characterisation of amine-functionalised SiNPs produced by top down and bottom up techniques. The full detailed evaluation of the products obtained from each method will be discussed as well as the advantages and disadvantages of each technique. Based on the data obtained and considering the strengths and weaknesses of each type, the top down NH_2 SiNPs were chosen for the remainder of the project due to the

higher level of purity they exhibited. These particles were used as control material in nanoscale within Chapter 3 and 4. In addition, amine functional group in these compounds can be used for further functionalisation to synthesise ITC SiNPs (Chapter 4).

The rest of this chapter will focus on the synthesis and characterisation of thiourea-functionalised SiNP. A thiourea ligand was synthesised followed by hydrosilylation to functionalise SiNPs with this specific functional group. The hydrogen terminated SiNPs were first prepared through the electrochemical etching of porous silicon and later functionalised by thiourea. These functionalised SiNPs were tested in terms of cytotoxicity to colorectal cancer and primary cells and active EGFR-mediated targeting. In several respects, these novel nanoparticles offer significant advantages compared to conventional therapeutics. These include the integration of the targeting moiety and therapeutic moiety in the same system, the use of inexpensive materials and more significantly the production of a highly stable nanosystem.

3.2. Synthesis of Hydrogen-terminated Silicon Nanoparticles

Hydrogen terminated SiNPs were synthesised by galvanostatic anodization of porous Silicon layer (boron-doped p-Si (100) chip with 1.25 × 1.25 cm^2 size) in a 1:1 v/v solution of 48% aqueous HF and ethanol as described in Chapter 2 and reported previously.[14] As these obtained SiNPs rapidly undergo oxidation in air, it is important to stabilise them using different surface functionalisation.

3.3. Synthesis of Amine-functionalised Silicon Nanoparticles by Top Down Method

One of the methods to functionalise SiNPs uses allylamine which can avoid oxidation on the nanoparticle surface, and also solubilise nanoparticles in polar solvents such as water and alcohol. Moreover, introducing the amine functional group can produce a platform as a common starting material ideally suited for further functionalisation, as this functional group is reactive and has the potential for further modification. These factors contribute to the development of a nanosystem with more specialised characteristics for biomedical applications.

Amine-functionalised SiNPs were synthesised by reacting the hydrogen-terminated porous silicon with allylamine, in the presence of H_2PtCl_6 catalyst in isopropanol (Scheme 3.1).

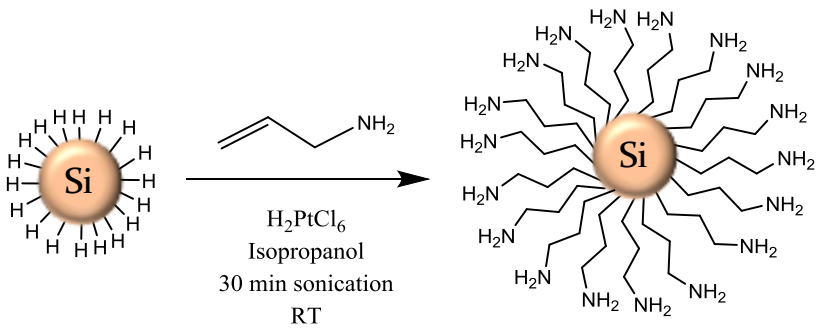

Scheme 3.1. Schematic illustration of the top down synthesis of NH_2 SiNPs.

3.4. Synthesis of Amine-terminated Silicon Nanoparticles by Bottom Up Method

There are several issues relating to the nanoparticles obtained from top down methods which limit their large scale industrial biomedical applications. Examples of these are the low quantity of materials obtained from each batch, and less control over the shape and size of nanoparticles.[15] Therefore, it is important to investigate bottom up methods as an alternative, which may remedy some of these drawbacks. Here, an attempt to synthesise NH_2 SiNPs by bottom up methods was undertaken in order to understand how such issues might be addressed.

NH_2 SiNPs were synthesised using a method outlined by Wang *et al*.[16] by adding APTES to an aqueous solution while stirring. Next, ascorbate sodium was added to the mixture followed by stirring for 20 min. This was a simple one-step reaction (Scheme 3.2).

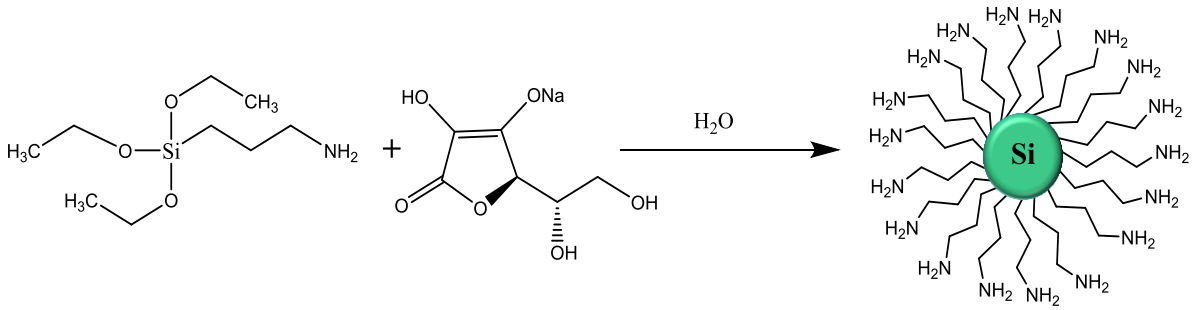

Scheme 3.2. Schematic illustration of the bottom up synthesis of NH_2 SiNPs.

3.5. Characterisation of Amine-terminated Silicon Nanoparticles

In order to evaluate which group of NH_2 SiNPs has potential to be used in this project, chemical and optical characterisation was performed on both products. This was followed by a cytotoxicity assay to determine the suitability of these nanoparticles for biomedical applications.

3.5.1. Chemical Bonding by FTIR

Using FTIR as a spectroscopic tool, NH_2 SiNPs prepared by different methods, were analysed. The spectrum of top down NH_2 SiNPs is shown in Figure 3.1 (a). The observed peaks

at 1260 and 1450 cm^{-1} are representative of Si-C symmetric bending and Si-CH_2 scissoring modes respectively.[17] The features at around 2800 to 2900 cm^{-1} are assigned to the C-H stretching of the alkane in the ligand. The N-H stretching of the amine functional group was observed around 3400 cm^{-1} in top down NH_2 SiNPs as well as the bottom up product in spectrum (b).[18] The N-H wagging and scissoring were observe at around 970 and 1590 cm^{-1} respectively.[14, 16] The combination of these features demonstrate the successful functionalisation of both synthetic procedures. Further oxidation was observed for the bottom up NPs with the wider signal observed at about 1000 cm^{-1} characteristic of Si-O bond.[19]

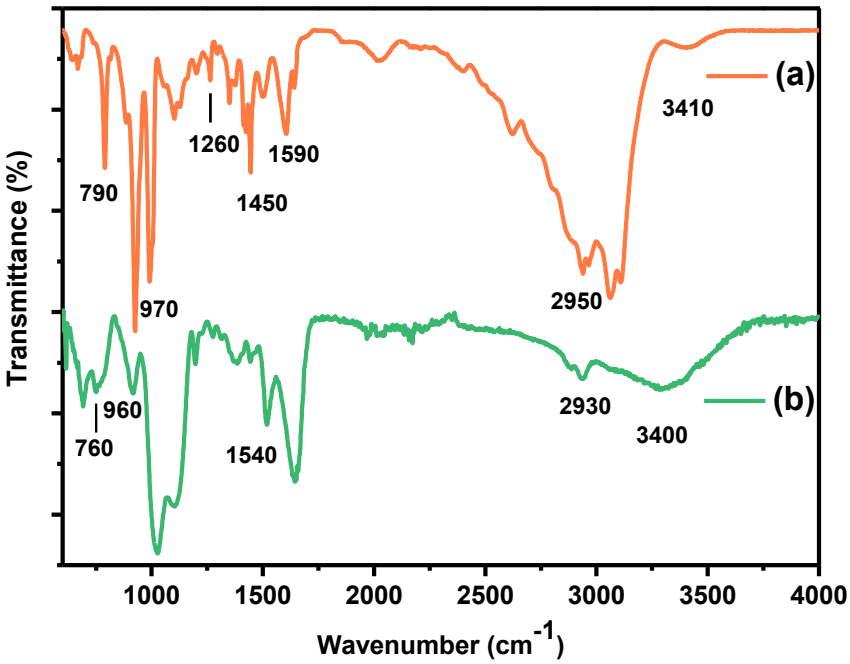

Figure 3.1. FTIR spectra of NH_2 SiNPs synthesised by top down (a) and bottom up method (b).

3.5.2. Elemental Analysis EDX

Elemental analysis of the NH_2 SiNPs using energy-dispersive X-ray spectroscopy (EDS) analysis is shown in Figure 3.2 (a) and (b). Nanoparticles were coated with a layer of gold prior to the measurement. The analysis clearly indicated the presence of silicon and carbon in spectra and elements appeared in the expected ratios. However the ratio of oxygen to silicon appeared higher in the spectra of bottom up NH_2 SiNPs compared to the top down NPs. This could be due to the presence of oxygen on saline compounds which are used as the starting material in the synthesis of bottom up nanoparticles. Moreover, there were impurities observed in the

bottom up samples which came from the reagent ascorbate sodium used in the synthesis of bottom up nanoparticles. It should be noted that although dialysis was undertaken for 24 and 48 h to purify the bottom up nanoparticles, there was still signs of impurities after these purification steps. On the other hand, the level of oxide on NPs increased after the long term dialysis which might be due to the long exposure to the solvent.

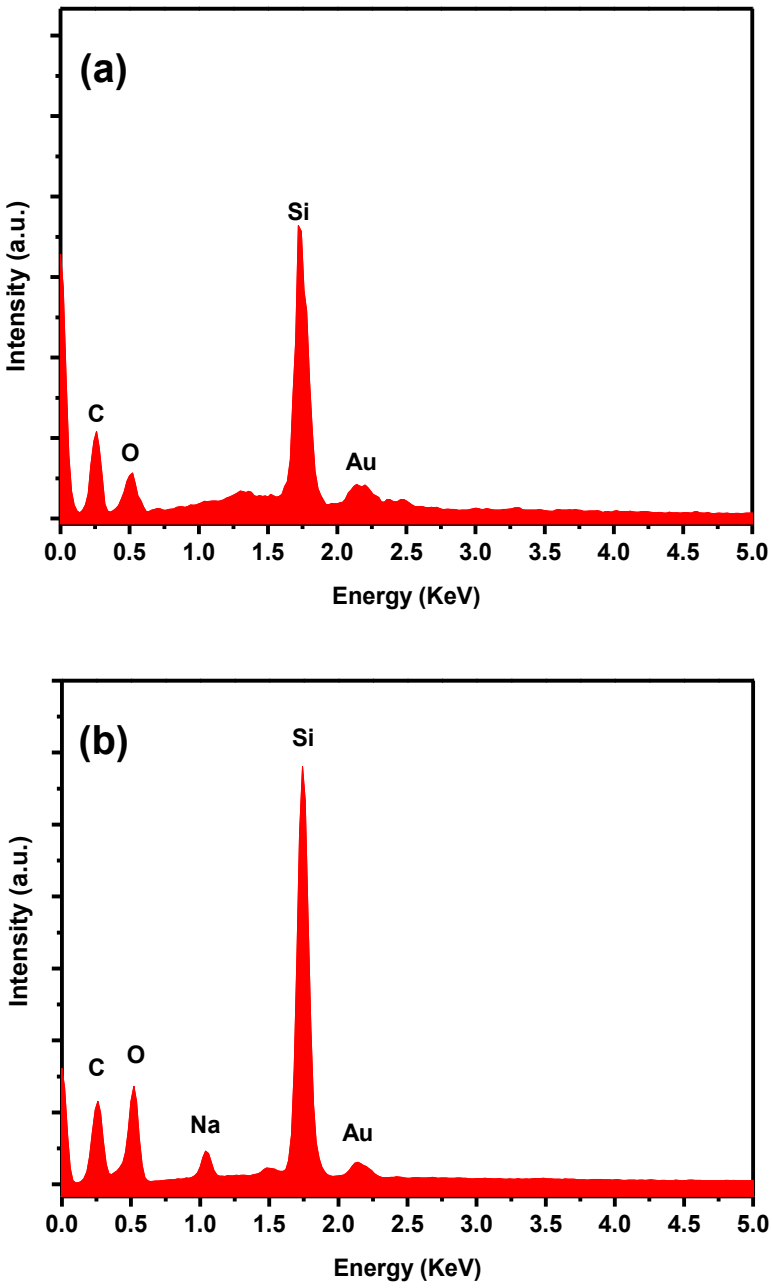

Figure 3.2. EDX spectrum of NH_2 SiNPs synthesised by top down (a) and bottom up (b) methods.

3.6. Size and Dispersity Measurement of Amine-functionalised SiNPs

3.6.1. Visualisation and Size Measurement by TEM

TEM images of NH_2 SiNPs are shown in Figure 3.3 top down and Figure 3.4 bottom up. Part (c) each figure gives the size distribution of SiNPs with an average diameter of 5.02 nm for the top down and 1.46 nm for the bottom up nanoparticles. The lattice spacing values of 0.31 and 0.29 nm are consistent with the Si (111) plane [20] (part (d) in each figure).

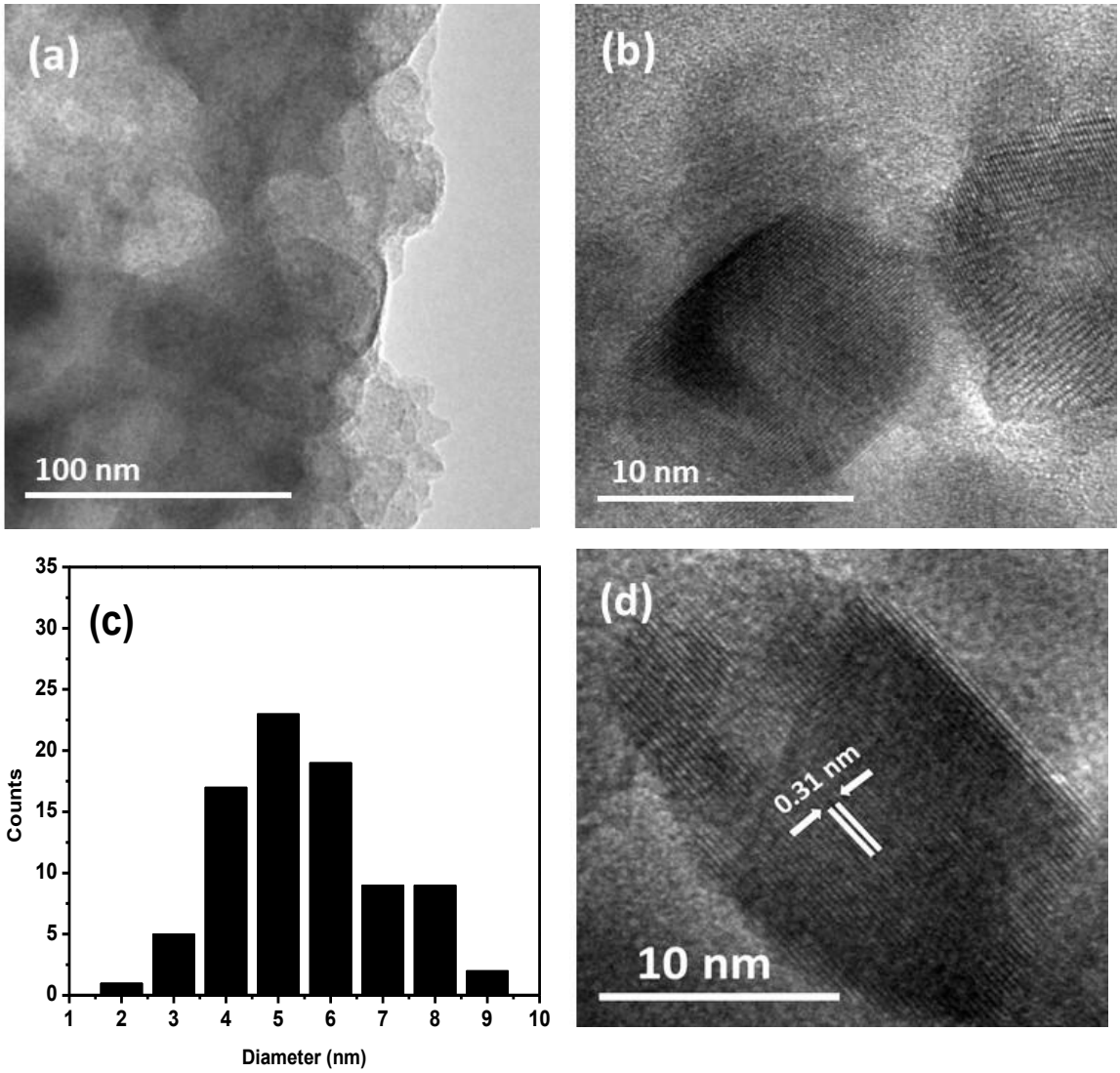

Figure 3.3. TEM images of top down NH_2 SiNPs (a) and (b) and the histogram showing the distribution of nanoparticle diameters (c) from 85 nanoparticles and the lattice spacing of Si (111) plane (d).

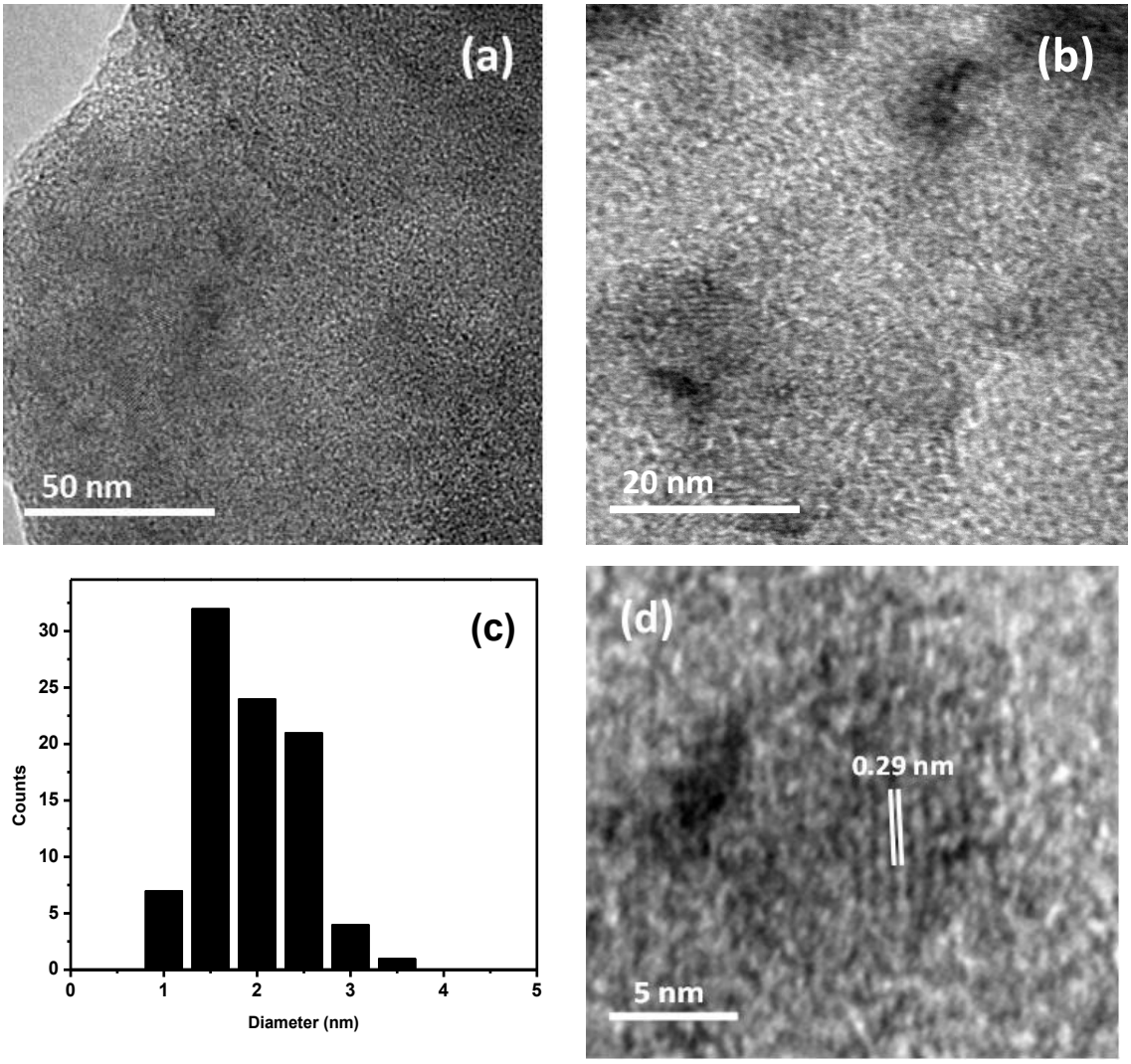

Figure 3.4. TEM images of bottom up NH_2 SiNPs (a) and (b) and the histogram showing the distribution of nanoparticle diameters (c) from 100 nanoparticles and the lattice spacing of Si (111) plane (d).

3.6.2. Hydrodynamic Size and Zeta Potential Measurement by DLS

The hydrodynamic diameters of NH_2 SiNPs in water were was measured by DLS. Top down nanoparticles had an average of 7.45 nm which was slightly larger than the core size obtained from TEM, as expected.[21, 22] This could be due to the presence of the amine groups, which increase the hydrophilicity of SiNPs and form a hydration shell around the nanoparticles.[23] The small size of bottom up nanoparticles was confirmed by DLS, measured as 4.05 nm in water (Figure 3.5). As particles smaller than 5 nm benefit the renal clearance *in vivo*, the smaller size of bottom up nanoparticles might offer the advantage of this method for biomedical applications.[24]

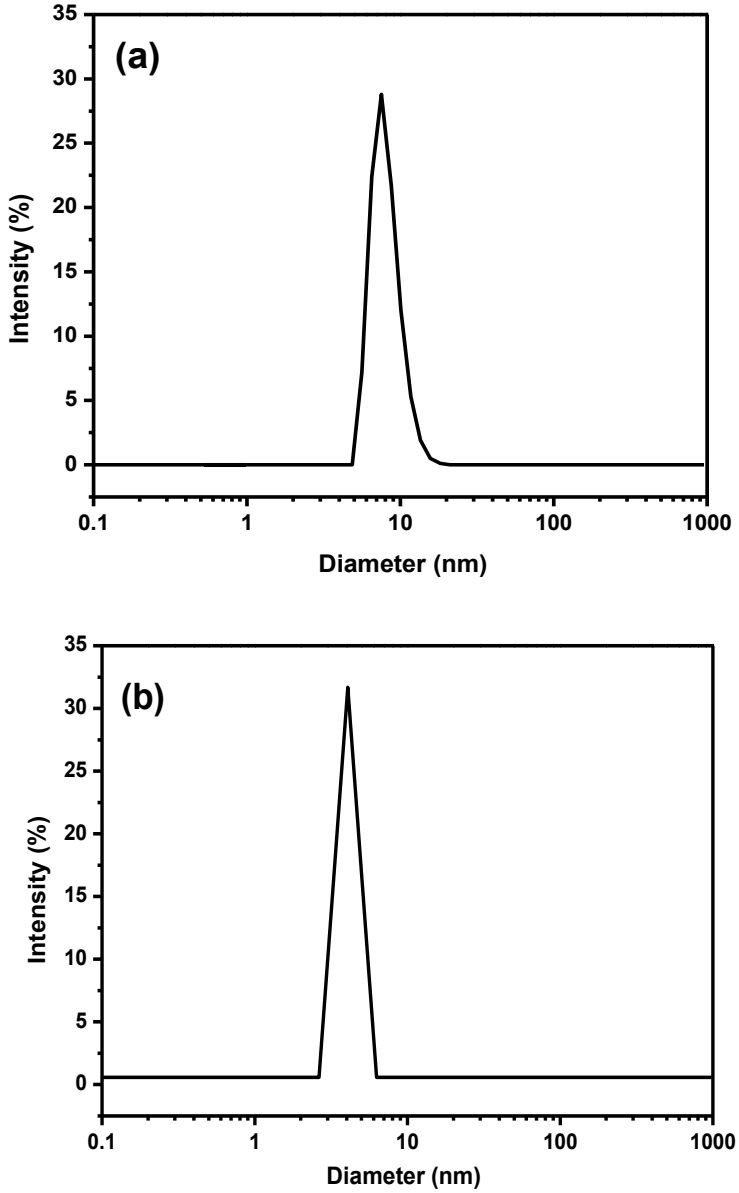

Figure 3.5. Hydrodynamic size of NH_2 SiNPs synthesised by top down (a) and bottom up (b) methods dispersed in water measured by DLS.

The positive zeta potential for both types of NH_2 SiNPs confirmed the presence of NH_2 terminal group which renders the nanoparticles positively charged. The surface charge of +22 and +30 mV were obtained for the top down and bottom up nanoparticles respectively (Figure 3.6). This positive charge makes the nanoparticles repel each other and therefore become well dispersed in aqueous solution. In addition, as the surface of living cells is negatively charged, the positively charged surface of nanoparticles provides a greater probability of internalisation for cell staining applications. The higher positive zeta potential of bottom up nanoparticles can be attributed to the fact that the coverage of amine functional group on the surface of

nanoparticles is better than the top down nanoparticles. This is due to the use of saline at the beginning of the synthesis (for bottom up NPs), which already has NH_2 with this compound. This fact can show a better colloidal dispersity of particle obtained from bottom up techniques due to the better surface coverage by the ligand.

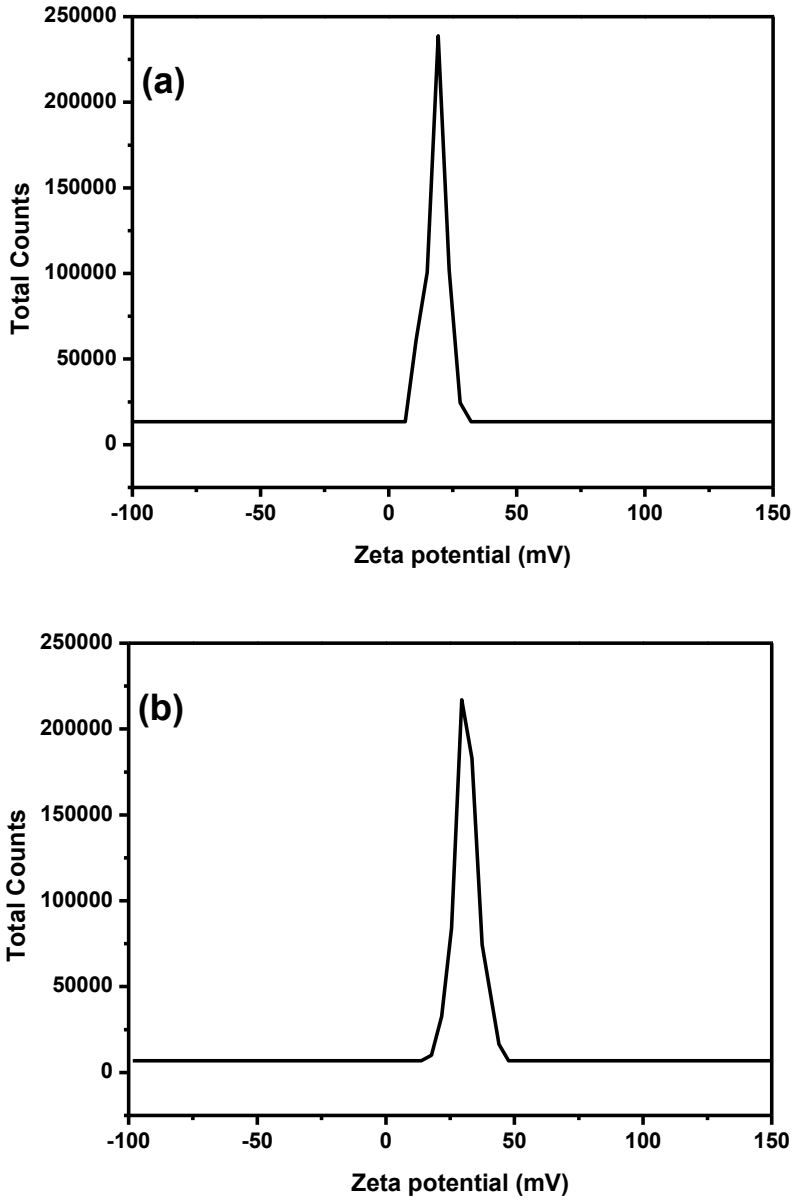

Figure 3.6. Zeta potential of NH_2 SiNPs synthesised by top down (a) and bottom up (b) methods.

3.7. Optical Properties of Amine-functionalised SiNPs

3.7.1. Absorption and Emission Spectra

The absorption and emission spectra of NH_2 SiNPs in water are presented in Figure 3.7 by top down (a) and bottom up (b) methods. There was a gradual increase in absorbance with a decrease in the wavelength from the onset of 450 nm for both types of NH_2 SiNPs. The emission spectrum of nanoparticles in water was centred at 440 nm for the top down and 460 nm for the bottom up with a full width at half maximum height (FWHM) of 99 and 70 nm respectively (Excitations: 360 and 400 nm).

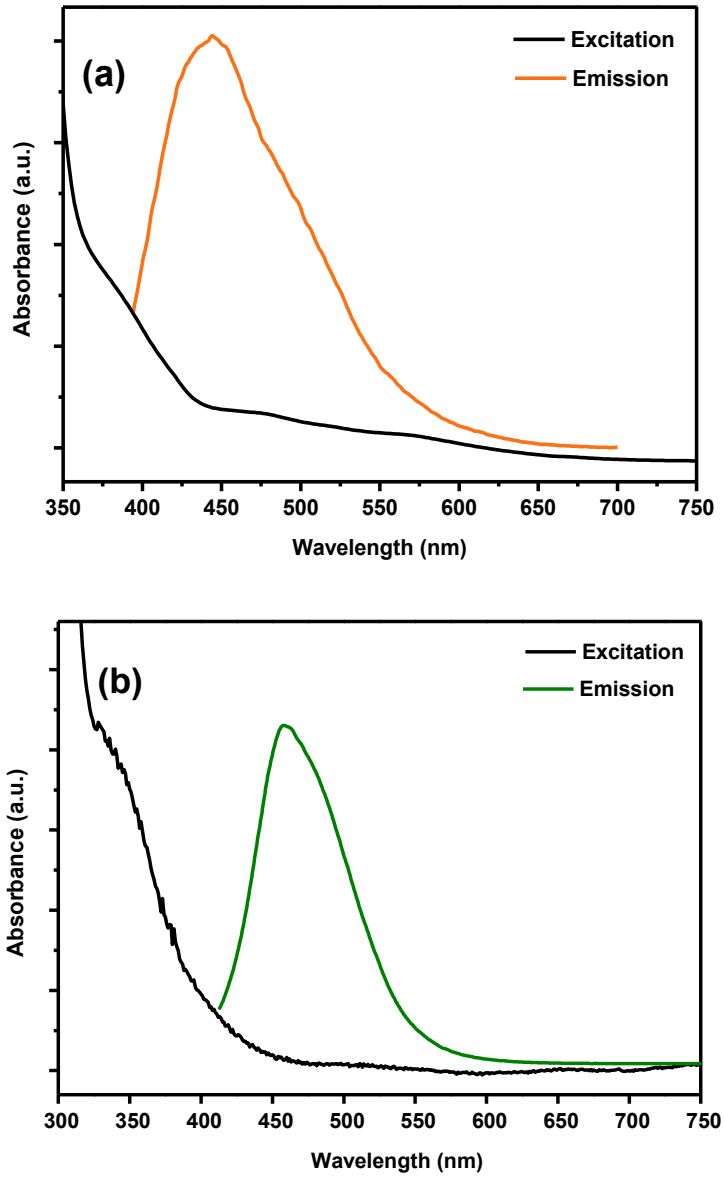

Figure 3.7. Absorption and emission spectra of top down NH_2 SiNPs (a) and bottom up NH_2 SiNPs (b) dispersed in water (The excitation wavelength was set at 360 and 400 nm respectively).

3.8. Biomedical Studies of Amine-functionalised SiNPs

3.8.1. *In vitro* Cytotoxicity Assay by MTT

The purpose of using NH_2 SiNPs in this project is firstly to use them as control samples for biological experiments in order to compare the efficiency of other types of nanoparticles (thiourea and ITC-functionalised SiNPs) with these non-toxic nanoparticles. In addition, they can be also exploited to be used as the starting material for further surface modifications. As a result, the toxicity should be measured and regulated if it is to be used as an appropriate control. MTT assay was performed on both types of NH_2 SiNPs to assess the cell viabilities. Caco-2 cells were incubated with different concentrations of NH_2 SiNPs for 24 and 48 h. As shown in Figure 3.8 (a), the cytotoxicity of top down nanoparticles was very low for both time points and even after 48 h incubation cells remained at 80% of their initial cell viability after incubation with 100 µg/mL nanoparticles. However, when the concentration of bottom up nanoparticle increases, a slight reduction in cell viability was observed. The loss of cell viability continued to ~ 60 % after 48 h incubation with 100 µg/mL NH_2 SiNPs (Figure 3.8 (b)). Using the bottom up approach to synthesise SiNPs often adds unwanted impurities,[25, 26] and so would cause the difference in toxic behaviour between the two types of NPs. This is confirmed by the EDX data (Figure 3.2).

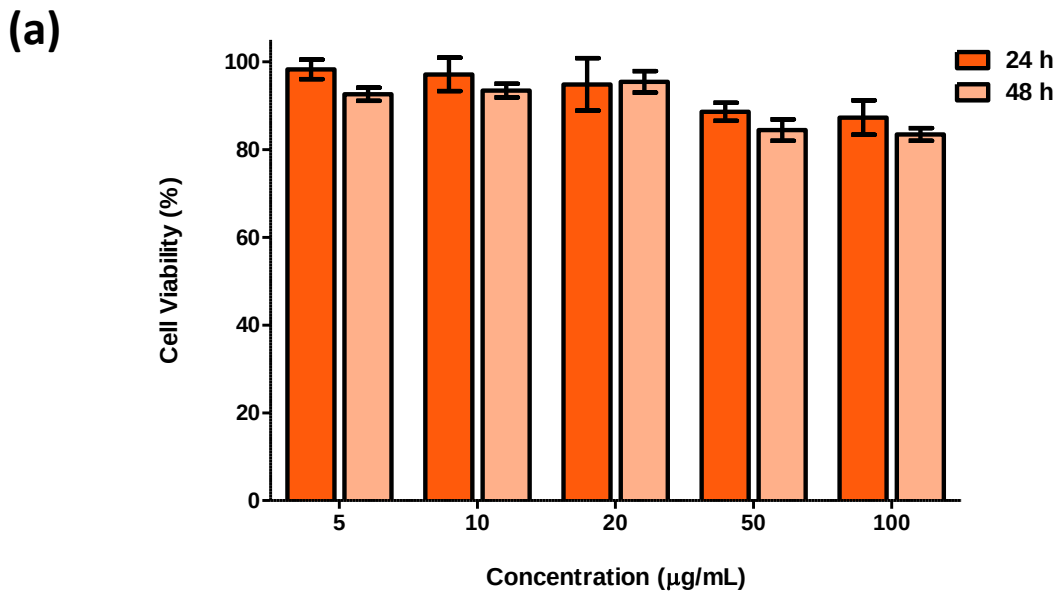

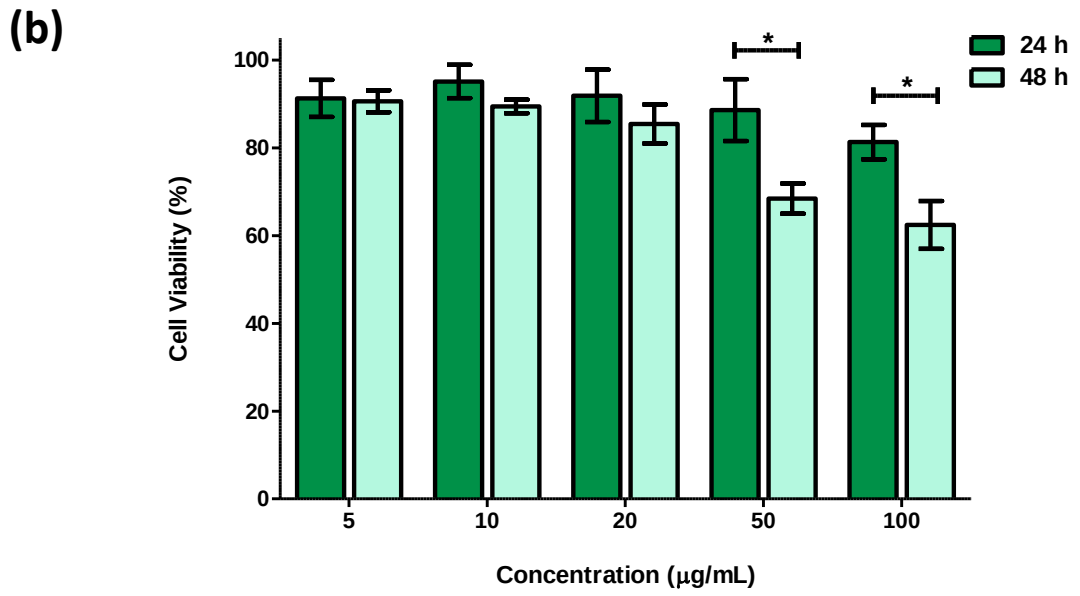

Figure 3.8. *In vitro* cytotoxicity of NH_2 SiNPs synthesised by top down (a) and bottom up (b) by MTT after incubation with Caco-2 at 24 and 48 h. Statistical significance was determined by two-way-ANOVA followed by a Bonferroni post-test (*P < 0.05). Results are expressed as mean ± SEM (n =3).

Consequently, by evaluating the chemical and physical characterisation data, the desired structure for NH_2 SiNPs was obtained in both synthesis methods. The greater positive surface charge of bottom up nanoparticles suggests the higher stability of nanoparticle in biological environments due to the better surface coverage by the amine functional group.[16] Although a bottom up approach offers a better chance to offer a more uniform size distribution (Figure 3.4 (c)) and a larger scale production, it requires an extensive purification protocol which results in substantial residue oxidation on the nanoparticle surface (Figure 3.1(b)). The key disadvantage of the top down method, on the other hand, could be considered to be the scalability for the industrial quantities. However, there are some examples of this method being successfully applied beyond milligram scales. The British company pSiMedica and Japanese company Tokao Yonehara of Canon Inc.[27] have developed functionalised porous silicon in large quantities. This can be done by directing the anodization of 10,000 silicon wafers per month. In this technique, layers of pure silicon are deposited onto the porous layer of a silicon wafer. Then, the wafer is bonded to another silicon wafer with an insulating silicon-oxide surface, in a way that the pure layer of silicon ends up sandwiched in the middle. The porous silicon is selectively dissolved away to leave the desired product which is silicon on top of an oxide layer on top of the silicon wafer. This technique can therefore scale up the

electrochemical etching to produce porous silicon and meet the requirements of manufacturing scale up.[27]

As the top down approach synthesises a purer form of NH_2 SiNPs, they are easily dispersed in aqueous solvents with no sign of aggregation as shown by Ahire *at el.*[14] Noting that these nanoparticle are to be used as probes in bioassays in for this project, their lower cytotoxicity is prioritised over a larger quantity of production, and therefore the top down NH_2 SiNPs were chosen for the rest of the project to act as control for biological experiments.

3.9. Synthesis of Thiourea-functionalised Silicon Nanoparticles

Conjugation of thiourea onto the SiNP surface has high potential for the active targeting of EGFR overexpressing cancer cells. This can therefore increase the stability of silicon, enhance the nanoparticle cell uptake and reduce the fast clearance of the nanoparticles from the body since the capping ligand renders hydrogen terminated SiNPs hydrophilic to provide stable dispersions. In order to evaluate the potential of such systems, a ligand containing a thiourea segment was synthesized via the reaction between sulforaphane and allylamine and subsequently used to functionalise the surface of hydrogen terminated SiNPs (Scheme 3.3).

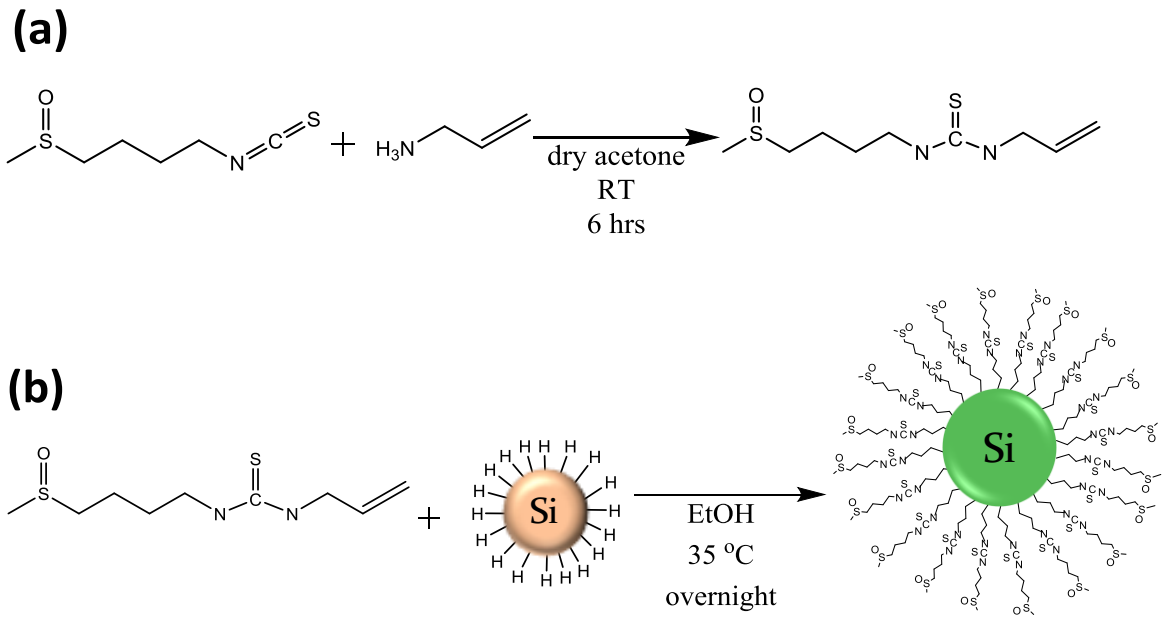

Scheme 3.3. Schematic illustration of (a) the chemical synthesis of thiourea ligand and (b) the conjugation of thiourea onto the surface of hydrogen capped silicon nanoparticles via hydrosilylation reaction.

3.10. Chemical Characterisation of Thiourea-functionalised SiNPs

3.10.1. Chemical Bonding by FTIR

The FTIR spectra of Sulforaphane, thiourea and thiourea-functionalised SiNPs are presented in Figure 3.9. The absorption peak at 1012 represents S=O in the structure of Sulforaphane as the starting material. Vibrations related to C-N and C-S bonds can be seen at 1298 and 692 cm^{-1} respectively.[28, 29] The characteristic feature of the isothiocyanate functional group can be clearly observed as a prominent double peak at 2099 cm^{-1}.[30] These peaks disappeared after reacting with allylamine but the stretching frequencies related to N-C-N vibrations in thiourea group were found at 1545 cm^{-1}. The band at 3279 cm^{-1} represent the stretching vibration of the N-H bond in the derivative thiourea.[31] After surface functionalisation of SiNPs with thiourea, a peak at 1258 cm^{-1} can be seen which is a strong indicator of Si-C bonding.[17] In addition, there was no evidence of Si-H stretching at 2100 cm^{-1}.[32] Therefore, the thiourea ligand with a terminal double bond reacted with the hydrogen terminated silicon surface via hydrosilylation in order to give a covalent Si-C linkage on the surface of the nanoparticles.

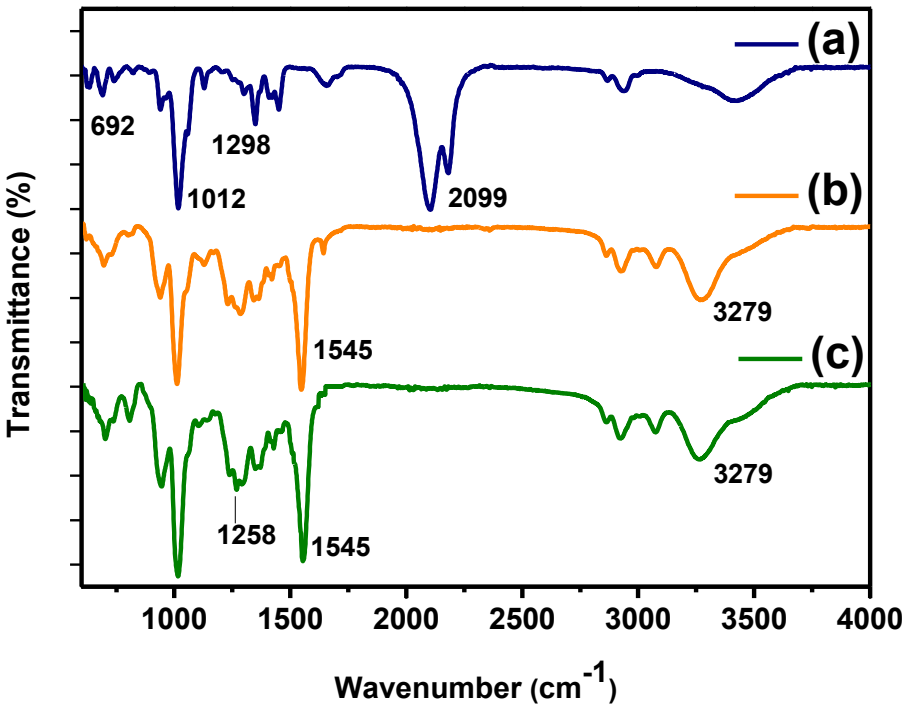

Figure 3.9. FTIR spectra of (a) sulforaphane; (b) thiourea and (c) thiourea-functionalised SiNPs. The relevant features of each spectrum are highlighted.

3.10.2. Elemental Analysis by EDX

EDX analysis was performed on thiourea-functionalised SiNPs coated with gold (Au) as the reference. A sharp signal was detected indicative of the silicon core and the surface of nanoparticles was shown to be coated with carbon, sulphur and oxygen atoms (Figure 3.10).

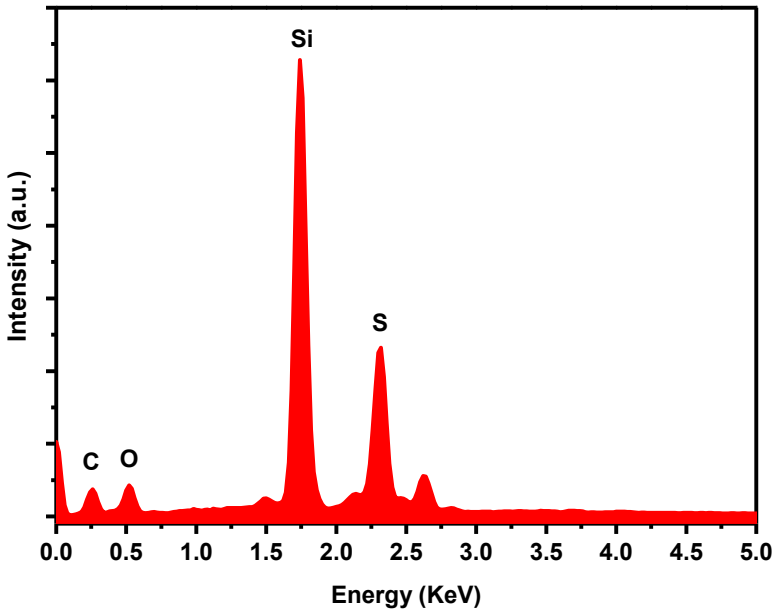

Figure 3.10. EDX spectra of thiourea-functionalised SiNPs.

3.10.3. Elemental Analysis by XPS

For further evidence of the nanoparticle structure, the surface chemical bonding was investigated using the full survey and high resolution XPS spectroscopy. Figure 3.11 shows the full survey of the photoelectron spectrum. The high resolution XPS spectra of Si2p, C1s, O1s and N1s regions taken on a thin film of thiourea-functionalised SiNPs are presented in Figures 3.12 to 3.15.

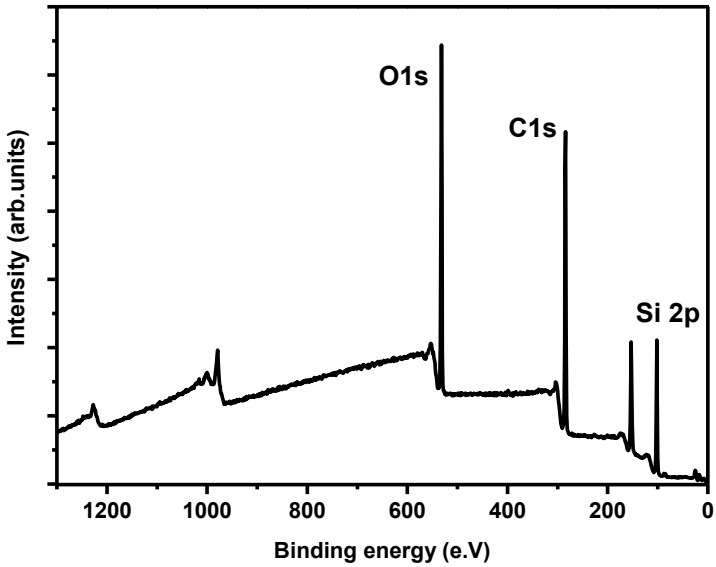

Figure 3.11. XPS full survey spectrum from thiourea-functionalised SiNPs deposited on a gold substrate.

Figure 3.12 indicates that the Si2p spectrum is fitted with three components and a Shirley background. The three peaks are located at 101.95, 102.73 and 100.91 eV. The first peak is attributed to Si-C confirming the hydrogen on the surface of SiNPs is replaced with thiourea.[33] The second peak at binding energy 102.73 eV is related to Si-O due to partial surface oxidation under the ambient conditions.[34] The third component at 100.91 eV is assigned to Si-Si within silicon core of NPs.[35, 36]

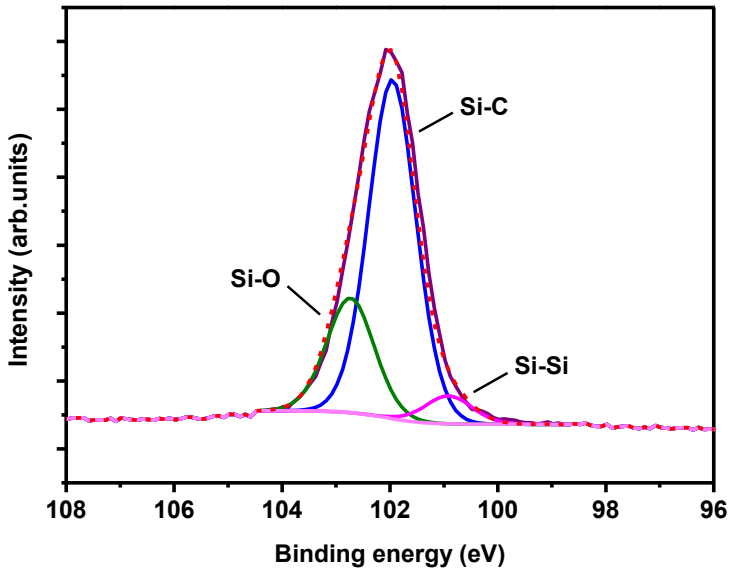

Figure 3.12. High resolution XPS spectrum from thiourea-functionalised SiNPs showing Si2p region.

The C1s spectrum is fitted with three components and a Shirley background (see Figure 3.13). The four peaks appeared at 284.65, 284.04, 285.50 and 286.72 eV. The first component at 284.65 eV is attributed to C-C bonding. The second peak at 284.04 eV relates to the existence of C-Si and finally the last two peaks at 285.50 and 286.72 eV are assigned to C-H and C-N respectively.[37, 38]

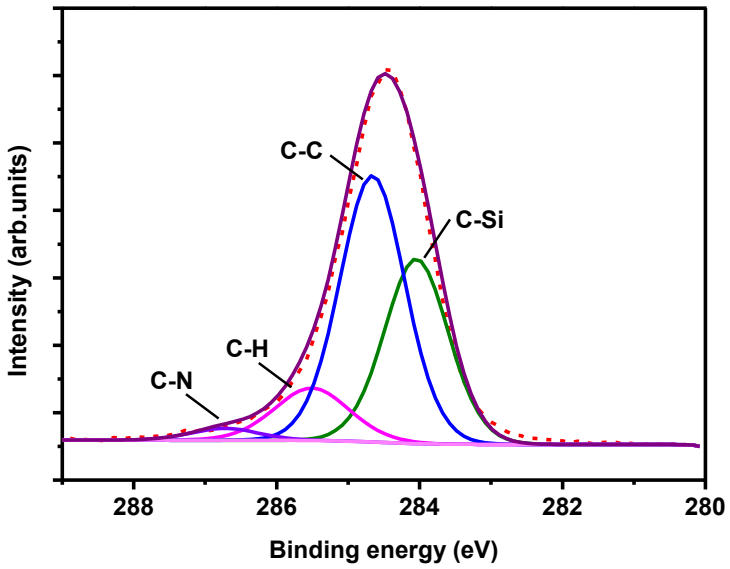

Figure 3.13. High resolution XPS spectrum from thiourea-functionalised SiNPs showing C1s region.

The O1s spectrum is presented in Figure 3.14 and fitted with three components and a Shirley background. The first peak is related to partial oxidation at 532.01 eV for Si-O. The second binding energy at 533.25 eV is attributed to some hydroxide O-H group. The last component of O1s spectrum is assigned to O-S at 531.10 eV.[36]

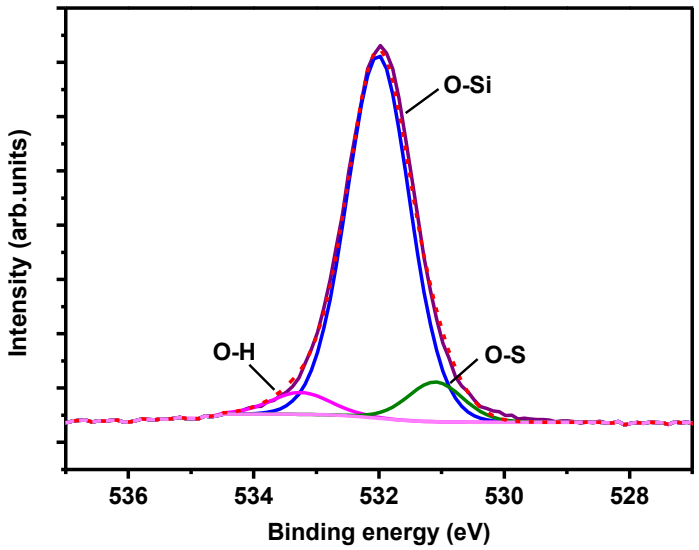

Figure 3.14. High resolution XPS spectrum from thiourea-functionalised SiNPs showing O1s region.

The N1s spectrum is presented in Figure 3.15 and fitted with two components and a Shirley background. The peak at 399.58 eV is assigned to C-N bonding in the thiourea. The other peak at 398.67 eV is attributed to N-C=S.[39]

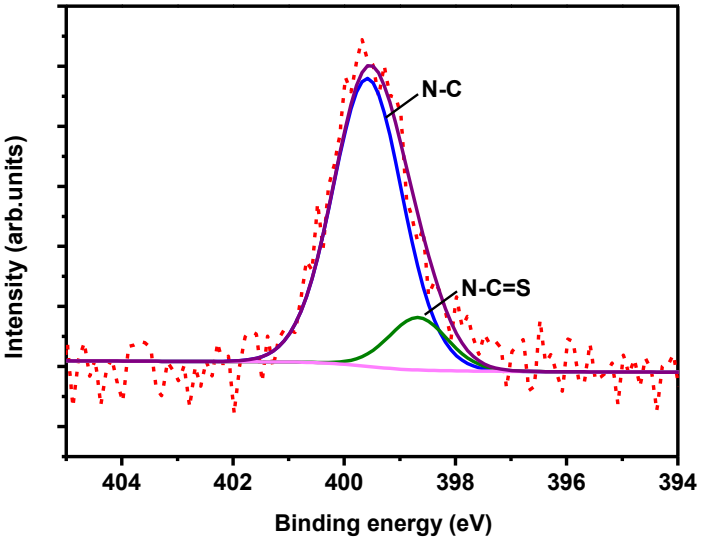

Figure 3.15. High resolution XPS spectrum from thiourea-functionalised SiNPs showing N1s region.

According to the surface chemistry data obtained from XPS the surface of SiNPs is fully capped with the ligand. A table with the quantification of XPS data can be seen in Table 3.1.

Table 3.1. XPS data with the detailed ratio of elements present on the surface of thiourea-functionalised SiNPs obtained by high resolution scans.

Scans	Positions	Position (eV)	FWHM	Area	%
Si 2p	Si-C	101.95	1.0320	11177.421	70.32
	Si-O	102.73	1.0369	3803.808	23.93
	Si-Si	100.91	1.0230	913.945	5.75
C 1s	C-C	284.65	1.0752	2304.59	51.23
	C-Si	284.04	1.0564	15674.85	34.82
	C-H	285.50	1.2336	5203.06	11.57
	C-N	286.72	1.1092	1057.05	2.23
O 1s	Si-O	532.01	1.1839	4278.528	86.96
	O-S	531.10	1.0372	4117.594	8.33
	O-H	533.25	1.1261	2461.856	4.33
N 1s	N-C	399.58	1.4741	1532.947	86.73
	N-C=S	398.67	1.237	234.52	13.27

3.11. Size and Dispersity Measurement of Thiourea-functionalised SiNPs

3.11.1. Visualisation and Size Measurement by TEM

Figure 3.16 (a) illustrates a TEM image of SiNPs on a carbon coated copper grid. A mean size and size distribution was found to be 4.5 nm after analysing approximately 100 SiNPs from different regions of the grid (Figure. 3.16 (b)). The insert figure shows the crystalline structure of the individual NPs. The measured lattice spacing in these crystalline particles is 0.31 nm, corresponding to the (111) interplanar spacing of the diamond cubic structure of silicon.[20]

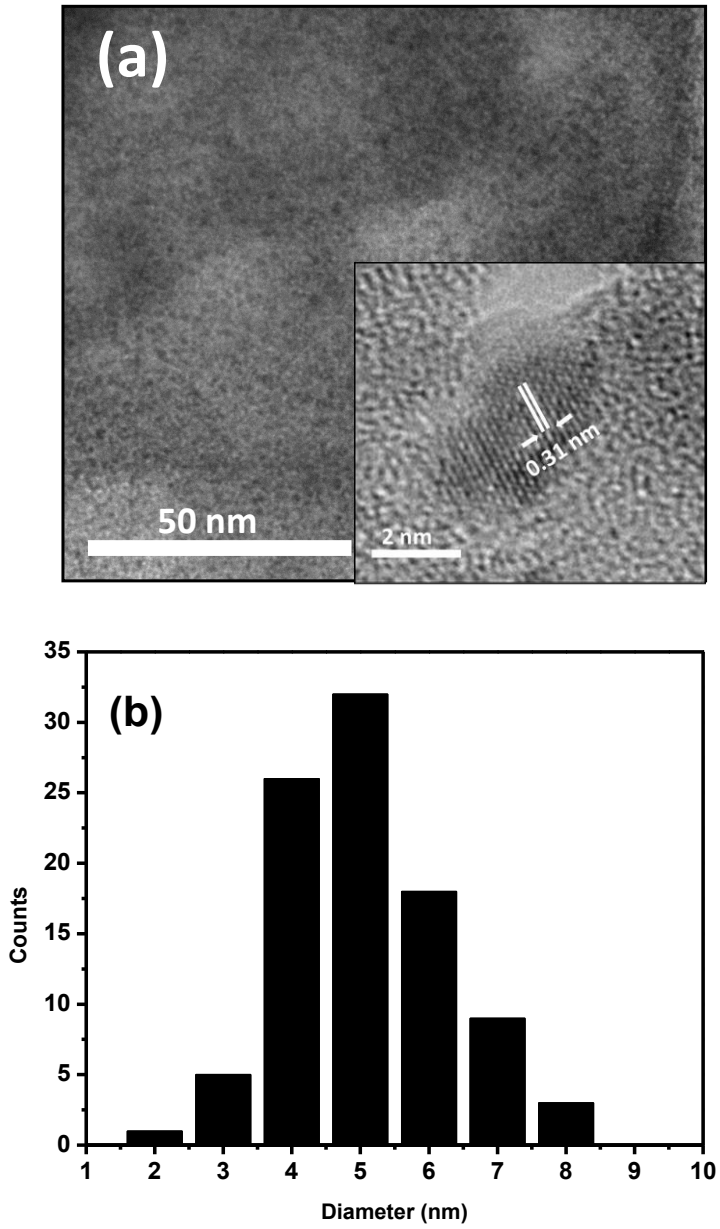

Figure 3.16. TEM image of thiourea-functionalised silicon nanoparticles (a). The insert shows an enlarge view of the high resolution image of the crystalline structure. The corresponding histogram of nanoparticle size distribution after analysing 88 particles (b).

3.11.2. Hydrodynamic Size Measurement by DLS

The size of nanoparticle plays a critical role in the efficiency of cellular uptake as it can determine the mechanism and uptake rate.[40] The investigation of particle size therefore will impact on the application of nanoparticles in biomedicine.[41]

The mean hydrodynamic diameters of thiourea-functionalised SiNPs are represented in Figure 3.17 and Table 3.2 in different solvents: water, PBS and the cell culture media RPMI

and RPMI/10% FBS. The observed hydrodynamic diameters are slightly larger than those observed in the corresponding TEM images; understandably, as hydrodynamic diameters are generally larger than the core particle sizes obtained by TEM. According to the data, SiNPs show almost the same average diameters in all solvents. This is more than double than the core size of SiNPs due to the formation of an outer shell after the interaction between the capping ligand and the surrounding environment.[42] However, the average diameter and the PdI are slightly increased for NPs in the RPMI containing 10% FBS, suggesting the expected adsorption of serum proteins on the surface of positively-charged SiNPs. This is because of the small size of SiNPs and their large surface area lead to partial aggregation in the biological media, and therefore the presence of proteins reduces the surface energy. Nevertheless, the aggregation was not significant as the main population of SiNPs was still observed around the expected sizes similar to other solvents less than 20 nm.

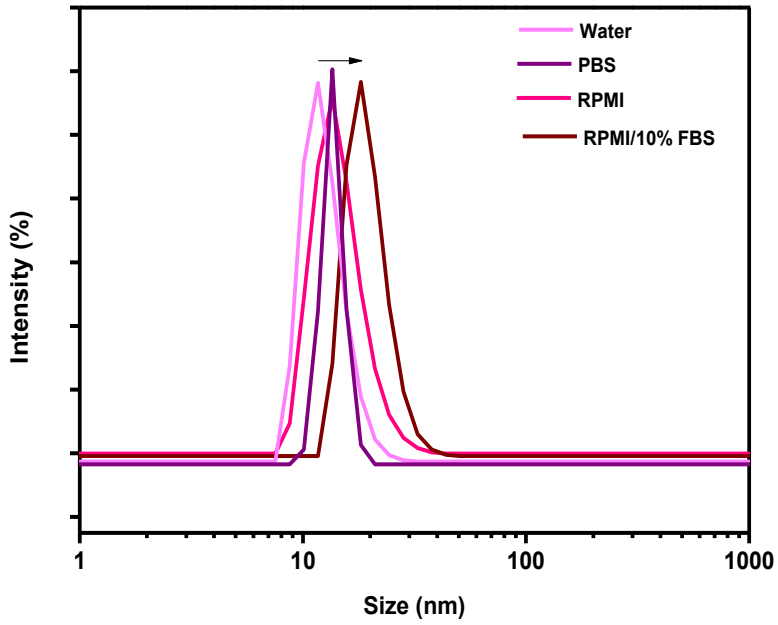

Figure 3.17. Hydrodynamic diameter of thiourea-functionalised SiNPs in different dispersing solvents.

Table 3.2. Mean hydrodynamic diameters and polydispersity index of thiourea-functionalised SiNPs measured by DLS in different media.

Solvent	Mean Particle Size (nm) ± SD	Polydispersity Index ± SD
Water	11.32 ± 0.05	0.16 ±0.05
PBS	12.20 ±1.05	0.22 ± 0.05
RPMI	12.50 ± 1.26	0.20 ± 0.10
RPMI/10%FBS	16.70 ± 4.80	0.33 ± 0.04

3.12. Zeta Potential and Stability of Thiourea-functionalised SiNPs in Human Plasma

The nanoparticles, especially if made in aqueous solution, have a surface charge to stabilise them against aggregation, which can happen via electrostatic repulsion. The magnitude of the zeta potential gives an indication of the potential stability of the colloidal system. Nanoparticles with a zeta potential between −10 and +10 mV are considered approximately neutral, while nanoparticles with zeta potentials values of greater than +30 mV or less than −30 mV are considered strongly cationic and anionic, respectively and therefore more stable.[43] If nanoparticles in a suspension have a large negative or positive zeta potential, they will tend to repel each other and therefore there will be no tendency for the particles to come together and aggregate. If the nanoparticles have low zeta potential, there will be no force to prevent the particles coming together and flocculating. Thiourea-functionalised SiNPs were centrifuged and re-suspended in Milli-Q water at a final concentration of 25 μg/mL prior to the measurement. The zeta potential was found to be 21 ± 0.80 mV.

The cellular growth media contains several components such as essential amino acids, serum proteins, vitamins, etc. These chemicals could interact with nanoparticles and change their physiochemical properties such as size, surface charge, surface chemistry and aggregation state.[44] The presence of electrolytes and high ionic strength of the biological media can cause

nanoparticle aggregation via electrostatic screening.[45] This aggregation can interfere with the ability of nanoparticles to interact with cells and therefore influence the cell internalisation. This would eventually add complexity to the system. As a result, if the aggregation state of SiNPs is not considered, difficulties arise when interpreting the data from uptake studies and nanoparticle biodistribution.[46]

When nanoparticles are introduced into the growth media or plasma, they adsorb plasma proteins and adopt the corresponding physiochemical properties of the protein shell which is called protein corona.[47] The protein adsorption can change the nanoparticle charge immediately to a similarly negative value as the serum proteins in the media.[48] As a result, nanoparticles with originally positive charge upon preparation are no longer cationic in the cellular plasma. This is significant in terms of the cytotoxicity and cellular uptake of NPs and is a counterpoint against the common concept in the literature that cationic nanoparticles disrupt the negatively charged membrane of cells by electrostatic interactions. The protein adsorption on NPs can mediate the uptake mechanism via receptor mediated endocytosis.[49] As a result, media with different protein compositions could lead to various levels of toxicity and uptake efficiency. This is important when comparing the results from different experimental parameters addressing the uptake and cytotoxicity of NPs.

The surface charge of thiourea-functionalised SiNPs was tested in human plasma to investigate the effect of protein adsorption on zeta potential values of NPs. The stability of NPs was tested in human plasma at different time points (Figure 3.18). Ideally, in order to avoid the rapid clearance of NPs from the body, nanoparticles should minimally interact with plasma proteins. Therefore the influence of the NP interactions with the plasma protein adsorption was tested by reacting at 37 ^{o}C for different time points. The rate of zeta potential decrease of thiourea-functionalised SiNPs was rapid for the first hour of the exposure, indicating an expected adsorption of plasma proteins. Thereafter, the rate of decrease slowed substantially. This suggests that the protein coating by itself may increase the stability of system.

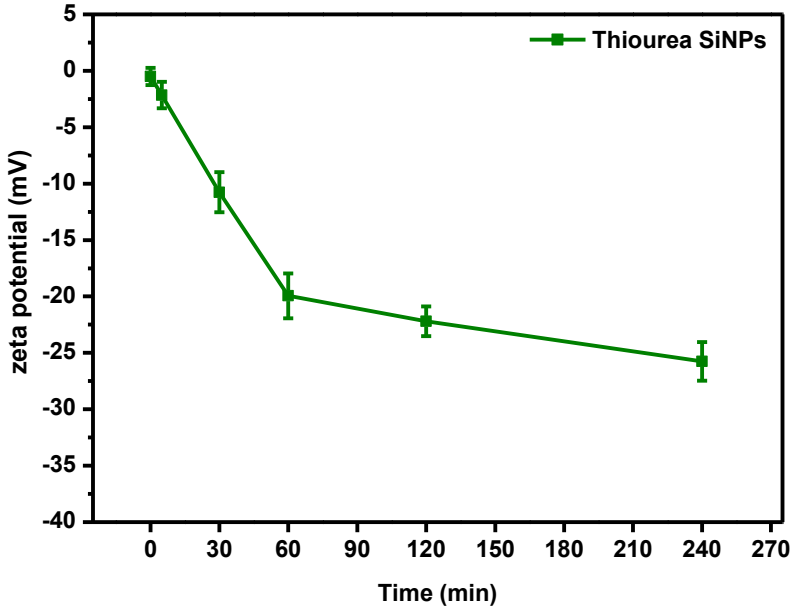

Figure 3.18. Zeta potential of thiourea SiNPs in human plasma at different time points.

3.13. Optical Properties of Thiourea-functionalised SiNPs

3.13.1. Absorption and Emission Spectra

Absorption and emission spectra of thiourea-functionalised SiNPs are presented in Figure 3.19. The inset photograph is the sample under UV illumination at 254 nm. NPs were dispersed in EtOH prior to the measurement as this improved the solubility of the sample. The gradual increase in the absorbance with decreasing excitation wavelength from the onset wavelength of 430 nm. The solid line shows the photoluminescence spectrum of thiourea-functionalised SiNPs with the maximum emission peak centre at approximately 420 nm and a full width at half-maximum height (FWHM) of 79 nm under an excitation wavelength of 340 nm.

Unlike direct bandgap semiconductors, there are still many uncertainties in the relationship between nanoparticle surface configuration and PL properties. Contrary to silicon wafers, the surface structure of SiNPs is inhomogeneous and therefore is far more complex. Among all the emissions from SiNPs, the mechanism of the blue emission is much more controversial and still unclear.[32, 50] Surface oxide might be one of the reasons which determines the emission photon energy. This blueshift is explained as a result of the size reduction of the core with oxidation (loss of surface atoms due to oxidation) according to the quantum confinement effect.[50] On the other hand, Kang *et al*.[51] confirmed the blue emission in 3 nm SiNPs originated from the silicon core and not from oxidation after examining the controlled oxidation on SiNPs.

This is because of the stable and efficient blue emission observed even after etching by HF. Chen *et al*.[52] has also suggested that the silicon oxide is not responsible for the blue shift in porous silicon. They explain that by observing a change in the peak position of the blue band after varying the excitation wavelengths. Considering these previous observations, and the fact that FTIR and XPS data did not show high levels of oxidation-induced defects on the silicon surface, the likelihood of hydrosilylation causing the blueshift is stronger.[53]

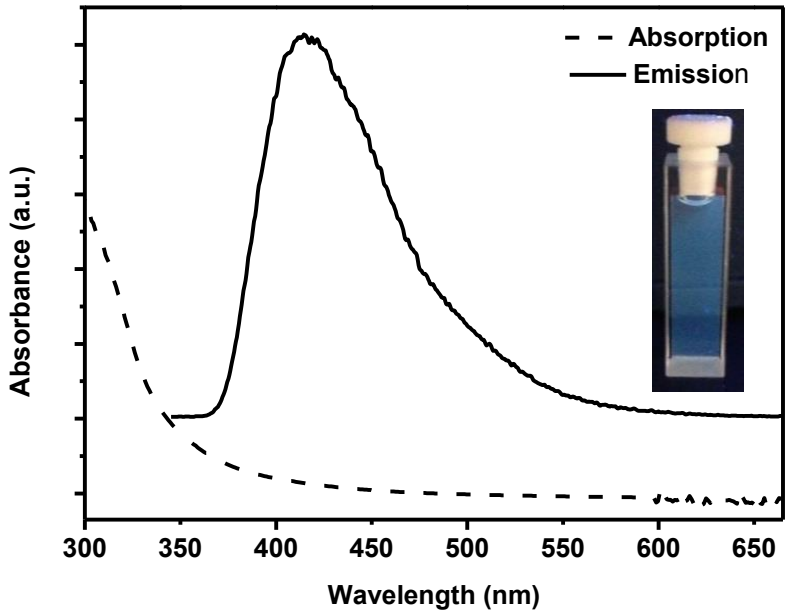

Figure 3.19. Absorption and emission spectra of thiourea-functionalised SiNPs at excitation at 340 nm. The inset image shows the fluorescence from a vial of sample in EtOH when excited with a UV lamp.

More importantly, a reasonable explanation of the origin of blue PL, found in this case, is provided by Veinot *et al*,[32] who confirmed that SiNPs obtained from the nitrogen containing reagents could provide a short-lived excited state that gives rise to the blue emission of SiNPs. They applied controlled experimental conditions on SiNPs exposed to nitrogen containing reagents in the absence of air and observed no blue PL. SiNPs were also exposed to air in the absence of nitrogen compounds in order to oxidise the surface and again no blue PL was observed. Finally, they tested SiNPs exposed to both air and nitrogen compounds and observed the appearance of blue PL. Therefore, the presence of nitrogen in the structure of thiourea ligand with the possibility of partial oxidation occurred during the synthesis is most likely the reason for the blue PL of thiourea-functionalised SiNPs.

3.13.2. Quantum Yield Measurement

A fluorescence quantum yield of thiourea-functionalised SiNPs was measured in EtOH by a comparative method described by Williams *et al*.[54] with a reference to quinine sulphate when dissolved in 0.1 M H_2SO_4. Five solutions with absorbance within 0.1 and 0.01 were prepared (Figure 3.20). The gradients were obtained from the plot of integrated fluorescence intensity *vs.* absorbance for the SiNPs and reference (Figure 3.22). The quantum yield of thiourea-functionalised SiNPs was calculated using by:

$$\boldsymbol{Q = Q_{Ref}\left(\frac{Grad_{SiNPs}}{Grad_{Ref}}\right)\left(\frac{\eta^2_{EtoH}}{\eta^2_{Ref}}\right)} \qquad \textbf{(Equation 3.1)}$$

Where $\boldsymbol{Q}$ is the quantum is yield of the sample and $\boldsymbol{Q_{Ref}}$ is the reference quantum yield of quinine sulphate in 0.1 M H_2SO_4 and is equal to 54.6%.[55] The gradient of quinine sulphate and thiourea-functionalized SiNPs were 851171 and 158767 respectively according to the plots of integrated fluorescence intensity *vs.* absorbance. The refractive index of both solvents were known ($\boldsymbol{\eta_{EtOH}}$=1.33 and $\boldsymbol{\eta_{Ref}}$= 1.346), thus the sample quantum yield can be calculated as follows:

$$\boldsymbol{Q = 54.6\%\left(\frac{158767}{851171}\right)\left(\frac{1.33^2}{1.346^2}\right) = 9.94\%} \qquad \textbf{(Equation 3.2)}$$

A quantum yield of 9.94% was calculated which is close to the previously reported quantum yields for SiNPs normally between 4 to 25%.[17, 33, 56]

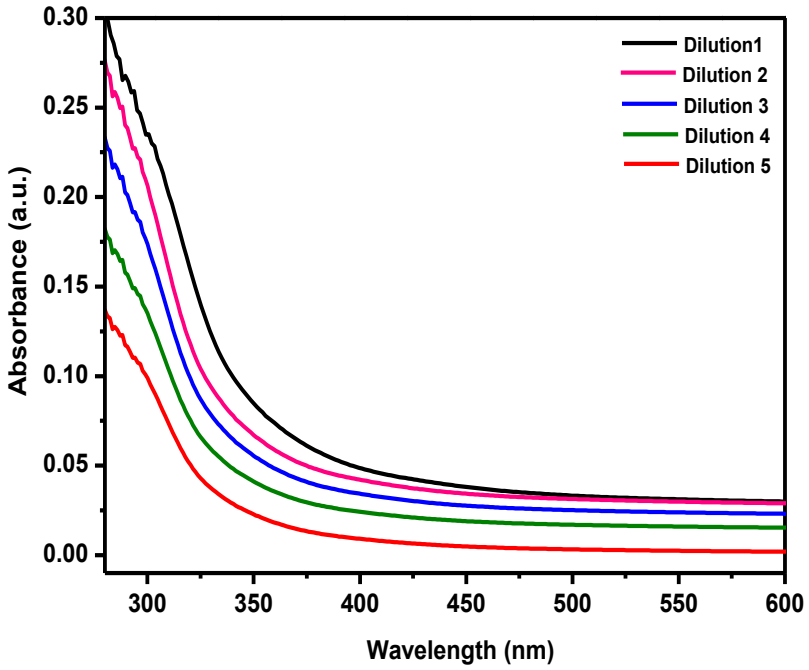

Figure 3.20. UV/Vis spectra at different dilutions of thiourea-functionalised SiNPs in EtOH.

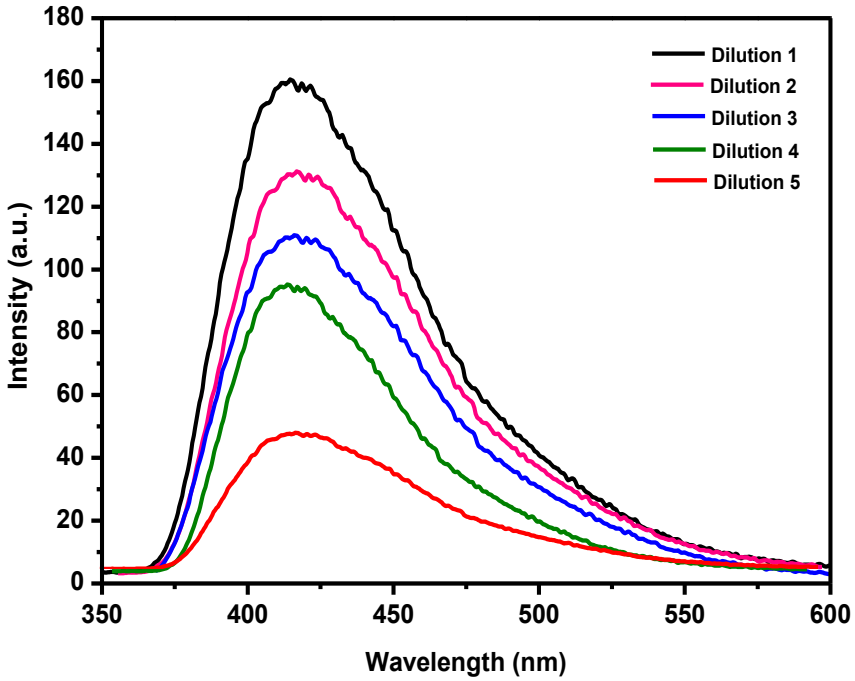

Figure 3.21. Emission spectra of thiourea-functionalised SiNPs at varying concentration in EtOH. (Excitation: 340 nm)

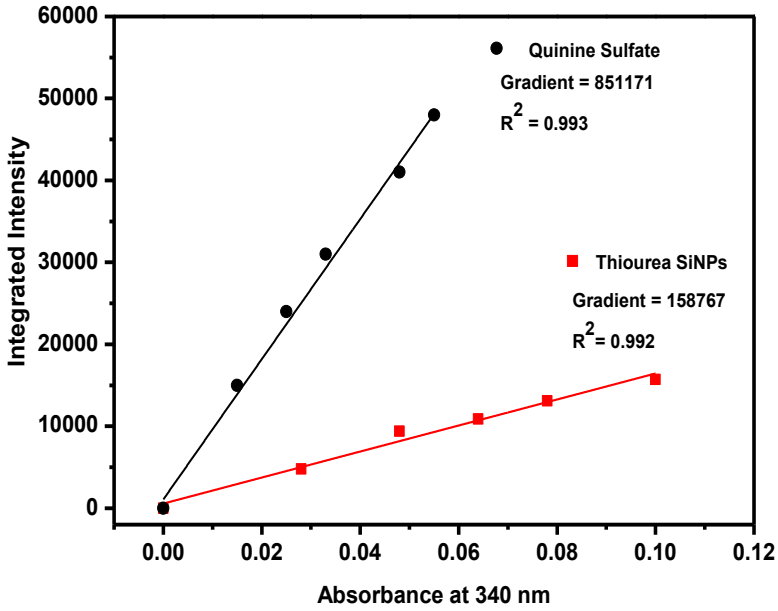

Figure 3.22. Plotted integrated intensity of emission against absorbance for both thiourea-functionalised SiNPs in EtOH and quinine sulphate in 0.1 M H_2SO_4.

3.13.3. Long-term PL Stability

In order to have a more efficient system in terms of biomedical applications, it is important to obtain NPs with suitable PL stability. The long-term stability of the synthesised SiNPs in EtOH was tested over a month and it was found that NPs can maintain about 80% of their initial PL after 30 days (Figure 3.23). The stabilisation of the PL by the coating ligand is attributed to the covalent passivation of the surface by the thiourea which can prevent the oxidation of the NP surface.

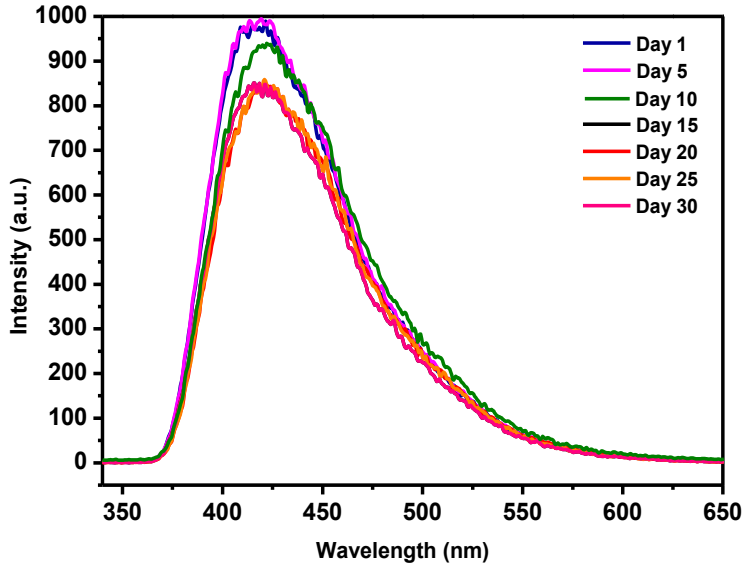

Figure 3.23. Long term PL stability of thiourea-functionalised SiNPs stored in EtOH.

3.13.4. Effect of pH on Photoluminescence stability

A successful surface functionalisation increases the stability and dispersity of SiNPs in various solvents. As a result, this will form SiNPs with high brightness/photoluminescence and stability through a wide range of pH values. The pH is a fundamental parameter for biomedical uses, and thus the PL stability of thiourea-functionalised SiNPs was tested over a range of different pH values. Figure 3.24 represents the changes in the intensity and peak wavelength of SiNPs of pH values from 4 to 9. Based on the data obtained, the photoluminescence intensity was stable over a range of physiologically relevant pH environments. Additionally, for pH levels 4-8 the peak position of the maximum PL emission remained unchanged, however for the most alkali pH 9 this shifted slightly to a lower wavelength. Taken overall, these results indicate that the inorganic capping ligand successfully isolates the silicon core from the surrounding environment and therefore makes SiNPs suitable for further biomedical investigations.

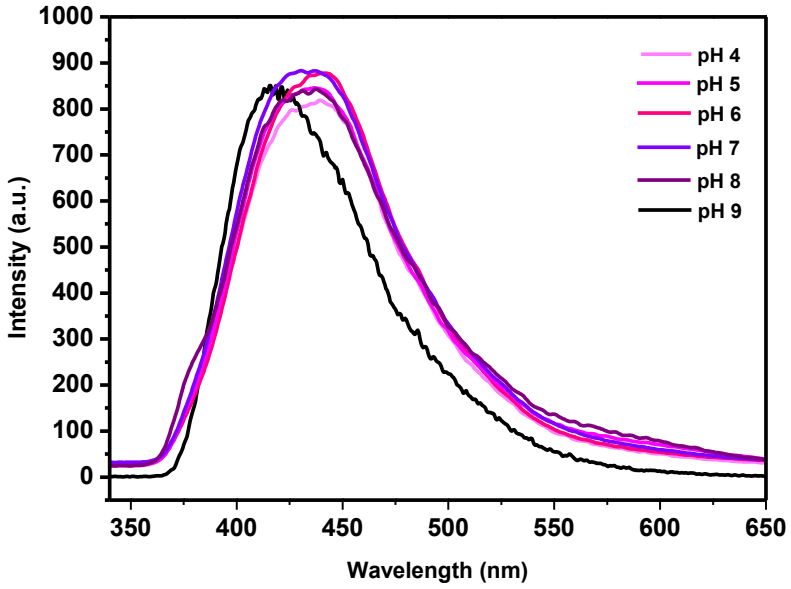

Figure 3.24. PL stability of thiourea-functionalised SiNPs in buffers of different pH values.

3.14. *In vitro* Biomedical Studies of Thiourea-functionalised SiNPs

3.14.1. Cytotoxicity Assay by MTT

Modifying the surface chemistry of NPs, given their large surface area, alters the toxicity and biological characteristics which can be beneficial for biomedical applications. In this study, the cytotoxicity of thiourea-functionalised SiNPs in colon cancer cells and their equivalent non-cancerous cell line is evaluated by MTT assay. Amine-functionalised SiNPs, which have been identified as a non-toxic biomaterial,[14] were used in this project as a control compound. Cells were exposed to increasing concentrations ranging from 5 to 1500 μg/mL thiourea and amine-functionalised SiNPs. After 24 h incubation, MTT assay was carried out in Caco-2 and CCD-841 cells and the absorbance values were normalised to the untreated cells. The results indicate that for the NPs used in the current study, concentrations up to 1500 μg/mL did not show any significant toxicity after 24 h incubation (Figure 3.25 (a) and (b)). For this time point, both thiourea and amine functionalised SiNPs reduced CCD-841 and Caco-2 cell viability by approximately 20-25%, which indicates that the anticancer activity of thiourea did not develop in this short incubation time.

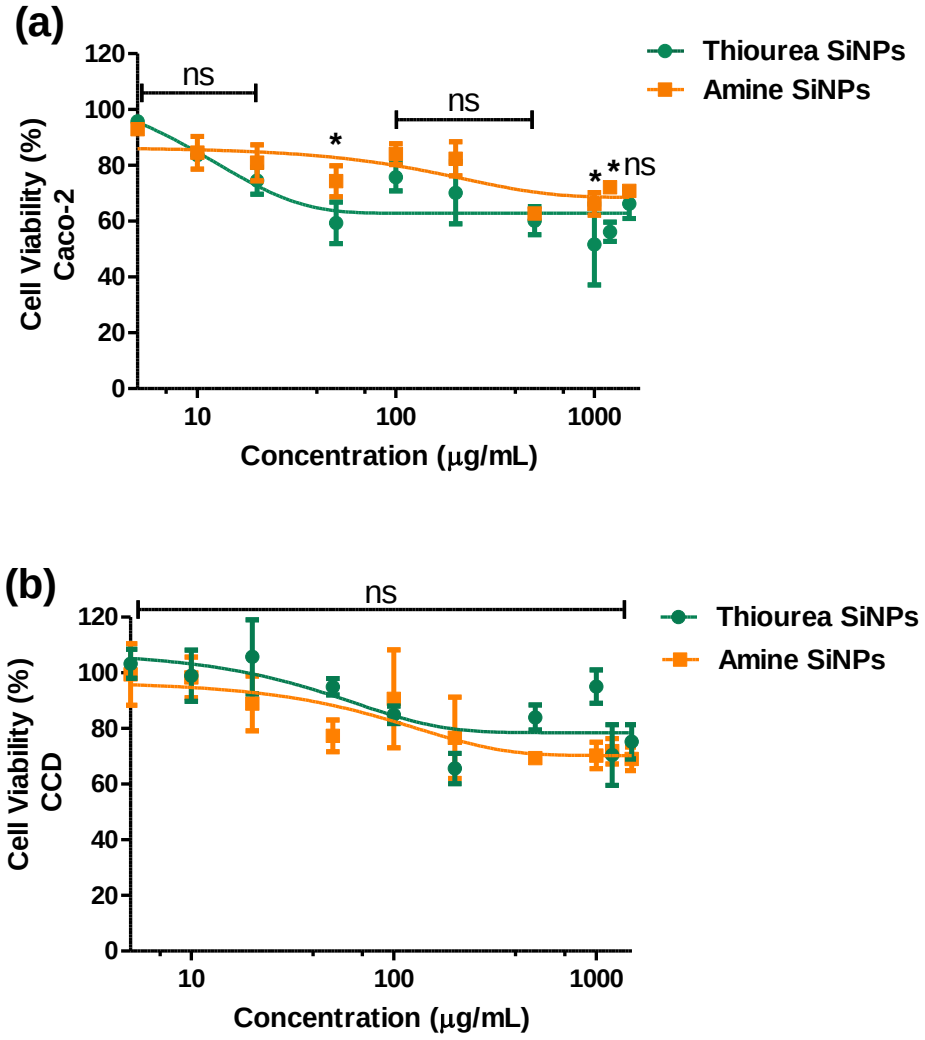

Figure 3.25. *In vitro* cytotoxicity of thiourea and amine capped SiNPs by MTT after incubation with Caco-2 (a) and CCD-841 (b) for **24 h** incubation at 37 ºC. (The results were normalised to non-stimulated cells.) Statistical significance was determined by two-way-ANOVA followed by a Bonferroni post-test (*P < 0.05 and ns statistically not significant). Results are expressed as mean ± SEM (n =3).

In Caco-2 cells, thiourea-functionalised SiNPs had a slightly larger effect than amine-functionalised SiNPs for concentrations around 50 µg/mL. For the longer 72 h exposure (Figure 3.26 (a) and (b)), the Caco-2 cell viability dropped by 60% for concentrations above 100 µg/mL, a result that was not reproduced by amine-functionalised SiNPs which had negligible effect beyond 24 hours. Lower cell viability was observed at lower concentrations of thiourea-functionalised SiNPs in Caco-2 cells than in CCD-841, which is important if the treatment is to be effective whilst having a less impactful effect on normal cells. In CCD-841 cells the behaviour was similar for both thiourea and amine-functionalised SiNPs.

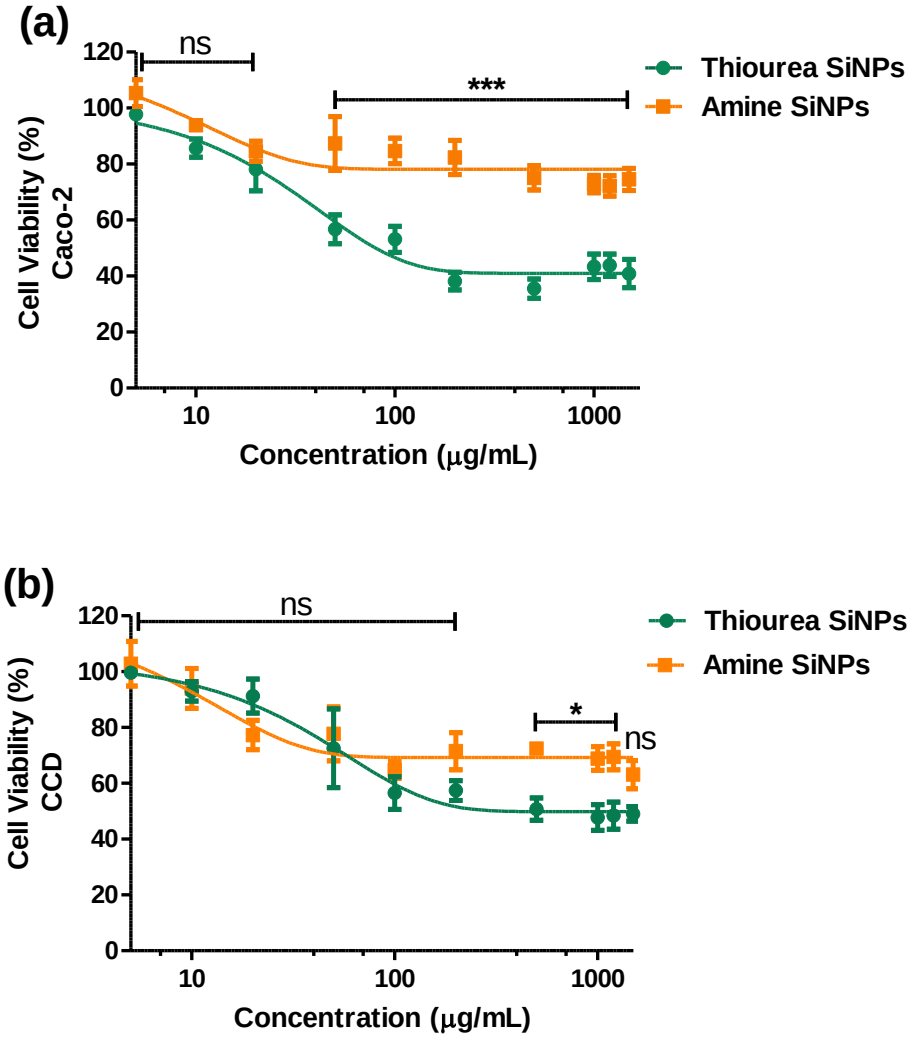

Figure 3.26. *In vitro* cytotoxicity of thiourea and amine capped SiNPs by MTT after incubation with Caco-2 (a) and CCD-841 (b) for **72 h** incubation at 37 ºC. (The results were normalised to non-stimulated cells.) Statistical significance was determined by two-way-ANOVA followed by a Bonferroni post-test (***P < 0.001 and ns statistically not significant). Results are expressed as mean ± SEM (n =3).

For the high dosage of nanoparticles to be effective in this case may not seem to be appropriate (1500 µg/mL), however, it should be mentioned that the concentration used for the MTT assay is calculated with the whole entity of functionalised SiNPs, i.e. drug with the covalently bonded silicon core and thus for thiourea-functionalised SiNPs to be more effective in terms of the cytotoxic effects, a higher dose of nanoparticles needed (more than 100 µg/mL).

In addition, considering the naturally low toxicity of silicon nanoparticles, this would make the application of nanoparticles at such high dosage appropriate as there would be little concern regarding the safety of silicon used in these multifunctional nanomaterials.

3.14.2. Cellular Uptake Studies

3.14.2.1. Confocal Microscopy

In order to understand the uptake behaviour of thiourea-functionalised SiNPs at the cellular level, the cellular internalisation and intercellular distribution of NPs were evaluated by confocal imaging. Figure 3.27 shows the bright field confocal images of Caco-2 cells without any nanoparticle treatments and Figure 3.28 demonstrates the cells incubated with 100 μg/mL of thiourea-functionalised SiNPs for 2 h at 37 ºC. Cells were later treated with longer incubation time (4 h) as shown in Figure 3.29. As can be seen, the uptake was shown to be time dependent as the signal become more apparent for longer incubation time point.

In addition, cell staining was performed in Figures 3.30 and 3.31 for the control and Figures 3.32 and 3.33 for the treated cells. In order to make sure there was no interference in the fluorescence of nanoparticles by actin staining, Figure 3.33 was collected only from the cells with nuclei staining and treated with thiourea-functionalised SiNPs. Based on the images obtained, thiourea-functionalised SiNPs were successfully internalised within the cell cytoplasm as shown by the green fluorescence.

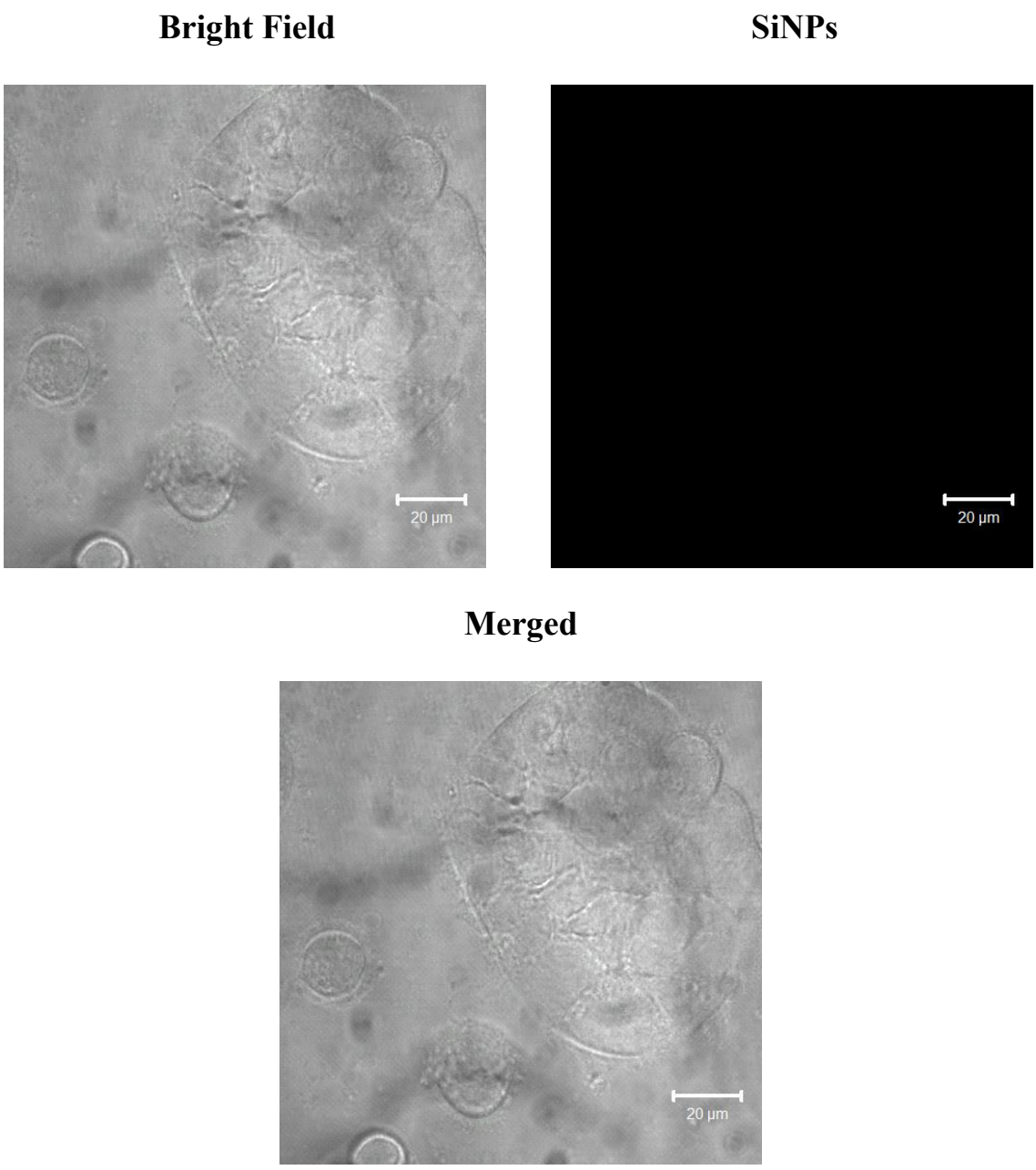

Figure 3.27. Bright field confocal fluorescence images of Caco-2 cells without thiourea-functionalised SiNPs (control).

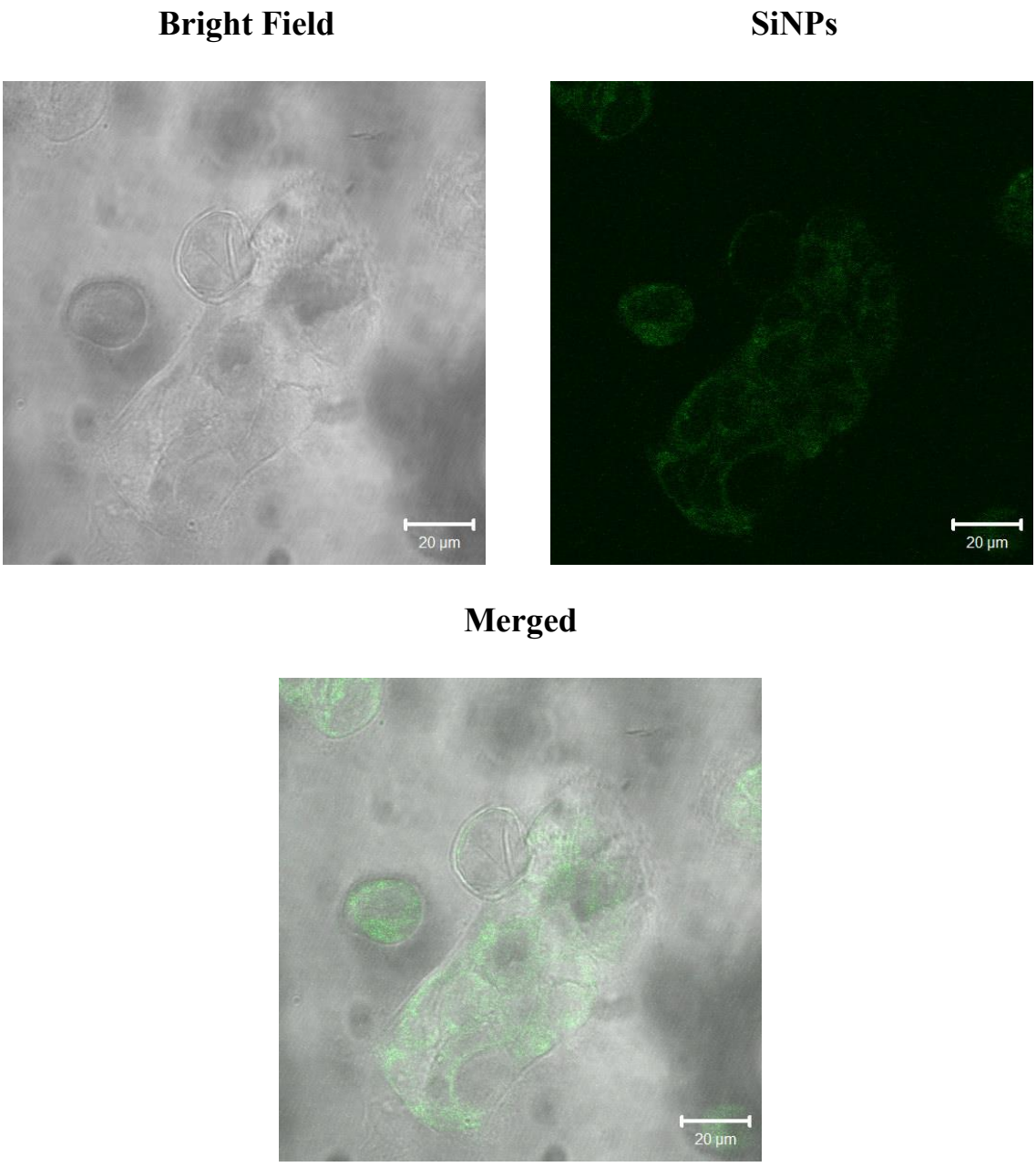

Figure 3.28. Bright field confocal fluorescence images of Caco-2 cells incubated with thiourea-functionalised SiNPs for 2 h. Green fluorescence from thiourea capped SiNPs.

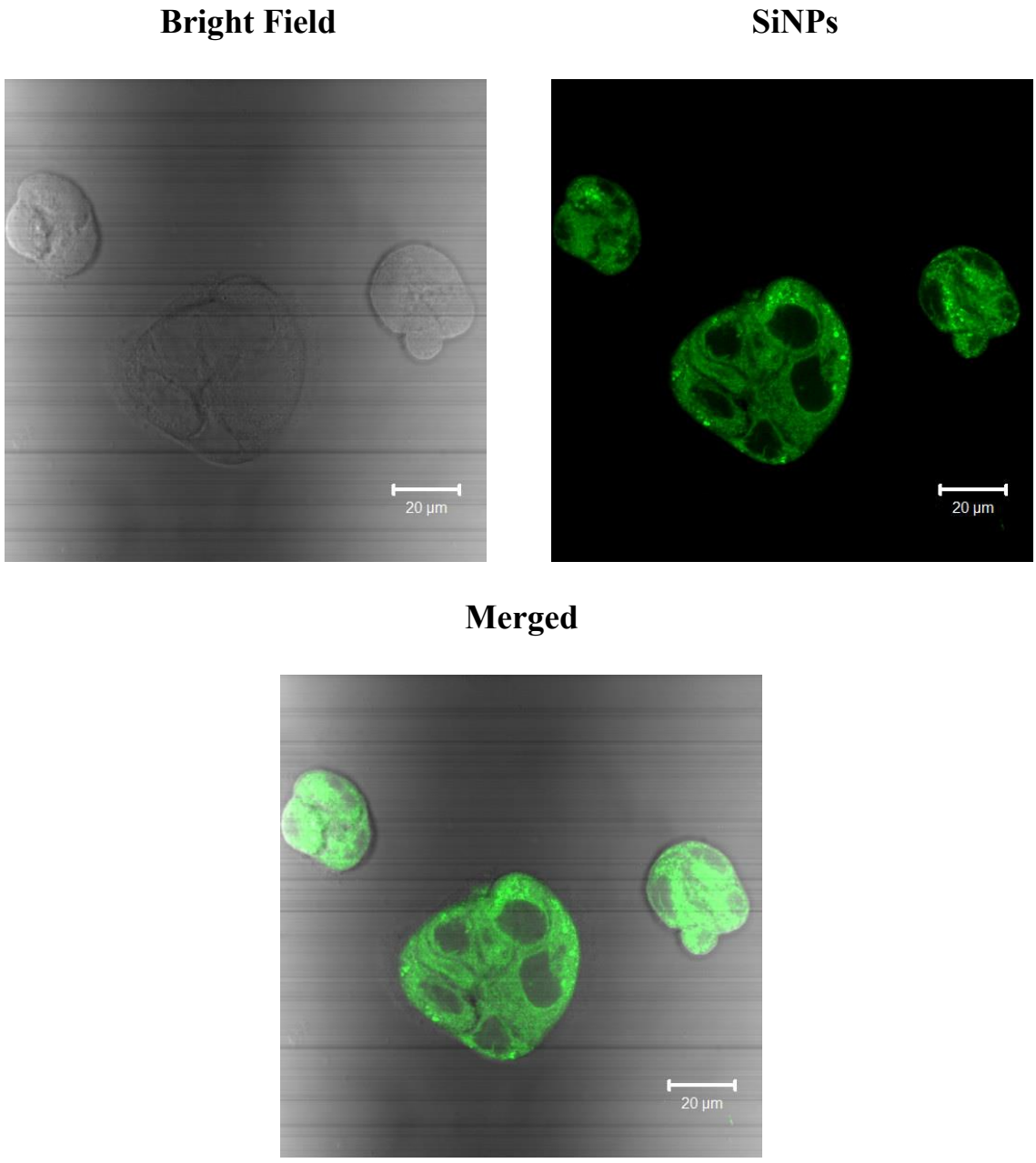

Figure 3.29. Bright field confocal fluorescence images of Caco-2 cells incubated with thiourea-functionalised SiNPs for 4 h. Green fluorescence from thiourea capped SiNPs.

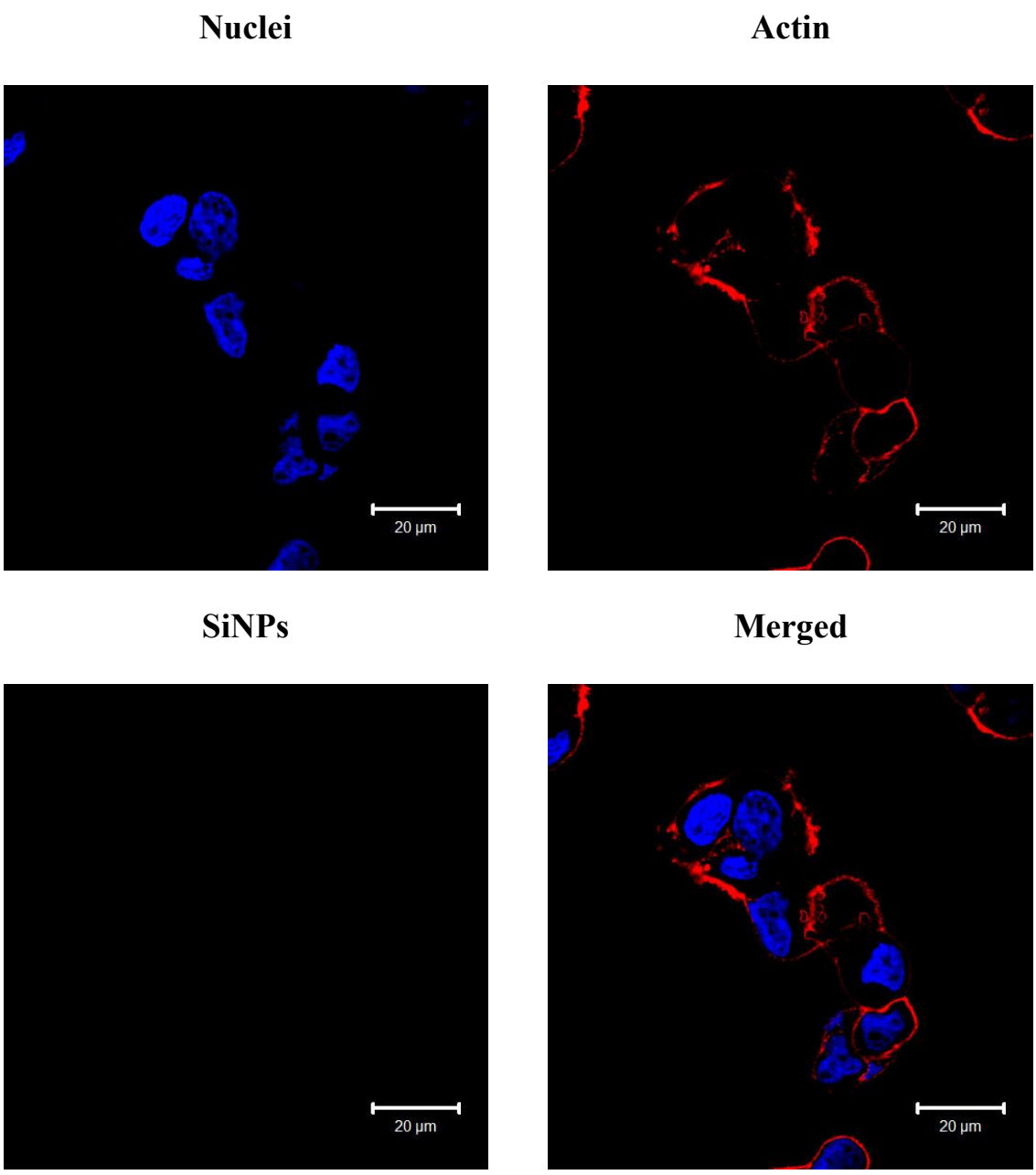

Figure 3.30. Confocal fluorescence images of Caco-2 control (untreated) cells. Blue from Hoechst for nuclei, red from Phalloidin for actin staining.

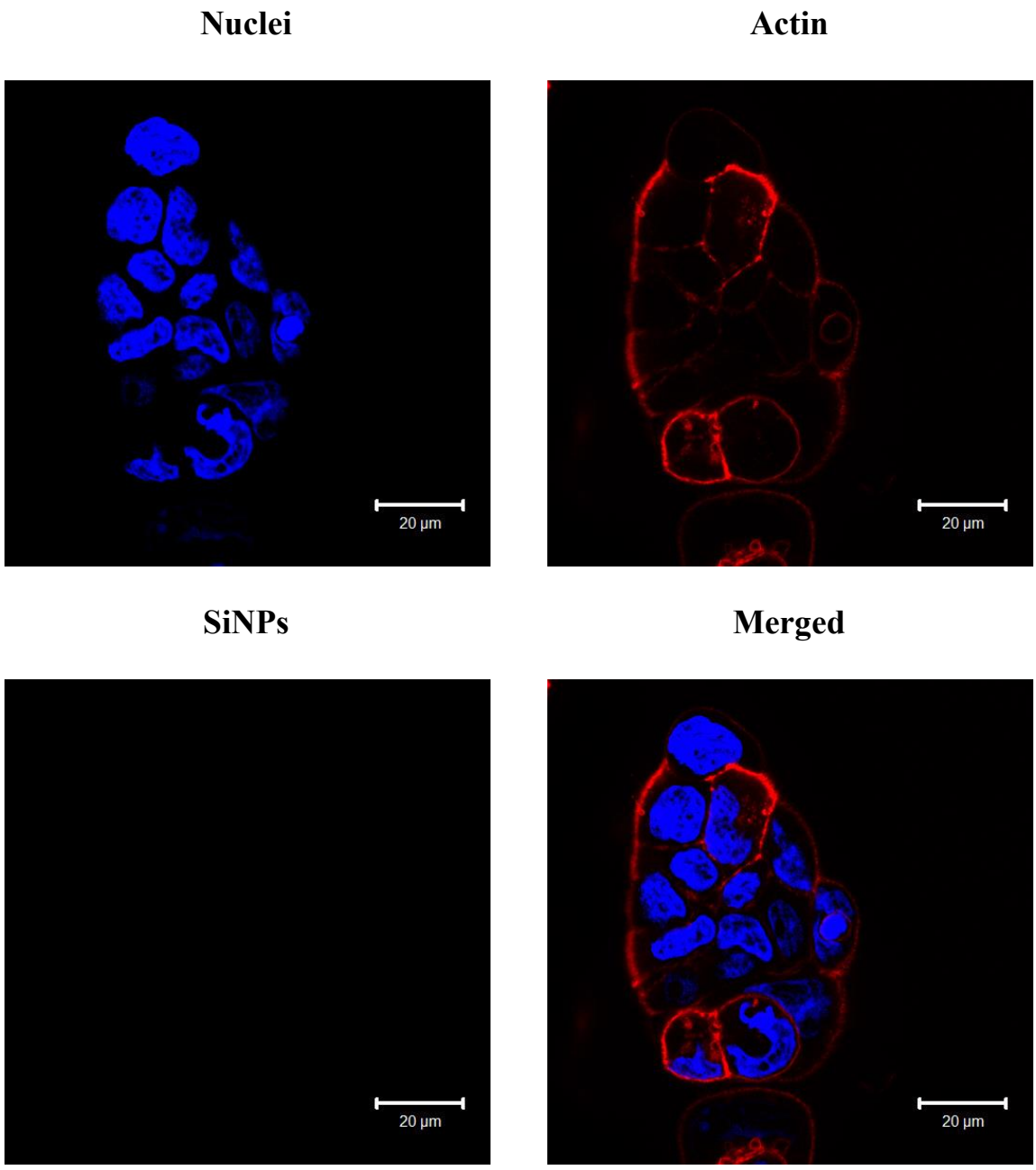

Figure 3.31. Confocal fluorescence images of Caco-2 control (untreated) cells. Blue from Hoechst for nuclei, red from Phalloidin for actin staining.

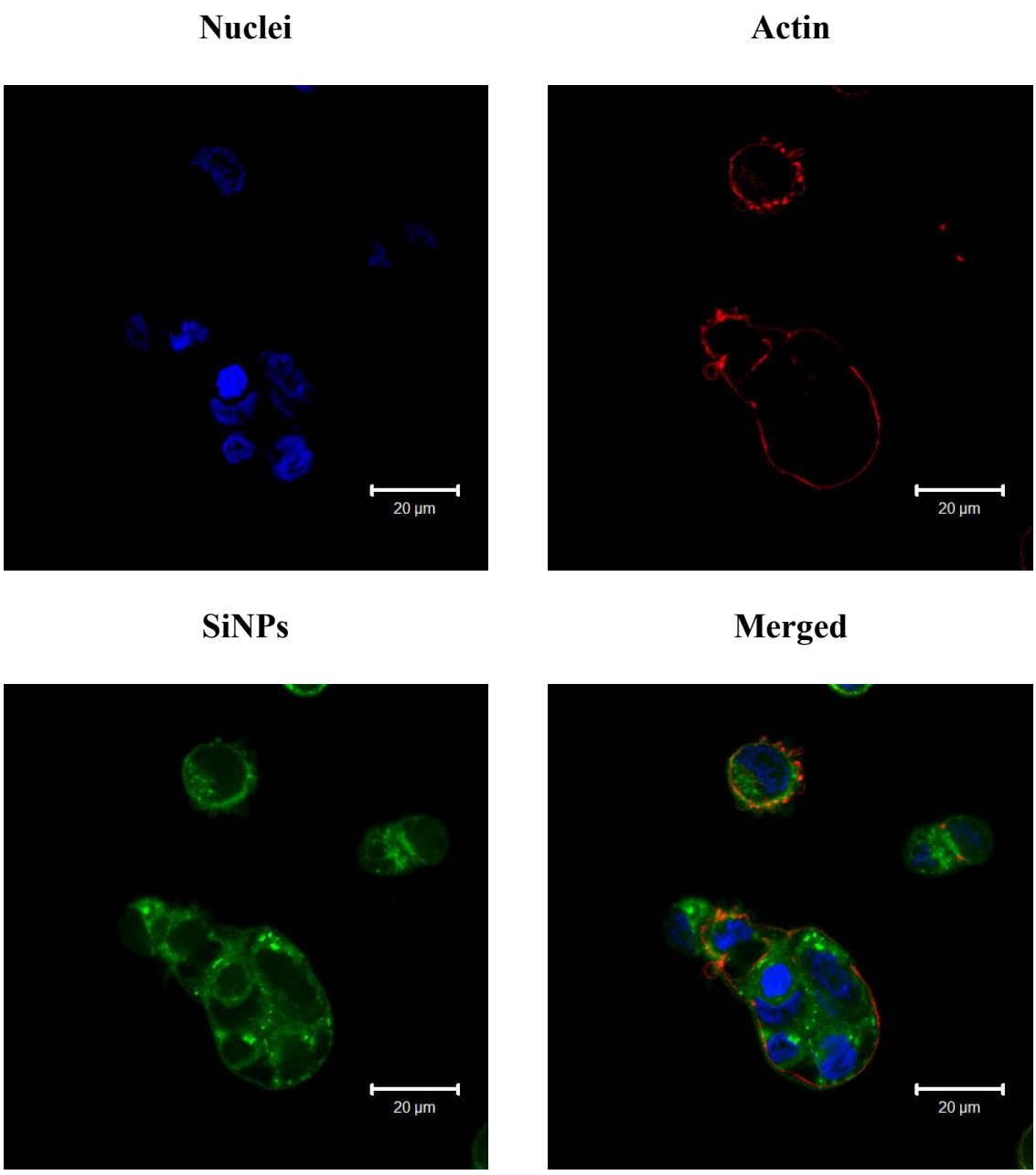

Figure 3.32. Confocal fluorescence images of Caco-2 cells incubated with thiourea capped SiNPs for 4 h. Blue from Hoechst for nuclei, red from Phalloidin for actin staining and green fluorescence from thiourea capped SiNPs.

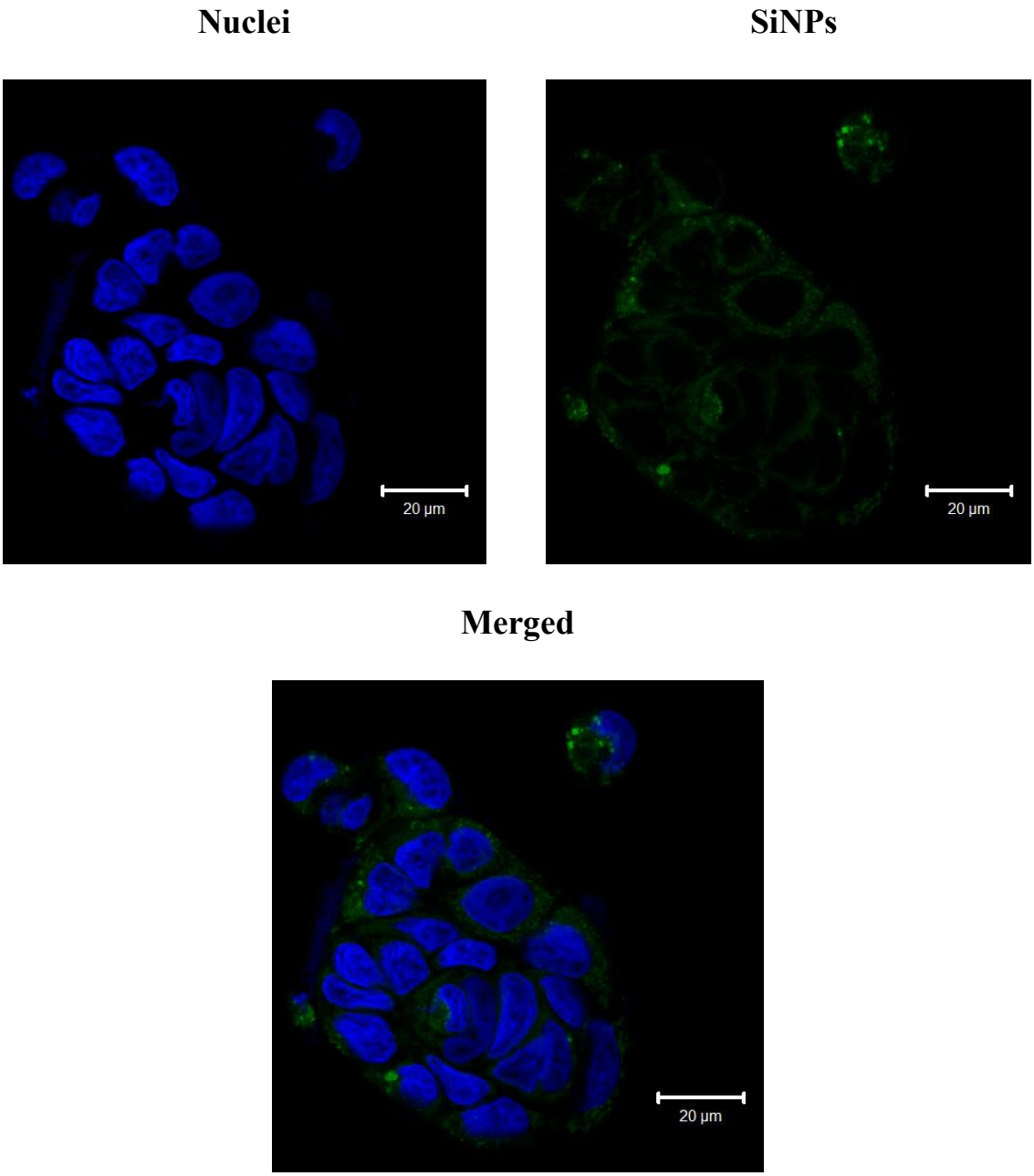

Figure 3.33. Confocal fluorescence images of Caco-2 cells incubated with thiourea capped SiNPs for 4 h. Blue from Hoechst for nuclei and green fluorescence from thiourea capped SiNPs.

For further evidence, the internal distribution of SiNPs was examined by a set of Z-stack images. Thiourea-functionalised SiNPs were taken up into Caco-2 cells as demonstrated in Figure 3.34 Nanoparticles were not only on the external cellular membrane, they were also observed throughout the cytoplasm inside the cells.

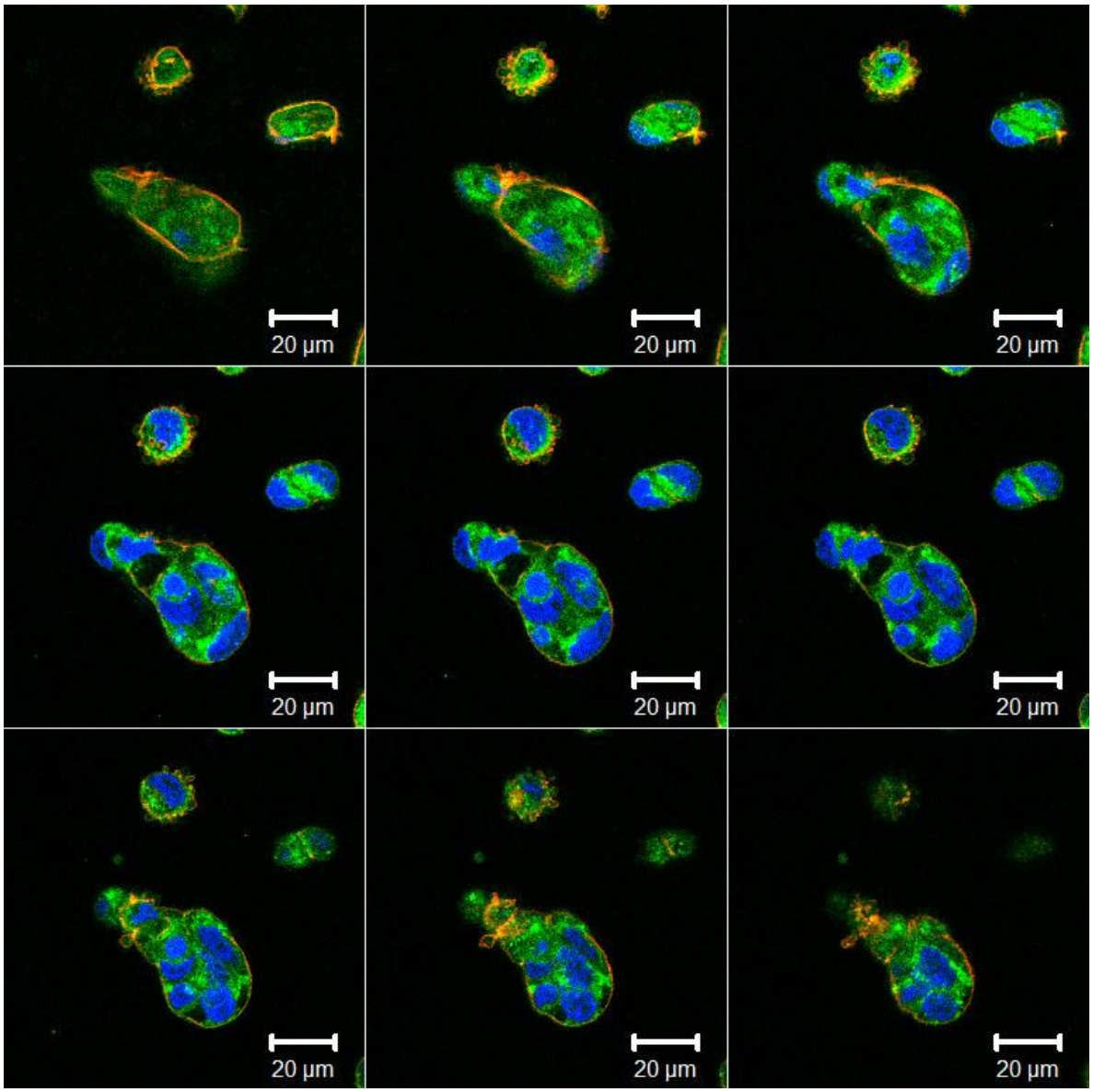

Figure 3.34. Confocal fluorescence images of Caco-2 cells incubated with thiourea capped SiNPs for 4 h. Blue from Hoechst for nuclei, red from Phalloidin for actin staining and green fluorescence from thiourea capped SiNPs.

3.14.2.2. Flow Cytometry

For additional SiNP uptake evidence, flow cytometry was used in both cancer and normal cells to semi-quantitatively measure cellular uptake of the NPs.

The two well-known cell lines, Caco-2 and CCD-841, were chosen because of their different expression of EGFR. Caco-2 cells have been shown to overexpress the EGFR mRNA by almost five times when normalised to the CCD-841 cells as control. In addition, CCD-841 cells did not show EGFR overexpression and lacked observable EGFR phosphorylation.[57]

Caco-2 cells were first incubated with various concentrations of thiourea and amine functionalised SiNPs (from 10 to 100 μg/mL) for 30 min (Figure 3.35). As can be seen the uptake was concentration dependent for both nanoparticles. There was not a significant difference in the uptake of two NPs for the concentrations from 10 to 50 μg/mL. However, there was a much higher level of uptake for thiourea-functionalised SiNPs at the highest concentration with showing almost twice as much as amine-functionalised SiNPs at 100 μg/mL. Higher concentrations were not considered here, as that would cause greater toxicity to the cells, as observed by MTT results, and therefore a fewer number of cells would be available to be detected. The same experiment was performed on Caco-2 cells with longer incubation time (4h) (Figure 3.36). A higher level of fluorescence was detected from the cells at this time point for both types of nanoparticles and for the last two high concentrations at 50 and 100 μg/mL; cells internalised significantly more thiourea SiNPs than amine SiNPs. As a higher level of uptake was observed at 100 μg/mL of thiourea SiNPs, it was decided to take this concentration and test various time points to evaluate which time point gives the optimal uptake rate thereafter use these parameters with the normal cell line.

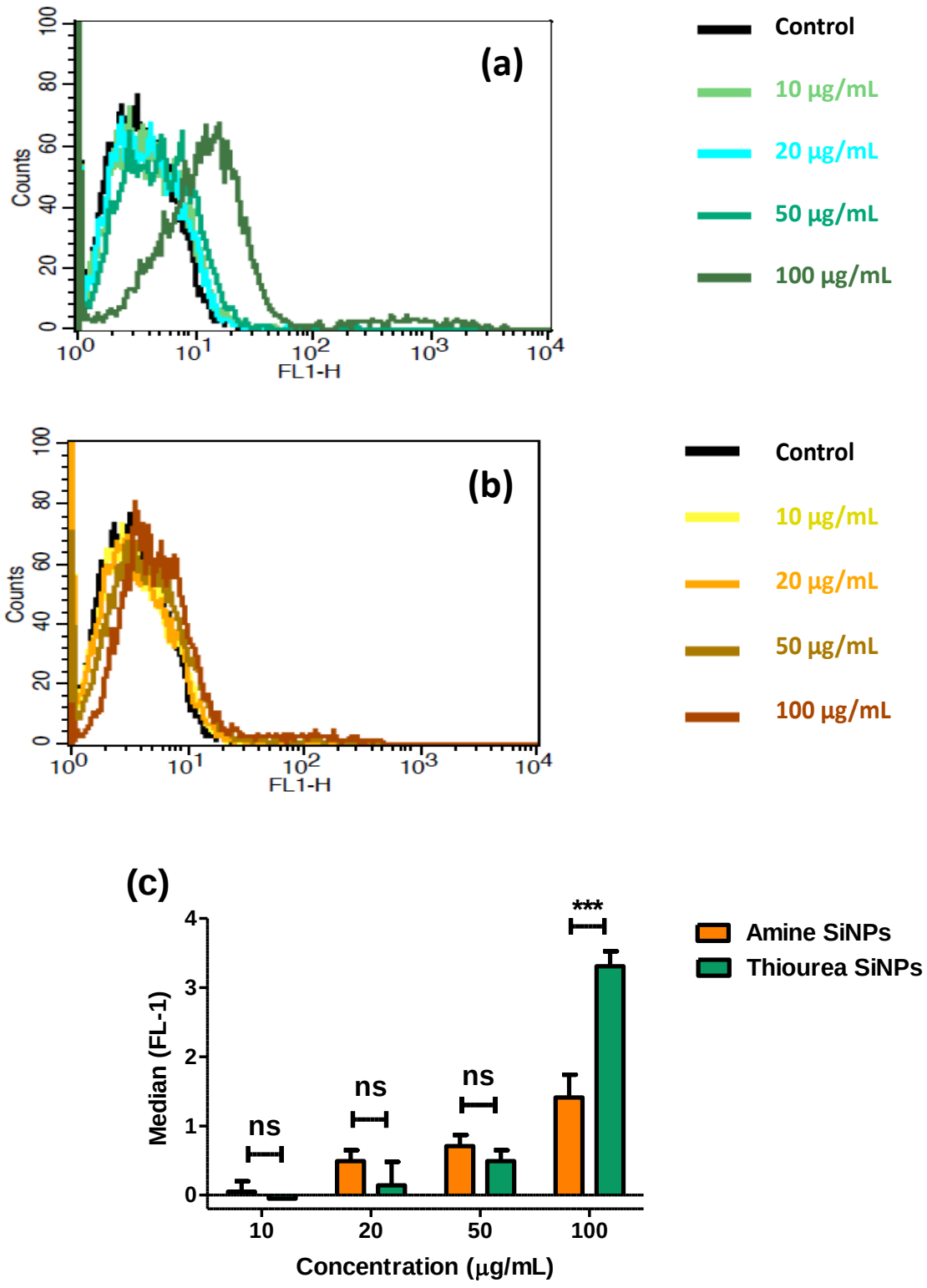

Figure 3.35. Uptake efficiency of thiourea-functionalised SiNPs (a) and amine-functionalised SiNPs (b) in **Caco-2** cells with various concentrations from 10 to 100 µg/mL after **30 min** incubation. Collective flow cytometric analysis results (c) which are presented as fluorescence median of cells after nanoparticle uptake. Statistical significance was determined by two-way-ANOVA followed by a Bonferroni post-test (***P < 0.001 and ns statistically not significant). Results are expressed as mean ± SEM (n =3).

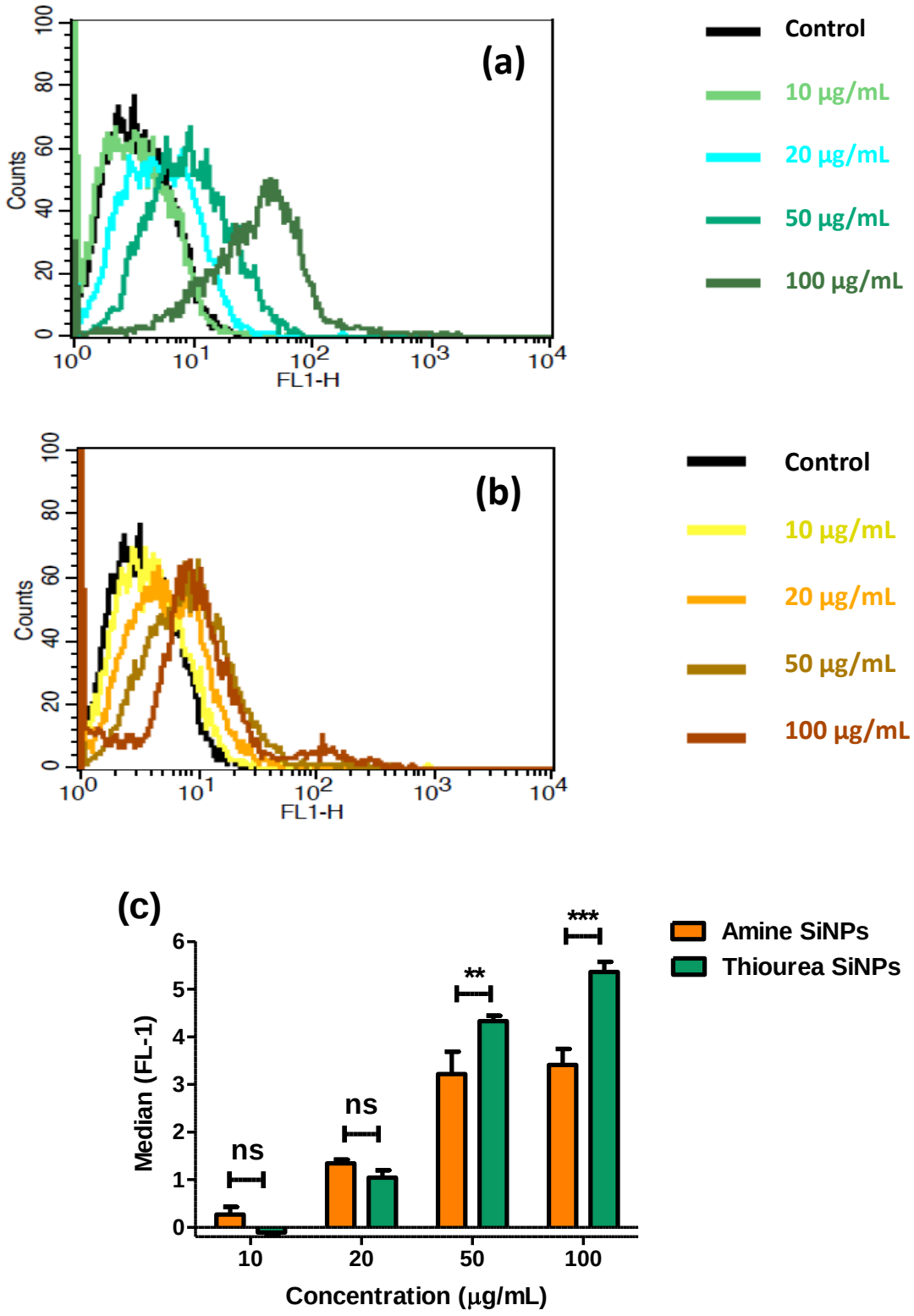

Figure 3.36. Uptake efficiency of thiourea-functionalised SiNPs (a) and amine-functionalised SiNPs (b) in **Caco-2** cells with various concentrations from 10 to 100 µg/mL after **4 h** incubation. Collective flow cytometric analysis results (c) which are presented as fluorescence median of cells after nanoparticle uptake. Statistical significance was determined by two-way-ANOVA followed by a Bonferroni post-test (***P < 0.001, **P < 0.01 and ns statistically not significant). Results are expressed as mean ± SEM (n =3).

Next, thiourea and amine functionalised SiNPs (each 100 µg/mL) were incubated with both cells (Caco-2 and CCD-841) for five different time periods (from 30 min to 8 h). Median fluorescence values demonstrate that cell uptake of thiourea and amine functionalised SiNPs. The data confirmed considerably more uptake of thiourea-functionalised SiNPs in Caco-2 cells compared to amine-functionalised SiNPs for all time points (Figure 3.37). Moreover, the fluorescent signal of thiourea-functionalised SiNPs increased gradually between 30 min and 4 h. At 4 h exposure the maximal thiourea-functionalised SiNP uptake was observed, whereas longer times (6 and 8 h) did not increase the cellular uptake. This suggests that thiourea-functionalised SiNPs reached an uptake saturation level, whereas the non-specific cellular uptake of amine-functionalised SiNPs increased over time. A plausible explanation for this result, consistent with previous known characteristics of thiourea-functionalised SiNPs, is that the thiourea-functionalised SiNP can inhibit the EGFR receptor activity.[58] Amine-functionalised SiNPs on the other hand have no known similar interaction, and thus the lower levels of internalisation are likely reached through passive targeting. Since a saturation level was reached for thiourea-functionalised SiNPs, it is more likely that EGFR are transported to endosome/lysosome for degradation rather than the possibility of the receptor recycling process, which would lead to the increase of uptake over time.[59] The introduction of thiourea-functionalised SiNPs in cancer cells can therefore potentially manage the multiple cellular processes in which EGFR is a key player and thus an inhibit tumour growth. However, the level of thiourea-functionalised SiNP uptake in CCD-841 cells seemed to be much lower (Figure 3.38). A higher florescence was observed at the shorter time point of 1 h incubation. For longer incaution times, up to 8 h exposure, the uptake decreased. One possible explanation for this behaviour could be that the presence of the ligand caused some steric alteration which reduced the uptake of thiourea-SiNPs for longer exposure. This may be compounded by the fact that expression of EGFR in primary epithelial colon cells is less than cancer cells.[60]

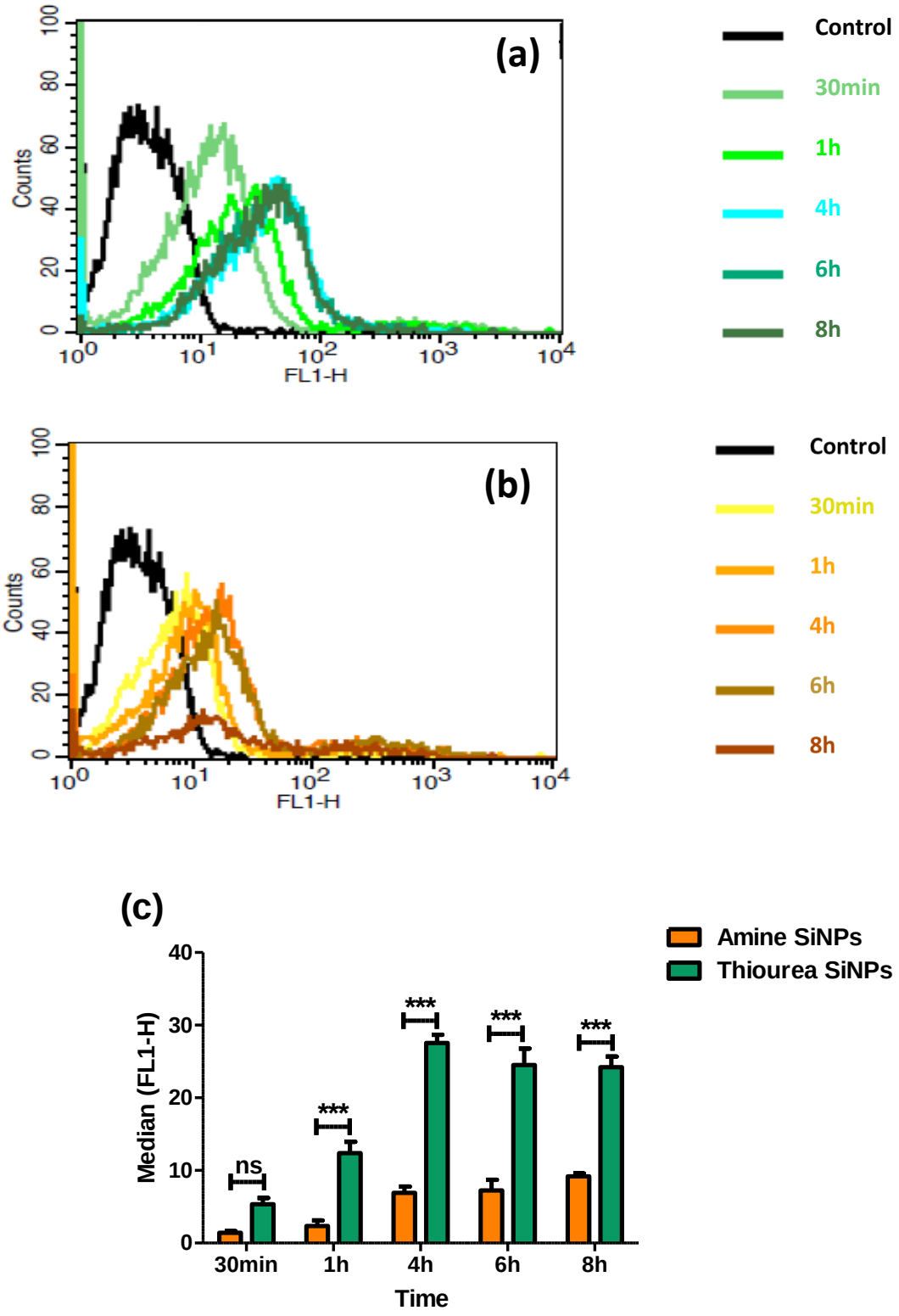

Figure 3.37. Uptake efficiency of thiourea-functionalised SiNPs (a) and amine-functionalised SiNPs (b) in **Caco-2** cells with **100 µg/mL** after various incubation time points from 30 min to 8 h. Collective flow cytometric analysis results (c) which are presented as fluorescence median of cells after nanoparticle uptake. Statistical significance was determined by two-way-ANOVA followed by a Bonferroni post-test (***P < 0.001 and ns statistically not significant). Results are expressed as mean ± SEM (n =3).

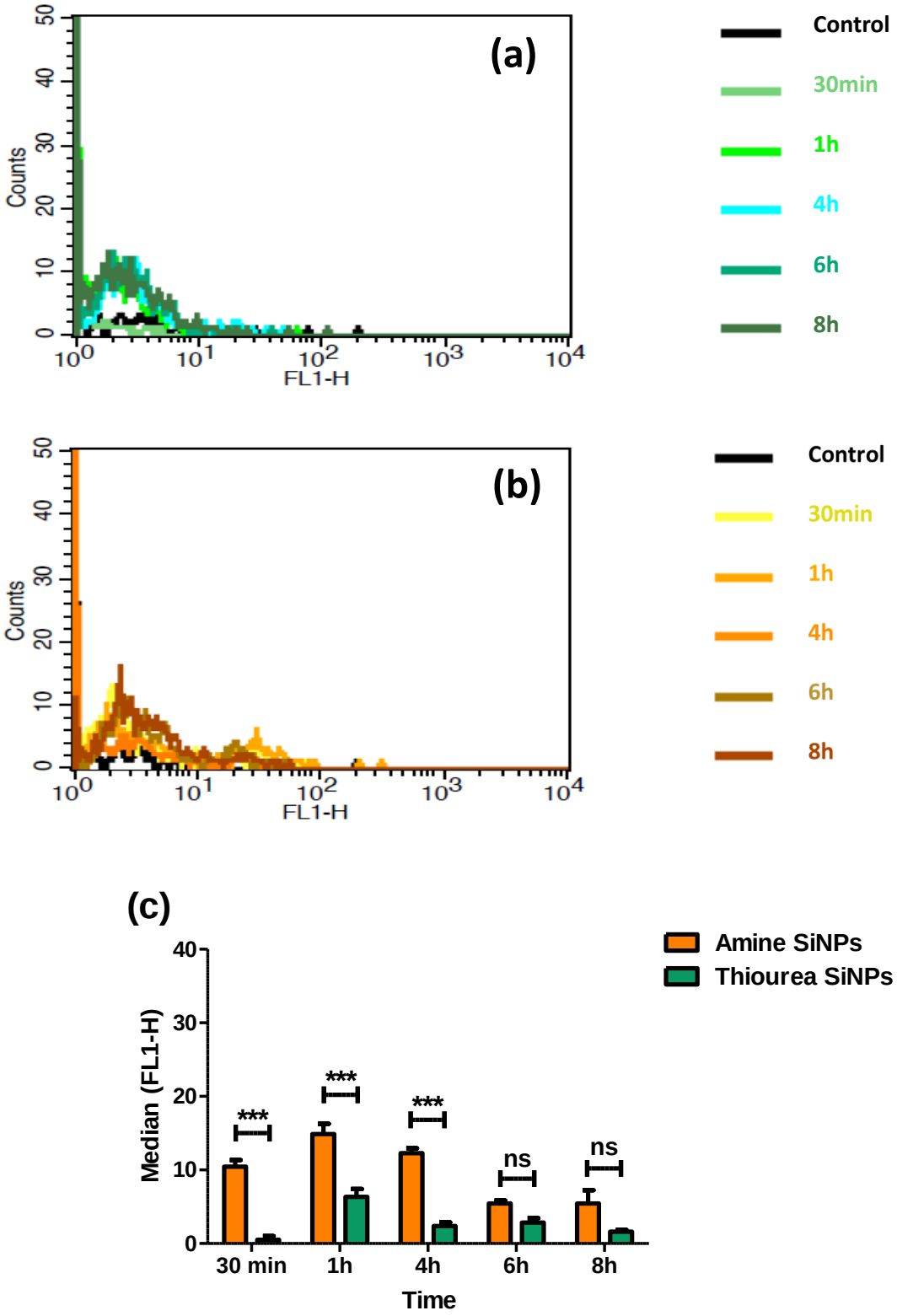

Figure 3.38. Uptake efficiency of thiourea-functionalised SiNPs (a) and amine-functionalised SiNPs (b) in **CCD-841** cells with **100 µg/mL** after various incubation time points from 30 min to 8 h. Collective flow cytometric analysis results (c) which are presented as fluorescence median of cells after nanoparticle uptake. Statistical significance was determined by two-way-ANOVA followed by a Bonferroni post-test (***P < 0.001 and ns statistically not significant). Results are expressed as mean ± SEM (n =3).

The hypothesis for the interaction between thiourea-functionalised SiNPs and ATP binding site of intracellular domain in EGFR receptors is depicted in Scheme 3.4.

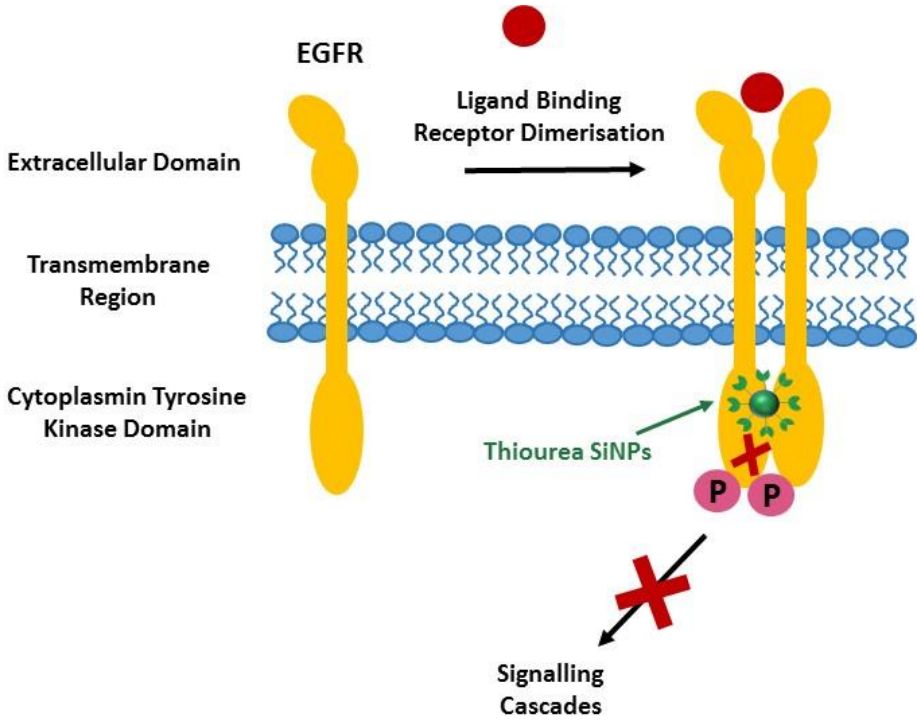

Scheme 3.4. Schematic illustration of the interaction between thiourea SiNPs and ATP binding site of intracellular domain in EGFR receptors.

3.14.3. ELISA Assay

The activity of thiourea-functionalised SiNPs towards EGFR was tested using Elisa assay. Figure 3.39 shows the different behaviour of thiourea and amine-functionalised SiNPs with different concentrations when antibodies, known to bind to EGFR, are introduced to Caco-2 cells. As can be seen, the normalised absorbance of thiourea-functionalised SiNPs was lower than amine-functionalised SiNPs due to the interaction of thiourea-functionalised SiNPs with EGFR which made the receptors unavailable for binding with antibodies. This behavior was concentration dependent and lower absorbance was detected from the cells treated with higher concentrations of thiourea-functionalised SiNPs. The positive control shows the cells treated with only primary antibody.

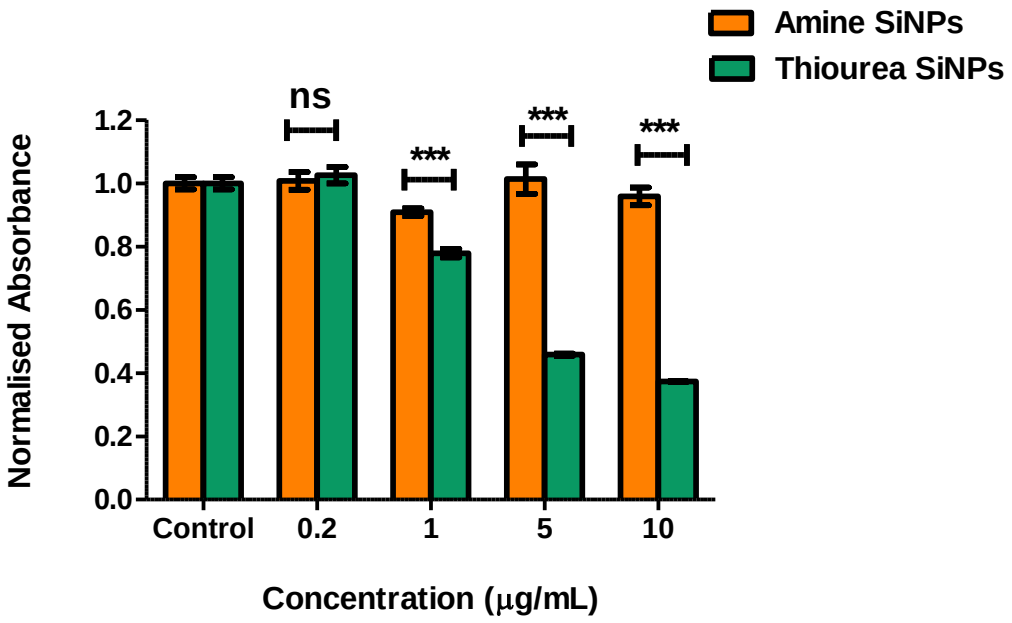

Figure 3.39. Normalised absorbance data of the ELISA test performed using the classical ELISA procedure, without targeted SiNPs (with amine-functionalised SiNPs) and the ELISA procedure using the thiourea-functionalised SiNPs in Caco-2 cells. Statistical significance was determined by two-way-ANOVA followed by a Bonferroni post-test (***P < 0.001 and ns statistically not significant). Results are expressed as mean ± SEM (n =3).

3.15. Summary and Conclusions

The fabrication of nanoparticles through chemical synthesis routes normally leaves impurities from various starting materials and reagents in the final product which is not ideal for biomedical applications. These impurities affect the stability of functionalised SiNPs in solvents and cause agglomeration. On the other hand, top down synthesis methods offer higher quality of nanoparticle with less by-products and impurities. These NPs are widely anticipated to be used in a growing number of applications and as it has been reported previously the issue regarding the scalability of top down techniques can be overcome by using large-scale Teflon cells as demonstrated by UK and Japanese companies.[27] As a result, for the purpose of developing a nanosytem suitable for biomedical applications, after analysing two well developed synthesis approaches of top down and bottom up for the synthesis of NH_2 SiNPs, it was decided to use the top down nanoparticles with higher purity for the continuation of the project. These NH_2 NPs are non-toxic and water soluble, making them ideal for use as control and starting material for further modification in this work.

We report here the synthesis of thiourea-functionalised SiNPs as a novel nanodelivery system, which can interact with cancer cells that overexpress EGFR. This approach makes use of the physiochemical and biological properties of both components of the nanosystem, in particular the photoluminescence of SiNPs and the anticancer activity of thiourea. According to the FTIR and elemental analysis, SiNPs are fully capped with the thiourea ligand. The stability of SiNPs in different biological media, as a result of the covalent conjugation of the ligand on the surface of nanoparticles, was shown by DLS. This result has addressed the challenges regarding the long term stability of nanoparticles for similar biomedical applications. The *in vitro* toxicity of the novel nanoparticles was evaluated by MTT assay in colorectal cancer and normal cells. The thiourea-functionalised SiNPs caused a loss of cell viability after 72 h exposure to the cancer cells. Considering the data obtained from uptake studies in both Caco-2 and CCD-841 cells, thiourea functionalised SiNPs were distributed within the cytoplasm, as visualised in confocal images. The uptake of thiourea-functionalised SiNPs was time dependent. As the fluorescent signal increased gradually between 30 min and 4 h. The saturation uptake level suggested that the ligand binds with the receptor and therefore the degradation of EGFR after 4 hours is likely to occur. This is significant in term of the development of future diagnostic tools for drug delivery systems. Overall, the nanodelivery system developed herein presents an encouraging platform for drug delivery, particularly aiming for the inhibiting of EGFR overexpression in cancer cells.

3.16. References

1. Peer, D.; Karp, J. M.; Hong, S.; FaroKhzad, O. C.; Margalit, R.; Langer, R., Nanocarriers as an emerging platform for cancer therapy. *Nature Nanotechnology* **2007,** *2* (12), 751-760.

2. Allen, T. M., Ligand-targeted therapeutics in anticancer therapy. *Nature Reviews Cancer* **2002,** *2* (10), 750-763.

3. Davis, M. E.; Chen, Z.; Shin, D. M., Nanoparticle therapeutics: an emerging treatment modality for cancer. *Nature Reviews Drug Discovery* **2008,** *7* (9), 771-782.

4. Hynes, N. E.; Lane, H. A., ERBB receptors and cancer: The complexity of targeted inhibitors. *Nature Reviews Cancer* **2005,** *5* (5), 341-354.

5. Sinha, R.; Kim, G. J.; Nie, S. M.; Shin, D. M., Nanotechnology in cancer therapeutics: bioconjugated nanoparticles for drug delivery. *Molecular Cancer Therapeutics* **2006,** *5* (8), 1909-1917.

6. Ullrich, A.; Schlessinger, J., Signal Transduction By Receptors With Tyrosine Kinase-Activity. *Cell* **1990,** *61* (2), 203-212.

7. Lynch, T. J.; Bell, D. W.; Sordella, R.; Gurubhagavatula, S.; Okimoto, R. A.; Brannigan, B. W.; Harris, P. L.; Haserlat, S. M.; Supko, J. G.; Haluska, F. G.; Louis, D. N.; Christiani, D. C.; Settleman, J.; Haber, D. A., Activating mutations in the epidermal growth factor receptor underlying responsiveness of non-small-cell lung cancer to gefitinib. *New England Journal of Medicine* **2004,** *350* (21), 2129-2139.

8. Carpenter, G., Receptors For Epidermal Growth-Factor And Other Polypeptide Mitogens. *Annual Review of Biochemistry* **1987,** *56*, 881-914.

9. Salomon, D. S.; Brandt, R.; Ciardiello, F.; Normanno, N., EPIDERMAL GROWTH FACTOR-RELATED PEPTIDES AND THEIR RECEPTORS IN HUMAN MALIGNANCIES. *Critical Reviews in Oncology/Hematology* **1995,** *19* (3), 183-232.

10. Li, J.; Tan, J.-z.; Chen, L.-l.; Zhang, J.; Shen, X.; Mei, C.-l.; Fu, L.-l.; Lin, L.-p.; Ding, J.; Xiong, B.; Xiong, X.-s.; Liu, H.; Luo, X.-m.; Jiang, H.-l., Design, synthesis and antitumor evaluation of a new series of N-substituted-thiourea derivatives. *Acta Pharmacologica Sinica* **2006,** *27* (9), 1259-1271.

11. Lv, P.-C.; Li, H.-Q.; Sun, J.; Zhou, Y.; Zhu, H.-L., Synthesis and biological evaluation of pyrazole derivatives containing thiourea skeleton as anticancer agents. *Bioorganic & Medicinal Chemistry* **2010,** *18* (13), 4606-4614.

12. Herbst, R. S., Review of epidermal growth factor receptor biology. *International Journal of Radiation Oncology Biology Physics* **2004,** *59* (2), 21-26.

13. Saeed, S.; Rashid, N.; Jones, P. G.; Ali, M.; Hussain, R., Synthesis, characterization and biological evaluation of some thiourea derivatives bearing benzothiazole moiety as potential antimicrobial and anticancer agents. *European Journal of Medicinal Chemistry* **2010,** *45* (4), 1323-1331.

14. Ahire, J. H.; Wang, Q.; Coxon, P. R.; Malhotra, G.; Brydson, R.; Chen, R.; Chao, Y., Highly Luminescent and Nontoxic Amine-Capped Nanoparticles from Porous Silicon: Synthesis and Their Use in Biomedical Imaging. *Acs Applied Materials & Interfaces* **2012,** *4* (6), 3285-3292.

15. Behari, J., Principles of nanoscience: An overview. *Indian J Exp Biol* **2010,** *48* (10), 1008-1019.

16. Wang, J.; Ye, D.-X.; Liang, G.-H.; Chang, J.; Kong, J.-L.; Chen, J.-Y., One-step synthesis of water-dispersible silicon nanoparticles and their use in fluorescence lifetime imaging of living cells. *Journal of Materials Chemistry B* **2014,** *2* (27), 4338-4345.

17. Wang, J.; Sun, S.; Peng, F.; Cao, L.; Sun, L., Efficient one-pot synthesis of highly photoluminescent alkyl-functionalised silicon nanocrystals. *Chemical Communications* **2011,** *47* (17), 4941-4943.

18. Shiohara, A.; Hanada, S.; Prabakar, S.; Fujioka, K.; Lim, T. H.; Yamamoto, K.; Northcote, P. T.; Tilley, R. D., Chemical Reactions on Surface Molecules Attached to Silicon Quantum Dots. *Journal of the American Chemical Society* **2010,** *132* (1), 248-253.

19. Warner, J. H.; Hoshino, A.; Yamamoto, K.; Tilley, R., Water-Soluble Photoluminescent Silicon Quantum Dots. *Angewandte Chemie* **2005,** *117* (29), 4626-4630.

20. Morales, A. M.; Lieber, C. M., A laser ablation method for the synthesis of crystalline semiconductor nanowires. *Science* **1998,** *279* (5348), 208-211.

21. Zhong, Y.; Peng, F.; Wei, X.; Zhou, Y.; Wang, J.; Jiang, X.; Su, Y.; Su, S.; Lee, S. T.; He, Y., Microwave-Assisted Synthesis of Biofunctional and Fluorescent Silicon Nanoparticles Using Proteins as Hydrophilic Ligands. *Angewandte Chemie International Edition* **2012,** *51* (34), 8485-8489.

22. He, Y.; Zhong, Y.; Peng, F.; Wei, X.; Su, Y.; Su, S.; Gu, W.; Liao, L.; Lee, S. T., Highly Luminescent Water-Dispersible Silicon Nanowires for Long-Term Immunofluorescent Cellular Imaging. *Angewandte Chemie* **2011,** *123* (13), 3136-3139.

23. Wang, Q.; Bao, Y.; Zhang, X.; Coxon, P. R.; Jayasooriya, U. A.; Chao, Y., Uptake and Toxicity Studies of Poly-Acrylic Acid Functionalized Silicon Nanoparticles in Cultured Mammalian Cells. *Advanced Healthcare Materials* **2012,** *1* (2), 189-198.

24. Su, Y.; Peng, F.; Jiang, Z.; Zhong, Y.; Lu, Y.; Jiang, X.; Huang, Q.; Fan, C.; Lee, S.-T.; He, Y., In vivo distribution, pharmacokinetics, and toxicity of aqueous synthesized cadmium-containing quantum dots. *Biomaterials* **2011,** *32* (25), 5855-5862.

25. AL-Kazazz, F. F., A Simple Method for Synthesis, Purification and concentration Stabilized Goldnanoparticles. *International Journal of engineering Research and Applications 1* (3), 21-30.

26. Lazarus, L. L.; Riche, C. T.; Malmstadt, N.; Brutchey, R. L., Effect of ionic liquid impurities on the synthesis of silver nanoparticles. *Langmuir* **2012,** *28* (45), 15987-15993.

27. Canham, L.; Aston, R., Will a chip every day keep the doctor away? *Physics World* **2001,** *14* (7), 27-31.

28. Wu, H.; Liang, H.; Yuan, Q.; Wang, T.; Yan, X., Preparation and stability investigation of the inclusion complex of sulforaphane with hydroxypropyl-beta-cyclodextrin. *Carbohydrate Polymers* **2010,** *82* (3), 613-617.

29. Medda, F.; Pirrie, L.; Poupart, S.; Russell, R. J.; Higgins, M.; McCarthy, A. R.; Campbell, J.; Slawin, A. M. Z.; Lane, D. P.; Lain, S.; Westwood, N. J., Novel cambinol analogs as sirtuin inhibitors: Synthesis, biological evaluation and rationalisation of activity. *Abstracts of Papers of the American Chemical Society* **2010,** *240*.

30. Medda, F.; Russell, R. J. M.; Higgins, M.; McCarthy, A. R.; Campbell, J.; Slawin, A. M. Z.; Lane, D. P.; Lain, S.; Westwood, N. J., Novel Cambinol Analogs as Sirtuin Inhibitors: Synthesis, Biological Evaluation, and Rationalization of Activity. *Journal of Medicinal Chemistry* **2009,** *52* (9), 2673-2682.

31. Koca, I.; Ozgur, A.; Coskun, K. A.; Tutar, Y., Synthesis and anticancer activity of acyl thioureas bearing pyrazole moiety. *Bioorganic & Medicinal Chemistry* **2013,** *21* (13), 3859-3865.

32. Dasog, M.; Yang, Z.; Regli, S.; Atkins, T. M.; Faramus, A.; Singh, M. P.; Muthuswamy, E.; Kauzlarich, S. M.; Tilley, R. D.; Veinot, J. G. C., Chemical Insight into the Origin of Red and Blue Photoluminescence Arising from Freestanding Silicon Nanocrystals. *Acs Nano* **2013,** *7* (3), 2676-2685.

33. Wang, Q.; Ni, H.; Pietzsch, A.; Hennies, F.; Bao, Y.; Chao, Y., Synthesis of water-dispersible photoluminescent silicon nanoparticles and their use in biological fluorescent imaging. *Journal of Nanoparticle Research* **2011,** *13* (1), 405-413.

34. Mekki, A.; Holland, D.; McConville, C. F.; Salim, M., An XPS study of iron sodium silicate glass surfaces. *Journal of Non-Crystalline Solids* **1996,** *208* (3), 267-276.

35. Du, H. H.; Tressler, R. E.; Spear, K. E.; Pantano, C. G., Oxidation Studies Of Crystalline Cvd Silicon-Nitride. *Journal of the Electrochemical Society* **1989,** *136* (5), 1527-1536.

36. Chao, Y.; Wang, Q.; Pietzsch, A.; Hennies, F.; Ni, H., Soft X-ray induced oxidation on acrylic acid grafted luminescent silicon quantum dots in ultrahigh vacuum. *Physica Status Solidi a-Applications and Materials Science* **2011,** *208* (10), 2424-2429.

37. Albert C Thompson, J. K., David T. Attwood, Eric M Gullikson, Malcolm R. Howells, *X-Ray Data Booklet*. Lawrence Berkeley National Laboratory: Berkeley, California, **2009.**

38. Barber, M.; Connor, J. A.; Guest, M. F.; Hillier, I. H.; Schwarz, M., Bonding In Some Donor-Acceptor Complexes Involving Boron-Trifluoride - Study By Means Of Esca And Molecular-Orbital Calculations. *Journal of the Chemical Society-Faraday Transactions Ii* **1973,** (4), 551-558.

39. Dementjev, A. P.; de Graaf, A.; van de Sanden, M. C. M.; Maslakov, K. I.; Naumkin, A. V.; Serov, A. A., X-ray photoelectron spectroscopy reference data for identification of the C3N4 phase in carbon-nitrogen films. *Diamond and Related Materials* **2000,** *9* (11), 1904-1907.

40. Lee, K. D.; Nir, S.; Papahadjopoulos, D., Quantitative analysis of liposome-cell interactions in vitro: rate constants of binding and endocytosis with suspension and adherent J774 cells and human monocytes. *Biochemistry* **1993,** *32* (3), 889-899.

41. Lu, F.; Wu, S. H.; Hung, Y.; Mou, C. Y., Size effect on cell uptake in well-suspended, uniform mesoporous silica nanoparticles. *Small* **2009,** *5* (12), 1408-1413.

42. Fabrega, J.; Luoma, S. N.; Tyler, C. R.; Galloway, T. S.; Lead, J. R., Silver nanoparticles: Behaviour and effects in the aquatic environment. *Environment International* **2011,** *37* (2), 517-531.

43. Zeta Potential Analysis of Nanoparticles. https://cdn.shopify.com/s/files/1/0257/8237/files/nanoComposix_Guidelines_for_Zeta_Potential_Analysis_of_Nanoparticles.pdf (accessed September **2012**).

44. Cedervall, T.; Lynch, I.; Lindman, S.; Berggård, T.; Thulin, E.; Nilsson, H.; Dawson, K. A.; Linse, S., Understanding the nanoparticle–protein corona using methods to quantify exchange rates and affinities of proteins for nanoparticles. *Proceedings of the National Academy of Sciences* **2007,** *104* (7), 2050-2055.

45. Vesaratchanon, S.; Nikolov, A.; Wasan, D. T., Sedimentation in nano-colloidal dispersions: effects of collective interactions and particle charge. *Advances in colloid and interface science* **2007,** *134*, 268-278.

46. Alkilany, A. M.; Murphy, C. J., Toxicity and cellular uptake of gold nanoparticles: what we have learned so far? *Journal of nanoparticle research* **2010,** *12* (7), 2313-2333.

47. Lundqvist, M.; Stigler, J.; Elia, G.; Lynch, I.; Cedervall, T.; Dawson, K. A., Nanoparticle size and surface properties determine the protein corona with possible implications for biological impacts. *Proceedings of the National Academy of Sciences* **2008,** *105* (38), 14265-14270.

48. Alkilany, A. M.; Nagaria, P. K.; Hexel, C. R.; Shaw, T. J.; Murphy, C. J.; Wyatt, M. D., Cellular uptake and cytotoxicity of gold nanorods: molecular origin of cytotoxicity and surface effects. *small* **2009,** *5* (6), 701-708.

49. Conner, S. D.; Schmid, S. L., Regulated portals of entry into the cell. *Nature* **2003,** *422* (6927), 37-44.

50. Ghosh, B.; Shirahata, N., Colloidal silicon quantum dots: synthesis and luminescence tuning from the near-UV to the near-IR range. *Science and Technology of Advanced Materials* **2014,** *15* (1), 014207.

51. Kang, Z.; Liu, Y.; Tsang, C. H. A.; Ma, D. D. D.; Fan, X.; Wong, N. B.; Lee, S. T., Water-Soluble Silicon Quantum Dots with Wavelength-Tunable Photoluminescence. *Advanced Materials* **2009,** *21* (6), 661-664.

52. Chen, Q.; Li, X.; Jia, Y.; Zhu, J.; Yuheng, Z., The role of in the blue luminescence in hydrothermally prepared porous silicon. *Journal of Physics: Condensed Matter* **1997,** *9* (10), L151.

53. Wolkin, M.; Jorne, J.; Fauchet, P.; Allan, G.; Delerue, C., Electronic states and luminescence in porous silicon quantum dots: the role of oxygen. *Physical Review Letters* **1999,** *82* (1), 197.

54. Williams, A. T. R.; Winfield, S. A.; Miller, J. N., Relative Fluorescence Quantum Yields Using A Computer-Controlled Luminescence Spectrometer. *Analyst* **1983,** *108* (1290), 1067-1071.

55. Eaton, D. F., Reference Materials For Fluorescence Measurement. *Pure and Applied Chemistry* **1988,** *60* (7), 1107-1114.

56. Dickinson, F.; Alsop, T.; Al-Sharif, N.; Berger, C.; Datta, H.; Šiller, L.; Chao, Y.; Tuite, E.; Houlton, A.; Horrocks, B., Dispersions of alkyl-capped silicon nanocrystals in aqueous media: photoluminescence and ageing. *Analyst* **2008,** *133* (11), 1573-1580.

57. Mozzi, A.; Forcella, M.; Riva, A.; Difrancesco, C.; Molinari, F.; Martin, V.; Papini, N.; Bernasconi, B.; Nonnis, S.; Tedeschi, G.; Mazzucchelli, L.; Monti, E.; Fusi, P.; Frattini, M., NEU3 activity enhances EGFR activation without affecting EGFR expression and acts on its sialylation levels. *Glycobiology* **2015,** *25* (8), 855-868.

58. Le Roy, C.; Wrana, J. L., Clathrin- and non-clathrin-mediated endocytic regulation of cell signalling. *Nature Reviews Molecular Cell Biology* **2005,** *6* (2), 112-126.

59. Björkelund, H.; Gedda, L.; Malmqvist, M.; Andersson, K., Resolving the EGF-EGFR interaction characteristics through a multiple-temperature, multiple-inhibitor, real-time interaction analysis approach. *Molecular and clinical oncology* **2013,** *1* (2), 343-352.

60. SiShi, L.; Buchbinder, E.; Wu, L.; Bjorge, J.; Fujita, D.; Zhu, S., EGFR and HER2 levels are frequently elevated in colon cancer cells. *Discoveries Reports* **2014,** *1* (1), e1.

Chapter 4:
Synthesis and Characterisation of Isothiocyanate-functionalised Silicon Nanoparticles

4.1. Overview

Isothiocyanates (ITCs) are known to induce phase II enzymes, related to the detoxification process of chemical carcinogens, and thus can prevent the start of carcinogenesis and act as chemo-preventive functional groups.[1] Although many studies have investigated the effect of ITCs on phase II enzymes,[2, 3] few have looked at their effects when it comes to nanoscale systems in specific conjugation with nanoparticles.

In the following chapter, isothiocyanate-functionalised SiNPs (ITC SiNPs) were synthesised using two different methods which were initiated from two different types of SiNPs as starting materials. The surface chemistry of these particles were characterised and their optical properties and long term stability examined to assess the advantages and disadvantages of each type of synthesis approach. NH_2 SiNPs obtained from the top down synthesis route (discussed in Chapter 3 (Section 3.3)), were used as one of the precursors and another type of SiNPs covered by the allyl bromide functional group were used as a precursor for the other synthesis route. Thermal hydrosilylation was run to produce bromine-functionalised SiNPs (Br SiNPs) and their chemical and optical properties were characterised.

Characterisation showed the successful synthesis of ITC SiNPs by both methods. However, the samples produced from the precursor Br SiNPs (ITC SiNPs (P Br SiNPs) exhibited strong photoluminescence whereas the second route using NH_2 SiNPs as precursor (ITC SiNPs (P NH_2 SiNPs)) produced nanoparticles with weak quantum yield and therefore lower optical efficiency. As a result, only ITC SiNPs (P Br SiNPs) were used for uptake studies in this chapter.

4.2. Synthesis of Bromine Capped Silicon Nanoparticles

Several attempts were made to synthesise Br SiNPs using the microwave method and thermally induced hydrosilylation reaction by refluxing.

First, the H-terminated SiNPs were reacted with allyl bromide using a microwave in a 1% volumetric ratio. The reaction was attempted in various solvents such as DCM, THF and toluene. The obtained solution was filtered and the solvent was removed under vacuum. The resulting powder was characterised by FTIR after filtering the silicon chips and removing the solvent. The spectra did not show any Si-C bonding on the surface of SiNPs. The length of the reaction was increased from 30 min to 1 h but there was no significant improvement.

Following this, the thermal hydrosilylation reaction was attempted and tested under various experimental parameters. Table 4.1 shows the different parameters examined in this synthesis to achieve the desired product. The hydrosilylation reaction in dry toluene at 65 ^{o}C with 2 mL of the allyl bromide (which was run overnight) gave the greatest yield out of all the methods (Table 4.1). The FTIR spectrum of this product confirmed the formation of bromine-functionalised SiNPs (Figure 4.1) and will be discussed in the following section. In all of these experiments the H-terminated SiNPs, which were used as the starting point, were obtained from the etching of four silicon chips and the reaction was followed in 10 mL of each solvent.

As a result of this analysis to determine the optimal experimental parameters providing the greatest yield (Table 4.1), Br SiNPs were synthesised using the thermal hydrosilylation reaction of H-terminated SiNPs with allyl bromide in dry toluene and left at reflux overnight (Scheme 4.1). The residual allyl bromide was removed by heating under reduced pressure and centrifugation. This synthetic procedure gave a yield of approximately 25 mg of powder like material. The yield was consistent over several reactions.

Table 4.1. Synthesis of bromine-functionalised SiNPs under various reaction parameters.

Parameters / Solvent	Allyl bromide (mL)	Time (h)		Temperature (ºC)	Product Weight (mg)	
Dry DCM	1	12	24	35	10	10
	2	12	24		13	15
	4	12	24		15	17
Dry Toluene	1	12	24	**65**	15	15
	2	12	**24**		20	**25**
	4	12	24		15	18
Dry THF	1	12	24	60	17	18
	2	12	24		18	20
	4	12	24		20	20

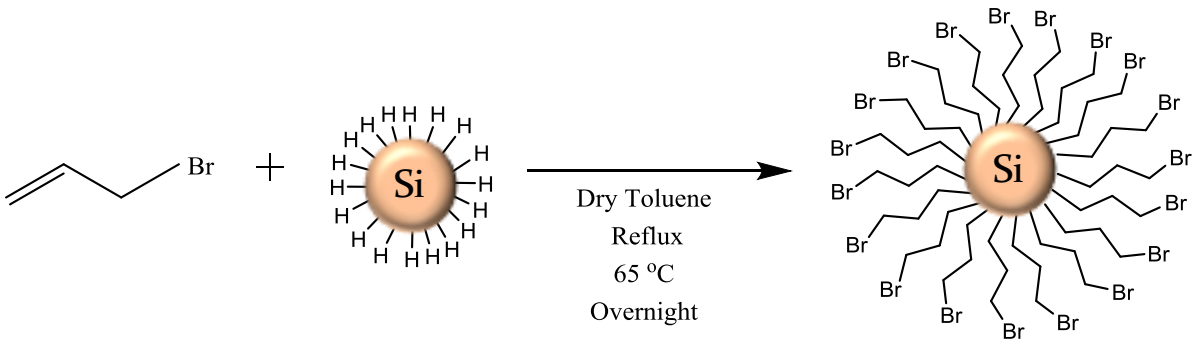

Scheme 4.1 Schematic illustration of the synthesis of Br SiNPs.

In order to evaluate if these synthesised SiNPs can be used as precursor to produce the desired ITC functional group, the initial characterisation was performed on the samples.

4.3. Chemical Characterisation of Bromine-functionalised SiNPs

4.3.1. Chemical bonding by FTIR

To confirm the existence of the covalent Si-C bond on the surface of SiNPs, FTIR was performed on a dry powder of Br SiNPs obtained from each synthesis method outlined in Table 4.1. Figure 4.1 shows the FTIR spectra of allyl bromide ligand (Figure 4.1 (a)) compared to the product after the microwave hydrosilylation (Figure 4.1 (b)). Due to the large amount of oxide, which occurs under the microwave condition, many signals were not detectable. Although there was a small peak at 1261 cm^{-1} which could be related to the formation of Si-C bond in this product,[4] the existence of the Si-H peak at 2100 cm^{-1} shows the unsuccessful synthesis in the case.[5] This could therefore show the poor surface coverage by the ligand as well as high level of oxide layer on the surface of SiNPs. Table 4.2 shows the relevant vibrations observed for this batch.

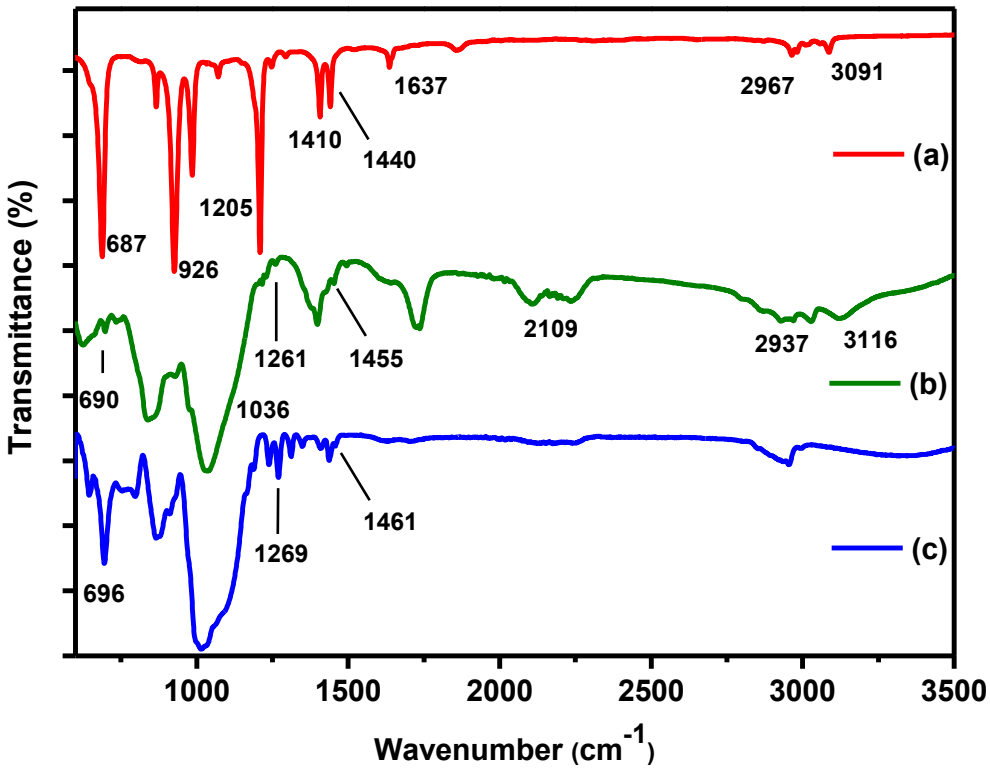

Figure 4.1. FTIR spectra of allyl bromide (a), bromine-functionalised SiNPs obtained from the microwave method (b) and from the thermal hydrosilylation method (c).

Given that microwave hydrosilylation was unsuccessful, thermal hydrosilylation was considered as an alternative method. The IR spectra of the product produced from thermal hydrosilylation is shown in Figure 4.1 (c). The spectrum displayed no bands characteristic to Si-H stretching around 2100 to 2200 cm^{-1}.[5] Moreover, the covalent Si-C bond was confirmed with the relative signals at 1269 and 1461 cm^{-1} for the Si-C symmetric bending and Si-CH_2 scissoring vibrations respectively.[4] This combined with the absence of a peak at 1637 cm^{-1} which would correspond to C=C bond in allyl bromide, suggests that the ligand was attached to the SiNPs.[6] Therefore, this method almost certainly produces the required fully capped bromine-functionalised SiNPs (see Table 4.2).

Table 4.2. Molecular vibrational information of allyl bromide (a), Br SiNPs obtained by microwave method (b), Br SiNPs obtained by thermal hydrosilylation (c).

Wavenumber (cm^{-1})	Vibrational Motion	Structural Feature	Spectrum
687	stretching	C-Br	(a) Allyl Bromide
921	=C-H bending	C-H	
1205	stretching	C-C	
1410, 1440	CH_2 scissoring	C-H	
1637	stretching	C=C	
2967, 3091	=C-H stretching	C-H	
690	stretching	C-Br	(b) Bromide SiNPs
1036	stretching	Si-O	
1261	symmetric bending	Si-C	
1455	scissoring stretching	Si-CH_2 C-C	

2109	stretching	Si-H	
2936, 3116	stretching	C-H	
696	stretching	C-Br	(c) Bromide SiNPs
1269	symmetric bending	Si-C	
1461	scissoring stretching	$Si-CH_2$ C-C	

4.3.2. Elemental Analysis by EDX

The Br SiNPs are rich in silicon and carbon. This can be confirmed from the EDX spectrum of samples which obtained from a number of spots on the material. The elemental components of the material were observed to be silicon, carbon, oxygen and bromine (Figure 4.2).

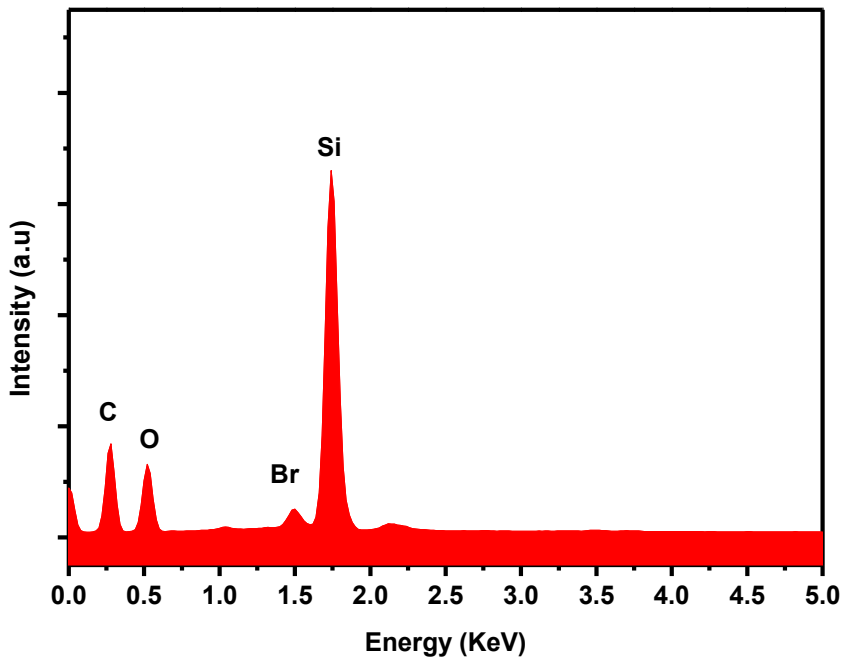

Figure 4.2. EDX spectrum of bromine-functionalised SiNPs.

4.3.3. Elemental Analysis by XPS

Chemical bonding of SiNPs with the allyl bromide ligand was also investigated by XPS analysis through both wide (Figure 4.3) and high resolution scans over Si2p, C1s, O1s and Br3d regions of the SiNPs (Figures 4.4 to 4.7). The wide scan spectrum was dominated by signals attributed to Si2p, Si2s, C1s, O1s and Br3d.

XPS provided information on the elements present on the surface and indicated the environment in which these elements exist.

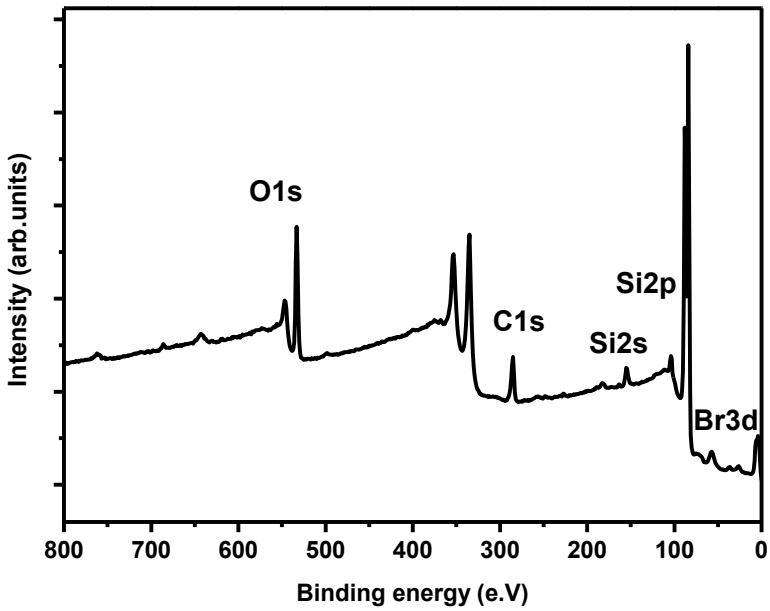

Figure 4.3. XPS full survey spectrum from Br SiNPs deposited on a gold substrate.

The Si2p spectrum was curve-fitted into three peak components against a Shirley background (Figure 4.4). The first component at 103.67 eV is attributed to Si-C bonding.[7] The second at 103.06 eV is assigned to Si-O from SiO_2 at the surface of SiNPs [8] and the third at 102.15 eV is for Si-Si within the silicon core of the SiNPs.[9] The presence of Si-C component in the Si2p region suggests that the surface silicon atoms change from Si-H to Si-C bonding. By the fitting performed almost 72% of the silicon surface was estimated to bind by Si-C bonds to the allyl bromide capping layer and 10% to the Si-Si bonding (Table 4.3). The remaining 17% was related to the oxidised Si on the surface on NPs. The degree of oxidation is a qualitative estimation based on the structure and chemical makeup of these type of NPs. An estimated 80% of the available surface has undergone ligand capping. These results are

consistent with previous studies which found that H-terminated silicon surfaces bound to organic monolayers with normally 50% surface coverage.[10, 11]

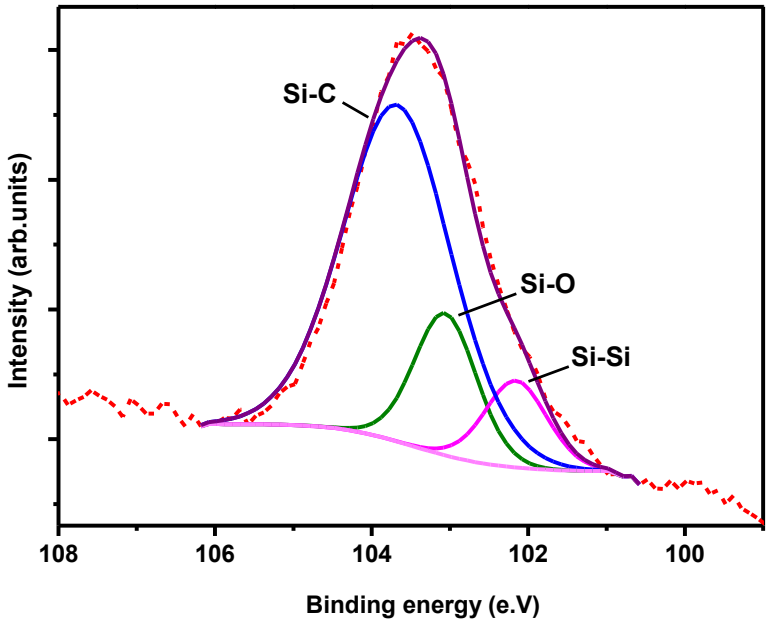

Figure 4.4. High resolution XPS spectrum from Br SiNPs showing Si2p region.

The C1s spectrum was also fitted with three components and a Shirley background. They appeared at 284.92, 284.10 and 286.46 eV (Figure 4.5). The first peak at binding energy 284.92 eV is attributed to C-C bonds and the second component, at binding energy 284.10 eV, is related to C-Si bonds, covering almost 22% of the spectrum area (Table 4.3).[12] The final binding energy at 286.46 eV is characteristic of C-Br bonds.[13]

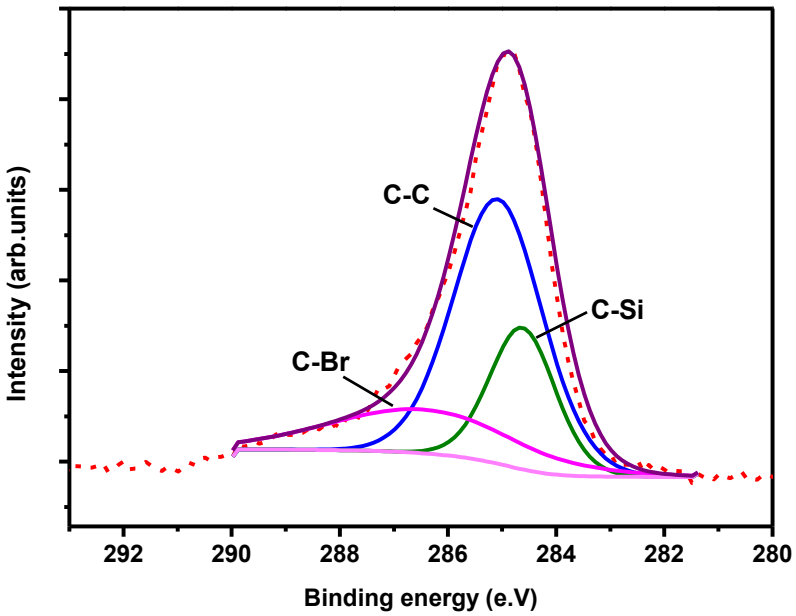

Figure 4.5. High resolution XPS spectrum from Br SiNPs showing C1s region.

The O1s spectrum of Br SiNPs fitted with two components and a Shirley background can be seen in Figure 4.6. The fittings appeared at 532.45 and 534.44 eV (Figure 4.6). The peak at 532.45 eV corresponds to Si-O covering almost 97% of the spectrum (Table 4.3). This is most likely as a result of the chemical oxidation in part due to X-ray induced oxidation.[9]

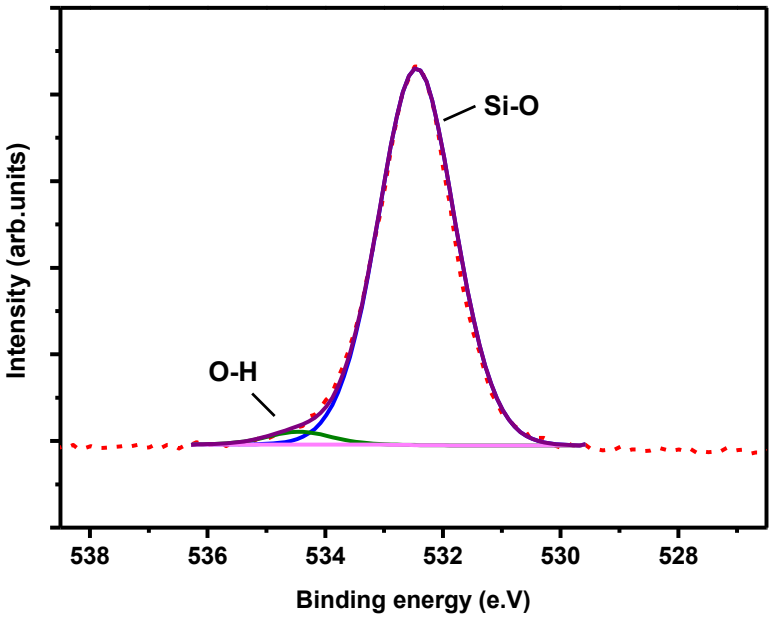

Figure 4.6. High resolution XPS spectrum from Br SiNPs showing O1s region.

The Br3d spectrum is shown in Figure 4.7 and fitted with one peak at 69.20 eV. This is a peak representative of C-Br.[14, 15] However, this signal was lower than would be expected, likely due to the shallow penetration depth of this technique and the gap between the bromine atom and the surface of SiNPs.

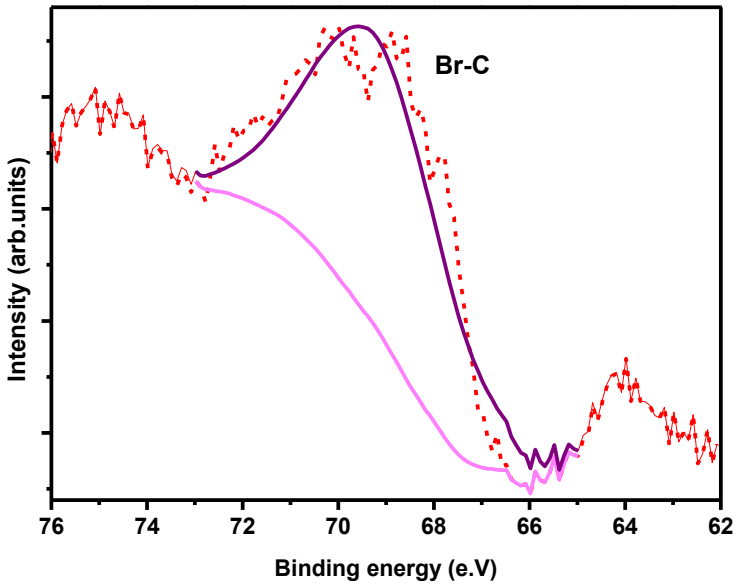

Figure 4.7. High resolution XPS spectrum from Br SiNPs showing Br3d region.

Table 4.3. XPS data with the detailed ratio of elements present on the surface of Br SiNPs obtained by high resolution scans.

Scans	Positions	Position (eV)	FWHM	Area	%
Si 2p	Si-C	103.6720	1.6227	13706.611	71.81
	Si-O	103.0601	0.9355	3338.186	17.49
	Si-Si	102.1563	0.9366	2041.875	10.70
C 1s	C-C	284.92	1.9377	21467.324	75.30
	C-Si	284.10	1.4277	8471.041	22.61
	C-Br	286.46	4.1114	7525.297	20.08
O 1s	Si-O	532.45	1.526	35976.84	97.28
	O-H	534.44	1.263	1006.98	2.72
Br 3d	Br-C	69.20	3.3389	4462.412	100

4.4. Size and Dispersity Measurement of Bromine-functionalised SiNPs

4.4.1. Visualisation and Size Measurement by TEM

The TEM micrographs confirm that Br SiNPs have been successfully synthesised (Figure 4.8). The distribution of SiNPs diameters was 2-10 nm. The mean nanoparticle diameter was 6.02 nm, calculated from the average of 100 particles obtained from different regions of the grid. The diameter which occurred most frequently was 5 nm which is 1 nm lower than the mean diameter, indicating a slightly skewed distribution.

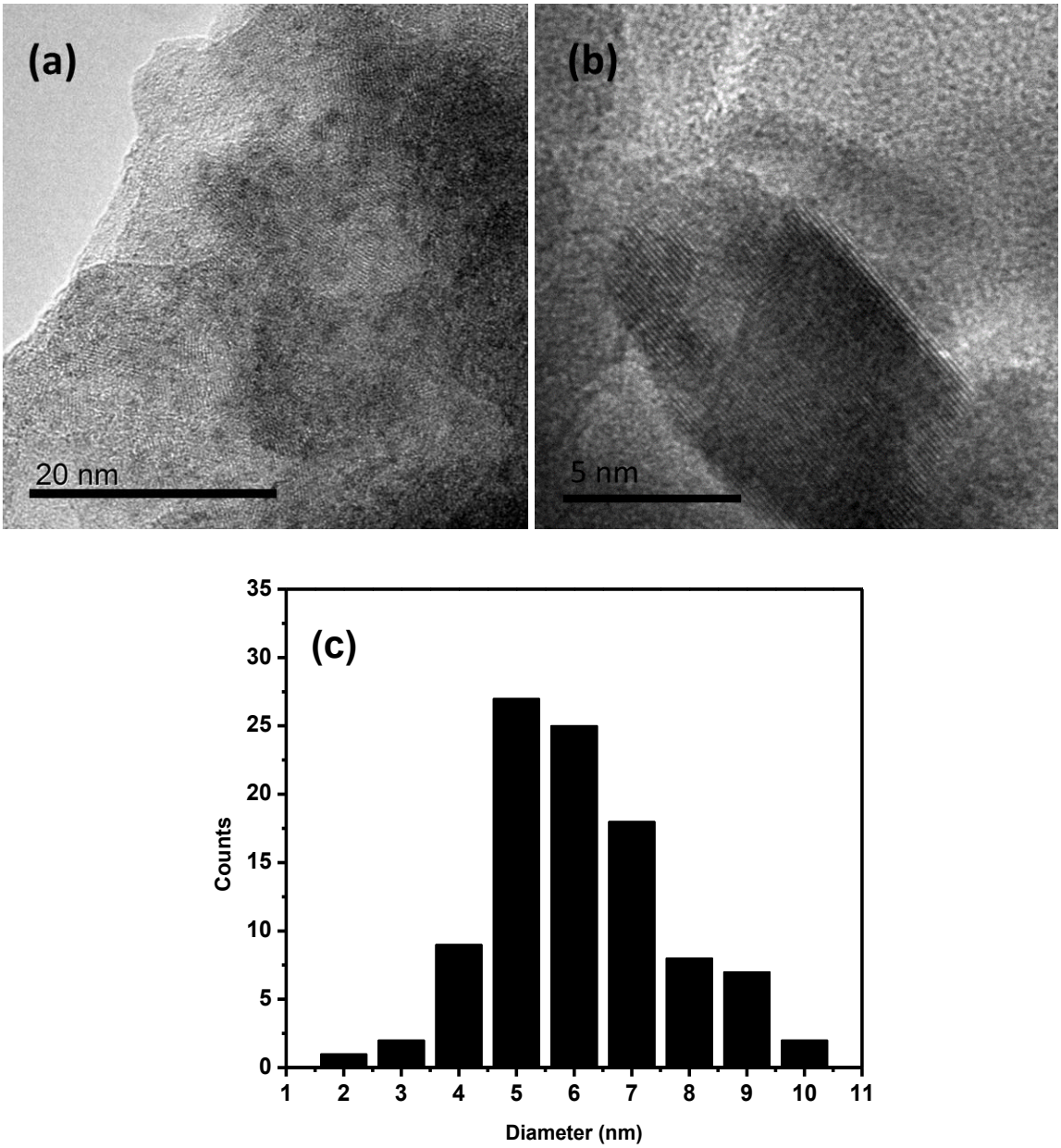

Figure 4.8. TEM images of Br SiNPs (a) and (b) and the histogram showing the distribution of Br SiNPs diameters (c).

4.4.2. Hydrodynamic Size Measurement by DLS

DLS measured the hydrodynamic diameter of Br SiNPs in toluene. The size was 7.46 ± 0.05 nm in toluene (Figure 4.9). DLS demonstrated a very close size to that obtained from the TEM. The presence of anything attracted to the surface of SiNPs, such as a surrounding layer or capping ligands, can increase SiNP diameter size in toluene, and produced a well dispersed solution of nanoparticles without any sign of aggregation.

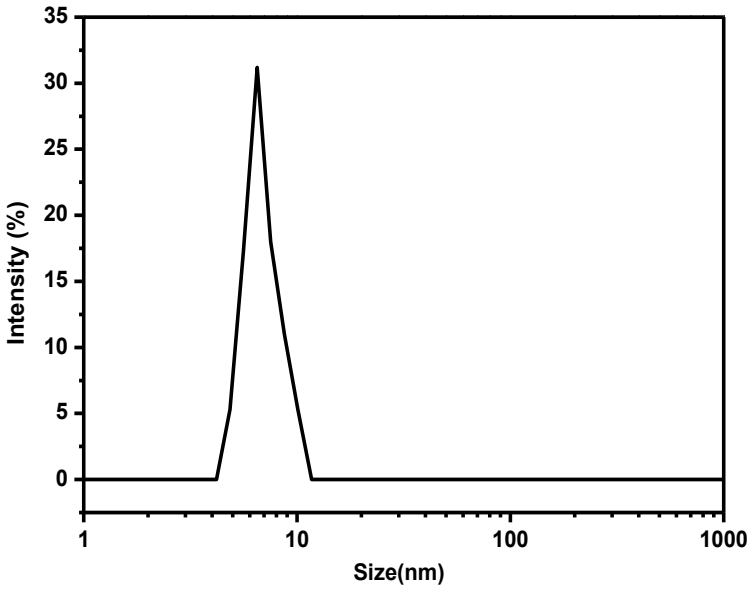

Figure 4.9. Hydrodynamic size of Br SiNPs dispersed in toluene measured by DLS.

4.5. Optical properties of Bromine-functionalised SiNPs

4.5.1. Absorption and Emission Spectra

The emission and absorption spectra of Br SiNPs in toluene are presented in Figure 4.10. A gradual increase in the absorbance was observed with a decreasing wavelength. For wavelengths below than 475 nm the absorbance increased at a greater rate. The solid line shows the PL spectrum of Br SiNPs in toluene at room temperature. The maximum emission peak was observed at 400 nm with a full width at a half maximum height (FWHM) of 150 nm under an excitation wavelength of 310 nm.

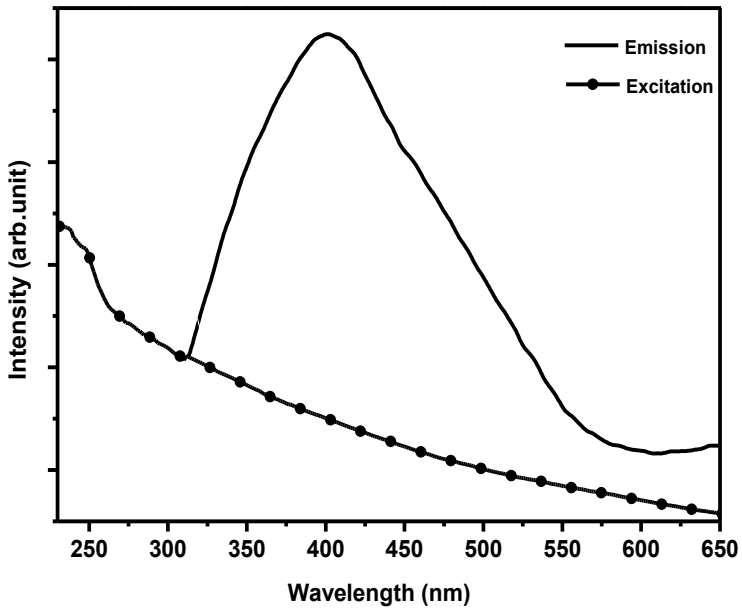

Figure 4.10. Absorption (dotted line) and emission (solid line) spectra of bromine-functionalised SiNPs dispersed in toluene (The excitation wavelength was set at 310 nm).

Considering the data obtained from the characterisation of Br SiNPs, the desired structure was achieved and nanoparticles showed acceptable optical properties. Therefore, they could be used for further synthesis to obtain the ITC functional group on the surface of SiNPs.

4.6. Synthesis of Isothiocyanate-functionalised Silicon Nanoparticles

Two different approaches have been investigated to synthesise isothiocyanate-functionalised SiNPs. The first attempt involved using the allyl isothiocyanate directly in order to introduce this functional group to the surface of H-terminated SiNPs via hydrosilylation (Scheme 4.2). The refluxing was performed in dry toluene initially for 5 h, then for another seven hours (to 12 h), and finally to 24 h. Despite the extended refluxing time, the IR spectra of the products did not show any evidence of the presence of ITC group. This could be due to the high reactivity of the ITC which is more reactive compared to the C=C bond in the structure of ITC and therefore precluded hydrosilylation.

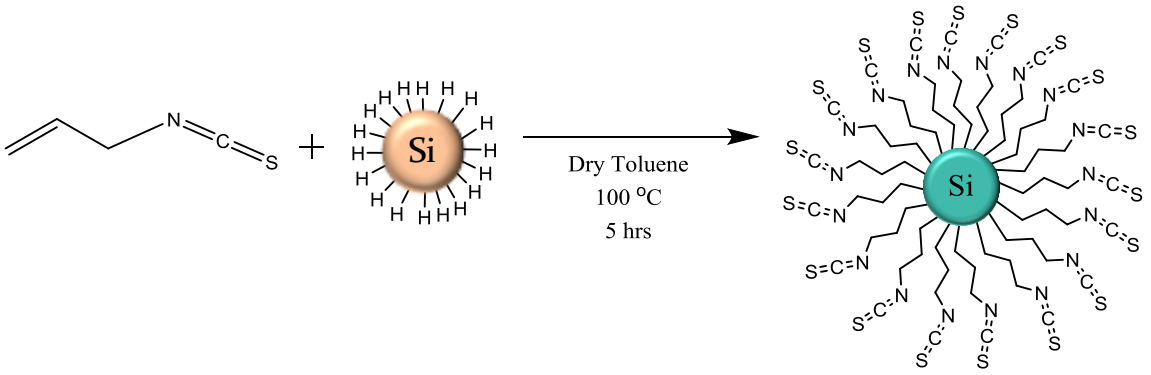

Scheme 4.2 Schematic illustration of the synthesis of ITC SiNPs using AITC.

Since this attempt at did not succeed, the experimental plan was altered to use other types of nanoparticles as precursors including the Br SiNPs and NH_2 SiNPs and then later synthesise the ITC group from Br and NH_2 functionalities which are already present on the surface. Thus, a detailed spectroscopic study was required for each synthesis to evaluate which group had the potential to be used as a multifunctional compound for further investigation.

4.6.1. The Use of Bromine-functionalised Silicon Nanoparticles Precursors

The bright ITC SiNPs were produced by reacting the mixture of bromine-functionalised SiNPs with KSCN in dry ethanol and refluxing overnight (Scheme 4.3). On completion of the reaction, the mixture was allowed to cool and then the solvent was removed under the reduced pressure. The residual starting material and by products were removed after washing with water and extraction of ITC SiNPs into diethyl ether. Approximately 25 mg of the desired NPs were obtained as an orange powder after removing the solvent.

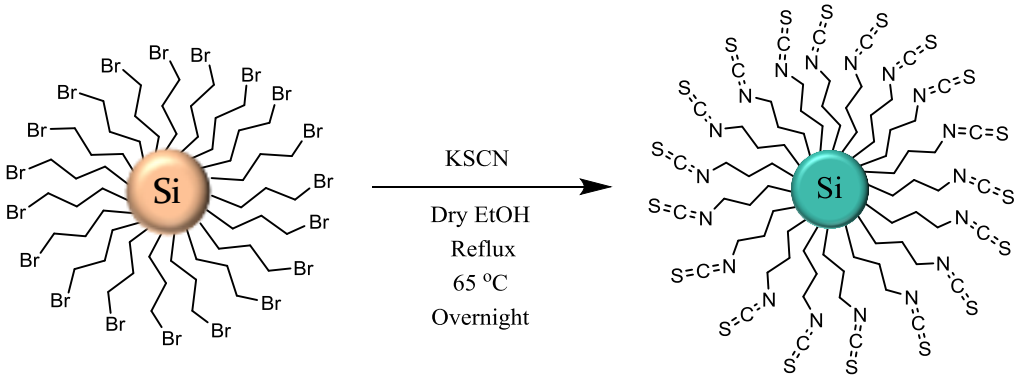

Scheme 4.3. Schematic illustration of the synthesis of ITC SiNPs (P Br SiNPs).

4.6.2. The Use of Amine-functionalised Silicon Nanoparticles Precursors

Through the second method amine capped SiNPs produced from the top down approach as described in Chapter 3 (Section 3.3) and reacted with CS_2 in an ice bath. After 3 h stirring, dicyandiamide was added followed by 3 drops of triethylamine (Scheme 4.4). The reaction was stirred for extra 3 hours. The desired SiNPs were extracted in ethyl acetate and impurities were washed by distilled water. Via this procedure, approximately 28 mg ITC SiNPs were obtained from each batch.

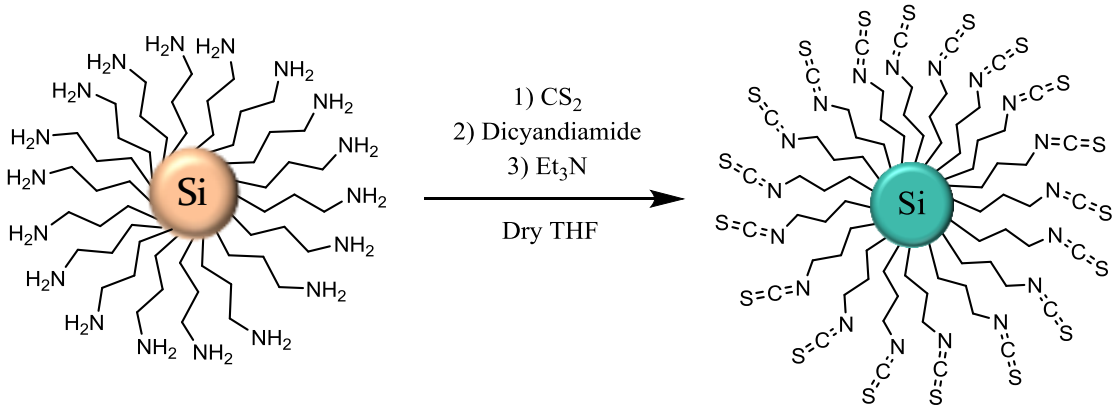

Scheme 4.4. Schematic illustration of the synthesis of ITC SiNPs (P NH_2 SiNPs).

4.7. Chemical Characterisation of ITC SiNPs

4.7.1. Chemical bonding by FTIR

Figure 4.11 shows the FTIR spectra of ITC SiNPs, produced from Br SiNPs (a), after 6 h (b), 12 h (c) and 24 h (d) refluxing at 65 ^{o}C. After 6 hours of reflux, the characteristic double bond featuring the ITC functional group had not developed yet. The growth was clear after longer time periods; after 12 hours refluxing at 65 ^{o}C, the double peak was observed clearly at 2039 cm^{-1} and finally reached to the maximum intensity after 24 h.[16] This result conforms the formation of the ITC group on the surface of SiNPs. The final spectrum shows a peak at 1269 cm^{-1} representing C-Si bonds,[4] and an absence of signal at 695 cm^{-1} indicative of the C-Br bond,[17] which was still present at 12 h. The C-H rocking of the alkane in the product appeared at 746 cm^{-1} (spectra (c) and (d)).[17] The ITC coated SiNPs displayed features from Si-O bonds at around 1015 cm^{-1}.[18] These features indicate the presence of only a very small number of Si-O bonds per nanoparticle, as they are easily visible due to the polarity of the Si-O bond.[19]

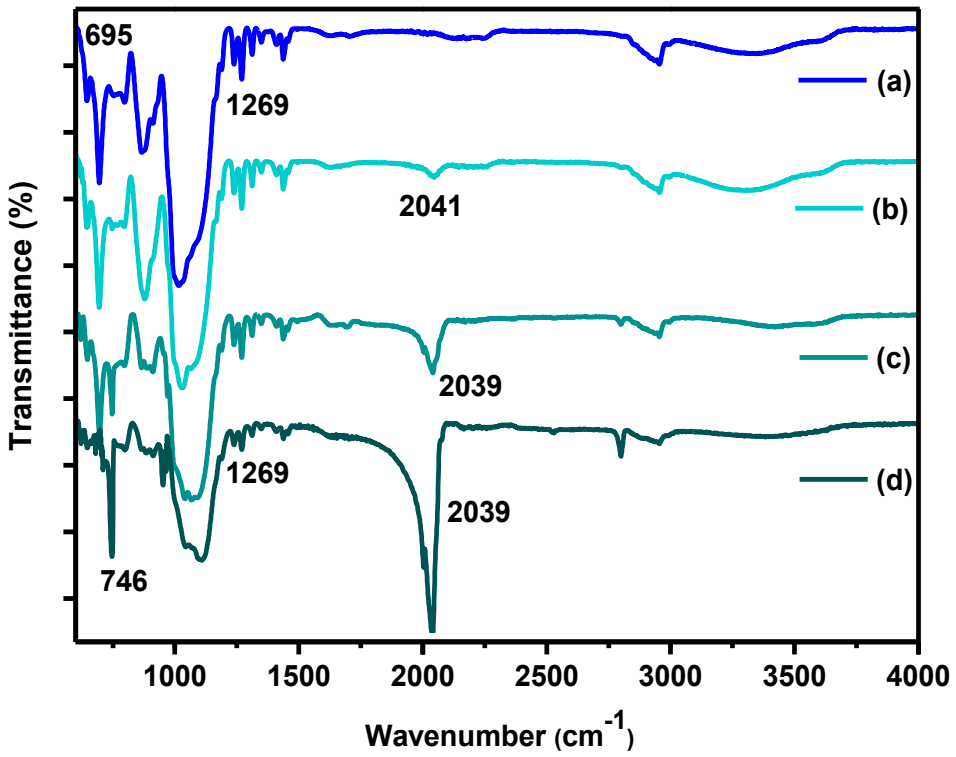

Figure 4.11. FTIR analysis for ITC SiNPs (P Br SiNPs) after 6 h (b), 12 h (c) and 24 h (d) refluxing compared to the spectrum of Br SiNPs (a).

For comparison, the ITC SiNPs (P NH_2 SiNPs) were also characterised by ATR analysis. Figure 4.12 (b) showed a clear double bond at around 2100 to 2200 cm^{-1} indicating the synthesis of ITC functional group.[16] Scissoring and stretching vibration bands of Si-CH_2 and Si-C bonds (at about 1450 and 1260 cm^{-1}, respectively) also show the covalent attachment of the ligand molecules in both nanoparticles to the surface of the H-terminated SiNPs.[4] After the synthesis, in spectrum (b) in Figure 4.12, there was no sign of N-H wagging and stretching at 790 and 3600 cm^{-1} respectively which were assigned to the amine functional group in the starting material (a).[20] Stretching signals with symmetric and asymmetric C-H stretching vibrations at 2800 and 2900 cm^{-1} respectively were observed in the FTIR spectra of both samples.[6]

Based on the IR data collected from both types of ITC SiNPs, the synthesis methods were successful. Both compounds represented the ITC functional group after the synthesis and the other differences in their spectra are attributed to the differences in reaction conditions in addition to the different staring materials.

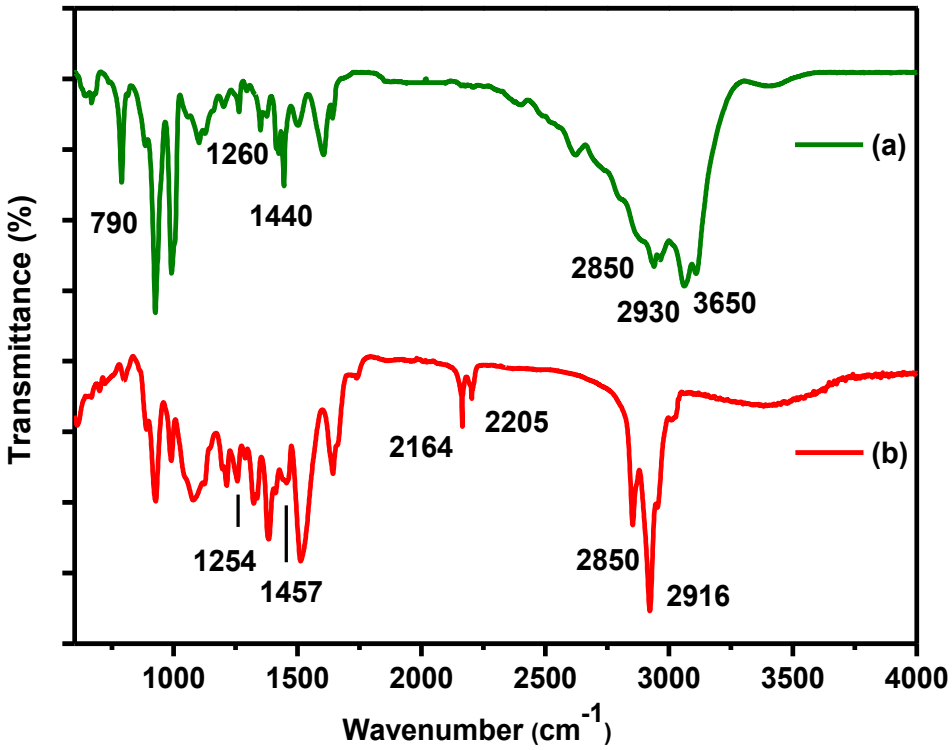

Figure 4.12. FTIR analysis for ITC SiNPs (P NH_2 SiNPs) (b) and NH_2 SiNPs as the precursor (a).

4.7.2. Elemental Analysis by EDX

The elemental composition was investigated using EDX. The EDX spectrum of ITC SiNPs (P Br SiNPs) (Figure 4.13) shows the presence of silicon, oxygen, and sulphur indicating a favourable elemental composition.

Nitrogen is often impossible to be detected by EDX as the nitrogen fingerprint closely resembles that of heavier chemical elements in the EDX spectrum. Such overlap can lead to misidentification of nitrogen by other elements.[21]

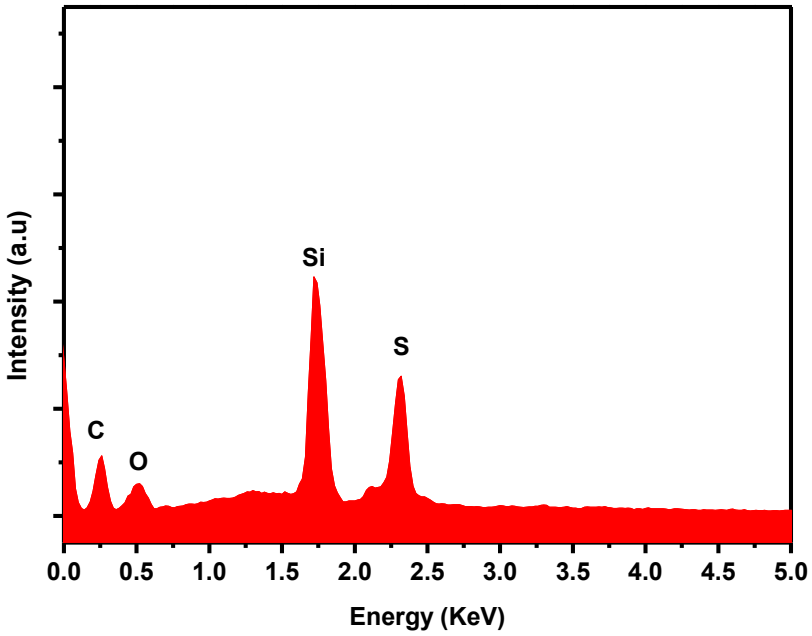

Figure 4.13. EDX spectra of ITC SiNPs (P Br SiNPs).

Silicon, carbon, oxygen and sulphur were also identified in the EDX spectrum of ITC SiNPs (P NH_2 SiNPs) (Figure 4.14). However, there were some partial amounts of platinum catalyst which were used in the synthesis of NH_2 SiNPs.

EDX is dependent on the atomic mass of the elements being analysed which means the lower the atomic mass (and number) the harder they are to detect. Therefore, when a sample of mixed elements, with a wide range of atomic numbers is being analysed, the detector peak sizes are not representative of the exact atomic ratios of the elements present.[22] As a result, EDX has predominantly been used to identify the existence of elements in nanoparticles and not to obtain the accurate elemental ratios, whereas the XPS method is used to provide more comprehensive information.

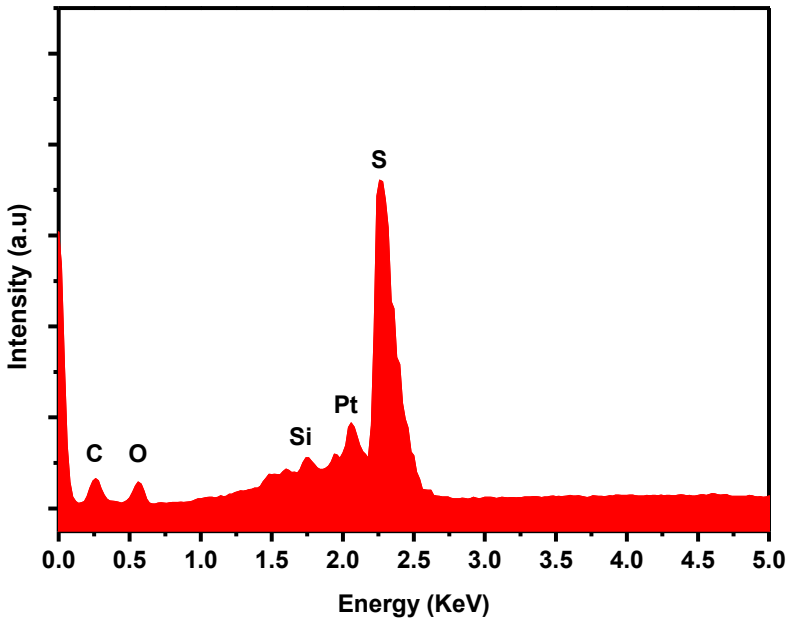

Figure 4.14. EDX spectra of ITC SiNPs (P NH_2 SiNPs).

4.7.3. Elemental Analysis by XPS

The detailed XPS was collected from ITC SiNPs synthesised by both methods to characterise the surface chemistry of these materials.

Figure 4.15 shows the full survey spectrum of ITC SiNPs (P Br SiNPs). From this spectrum, Si2p, Si2p, C1s, O1s and N1s peaks can be observed. The peaks not assigned on Figure 4.15 were for the Au substrate where nanoparticles where deposited on top. All spectra were calibrated to the Au4f peak. The oxygen level observed in XPS is typical of the X-ray induced oxidation of SiNPs during the measurement.

The high resolution XPS spectra are shown in the following Figures to confirm the surface chemical bonding.

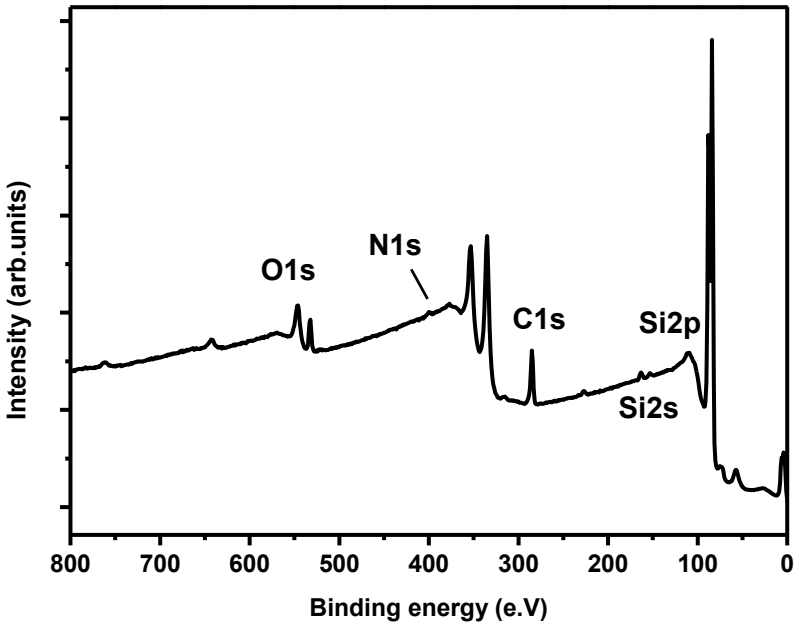

Figure 4.15. XPS full survey spectrum from ITC SiNPs (P Br SiNPs) deposited on a gold substrate.

The Si2p spectrum, shown in Figure 4.16, was fitted with three components and a Shirley background. The first peak appeared at 102.28 eV is attributed to Si-C bonding.[23] This peak covered approximately 62% of the spectrum (Table 4.4) which indicates the surface of SiNPs is terminated by the ligand. 27% was assigned to Si-O appearing at 102.91 eV and the smallest peak was at 101.62 eV is attributed to Si-Si bond within the nanoparticle core.[9, 24, 25]

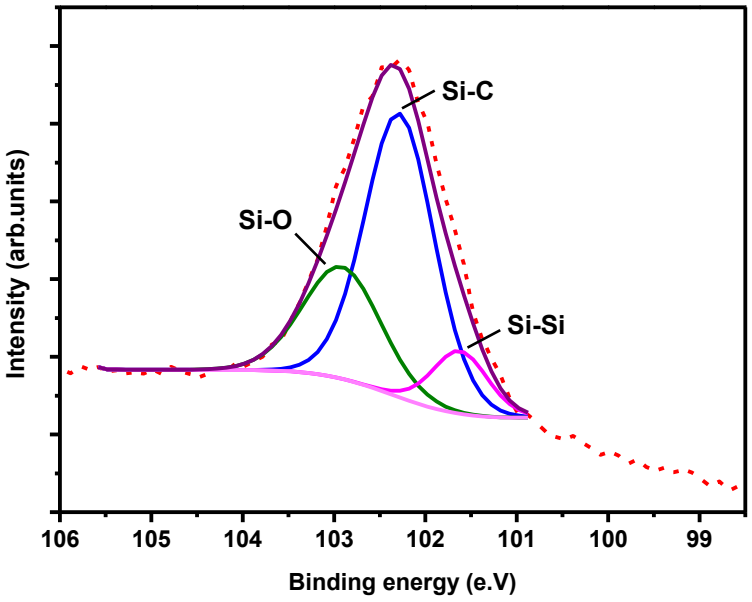

Figure 4.16. High resolution XPS spectrum from ITC SiNPs (P Br SiNPs) showing Si2p region.

The C1s spectrum was fitted with 4 components (Figure 4.17). The largest area covering 51% was for the peak appeared at 285.04 eV attributed to C-C.[12] The peak appeared at 284.60 is assigned to C-Si with approximately 26%. There was evidence for C-N bonding at 286.44 eV and a very low amount of C-O bond at 289.00 eV (~ 3%).[26]

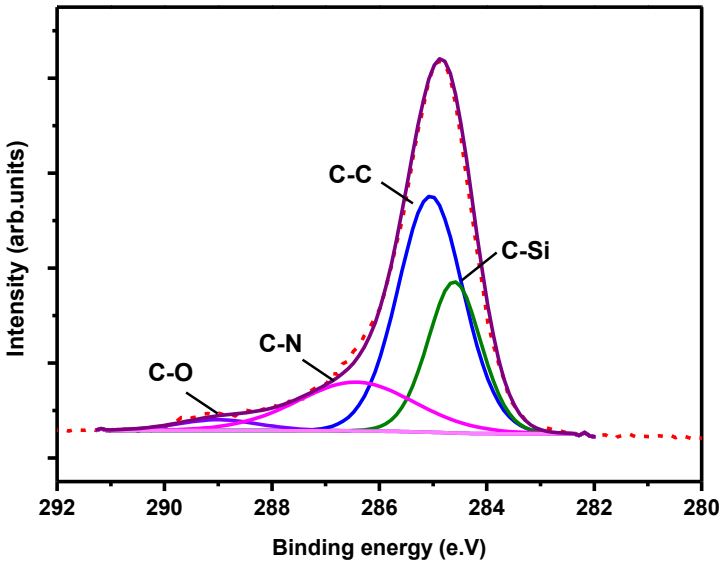

Figure 4.17. High resolution XPS spectrum from ITC SiNPs (P Br SiNPs) showing C1s region.

In Figure 4.18, the O1s spectrum is fitted with one component which makes up 100% of the spectrum. This peak appeared at 532.19 eV representative of Si-O bonding due to the oxidation caused by the X-ray beam.[9]

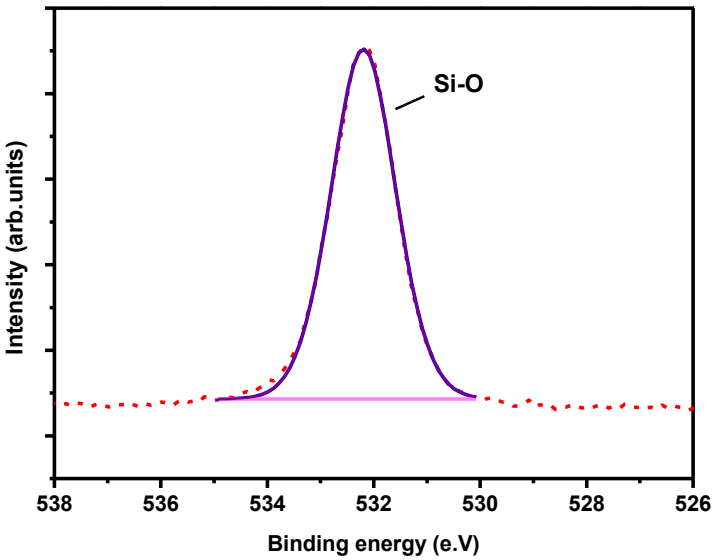

Figure 4.18. High resolution XPS spectrum from ITC SiNPs (P Br SiNPs) showing O1s region.

The N1s spectrum is fitted with two peaks and Shirley background (Figure 4.19). The main peak at 400.06 eV is assigned to the C-N bonding of the ITC ligand and the second peak at 398.34 eV is for N=C=S.[26] The existence of the second component confirms the presence of isothiocyanate functional group.

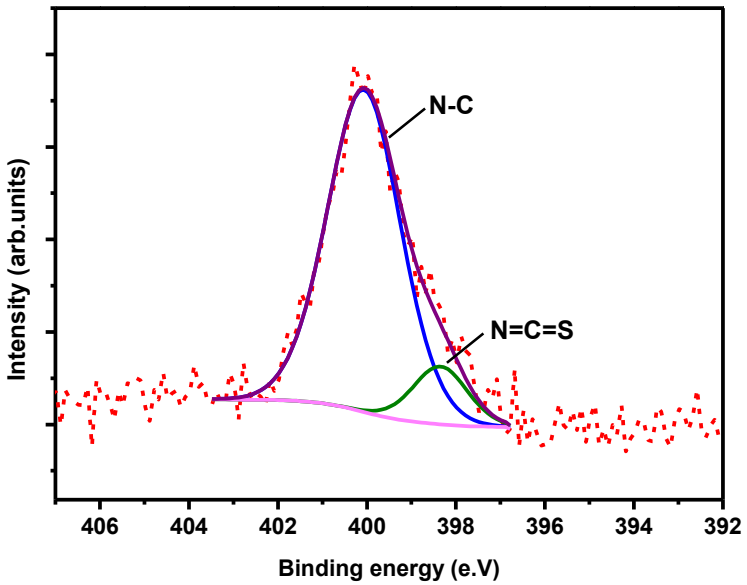

Figure 4.19. High resolution XPS spectrum from ITC SiNPs (P Br SiNPs) showing N1s region.

Table 4.4. XPS data with the detailed ratio of elements present on the surface of ITC SiNPs (P Br SiNPs) obtained by high resolution scans.

Scans	Positions	Position (eV)	FWHM	Area	%
Si 2p	Si-C	102.28	0.894	7085.34	61.82
	Si-O	102.91	1.001	3132.30	27.33
	Si-Si	101.62	0.708	1243.85	10.85
C 1s	C-C	285.0467	1.4363	31007.285	51.37
	C-Si	284.6036	1.1629	16086.168	26.65
	C-N	286.4418	2.5780	11493.093	19.04
	C-O	289.0017	1.7998	1772.406	2.94
O 1s	Si-O	532.19	1.422	63074.47	100
N 1s	N-C	400.0649	1.9383	5859.794	88.24
	N=C=S	398.3493	1.4366	780.779	11.76

Next, the chemical bonding of ITC SiNPs (P NH_2 SiNPs) was also investigated with both full survey (Figure 4.20) and high resolution scans over Si2p, C1s, O1s and N1s regions (Figures 4.21 to 4.24).

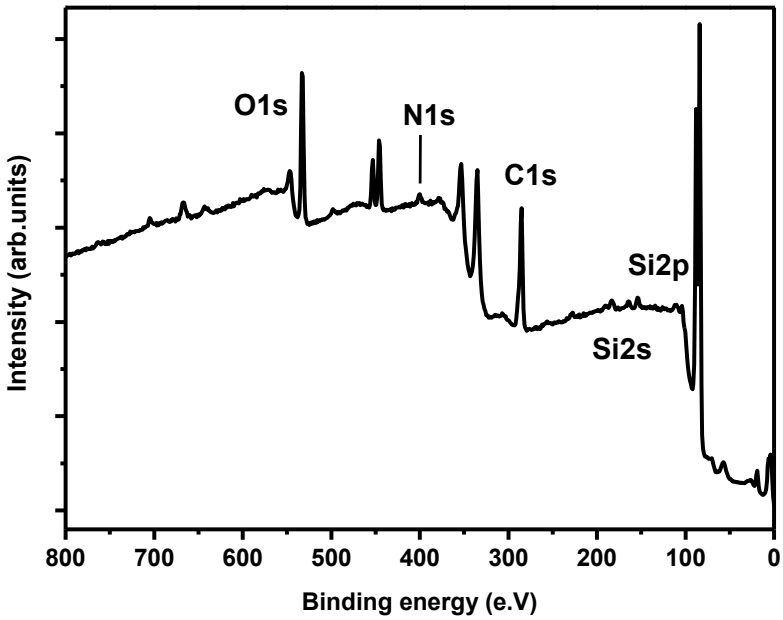

Figure 4.20. XPS full survey spectrum from ITC SiNPs (P NH_2 SiNPs) deposited on a gold substrate.

The Si2p spectrum was fitted with three components and a Shirley background (Figure 4.21). The first component at 102.08 eV is assigned to Si-C and this covered about 56% of the spectrum area (Table 4.5).[23] Two peaks at 102.77 and 101.39 as indicative of Si-O and Si-Si respectively.[9]

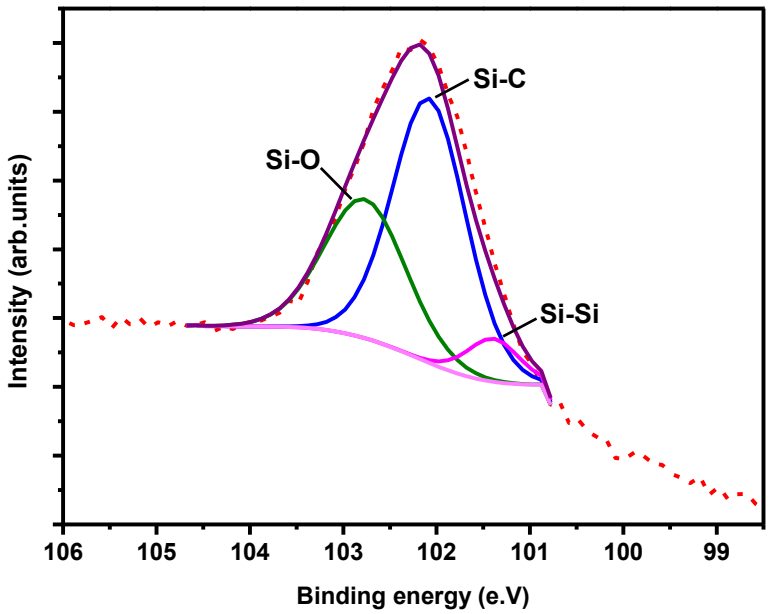

Figure 4.21. High resolution XPS spectrum from ITC SiNPs (P NH_2 SiNPs) showing Si 2p region.

The C1s spectrum of ITC SiNPs (P NH_2 SiNPs) presented in Figure 4.22 is fitted with peaks at 285.01, 286.45, 286.64 and 288.73 eV. C-C bonding with 43% and C-Si bonding with about 29% conformed to the expected bonding ratios. The last two peaks related to the C-N and C-O bonding had almost 16% and 12% of the C1s spectrum respectively (Table 4.5).[12]

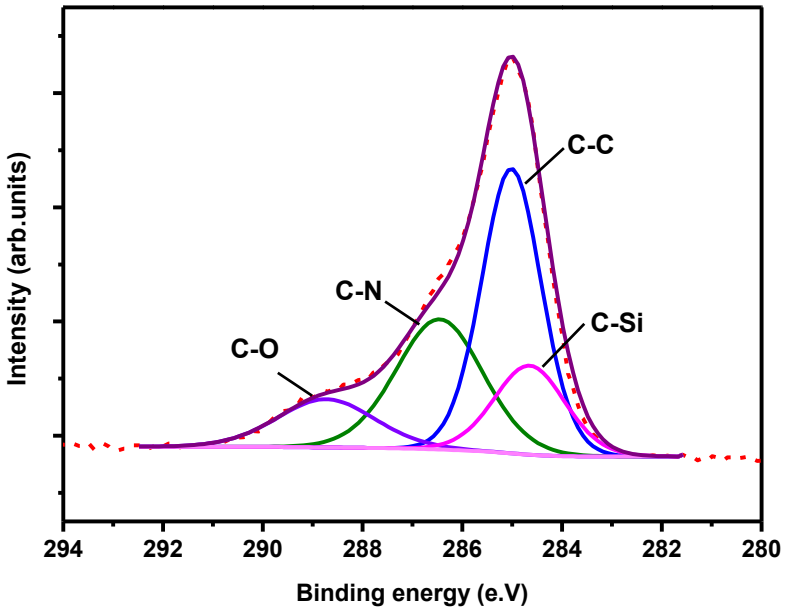

Figure 4.22. High resolution XPS spectrum from ITC SiNPs (P NH_2 SiNPs) showing C1s region.

About 95% of the Si2p spectrum is assigned to Si-O with a peak at 531.89 eV and the remaining 5% is assigned to O-H bonding (Figure 4.23 and Table 4.5).[9]

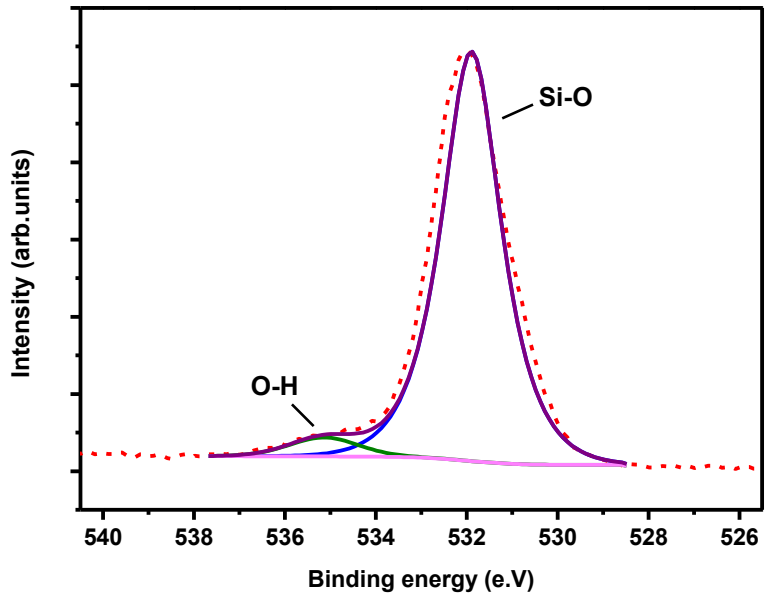

Figure 4.23. High resolution XPS spectrum from ITC SiNPs (P NH_2 SiNPs) showing O1s region.

The N1s spectrum was fitted with two components and a Shirley background. The peaks appeared at 400.15 and 398.53 eV representative of N-C (~92%) and N=C=S (~7%) respectively (Figure 4.24 and Table 4.5).[26]

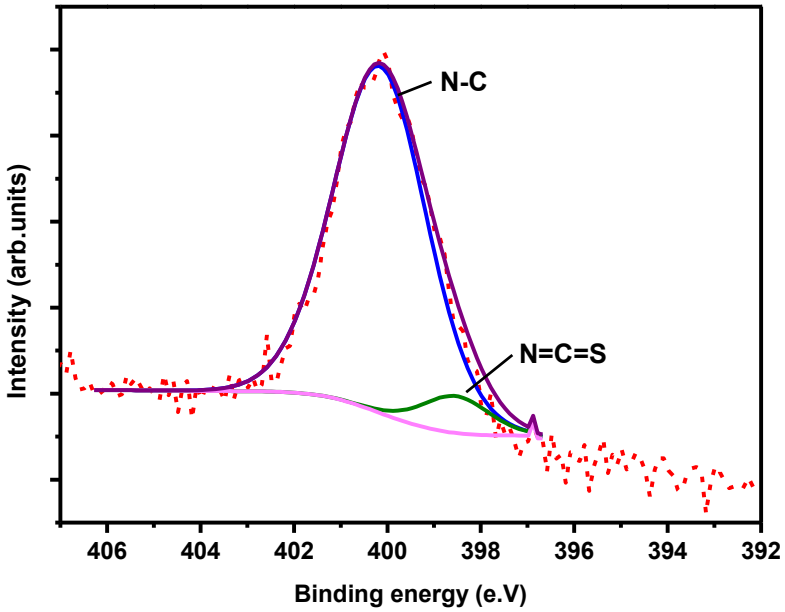

Figure 4.24. High resolution XPS spectrum from ITC SiNPs (P NH_2 SiNPs) showing N1s region.

Table 4.5. XPS data with the detailed ratio of elements present on the surface of ITC SiNPs (P NH_2 SiNPs) obtained by high resolution scans.

Scans	Positions	Position (eV)	FWHM	Area	%
Si 2p	Si-C	102.08	0.928	7733.79	58.79
	Si-O	102.77	1.033	4526.98	34.41
	Si-Si	101.39	0.658	894.83	6.80
C 1s	C-C	285.0133	1.4089	38090.087	43.22
	C-Si	286.4565	2.0528	25369.816	28.78
	C-N	286.6482	1.6723	14152.366	16.06
	C-O	288.7319	2.3009	10524.785	11.94
O 1s	Si-O	531.89	1.542	48936.71	95.36
	O-H	535.14	1.793	2382.82	4.64
N 1s	N-C	400.1580	2.3633	10331.406	92.95
	N=C=S	398.5392	1.6816	784.072	7.05

XPS data confirmed the presence of the expected atoms in both types of ITC SiNPs. However, the degree of oxidised atoms in ITC SiNPs (P Br SiNPs) seemed to be lower than ITC SiNPs (P NH_2 SiNPs) as there was only 3% of the C1s attributed to the C-O in in ITC SiNPs (P Br SiNPs) whereas 12% of the spectrum in ITC SiNPs (P NH_2 SiNPs) is attributed to this oxide (see Tables 4.4 and 4.5). This variation in oxidation levels might be attributed to differences in synthesis method, as these introduce dissimilar oxygen amounts into the nanosystem.

The Si/C ratio of 1:6 was obtained for ITC SiNPs (P Br SiNPs) and ratio of 1:8 for ITC SiNPs (P NH_2 SiNPs). Considering the expected ratio should be close to 1:4 in ITC SiNPs, the possibility of some unbound carbon impurities in ITC SiNPs (P NH_2 SiNPs) is higher than ITC SiNPs (P Br SiNPs).

4.8. Size, Dispersity and Surface Charge of ITC SiNPs

4.8.1. Visualisation and Size Measurement by TEM

Figure 4.25 shows the TEM images of ITC SiNPs (P Br SiNPs) with different magnifications. The size of approximately 100 chosen NPs was measured by transmission electron microscopy. These NPs have a mean diameter of 4.01 nm (Figure 4.26). It should be noticed that the observed dispersity of these particles corresponds very closely to the lattice spacing in silicon crystals confirming the high definition of these NPs. Given the electron density of the ITC chain, it is likely that only silicon core of the NPs is visible by TEM. The lattice spacing of 0.31 nm is consistent with the Si (111) plane.[27]

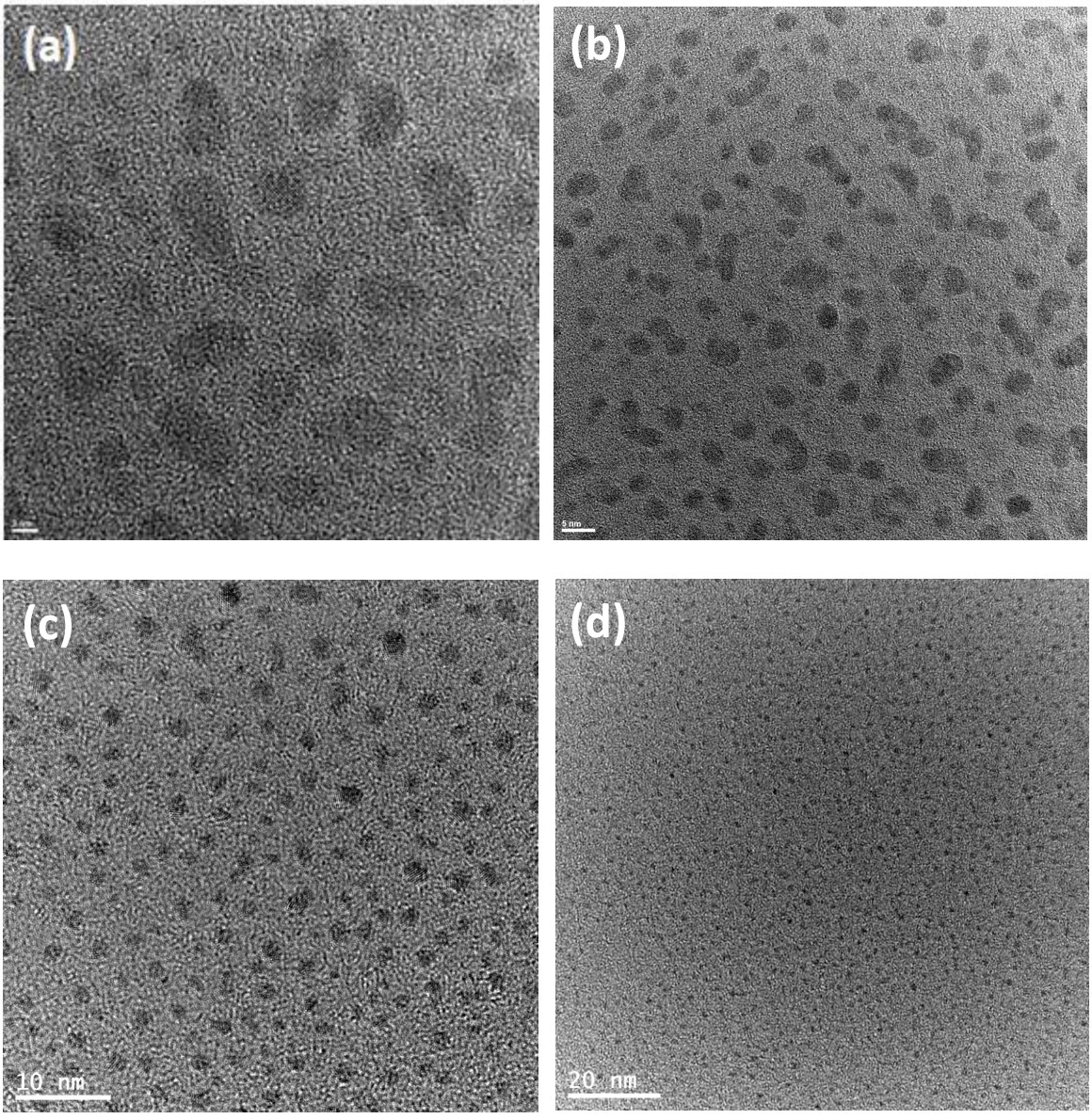

Figure 4.25. TEM images of ITC SiNPs (P Br SiNPs). The scale bars show 2 nm in (a), 5 nm in (b), 10 nm in (c) and 20 nm in (d).

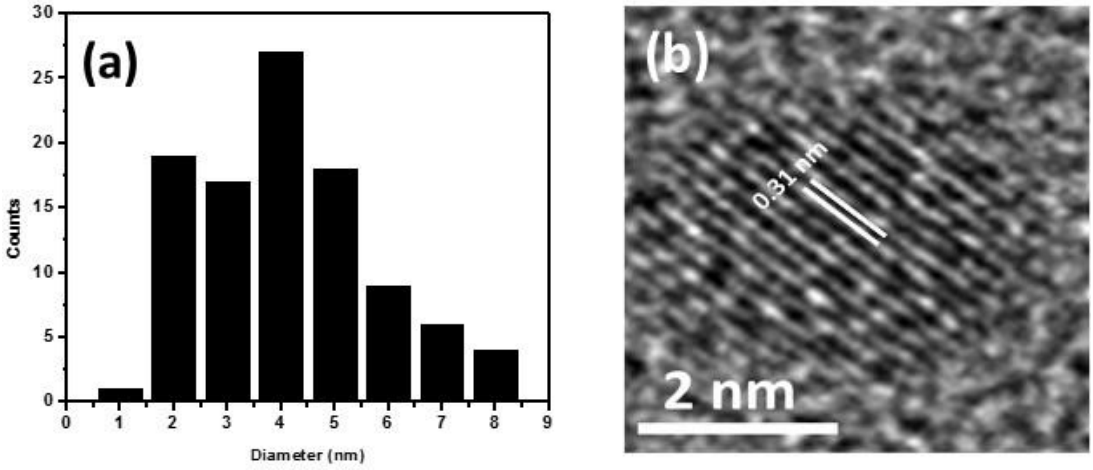

Figure 4.26. ITC SiNPs (P Br SiNPs) diameter histogram (a) and the lattice spacing the Si (111) plane (b).

TEM micrographs of ITC SiNPs (P NH_2 SiNPs) are also shown in Figure 4.27. The average size for these NPs, which is coming from the NH_2 SiNPs as the basis, was 4.21 nm which obtained after analysing 100 nanoparticles (Figure 4.28).

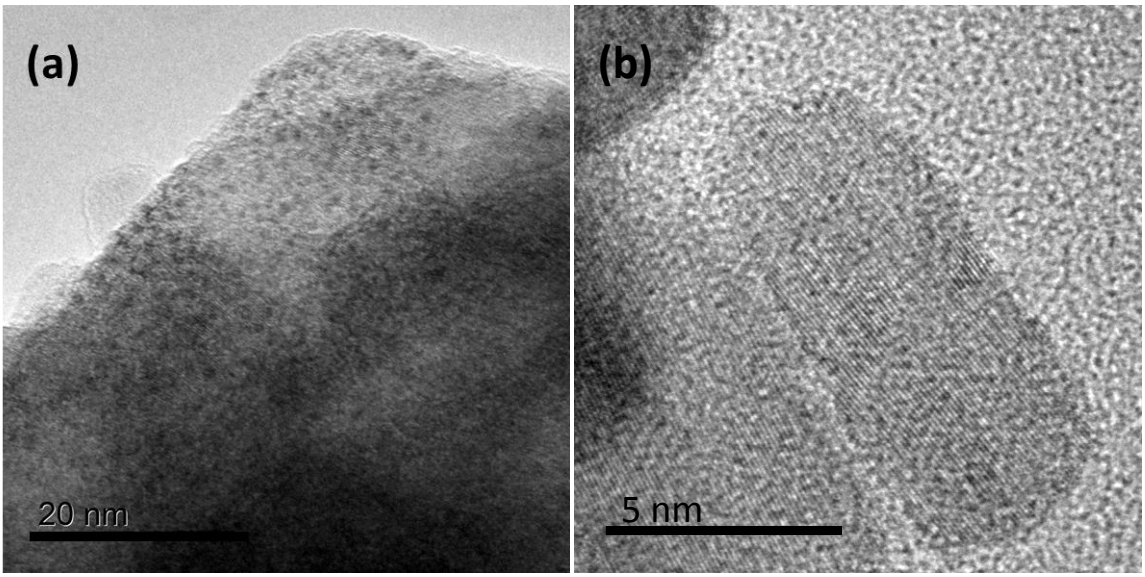

Figure 4.27. TEM images of ITC SiNPs (P NH_2 SiNPs).

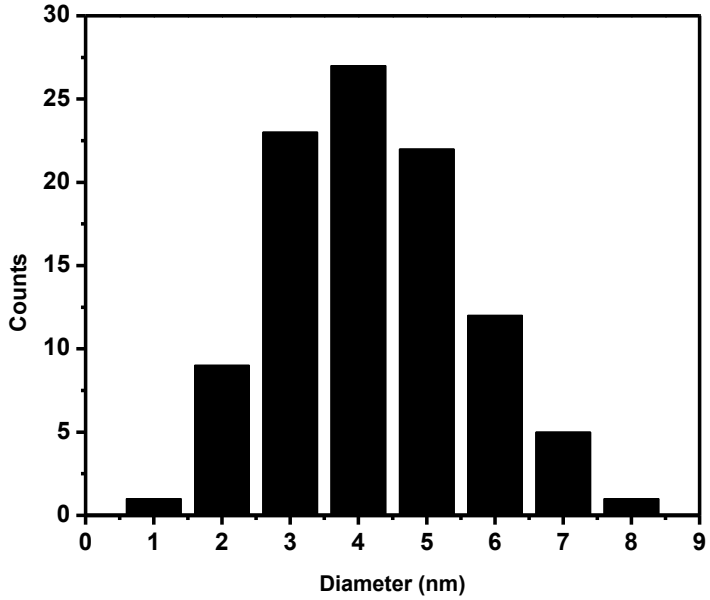

Figure 4.28. ITC SiNPs (P NH_2 SiNPs) diameter histogram.

4.8.2. Hydrodynamic Size Measurement by DLS

As mentioned previously in Chapter 1, the DLS measures the hydrodynamic diameter of SiNPs and is dependent on the interaction between the surrounding environment and the functionality present on the surface of SiNPs.[28] The DLS results of ITC SiNPs (P Br SiNPs) are shown in Figure 4.29. The nanoparticle diameter in RPMI containing the serum and DMSO was slightly larger than the diameters measured in the organic solvent (toluene), DMSO and RPMI without any supplements (Table 4.6). This could be due to either some partial aggregation in the media containing the serum or the formation of protein corona around the nanoparticles.

Protein adsorption on the nanoparticle surface can mediate the uptake of nanoparticles. Therefore, each media type with different protein compositions could result in various toxicity and uptake patterns. As a result, it is important to evaluate the size of NPs in the specific media they are going to be used for biological studies.[29, 30]

PdI, which is an indicator of the particle size distribution, was equal or less than 0.1 in toluene, DMSO and RPMI demonstrating the high monodispersibility of the prepared nanoparticle suspensions. The normal centrifugation before the measurement promoted the limited aggregation leading to the formation of ITC SiNPs with lower PdI.

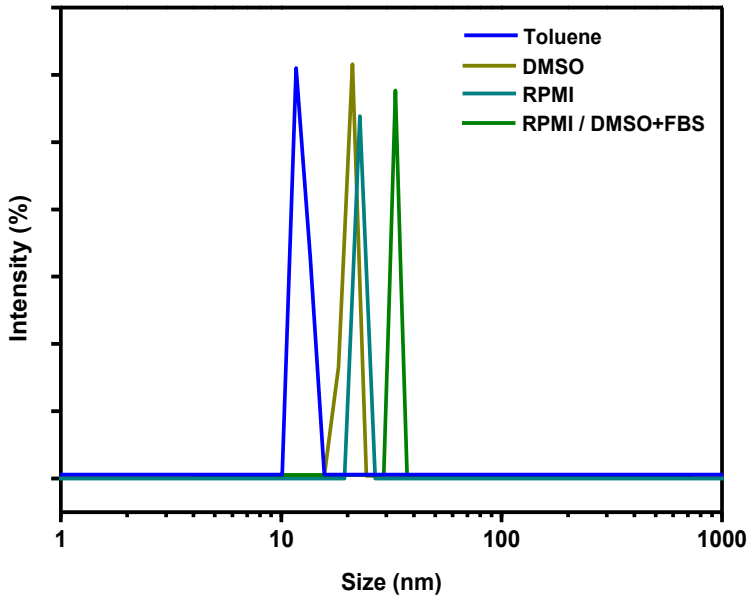

Figure 4.29. Hydrodynamic diameter of ITC SiNPs (P Br SiNPs) in different dispersing solvents.

Table 4.6. Mean hydrodynamic diameters and polydispersity index of ITC SiNPs (P Br SiNPs) measured by DLS in different media.

Solvent	Mean particle Size (nm) ± SD	Polydispersity Index ± SD
Toluene	11.85 ± 0.05	0.08 ± 0.02
DMSO	21.22 ± 1.20	0.10 ± 0.02
RPMI	22.70 ± 0.50	0.10 ± 0.13
RPMI/10% DMSO+10%FBS	33.01 ± 0.24	0.20 ± 0.08

The average size of the 18.24 nm was obtained for ITC SiNPs (P NH_2 SiNPs) in toluene (Figure 4.30). Further information about the size of these nanoparticles in various media is presented in Table 4.7. The synthesised nanoparticles were found to be rather monodispersed without any significant sign of aggregation and thus suitable for further experiments, although the PdI was more than what obtained for ITC SiNPs (P Br SiNPs).

It should be also noted in general the PdI for the nanoparticles obtained from the top down approaches such as ITC SiNPs are slightly larger than for those obtained from the bottom up techniques, and this is because they are typically not very narrow distributed.

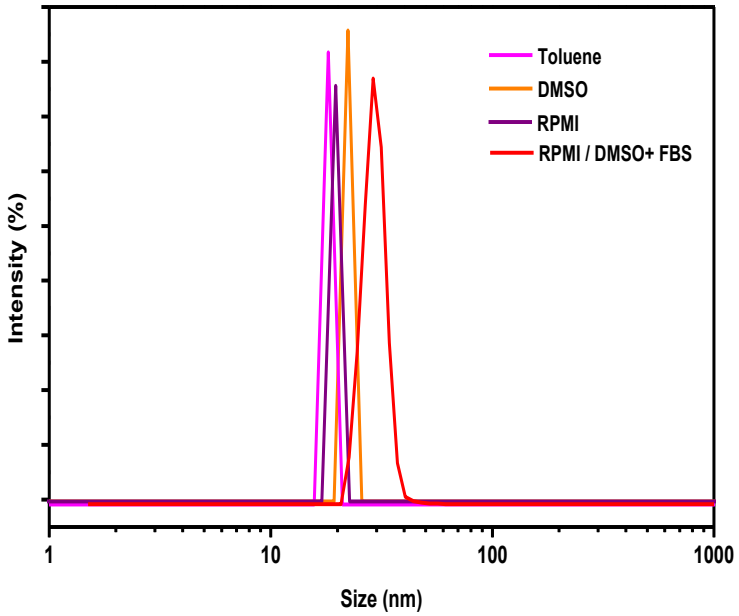

Figure 4.30. Hydrodynamic diameter of ITC SiNPs (P NH_2 SiNPs) in different dispersing solvents.

Table 4.7. Mean hydrodynamic diameters and polydispersity index of ITC SiNPs (P NH_2 SiNPs) measured by DLS in various media.

Solvent	Mean particle Size (nm) ± SD	Polydispersity Index ± SD
Toluene	18.24 ± 2.50	0.11 ± 0.05
DMSO	23.84 ± 1.15	0.14 ± 0.11
RPMI	19.68 ± 1.03	0.30 ± 0.04
RPMI/10% DMSO+10%FBS	29.05 ± 1.27	0.42 ± 0.12

4.9. Optical Properties of ITC SiNPs

4.9.1. Absorption and Emission Spectra

The surface composition and termination play a dominant role in determining the optical properties and stability of nanoparticles.[31] To evaluate the potential of ITC SiNPs and the validity of each synthesis route, the UV-Vis and PL measurements were performed on nanoparticles.

The UV/Vis absorption and emission spectra of these ITC SiNPs (P Br SiNPs) at room temperature can be seen in Figure 4.31 (a). Nanoparticles displayed an optical transition in the 300-360 nm range. The solid line is the PL spectrum of nanoparticles in toluene at room temperature. The PL showed a maximum emission in the blue region with a maximum at 450 nm when excited at the optimum wavelength of 360 nm with a full width at a half maximum height (FWHM) of 95 nm.

The UV-Vis spectrum of ITC SiNPs (P NH_2 SiNPs) showed a gradual increase from high to low wavelengths (Figure 4.31 (b)). The maximum emission was found at 410 nm with a full width at a half maximum height (FWHM) of 110 nm under an excitation wavelength of 360 nm.

The origin of the photoluminescence in ITC SiNPs is the product of the combination of both direct and indirect band gaps in SiNPs. Some theoretical evidence suggests that 1-2 nm SiNPs with carbon terminated surfaces show direct band gap optical transitions, leading to the photoluminescence in the blue region.[32-34] However, considering the size distribution of ITC SiNPs, these particles are too big to display blue PL by the quantum confinement effect. The possibility of the presence of nitrogen containing ligand caused the blue PL is higher as shown previously by Veinot *et al.* The presence of nitrogen atom in the structure of isothiocyanate functional group provided the mechanism of blue emission.[5]

The spectra were collected from the nanoparticles dispersed in toluene. The PL spectra for both types of ITC SiNPs showed that the strongest PL emission appeared in toluene suspension. This could be explained by the fact that the HOMO/LUMO gap in toluene is low, leading to a fast electron transfer between the NPs and the surface bonding structure with the solvent molecules.[35] Therefore, this could be utilised to improve the luminescence efficiency of the

composite of toluene and silicon. As a result, toluene was used for the optical characterisation of ITC SiNPs in this work.

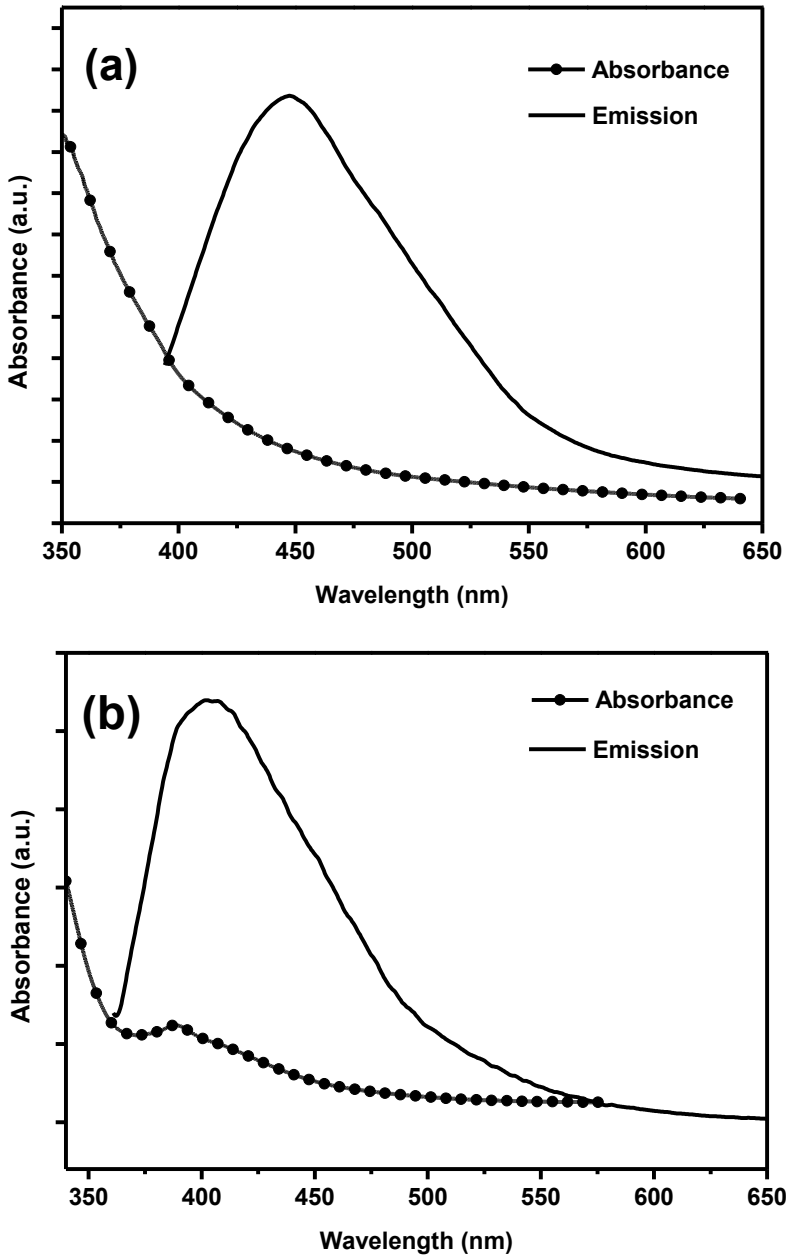

Figure 4.31. Absorption and emission spectra of ITC SiNPs (P Br SiNPs) (a) and ITC SiNPs (P NH_2 SiNPs) (b) at excitation at 360 nm in toluene.

Interestingly, the difference in synthesis methods did not greatly affect the size and optical properties of the SiNPs. Each group of ITC SiNPs show similar UV-Vis absorption peak and in each case the PL emission showed emission in blue region between 410 and 450 nm under

excitation at 360 nm. This is due to the similar nature of the nanoparticle core and the attached functional group.

4.9.2. Quantum Yield Measurement

The fluorescence quantum yield (QY) of a fluorophore is an important characteristic of molecules which shows the ratio of fluorescence photons emitted to photons absorbed by the sample. Here, the quantum yield is measured by a comparative method described by Williams *et al*.[36] Quinine sulphate was selected as standard because of the similar absorbance range to the SiNPs samples.

Figures 4.32 and 4.33 show the UV-Vis and PL spectra of ITC SiNPs (P Br SiNPs) at five different concentrations, respectively. The integrated intensity is plotted against the absorbance for nanoparticles and the quinine sulphate reference using all spectra where the absorbance (or optical density) at 360 nm is greater than 0.01 and less than 0.1. (Figure 4.34)

The quantum yield is calculated using the gradient shown in Figure 3.34 from the following equation:

$$Q = Q_{Ref}\left(\frac{Grad_{SiNPs}}{Grad_{Ref}}\right)\left(\frac{\eta^2_{Toluene}}{\eta^2_{Ref}}\right) \qquad \textbf{(Equation 4.1)}$$

Where Q_{Ref} is the quantum yield of the standard quinine sulphate and was considered to be 54.6% when dissolved in 0.5M H_2SO_4. $\eta_{Toluene}$ is the refractive index of the solvent = 1.497 and η_{Ref} is the refractive index of the reference = 1.346.

A quantum yield of 12.55% was calculated which is in agreement with the previously reported quantum yields for SiNPs which typically lie between 2% and 25%.[4, 23, 37]

These calculated quantum yields are bright enough for biological applications, however they may vary with different excitation wavelengths.

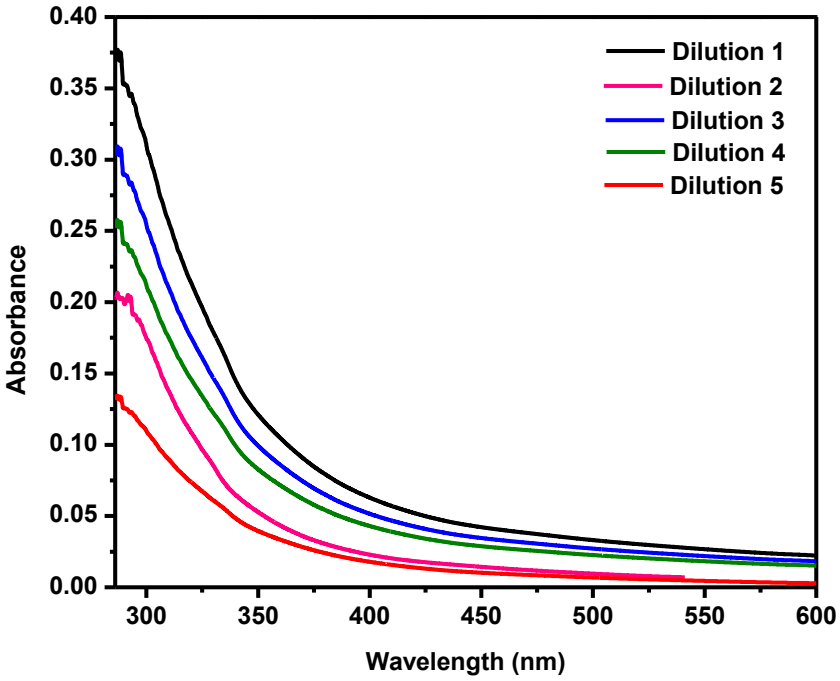

Figure 4.32. UV/Vis spectra at different dilutions of ITC SiNPs (P Br SiNPs) in toluene.

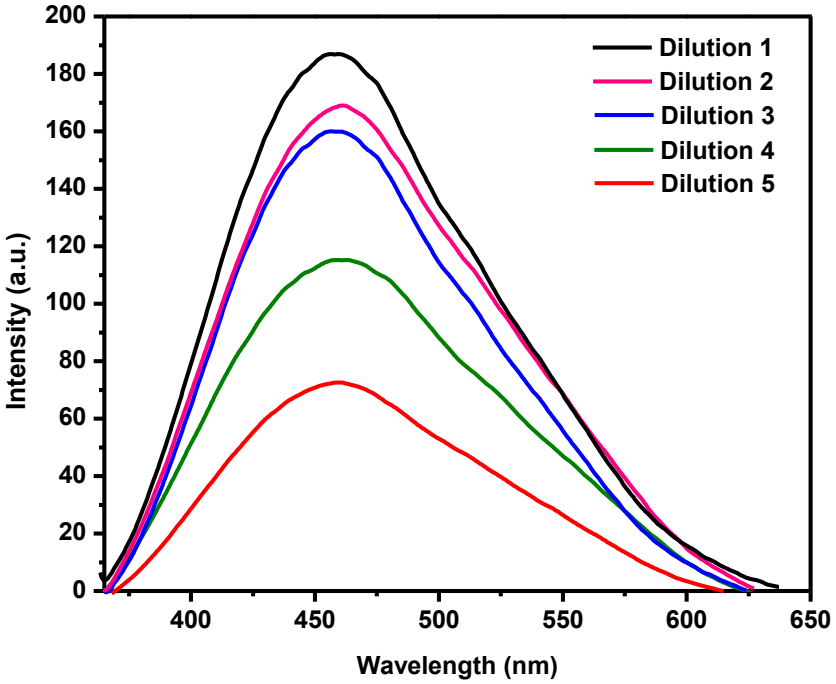

Figure 4.33. Emission spectra of ITC SiNPs (P Br SiNPs) at varying concentration in toluene (Excitation: 360 nm).

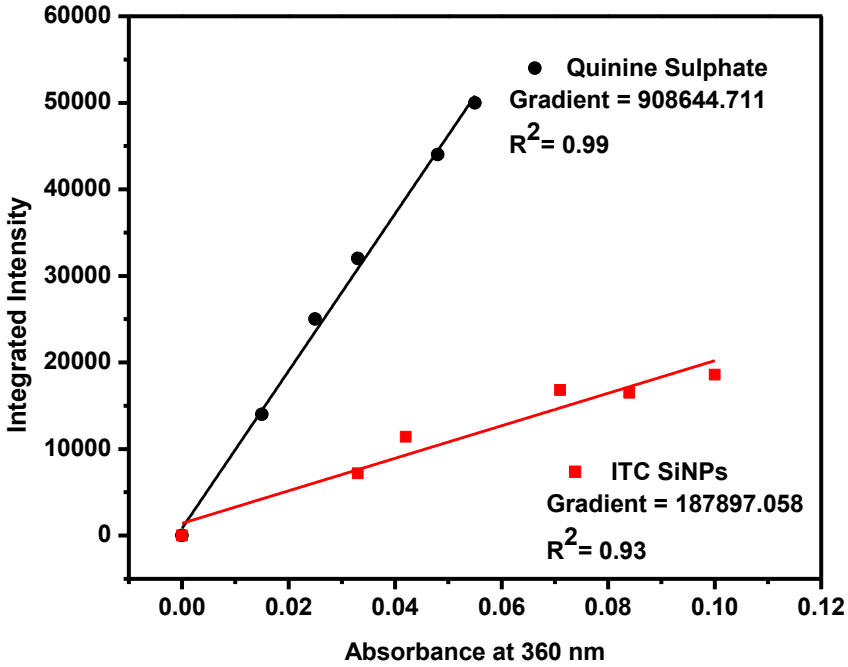

Figure 4.34. Plotted integrated intensity of emission against absorbance for both ITC SiNPs (P Br SiNPs) in toluene and quinine sulphate in 0.1 M H_2SO_4.

Figures 4.35 and 4.36 show the UV-Vis and PL spectra of ITC SiNPs (P NH_2 SiNPs) at five different concentrations, respectively. Following the same procedure the integrated intensity has been plotted against the absorbance for nanoparticles and the reference (Figure 4.37).

Using equation 4.1, the quantum yield of 2.61% was calculated for ITC SiNPs (P NH_2 SiNPs). The reasons for the low quantum yield of ITC SiNPs (P NH_2 SiNPs) could be the presence of more oxide layer on the surface of ITC SiNPs (P NH_2 SiNPs) compared to ITC SiNPs (P Br SiNPs), which can be explained by the formation of lower-energy mid gap states induced by newly formed defects, thus quenching the quantum yield of nanoparticles.[38] This quenching might be a result of differences in the synthesis method of each of type of ITC SiNPs. Therefore, reduction of ITC SiNPs (P NH_2 SiNPs) surface defects, in order to achieve brighter quantum yield, must be addressed.

As a result, for further bioimaging experiments they may not be strong enough to be detected by the microscope and therefore only ITC SiNPs (P Br SiNPs) will be used later to investigate the bioimaging applications of nanoparticles.

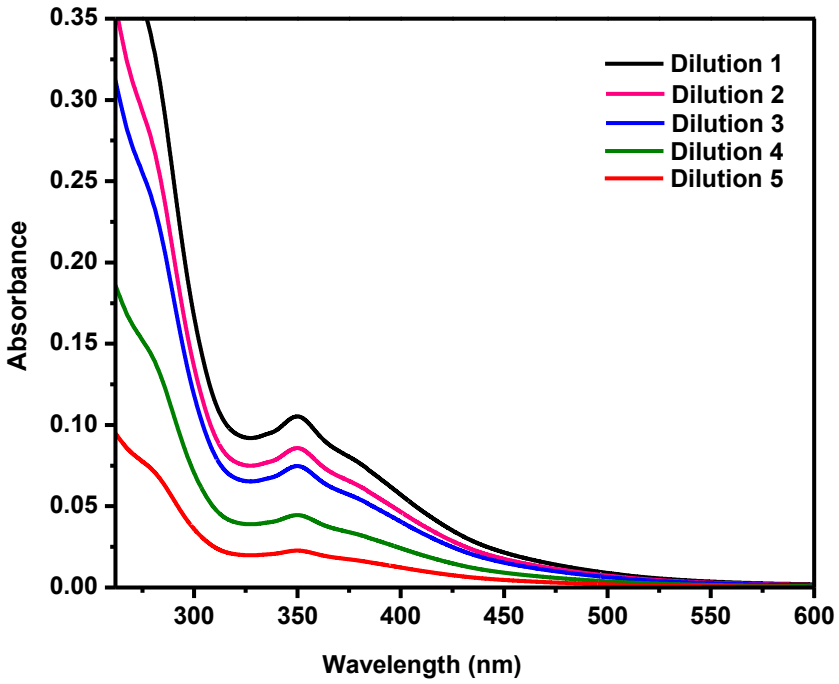

Figure 4.35. UV/Vis spectra at different dilutions of ITC SiNPs (P NH_2 SiNPs) in toluene.

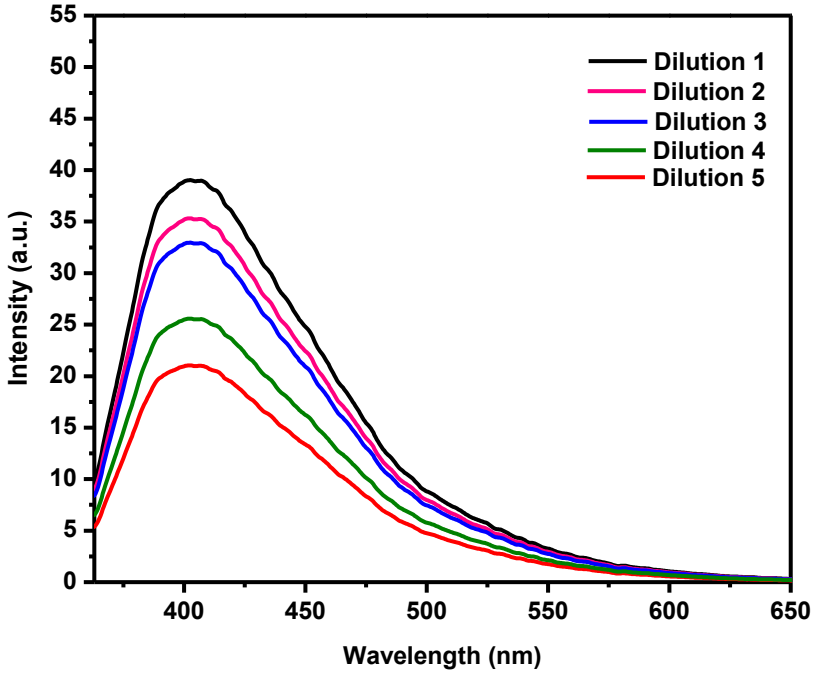

Figure 4.36. Emission spectra of ITC SiNPs (P NH_2 SiNPs) at varying concentration in toluene (Excitation: 360 nm).

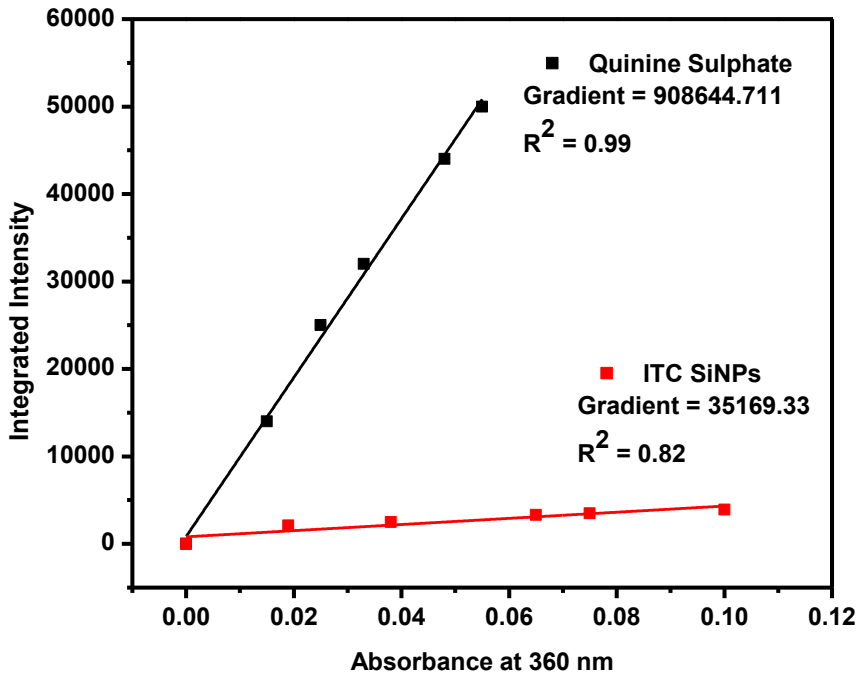

Figure 4.37. Plotted integrated intensity of emission against absorbance for both ITC SiNPs (P NH_2 SiNPs) in toluene and quinine sulphate in 0.1 M H_2SO_4.

4.9.3. Long Term PL Stability

The PL stability of ITC SiNPs was measured over 30 days. This is important due to the lack of PL stability of nanostructured silicon which limits their commercial viability in a wide range of biomedical applications. The photoluminescence intensity of samples was monitored over a month using an excitation wavelength at 360 nm (Figure 4.38). The results show that after 30 days, about 70% of the intensity was maintained which confirms the high stability of the samples.

Similar characteristics were observed for ITC SiNPs (P NH_2 SiNPs) as they were moderately stable over a month. The decrease in PL intensity was negligible over time and the overall intensity was still more than 80% of the initial PL (Figure 4.39).

Even though the monolayers formed on single crystal silicon surfaces are robust to oxidation over long periods it is likely that these monolayers contain some defects over time and therefore the solvent they are dispersed in can penetrate to the underlying silicon atom layers.

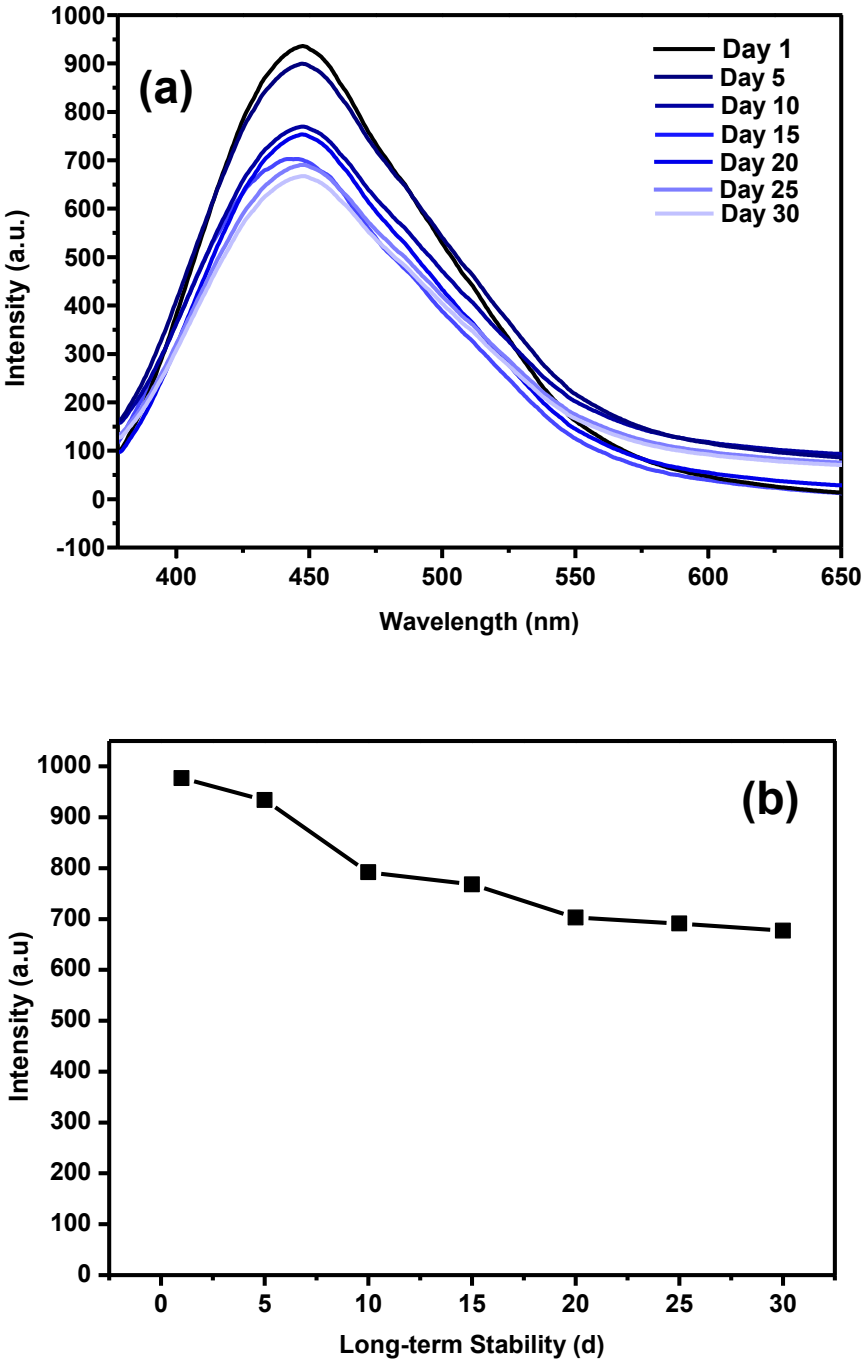

Figure 4.38. Long term PL stability of ITC SiNPs (P Br SiNPs) (a) and PL intensity of ITC SiNPs (P Br SiNPs) over 30 days (b).

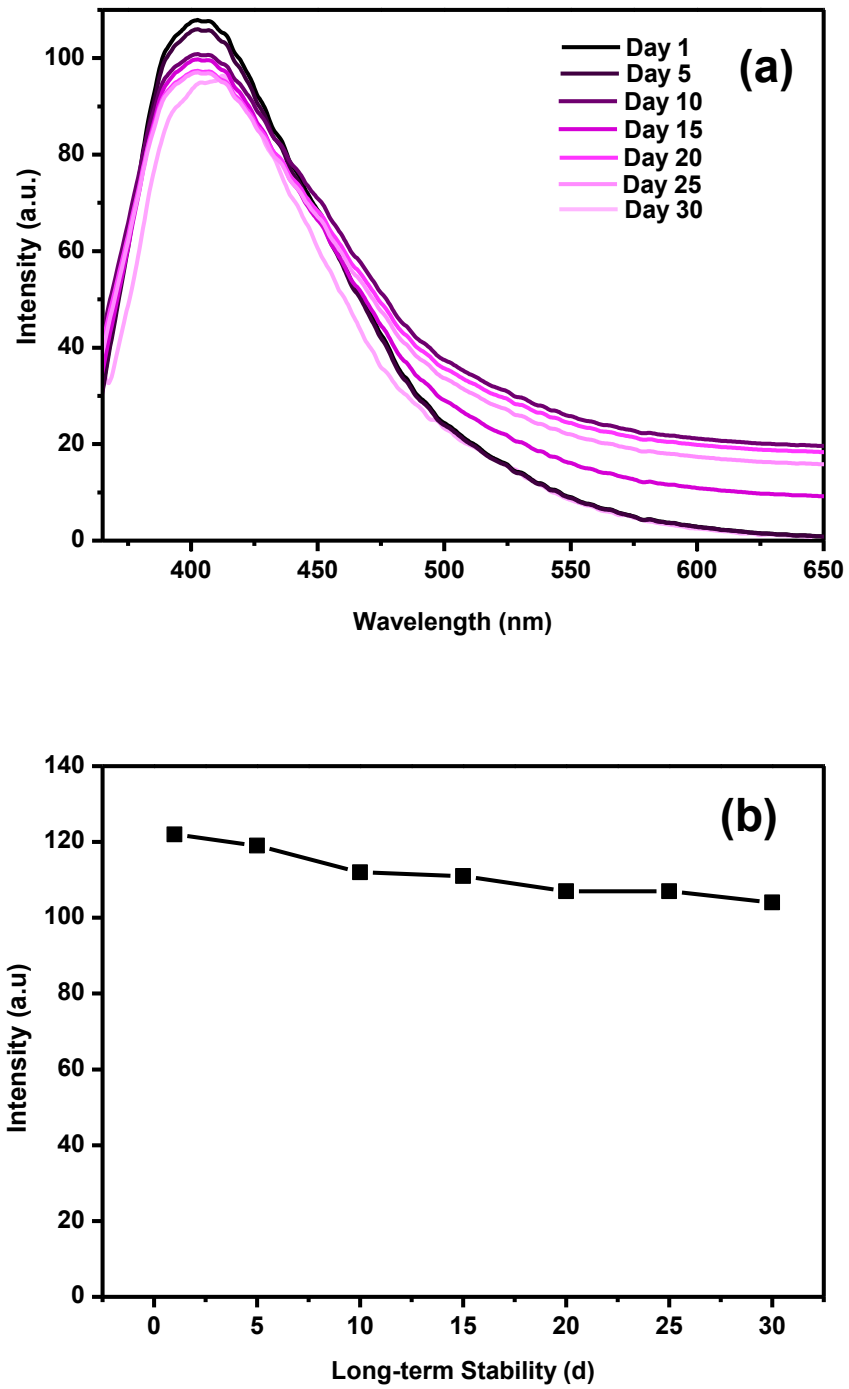

Figure 4.39. Long term PL stability of ITC SiNPs (P NH_2 SiNPs) (a) and PL intensity of ITC SiNPs (P NH_2 SiNPs) over 30 days (b).

4.9.4. Solvent Effect on Optical Properties of Silicon Nanoparticles

Four groups of ITC SiNPs suspensions were prepared to explore the influence of solvent polarity on the emission of nanoparticles. Hexane, toluene, dichloromethane and chloroform were selected as four solvents representative of a wide range of polarity indexes.

The experimental results demonstrate that solvent polarity has a large effect on the light – emitting properties of ITC SiNPs. A positive correlation was identified between the solvent polarity of both types of ITC SiNPs and the redshift of the PL peak (Figure 4.40). A possible mechanism for this phenomenon is suggested through consideration of SiNPs and the neighbouring solvent as a composite.[35] To begin with, the dipole moment of organic molecules in the excited state is normally different from that in ground state. When the molecules of the solvent rapidly absorb photons, electrons in the solvent will redistribute and thus alter the dipole moment.[39] When the sample is excited, the solvent undergoes a relaxation with a minimum free energy for the relaxed state. The higher the polarity of the solvent, the lower the energy of the relaxed state providing the larger red shift in the emission spectrum of the solvent.[35] The same mechanism applies in the case of the composition of nanoparticles and dispersing solvent. The energies of the excited state will decrease under illumination due to the influence of the polarity of the solvent. Therefore, the PL spectrum will show a red shift.

In this experiment, chloroform had the highest polarity index and showed the largest red shift for ITC SiNPs (both types). This is explained by the effect of the nanoparticle/solvent composite’s electronic state.

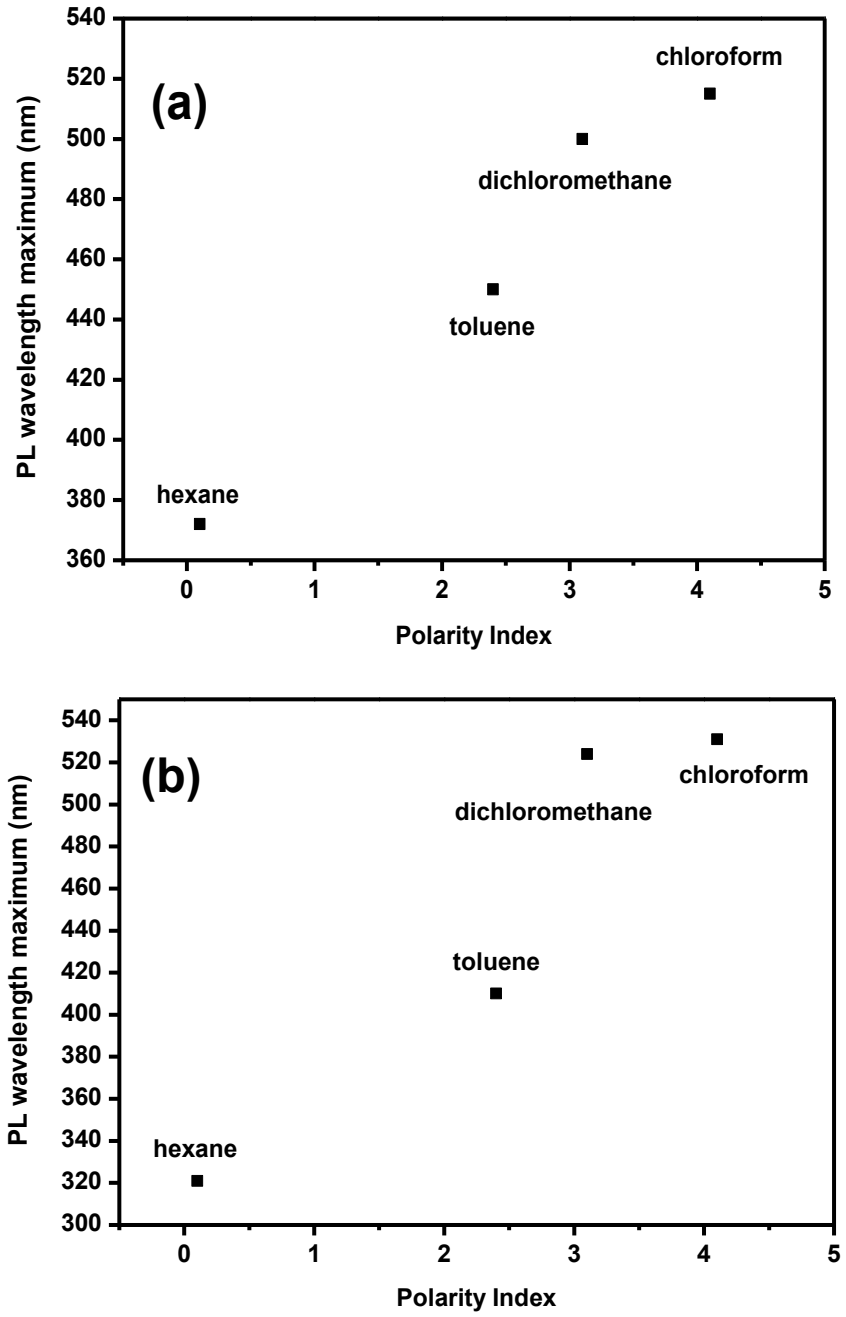

Figure 4.40. Effect of solvent polarity on PL stability of ITC SiNPs (P Br SiNPs) (a) and ITC SiNPs (P NH_2 SiNPs) (b).

4.10. TGA Analysis and Estimation of the Ligand on the Surface

TGA measurements were used to estimate the quantity of ligands on the surface of SiNPs. This is essential for biomedical applications as this amount needs to be known to compare the behaviour of these nanoparticles with an equivalent known control (drug).

As seen in the data, it was observed that the weight on the TGA trace starts to decrease due to the heat flow into the sample (Figure 4.41). This happened relatively rapidly which suggests the degradation of the capping ligand. The completion of the initial degradation happened at about 210 ^{o}C. Above 320 ^{o}C, the heat flow into the sample increases again and the weight continued to decrease in the TGA trace. A higher rate of weight loss was observed for this second stage of degradation as depicted by the derivative. The completion of the second degradation was observed at about 350 ^{o}C as there was only a small decrease in the weight.

The TGA measurement was performed after heating in an inert atmosphere, and the overall percentage weight loss from the initial temperature to 1000 ^{o}C was 64%. This reduction could have several causes such as the evaporation of the functionalised SiNPs or the degradation of the functional ligand.[14, 40] In this experiment, considering that the silicon core maintains stability even at higher temperatures,[41] the weight loss is better explained through the second process. Two derivative peaks were observed which could be attributed to the removal of bound functional groups (ITCs) from the silicon first and then decomposition of the Si-C from the nanoparticle surface. Thus, the estimation of the weight attributed to the ligand is approximately 60% of the total nanoparticle weight, with the remaining 40% the silicon core.

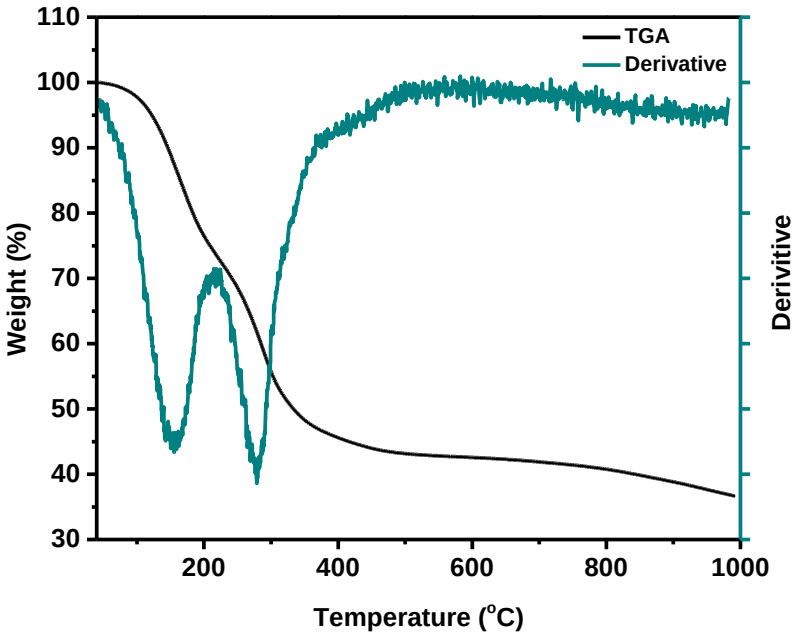

Figure 4.41. TGA and derivative of ITC SiNPs (P Br SiNPs).

Similar behaviour was observed for ITC SiNPs (P NH_2 SiNPs) after an identical TGA analysis. It is henceforth considered that this ligand weight estimate holds for both types of ITC SiNPs. Therefore, for the following biological assay 60% of each batch was taken to be ITC ligand.

4.11. *In Vitro* Biomedical Studies

4.11.1. Cytotoxicity Assays by MTT

The physiochemical properties of SiNPs determine the degree of toxicity in biological environments. In order to evaluate the cytotoxicity of the synthesised SiNPs, an MTT assay was performed to determine the loss of cell viability. Caco-2 and CCD-841 cells were seeded on a 96-well plate and incubated at 37 ^{o}C for 24 h. Next, the cells were treated with various concentrations of ITC SiNPs from 5 to 70 µg/mL for a period of 24 and 48 h. After this time the media was removed and cells were washed by PBS and the MTT protocol was performed as previously described in Chapter 2 (Section 2.4.2). The absorbance was recorded on a microplate reader at the wavelength of 570 nm and the percentage of the viable cells was calculated by comparison against untreated control cells. All experiments were repeated on three different occasions. In order to have a better understanding of the effect of nanoparticles on cells, two different graphs are provided for each experiment to make the comparison more straightforward. This is since the concentration needed to compare the nanoparticle effect, with the drug as control, needs to be shown as µM (group (a) in each graph). When NH_2 SiNPs is used as the control, on the other hand, the unit for nanoparticles is µg/mL (group (b) in each graph). As 60% of ITC nanoparticles is considered consists of the ligand, the following concentrations were used for the MTT assays:

Table 4.8. Concentrations of nanoparticles and AITC in MTT experiments.

µg/mL (ITC SiNPs)	5	10	15	20	30	50	70
60% of the weight (ligand)	3	6	9	12	18	30	38
µM (AITC)	30	60	90	120	181	302	380

NH_2 SiNPs have shown previously to act as a non-toxic material[42] and therefore are used here to evaluate the therapeutic properties of ITC SiNPs with another material at nanoscale.

Figure 4.42 (a), shows the cytotoxicity of ITC SiNPs in Caco-2 cells compared to the original drug, allyl isothiocyanate (AITC). As indicated, the change in cell viability was not statistically significant up to 120 µM, where nanoparticles started to decrease the viability to approximately 70%. At 181 µM, there was a large difference in terms of the effectiveness of nanoparticles compared to the drug as control which reduced the viability of cells to 40%. The highest concentration at 380 µM ITC SiNPs (P Br SiNPs) had a cytotoxic effect of approximately 58% viability after 24 h, while ITC SiNPs (P NH_2 SiNPs) showed a very similar effect to the AITC drug with the remaining cell viability of less than 40%.

Figure 4.42 (b) shows the results from the same experiment when compared to NH_2 SiNPs as non-toxic nanomaterials. For the highest concentration at 70 µg/mL, NH_2 SiNPs did not have any effect on cell viability with almost 90% of cells still alive in contrast with both groups of ITC SiNPs.

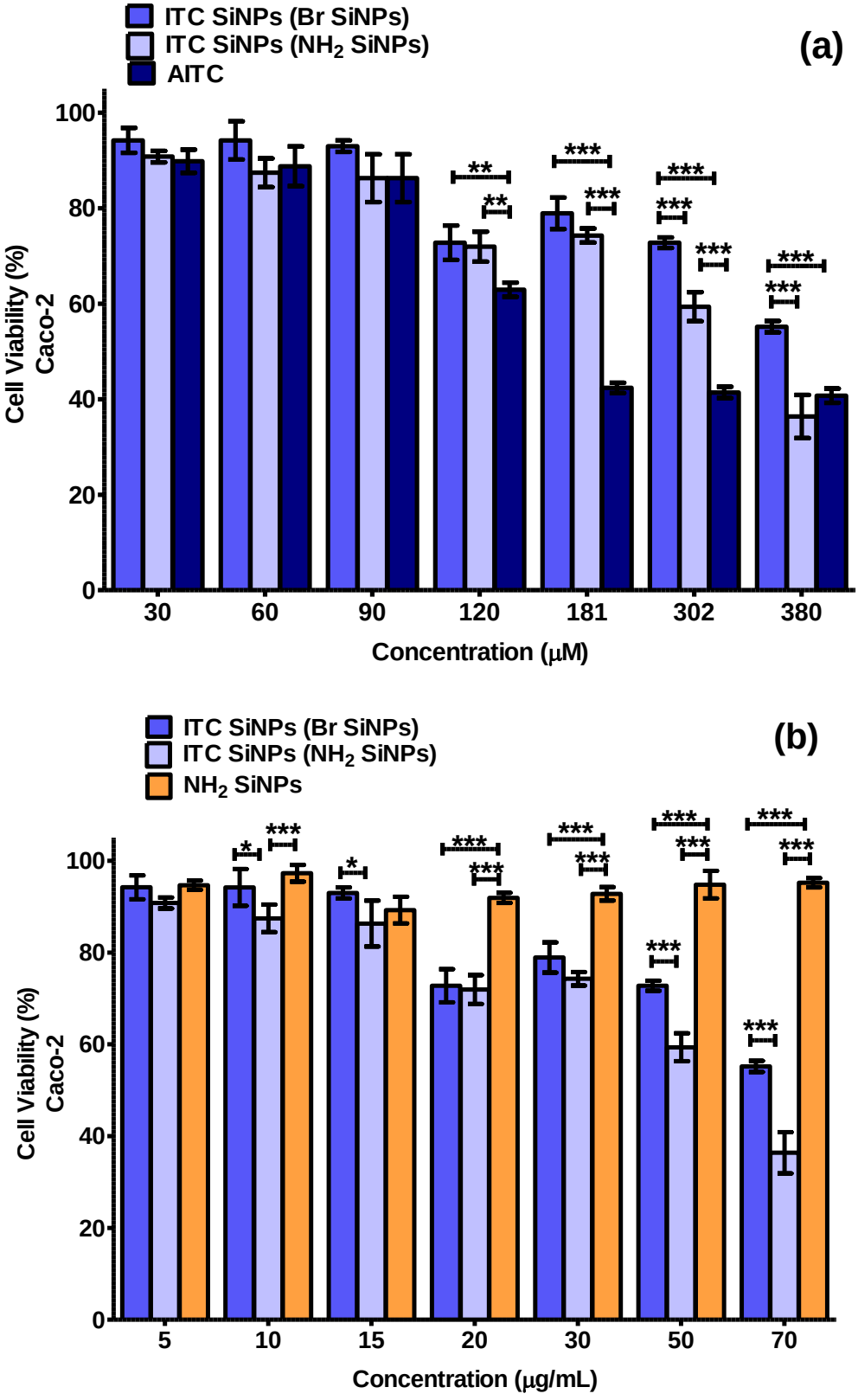

Figure 4.42. *In vitro* cytotoxicity of ITC SiNPs (P Br SiNPs) and ITC SiNPs (P NH_2 SiNPs) by MTT after incubation with **Caco-2** at **24 h** compared to AITC as control (a) and NH_2 SiNPs (b) as control. Statistical significance was determined by two-way-ANOVA followed by a Bonferroni post-test (***P < 0.001, **P < 0.01 and *P < 0.05). Results are expressed as mean ± SEM (n =3).

For longer incubation time points, such as after 48 h, (Figures 4.43 (a) and (b)) SiNPs did not show any statistically significant effect on cell viability at low concentrations, whereas the AITC reduced the cell viability from when they were first introduced to almost 70% for this low concentration. This might be attributed to the errors in the estimation of the ligand on the surface which may not be exactly equal to the amount of the AITC used as control for low concentrations, as this is a rough estimation for this measurement. However, at 181 μM, nanoparticles and AITC reduced the cell viability to less than 40%, and continued to become more cytotoxic at the highest concentration 380 μM which showed only about 20% cell viability. It should be noted for most concentrations, ITC SiNPs (P NH_2 SiNPs) seemed to be more cytotoxic than ITC SiNPs (P Br SiNPs), and presented closer behaviour to AITC as control.

In Figure 4.43 (b) it is observed that statistically significant differences between NH_2 SiNPs and ITC SiNPs occur for all concentrations for this 48 h incubation time, the magnitude of which becomes very large for the highest concentrations. ITC SiNPs, based on these results, are more effective in terms of their increased cytotoxicity for all concentrations. This is attributed to the capping functional ligand, as a similar effect was not observed for NH_2 SiNPs, with approximately 70% cell viability for the highest concentration after 48 h incubation.

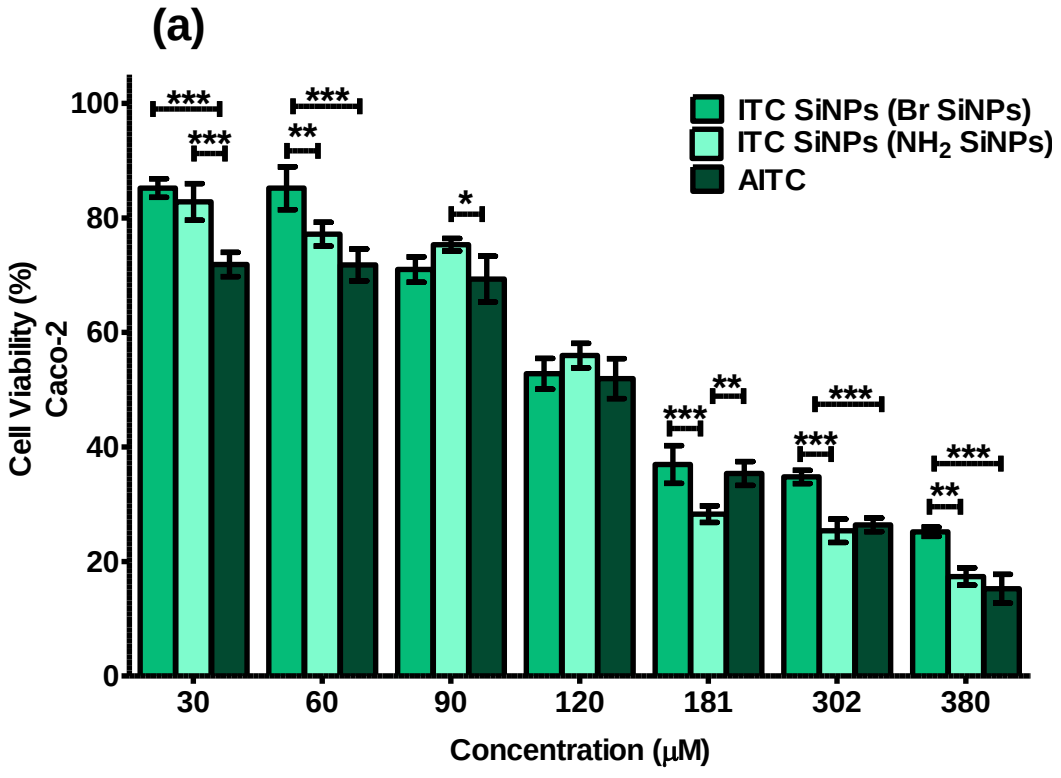

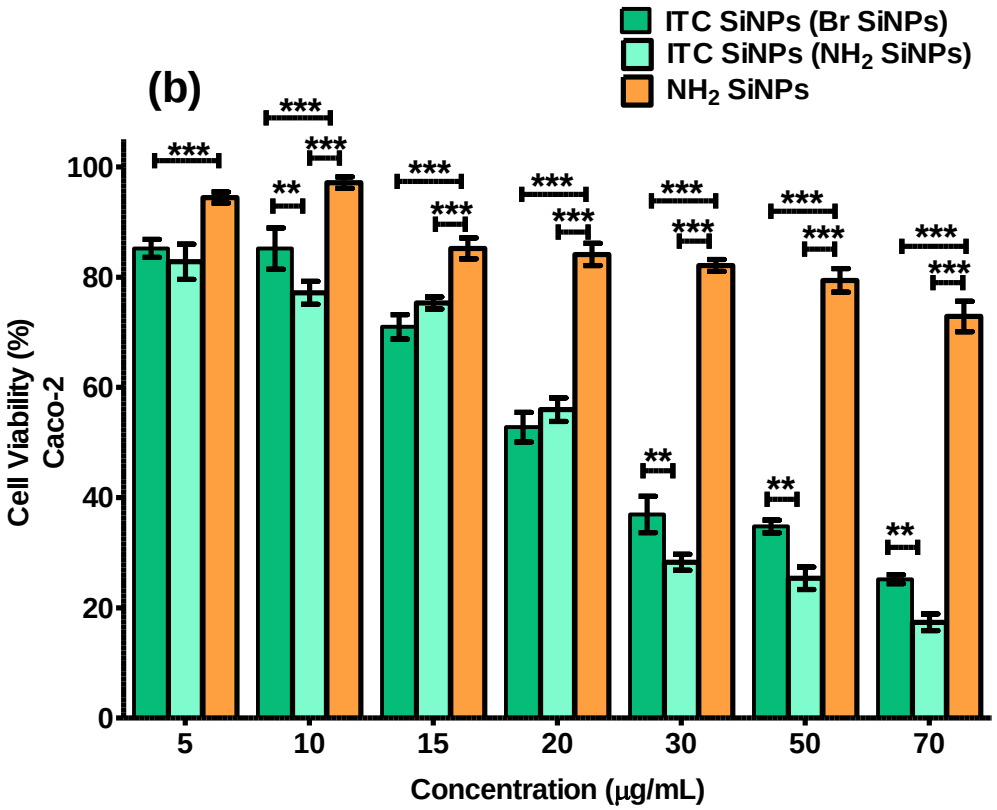

Figure 4.43. *In vitro* cytotoxicity of ITC SiNPs (P Br SiNPs) and ITC SiNPs (P NH_2 SiNPs) by MTT after incubation with **Caco-2** at **48 h** compared to AITC as control (a) and NH_2 SiNPs (b) as control. Statistical significance was determined by two-way-ANOVA followed by a Bonferroni post-test (***P < 0.001, **P < 0.01 and *P < 0.05). Results are expressed as mean ± SEM (n =3).

Figure 4.44 shows the overall comparison between two different time points for ITC SiNPs (P Br SiNPs) (a) and in ITC SiNPs (P NH_2 SiNPs) (b). It is clear that both types of nanoparticles need longer time periods, such as 48 h, to be effective. In addition, even though both nanoparticles seem to follow similar trends, the ITC SiNPs (P NH_2 SiNPs) appear to be slightly more cytotoxic, which could be related to the difference in the synthesis methods leading to a change in the purity level for each type of SiNPs. Moreover, the exact amount of the ITC on the surface of each type of SiNPs could be slightly different which would be due to the limitations related to the top down synthesis method. This would in turn make the active sites on the surface of H-terminated SiNPs inconsistent and therefore batch dependant.

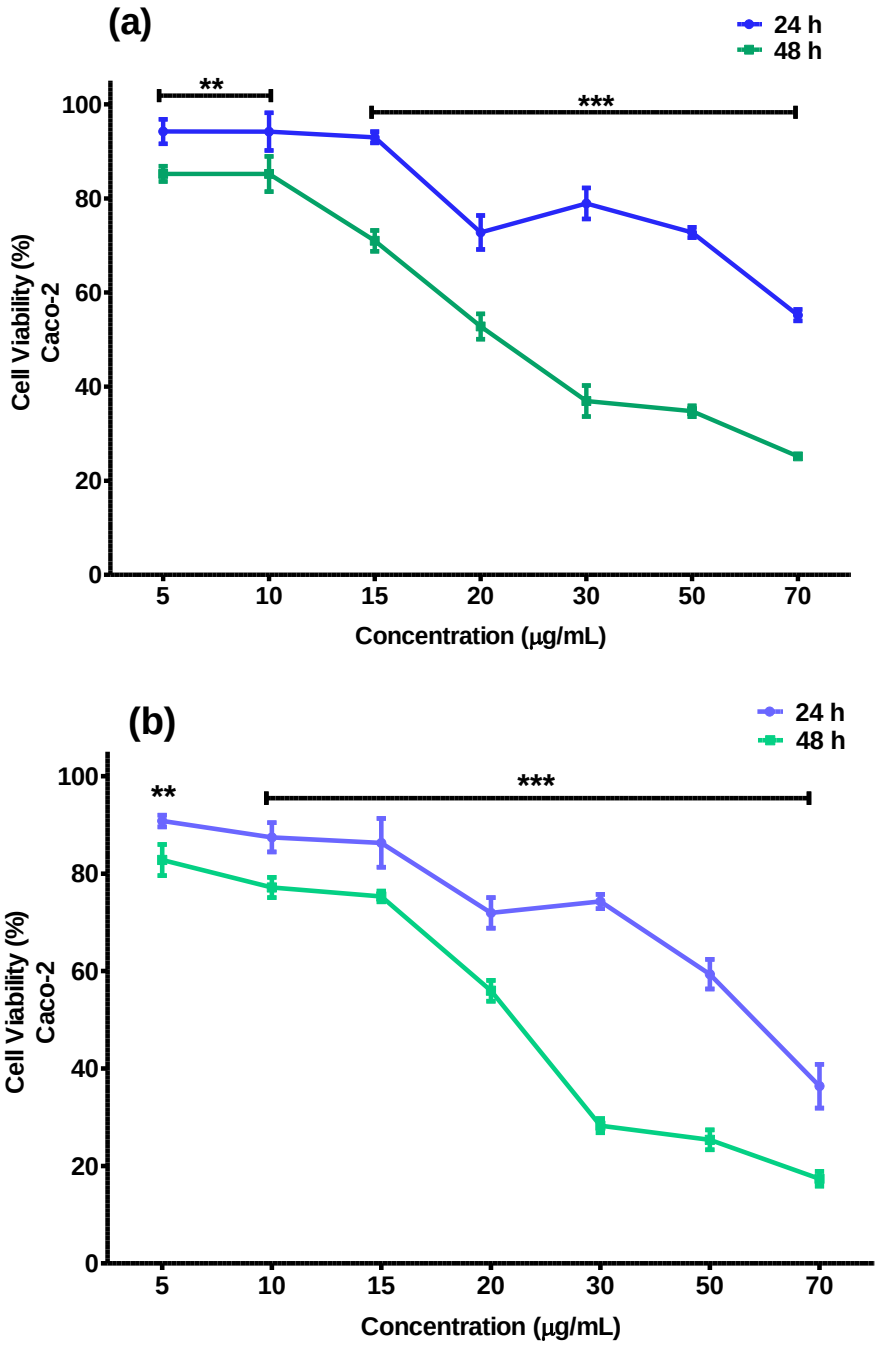

Figure 4.44. MTT of ITC SiNPs (P Br SiNPs) at 24 and 48 h (a) and ITC SiNPs (P NH_2 SiNPs) at 24 and 48 h (b) after incubation with **Caco-2** cells. Statistical significance was determined by two-way-ANOVA followed by a Bonferroni post-test (***P < 0.001 and **P < 0.01). Results are expressed as mean ± SEM (n =3).

Figure 4.45 (a) shows the MTT results in CCD-841 cells after 24 hours incubation with the SiNPs and AITC. It was concluded that ITC SiNPs (P NH_2 SiNPs) reduced the toxicity to 80% for the lowest concentration of nanoparticle which was very similar to the effect of AITC. On the other hand, ITC SiNPs (P Br SiNPs) started to show this effect for slightly higher

concentrations at 90 µM. For the 120 to 380 µM concentrations, the cell viability for both types of nanoparticles and the drug was moderately stable at around 60%. Finally, the highest dose of ITC SiNPs (P NH_2 SiNPs) were the most cytotoxic, decreasing cell viability by nearly 60%, while ITC SiNPs (P Br SiNPs) and AITC caused ~40 % loss of cell viability.

In Figure 4.45 (b), the actual effect of ITC SiNPs becomes clearer by comparing their effect with that of NH_2 SiNPs at 20 µg/mL concentration. At this level, they both reduced the cell viability to almost 60% vs 90% of the control cell viability respectively, which was independent of the concentration level above 20 µg/mL.

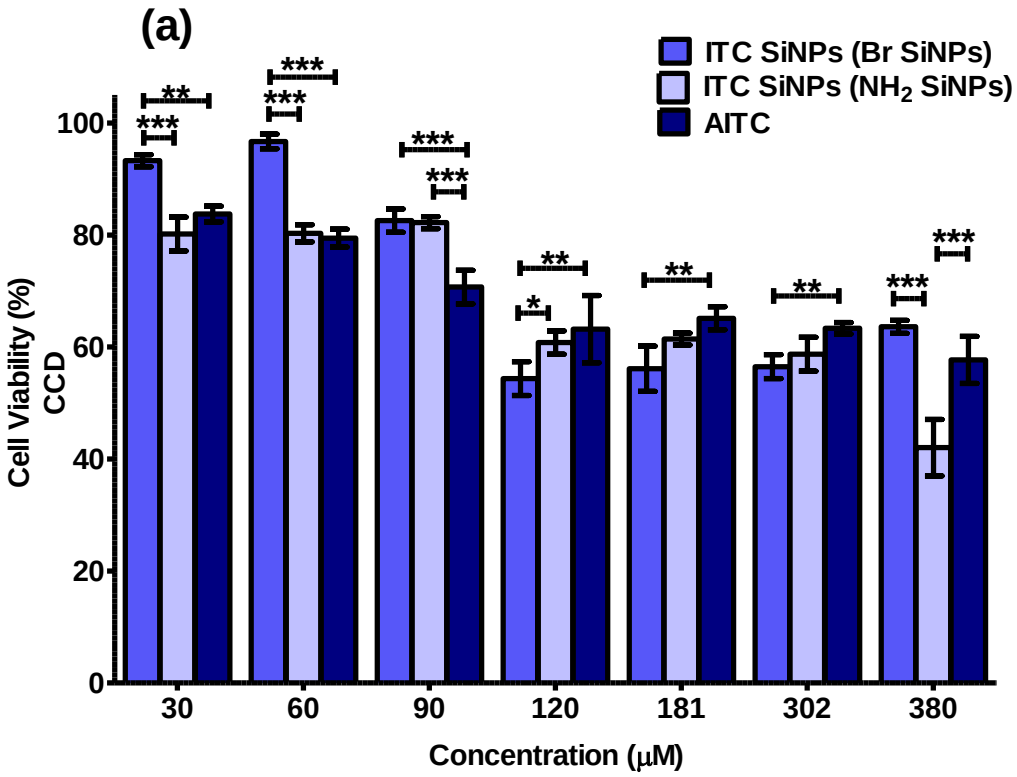

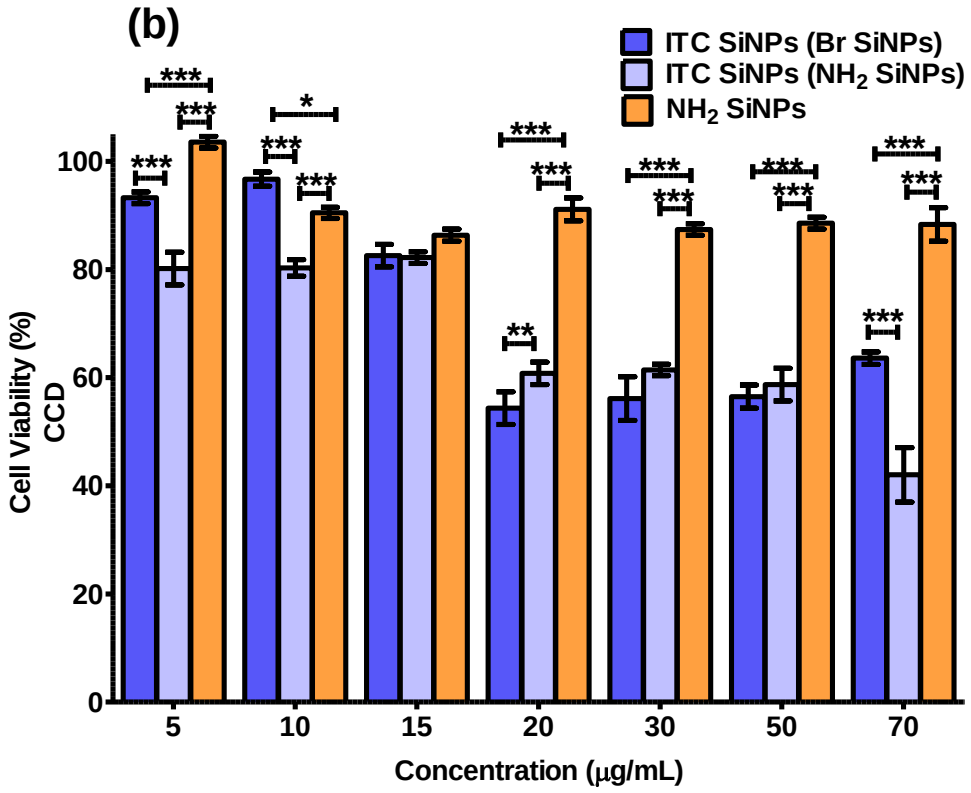

Figure 4.45. *In vitro* cytotoxicity of ITC SiNPs (P Br SiNPs) and ITC SiNPs (P NH_2 SiNPs) by MTT after incubation with **CCD-841** at **24 h** compared to AITC as control (a) and NH_2 SiNPs (b) as control. Statistical significance was determined by two-way-ANOVA followed by a Bonferroni post-test (***P < 0.001, **P < 0.01 and *P < 0.05). Results are expressed as mean ± SEM (n =3).

After 48 hours incubation in CCD-481 cells, the overall cytotoxicity of both types of ITC SiNPs was stronger specifically at concentrations above 120 µM. A minimum level of cell viability of approximately 20 and 18% (Figure 4.46 (a)) was observed for ITC SiNPs (P Br SiNPs) and ITC SiNPs (P NH_2 SiNPs) at 380 µM respectively. These cell viabilities were slightly higher than that of AITC (~ 13 %) and much lower than that of NH_2 SiNPs (~ 75%) for the equivalent concentration at 70 µg/mL (Figure 4.46 (b)).

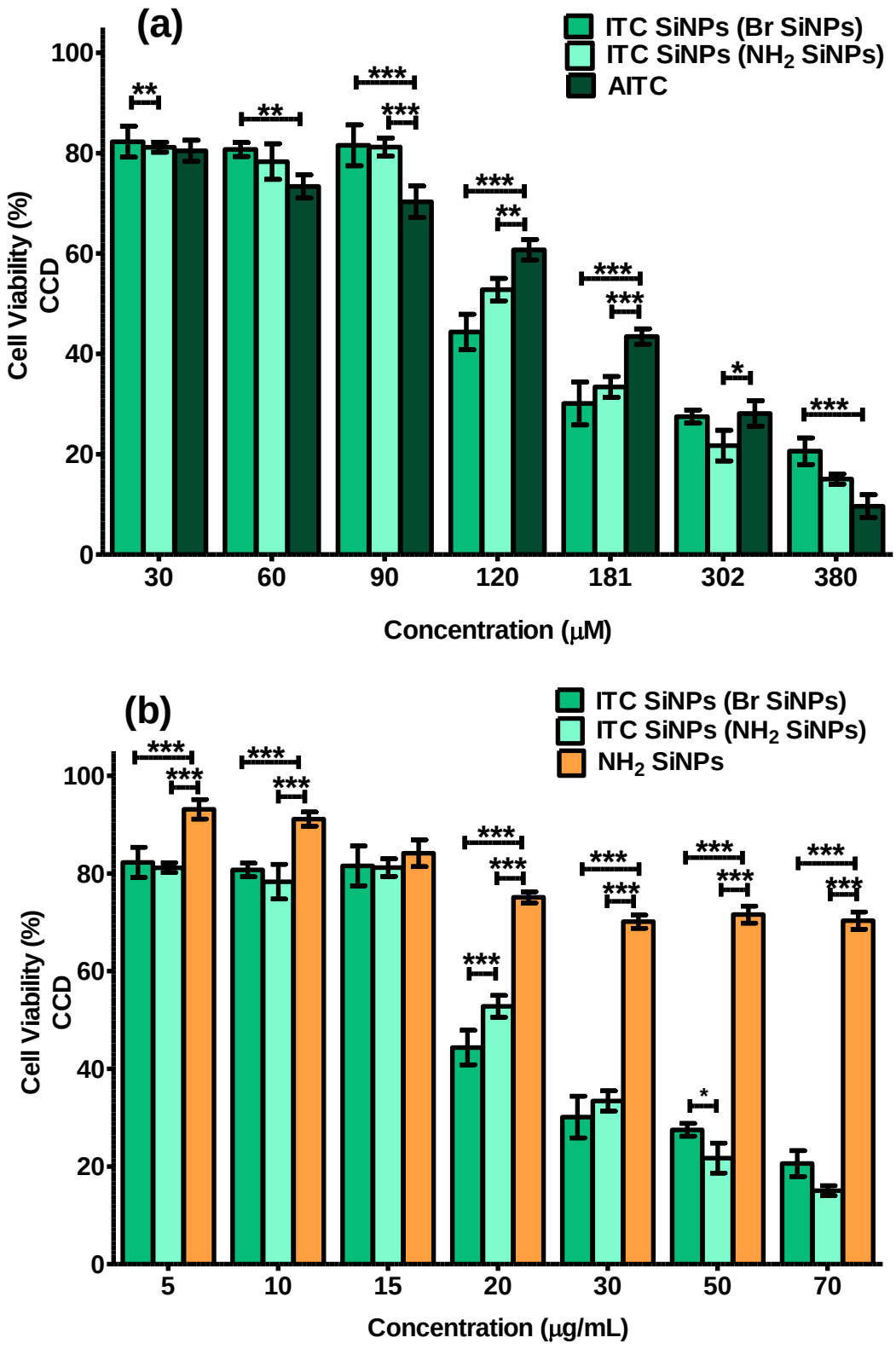

Figure 4.46. *In vitro* cytotoxicity of ITC SiNPs (P Br SiNPs) and ITC SiNPs (P NH_2 SiNPs) by MTT after incubation with **CCD-841** at **48 h** compared to AITC as control (a) and NH_2 SiNPs (b) as control. Statistical significance was determined by two-way-ANOVA followed by a Bonferroni post-test (***P < 0.001, **P < 0.01 and *P < 0.05). Results are expressed as mean ± SEM (n =3).

Figures 4.47 shows a comparison of the behaviour of ITC SiNPs (P Br SiNPs) (a) and that of ITC SiNPs (P NH_2 SiNPs) (b), at both time points (24 an 48 h) in CCD-841 cells. It is concluded that the fourth concentration used in the treatment of the CCD-841 cells (20 µg/mL) was of significance, since at this amount and above it, the cell viability changed dramatically for both types of ITC SiNPs. Overall, ITC SiNPs (P NH_2 SiNPs) were more cytotoxic in CCD-841 cells than Caco-2.

It should be noted that the cytotoxic effect of ITC SiNPs on CCD-841 cells is very dependent on the cell line sensitivity which leads to lower cell viability when exposed to any sort of foreign material.[43, 44] Thus, in order to have an appropriate comparison to the results obtained by the MTT assay, it is important to evaluate the behavioural differences between the ITC SiNPs and the controls of AITC and NH_2 SiNPs within the same cell line.

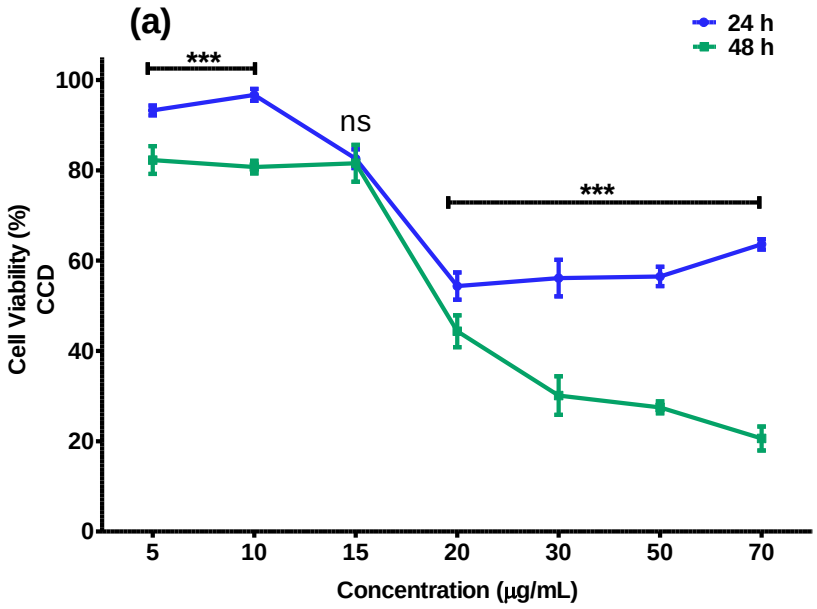

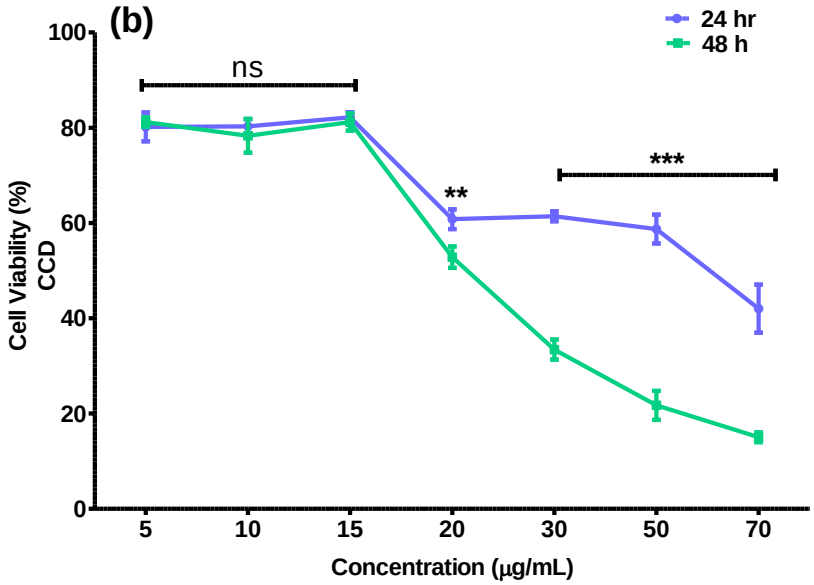

Figure 4.47. MTT of of ITC SiNPs (P Br SiNPs) at 24 and 48 h (a) and ITC SiNPs (P NH_2 SiNPs) at 24 and 24 h (b) after incubation with **CCD-841** cells. Statistical significance was determined by two-way-ANOVA followed by a Bonferroni post-test (***P < 0.001, **P < 0.01 and ns not statistically significant). Results are expressed as mean ± SEM (n =3).

In conclusion, ITC SiNPs (P NH_2 SiNPs) where slightly more cytotoxic than ITC SiNPs (P Br SiNPs) in MTT experiments. This might be due to the better surface coverage of SiNPs by the ITC ligand. However, the possibility of impurities originating from the synthesis method, leading to more cytotoxic effects, should be taken into the consideration in future work. In general, since the difference in the behaviour of these two types of SiNPs was negligible, for the further uptake studies only ITC SiNPs (P Br SiNPs) were selected. This choice was based on the better optical properties of these nanoparticles and their higher quantum yield. The low quantum yield of ITC SiNPs (P NH_2 SiNPs), on the other hand, would be a significant impediment for uptake studies, specifically imaging and flow cytometry. More specifically, for these latter two assays, the fluorescence of nanoparticles is more important than the cytotoxicity for therapeutic applications.

4.11.2. Cellular Uptake Studies

The ability of SiNPs to become internalised by cells is dependent on several factors, including the type of NP, the type of cell line and uptake mechanism.[45, 46] In order to understand and evaluate the behaviour of the ITC SiNPs at the cellular level, the cellular internalisation

and the intracellular distribution of both the nanoparticles were evaluated by flow cytometry and confocal imaging.

4.11.2.1. Confocal Microscopy

In this experiment, colon cancer cells (Caco-2) were incubated with a concentration of 50 μg/mL of ITC SiNPs (P Br SiNPs) for 6 and 12 h at 37 ºC.

Figures 4.48 to 4.49 show the confocal images of control Caco-2 cells without any nanoparticle treatment, followed by Figures 4.50 to 4.53 showing cells after the nanoparticle treatments. The cells were stained with Phalloidin for actin staining. It was clearly observed that SiNPs (green) were localised in the cells.

The internalisation was obviously time dependant as more ITC SiNPs were detected after 12 h incubation (Figures 4.52 and 4.53) compared to the samples after 6 h treatment (Figures 4.50 and 4.51).

For further evidence, Z-stack imaging was performed to examine the spread of ITC SiNPs within the cells. The images were collected at 0.37 μm intervals. As can be seen in Figure 4.54, SiNPs were evenly distributed within the cytoplasm rather than only being attached to the external surface of the cells.

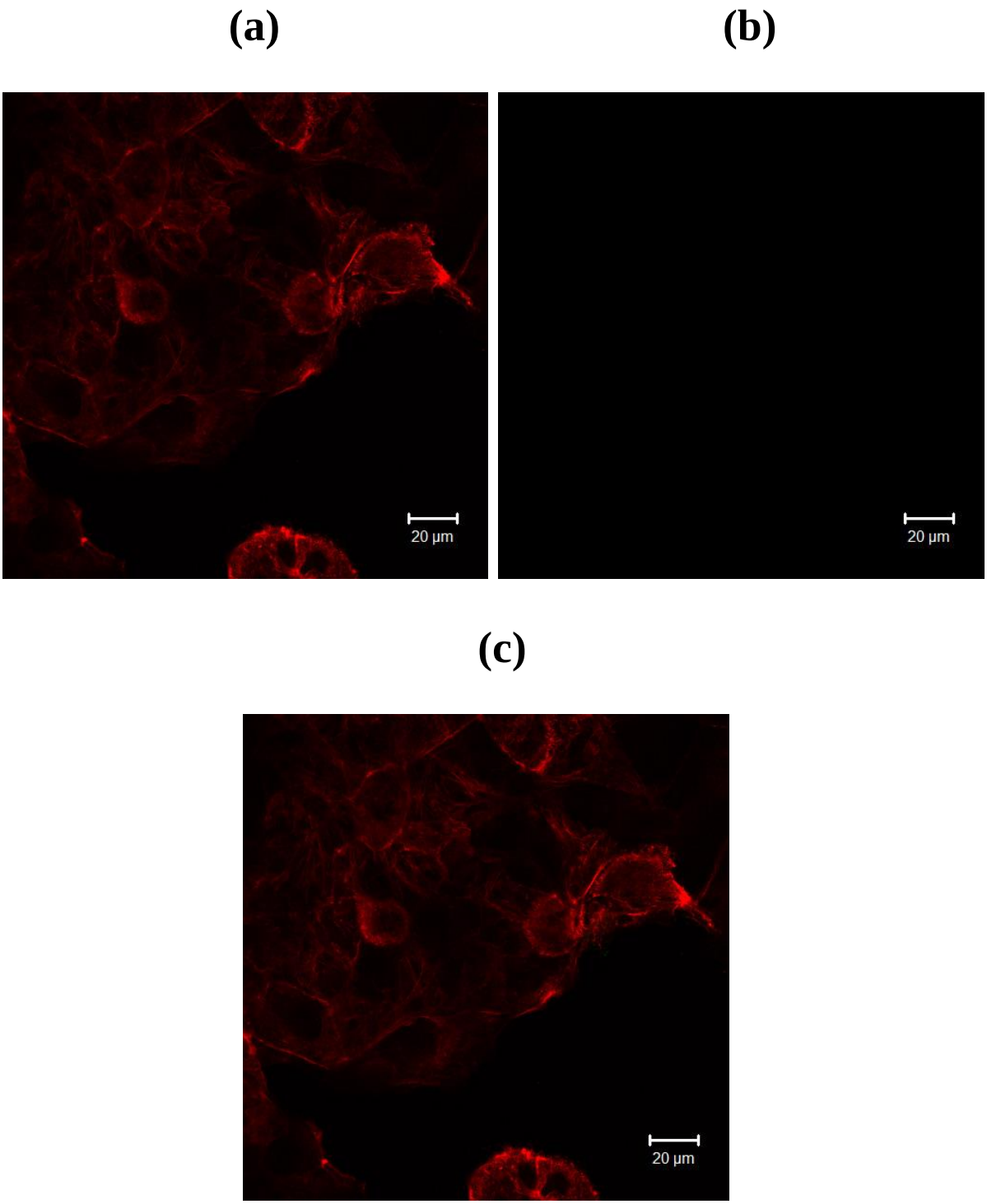

Figure 4.48. Confocal fluorescence images of control (untreated) Caco-2 cells. Red channel (a), green channel (b), merged (c). Red from Phalloidin for actin staining.

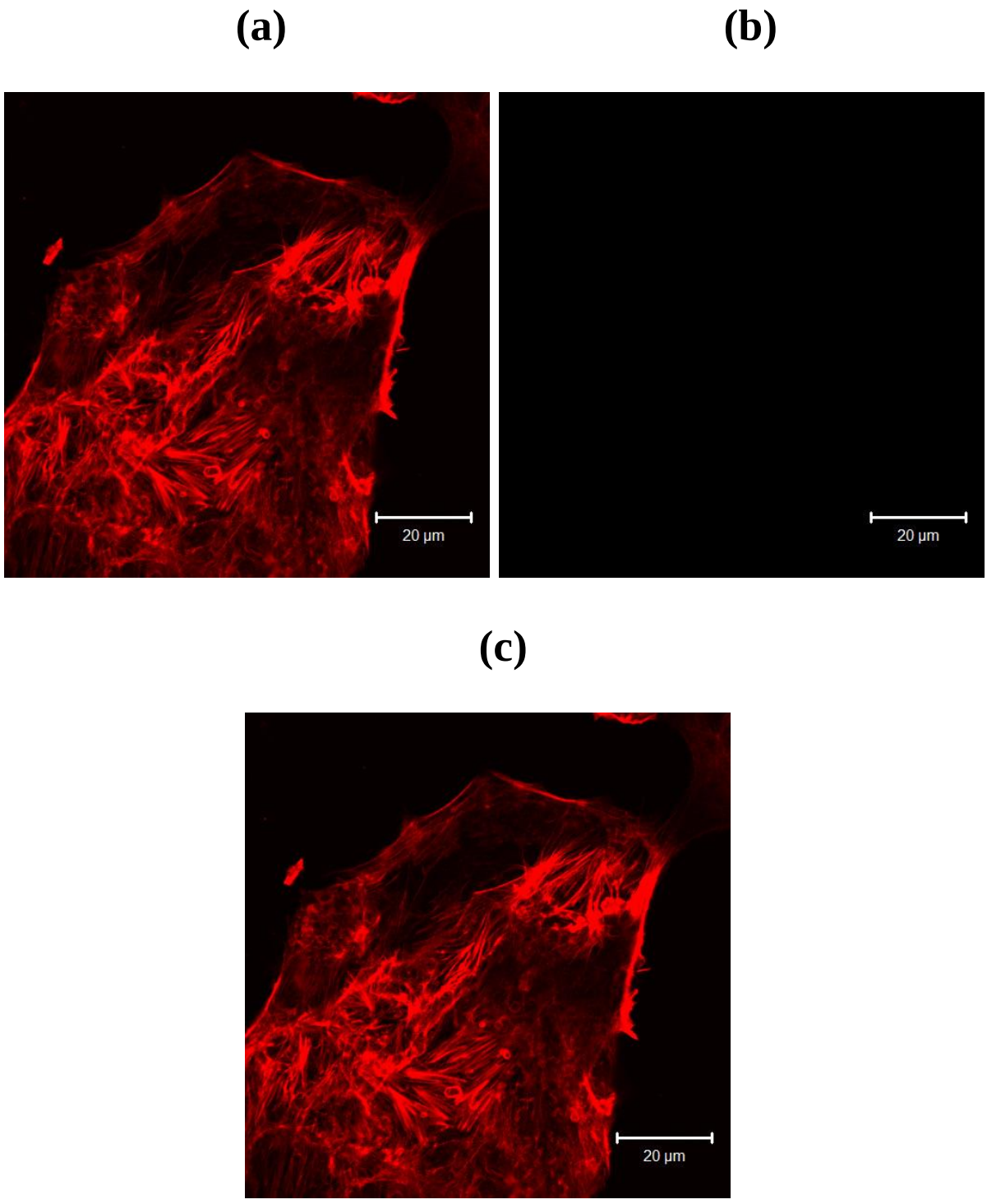

Figure 4.49. Confocal fluorescence images of control (untreated) Caco-2 cells. Red channel (a), green channel (b), merged (c). Red from Phalloidin for actin staining.

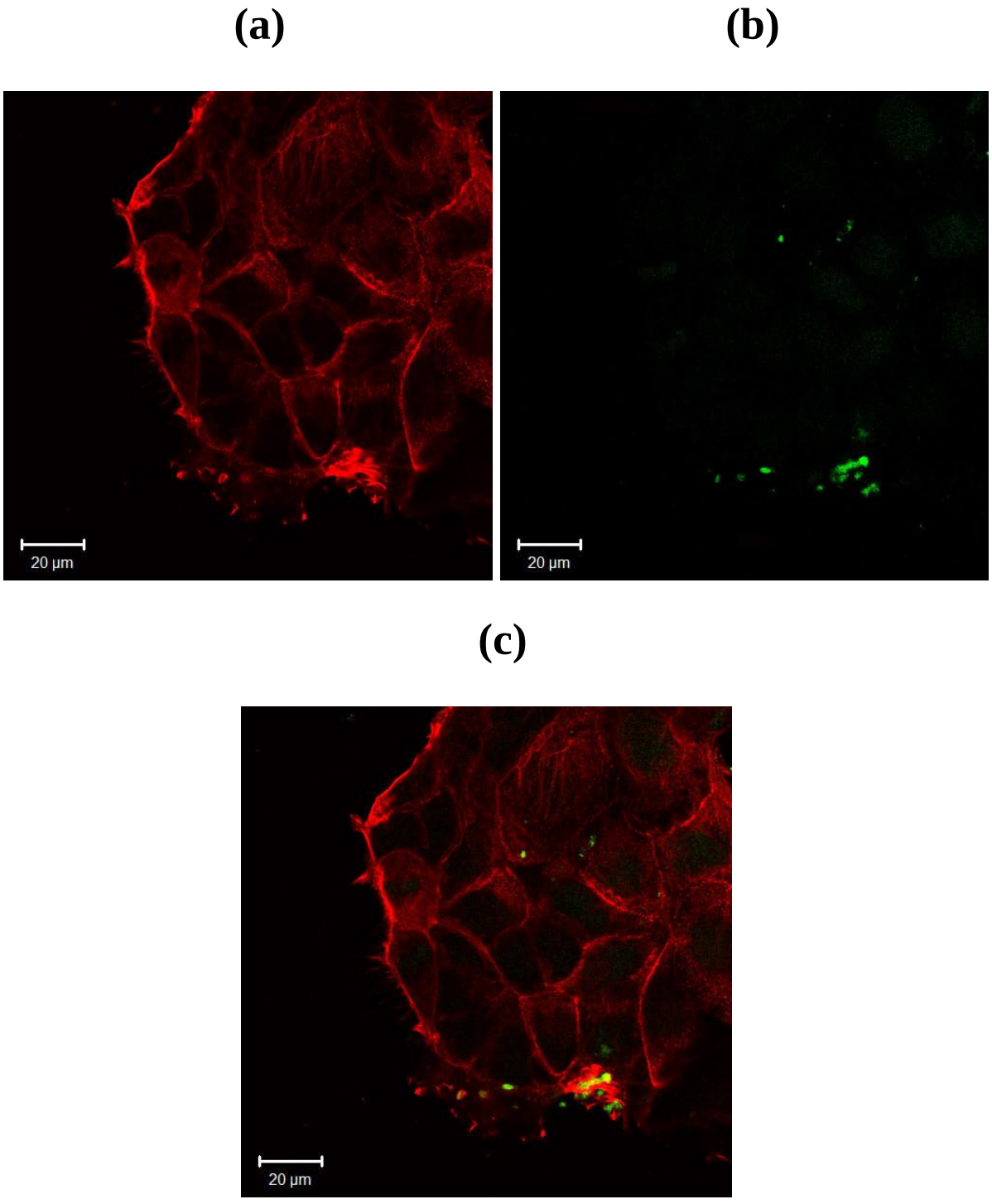

Figure 4.50. Confocal fluorescence images of Caco-2 cells incubated with ITC SiNPs (P Br SiNPs) for 6 h incubation. Red channel (a), green channel (b), merged (c). Red from Phalloidin for actin staining and green fluorescence from nanoparticles.

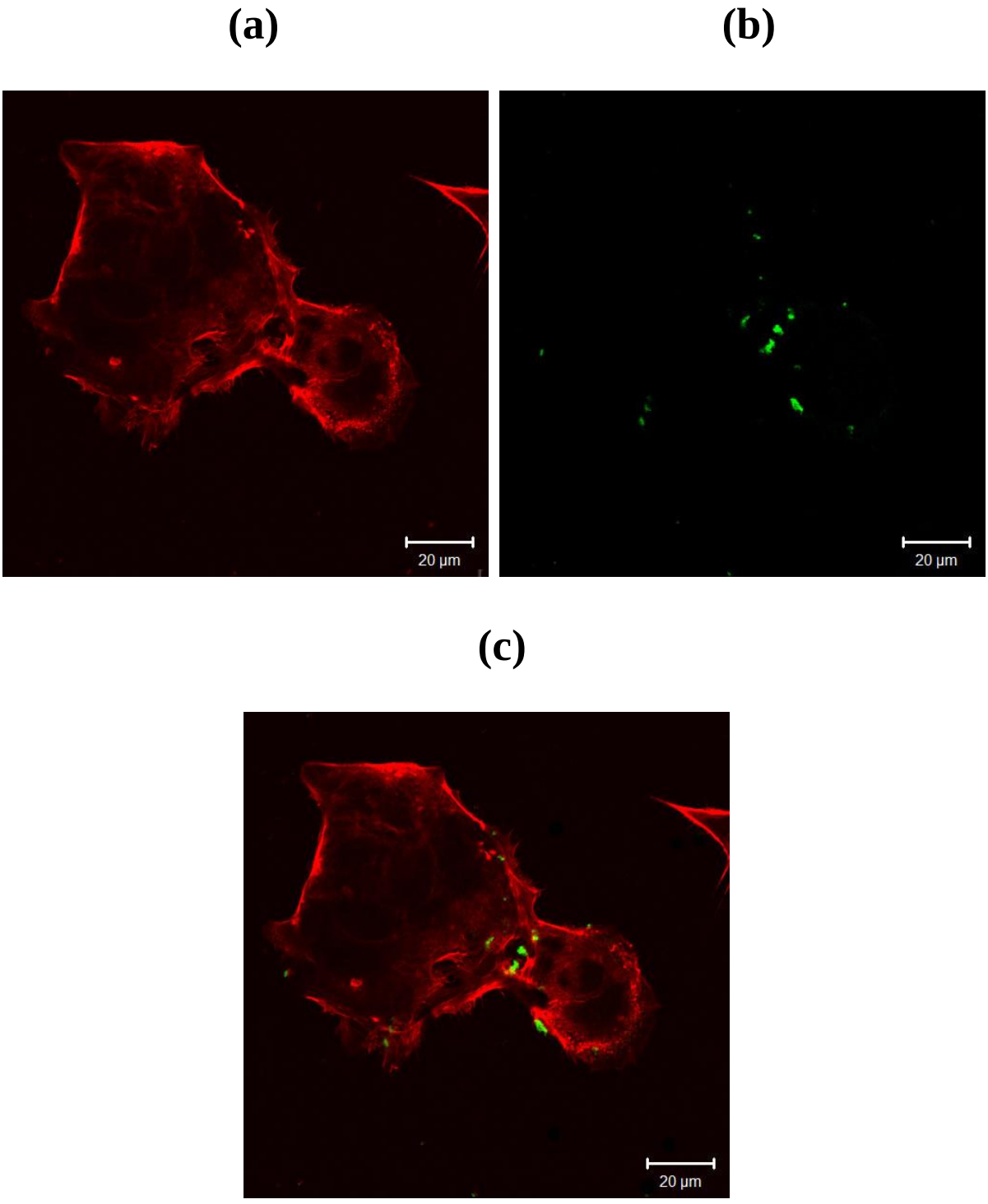

Figure 4.51. Confocal fluorescence images of Caco-2 cells incubated with ITC SiNPs (P Br SiNPs) for 6 h incubation. Red channel (a), green channel (b), merged (c). Red from Phalloidin for actin staining and green fluorescence from nanoparticles.

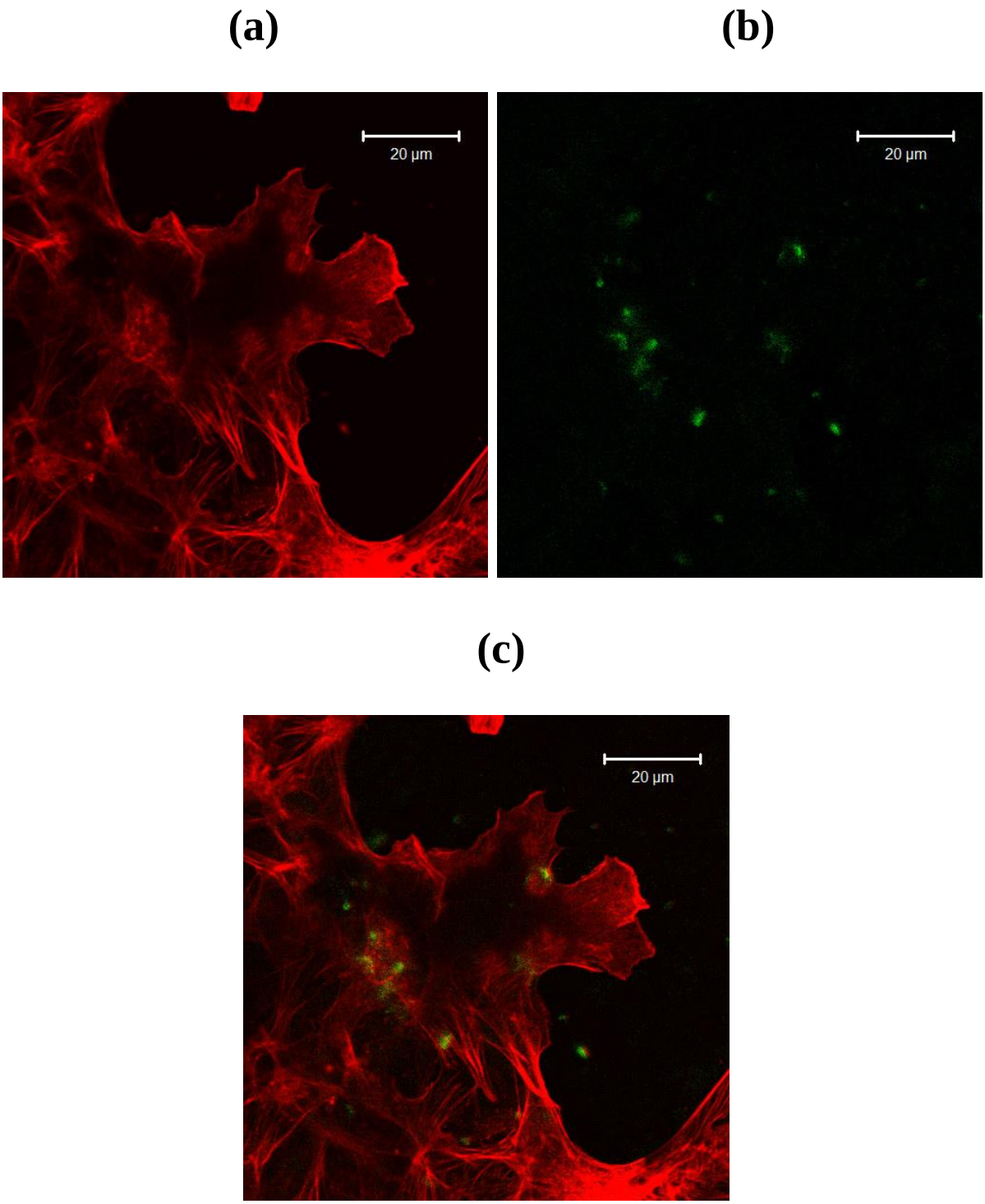

Figure 4.52. Confocal fluorescence images of Caco-2 cells incubated with ITC SiNPs (P Br SiNPs) for 12 h incubation. Red channel (a), green channel (b), merged (c). Red from Phalloidin for actin staining and green fluorescence from nanoparticles.

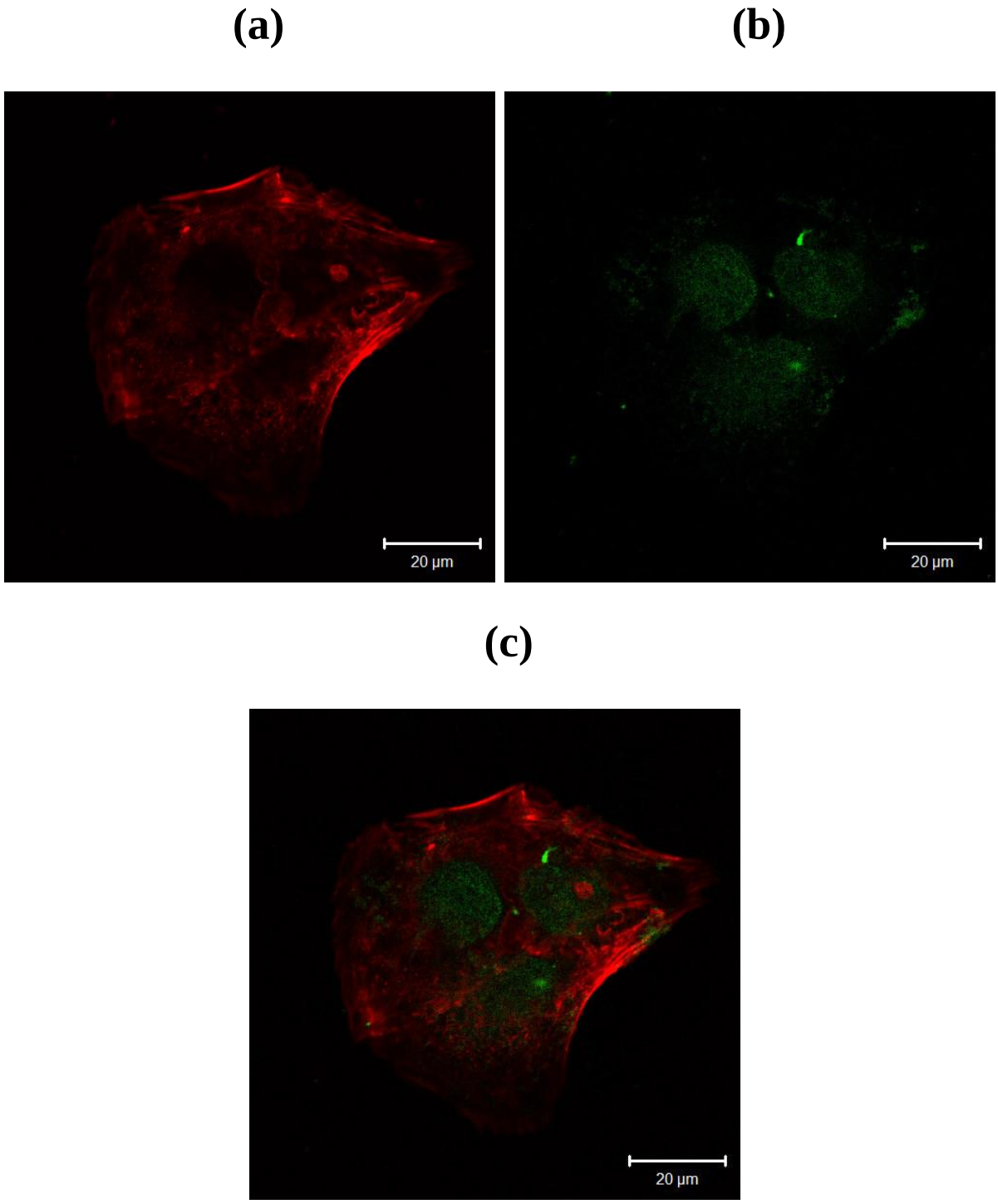

Figure 4.53. Confocal fluorescence images of Caco-2 cells incubated with ITC SiNPs (P Br SiNPs) for 12 h incubation. Red channel (a), green channel (b), merged (c). Red from Phalloidin for actin staining and green fluorescence from nanoparticles.

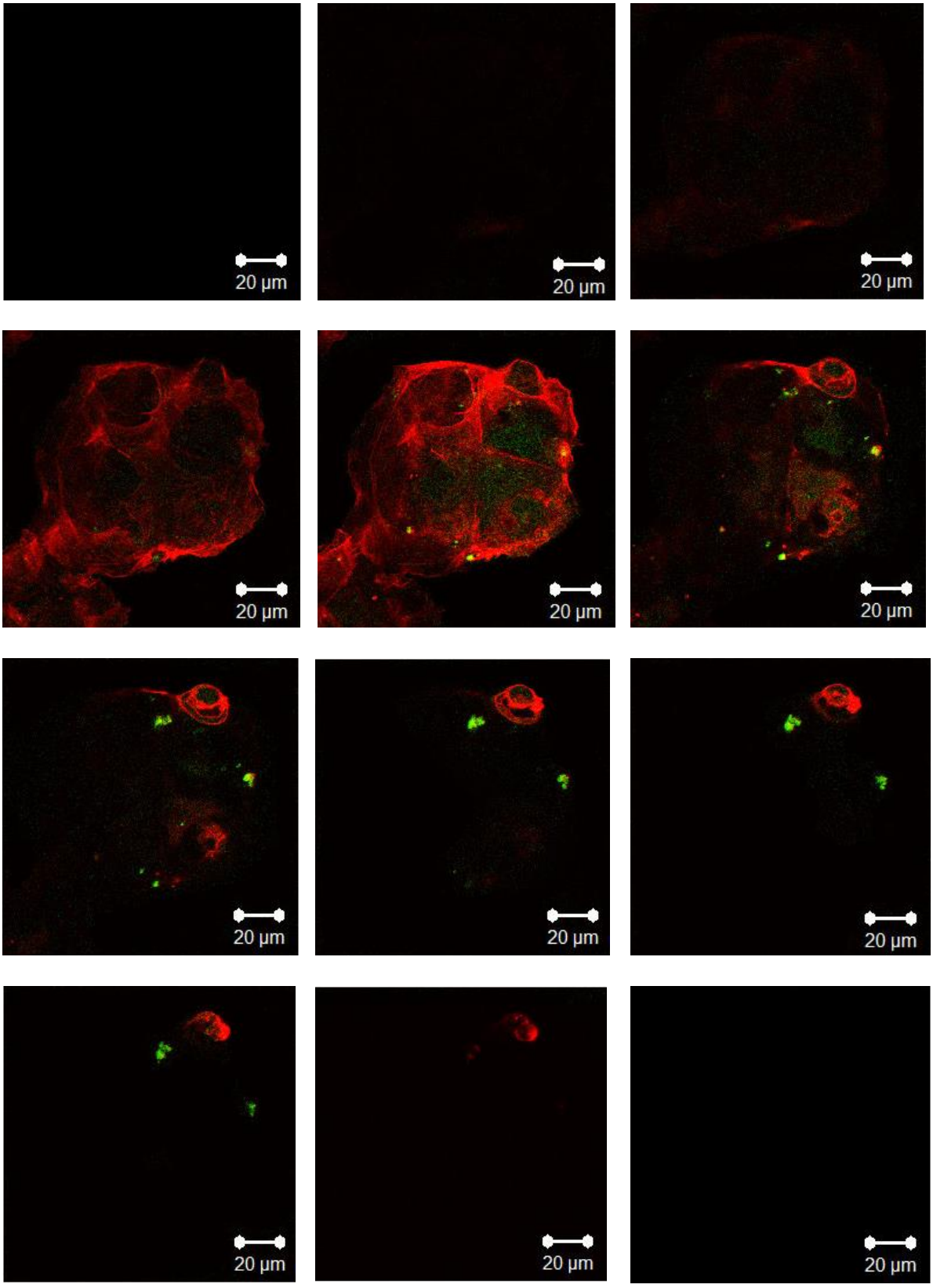

Figure 4.54. Z-stack confocal images of Caco-2 cells incubated with ITC SiNPs (P Br SiNPs) for 12 h incubation, collected at 0.37µm intervals. Red from Phalloidin for actin staining and green fluorescence from nanoparticles. The first row shows the bottom layer and the last row shows the top layer (The order is from left to right).

4.11.2.2. Flow Cytometry

To further investigate cell uptake, flow cytometry was undertaken using ITC SiNPs with Caco-2 cells. The total fluorescence intensity of particles was measured in 10,000 cells. Figures 4.55 and 4.56 show the uptake efficiency of ITC SiNPs (P Br SiNPs) using FL1 channel detector.

Cells were treated with two different concentrations of nanoparticles (20 and 70 µg/mL) for various time points (6 to 48 h). As can be seen in Figure 4.55 (a), the fluorescence detected from the cells when treated with 20 µg/mL of ITC SiNPs was very low and changed just slightly over time. On the other hand, by increasing the nanoparticle concentration to 70 µg/mL (Figure 4.55 (b)), the time dependant behaviour of ITC SiNPs, in addition to the higher uptake level for this concentration, was clear.

The overall median of the fluorescence for both concentrations is shown in Figure 4.56, after 6 and 12 h incubation. It was observed that the difference between the two different concentrations was not statically significant. However, it became significant for the 24 and 48 h time periods.

This relationship suggest that the amount of nanoparticle inside the cells is dependent on the dose applied to treat the cells, in addition to the specific time point for each treatment. The flow cytometric data in general confirmed the uptake of ITC SiNPs in Caco-2 cells in a similar time and dose dependant manner.

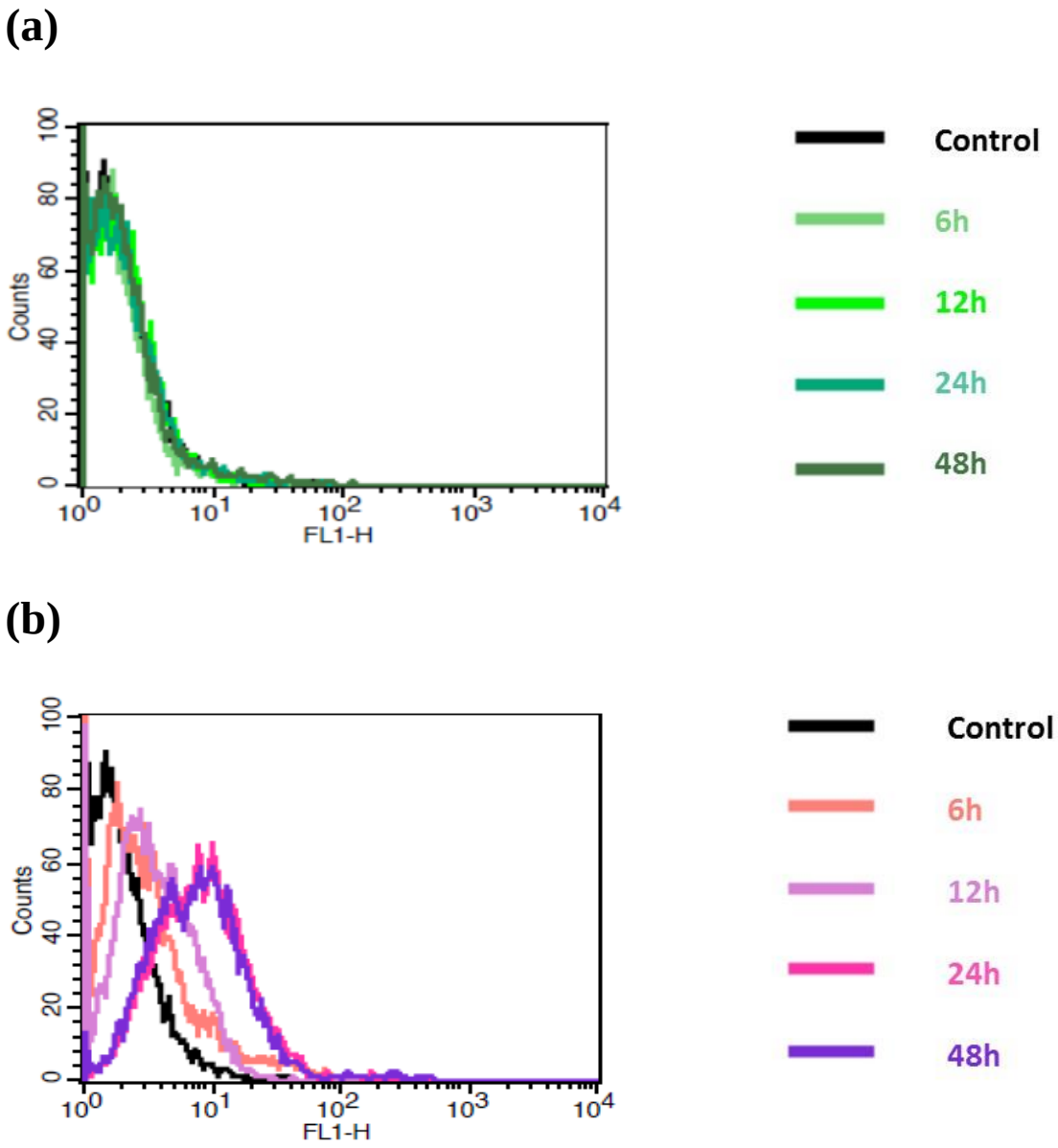

Figure 4.55. Uptake efficiency of ITC SiNPs (P Br SiNPs) in Caco-2 cells with various incubation times from 6 to 24 h. Cells were exposed to two nanoparticle concentrations of 20 µg/mL (a) and 70 µg/mL (b).

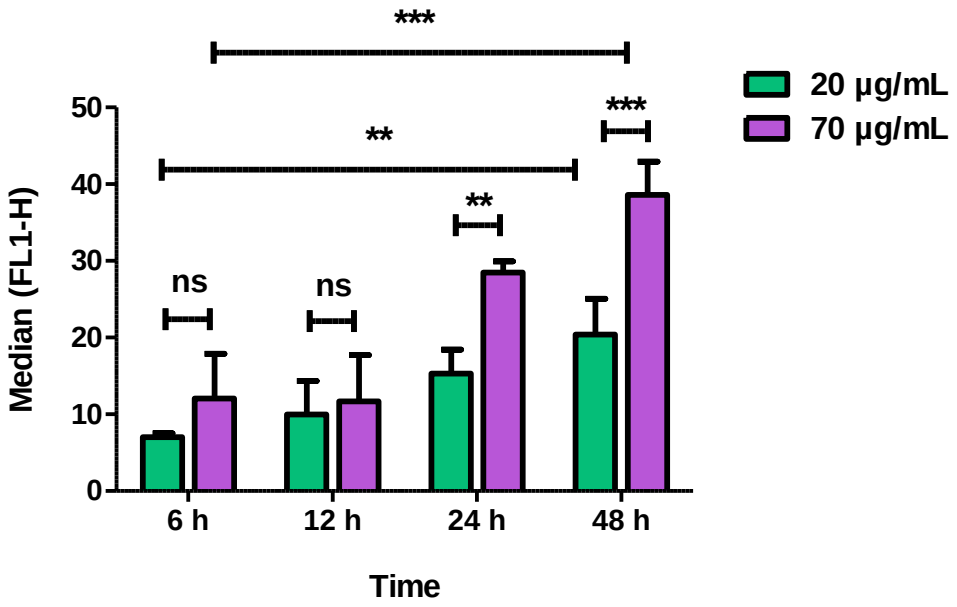

Figure 4.56. Collective flow cytometric analysis results, which are presented as fluorescence median of cells after nanoparticle uptake showing the time dependent behaviour of uptake. Statistical significance was determined by two-way-ANOVA followed by a Bonferroni post-test (***P < 0.001, **P < 0.01 and ns not statistically significant). Results are expressed as mean ± SEM (n =3).

To study further, the internalisation mechanism of ITC SiNPs was investigated. It has been shown previously that diffusion and active transport of molecules across the cell membrane are temperature dependant.[47] The transport activity is significantly less at low temperatures and therefore the uptake of molecules could be considered as non-specific diffusional entry. Even though the ligands have been shown to attach to the cell membrane, the internalisation can be affected at low temperatures.[46] Low temperatures can affect the binding of the ligands to specific receptors, and moreover the mobility of the ligand-receptor complex could be interfered as well.[48] It has furthermore been shown that the transport of the endocytosed material from endosomes to lysosomes can be interfered with at low temperatures.[45]

Small particles are beneficial to enter the cells more rapidly.[46] Endocytosis is known as the main mechanism of cellular internalisation for many nanoparticles.[49] However, if the nanoparticle diameter is smaller than 5 nm, it is more likely they enter the cells by other pathways such as translocation.[49] Particles with the size of ~25 nm were shown to have a higher rate of uptake by endocyosis.[46] This size is close to the hydrodynamic size of ITC SiNPs in biological media (Tables 4.6 and 4.7). The efficiency of endocytosis is dependent on the physiochemical properties of nanoparticles such as surface chemistry, size, shape and the cell type being exposed to NPs.[50] In the endocytotic process, the size of the vesicles containing

nanoparticles varies based on the specific pathway. The nanoparticle size is a crucial parameter in determining which pathway will be taken.[51]

Since ITC SiNPs could be effectively internalised into Caco-2 cells, different temperatures (4 °C and 37 °C) for the cell incubation were used to investigate the underlying uptake mechanism. Cells were treated with 70 µg/mL ITC SiNPs at 4 °C for various time points (Figure 4.57) and the data was compared to that obtained from the treated cells at normal physiological temperature (37 °C) (Figure 4.58). ITC SiNPs uptake was impeded when incubated at 4 °C while the internalisation was confirmed through fluorescence observations at 37 °C. As a result, flow cytometry data indicated that the uptake of ITC SiNPs is most likely energy-dependant.

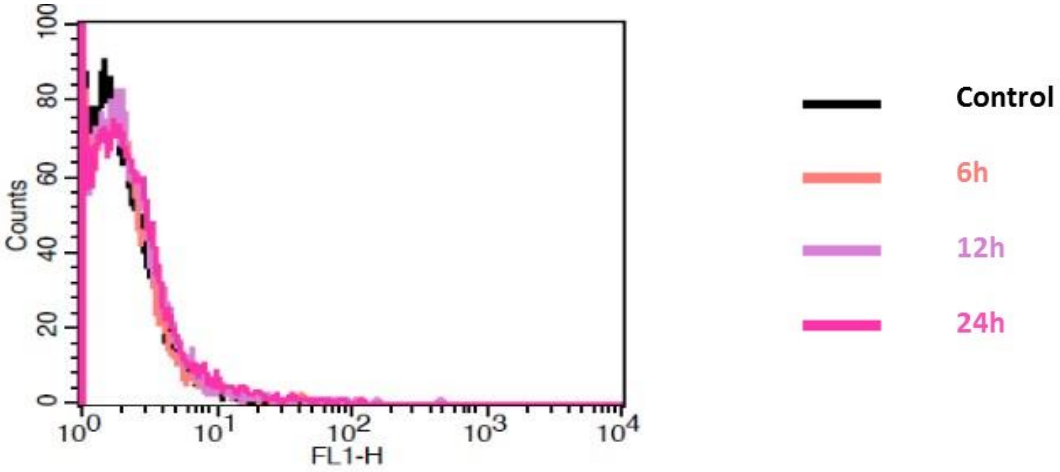

Figure 4.57. Uptake efficiency of ITC SiNPs (P Br SiNPs) in Caco-2 cells when incubated at 4 °C.

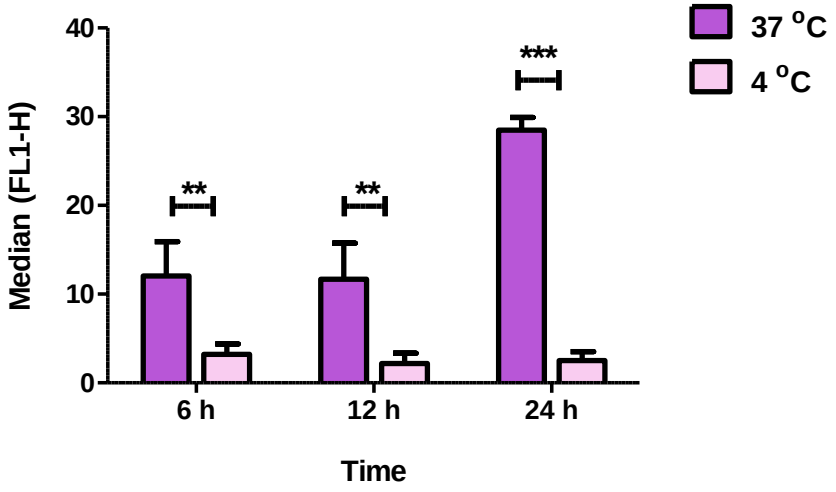

Figure 4.58. Collective flow cytometric analysis results after Caco-2 cells were incubated with ITC SiNPs (P Br SiNPs) at 37 °C and 4 °C. Statistical significance was determined by two-way-ANOVA followed by a Bonferroni post-test. (***P < 0.001 and **P < 0.01). Results are expressed as mean ± SEM (n =3).

4.12. Summary and Conclusions

For many applications, it is desirable to prepare SiNPs with functional groups which can facilitate their conjugation to other molecules. It has been shown that NH_2 SiNPs and Br SiNPs can be used as starting material to achieve nanoparticles with the ITC functional group.

The successful synthesis of ITC SiNPs using two different approaches shows both types of nanoparticle are fully capped by the ITC group. Although using different starting materials and reagents, the final products behaved similarly when characterised by various physiochemical techniques. Both SiNPs types have been shown to be rich in silicon and with crystalline structures.

ITC SiNPs obtained from Br SiNPs show higher levels of purity since the only reagent used is the synthesis method was a salt (KSCN) which was easily separated by washing and separation in non-miscible solvents. On the other hand, ITC SiNPs obtained from NH_2 SiNPs as the starting material, showed the presence of impurities (by-products) even after several attempts of purification. Therefore, the higher toxicity of ITC SiNPs (P NH_2 SiNPs) may not attributed to the therapeutic effects of the ITC functional group with confidence.

It was shown that ITC SiNPs (P Br SiNPs) have a higher quantum yield than ITC SiNPs (P NH_2 SiNPs), and were bright enough to be clearly detected by the confocal microscope and flow cytometer for uptake studies.

The internalisation of ITC SiNPs (P Br SiNPs) was confirmed and it is most likely to be based on the receptor mediated endocytosis mechanism since the temperature behaviour was observed in the uptake process of SiNPs.

Even though ITC SiNPs are not soluble in aqueous media, this is not a major concern for biomedical applications since they can be dispersed as lyophobic aqueous sols. This can be achieved by first dissolving the nanoparticles in small amounts of suitable organic solvents and later diluting them in polar solvents.

In summary, this chapter has demonstrated the development and assessment of a novel, promising multifunctional nanosystem, which can be used for bioimaging applications, with the inherited therapeutic properties of the functional ligand. Furthermore, these nanoparticles are indeed compatible with cells, and can be exploited as potential probes in bioimaging assays and in further investigations.

4.13. References

1. Fahey, J. W.; Zhang, Y. S.; Talalay, P., Broccoli sprouts: An exceptionally rich source of inducers of enzymes that protect against chemical carcinogens. *Proceedings of the National Academy of Sciences of the United States of America* **1997,** *94* (19), 10367-10372.

2. Munday, R.; Munday, C. M., Selective induction of phase II enzymes in the urinary bladder of rats by allyl isothiocyanate, a compound derived from Brassica vegetables. *Nutr. Cancer* **2002,** *44* (1), 52-59.

3. Munday, R.; Munday, C. M., Induction of phase II detoxification enzymes in rats by plant-derived isothlocyanates: Comparison of allyl isothiocyanate with sulforaphane and related compounds. *Journal of Agricultural and Food Chemistry* **2004,** *52* (7), 1867-1871.

4. Wang, J.; Sun, S.; Peng, F.; Cao, L.; Sun, L., Efficient one-pot synthesis of highly photoluminescent alkyl-functionalised silicon nanocrystals. *Chemical Communications* **2011,** *47* (17), 4941-4943.

5. Dasog, M.; Yang, Z.; Regli, S.; Atkins, T. M.; Faramus, A.; Singh, M. P.; Muthuswamy, E.; Kauzlarich, S. M.; Tilley, R. D.; Veinot, J. G. C., Chemical Insight into the Origin of Red and Blue Photoluminescence Arising from Freestanding Silicon Nanocrystals. *Acs Nano* **2013,** *7* (3), 2676-2685.

6. Svatos, A.; Attygalle, A. B., Characterization of vinyl-substituted, carbon-carbon double bonds by GC/FT-IR analysis. *Analytical Chemistry* **1997,** *69* (10), 1827-1836.

7. Tsvetkova, T.; Balabanov, S.; Bischoff, L.; Krastev, V.; Stefanov, P.; Avramova, I. In *X-ray photoelectron study of Si+ ion implanted polymers*, Journal of Physics: Conference Series, IOP Publishing: **2010;** p 012070.

8. Hagio, T.; Takase, A.; Umebayashi, S., X-ray photoelectron spectroscopic studies of β-sialons. *Journal of materials science letters* **1992,** *11* (12), 878-880.

9. Chao, Y.; Wang, Q.; Pietzsch, A.; Hennies, F.; Ni, H., Soft X-ray induced oxidation on acrylic acid grafted luminescent silicon quantum dots in ultrahigh vacuum. *Physica Status Solidi a-Applications and Materials Science* **2011,** *208* (10), 2424-2429.

10. Sieval, A. B.; van den Hout, B.; Zuilhof, H.; Sudhölter, E. J., Molecular modeling of covalently attached alkyl monolayers on the hydrogen-terminated Si (111) surface. *Langmuir* **2001,** *17* (7), 2172-2181.

11. Wallart, X.; Henry de Villeneuve, C.; Allongue, P., Truly quantitative XPS characterization of organic monolayers on silicon: study of alkyl and alkoxy monolayers on H-Si (111). *Journal of the American Chemical Society* **2005,** *127* (21), 7871-7878.

12. Albert C Thompson, J. K., David T. Attwood, Eric M Gullikson, Malcolm R. Howells, *X-Ray Data Booklet*. Lawrence Berkeley National Laboratory: Berkeley, California, 2009.

13. Barber, M.; Connor, J. A.; Guest, M. F.; Hillier, I. H.; Schwarz, M., Bonding In Some Donor-Acceptor Complexes Involving Boron-Trifluoride - Study By Means Of Esca And

Molecular-Orbital Calculations. *Journal of the Chemical Society-Faraday Transactions Ii* **1973,** (4), 551-558.

14. Li, W.; Xu, Y.; Zhou, Y.; Ma, W.; Wang, S.; Dai, Y., Silica nanoparticles functionalized via click chemistry and ATRP for enrichment of Pb (II) ion. *Nanoscale research letters* **2012,** *7* (1), 1-7.

15. Gassman, P. G.; Winter, C. H., Understanding electronic effects in organometallic complexes. Influence of methyl substitution on hafnocene dihalides. *Organometallics* **1991,** *10* (5), 1592-1598.

16. Pedras, M. S. C.; Zheng, Q.-A.; Gadagi, R. S., The first naturally occurring aromatic isothiocyanates, rapalexins A and B, are cruciferous phytoalexins. *Chemical Communications* **2007,** (4), 368-370.

17. Gremlich, H. G. H.-U., *IR Spectroscopy: An Introduction*. Wiley-VCH: **2002;** p 374.

18. Lie, L. H.; Duerdin, M.; Tuite, E. M.; Houlton, A.; Horrocks, B. R., Preparation and characterisation of luminescent alkylated-silicon quantum dots. *Journal of Electroanalytical Chemistry* **2002,** *538*, 183-190.

19. Shokri, B.; Firouzjah, M. A.; Hosseini, S. In *FTIR analysis of silicon dioxide thin film deposited by metal organic-based PECVD*, Proceedings of 19th international symposium on plasma chemistry society, Bochum, Germany, **2009.**

20. Shiohara, A.; Hanada, S.; Prabakar, S.; Fujioka, K.; Lim, T. H.; Yamamoto, K.; Northcote, P. T.; Tilley, R. D., Chemical Reactions on Surface Molecules Attached to Silicon Quantum Dots. *Journal of the American Chemical Society* **2010,** *132* (1), 248-253.

21. Mullejans, H.; Bruley, J., Electron-Energy-Loss Spectroscopy (Eels)-Comparison With X-Ray-Analysis. *Journal De Physique IV* **1993,** *3* (C 7), 2083-2092.

22. Pawley, J. B., *Handbook of Biological Confocal Microscopy (3rd ed.)*. Springer: Berlin, **2006.**

23. Wang, Q.; Ni, H.; Pietzsch, A.; Hennies, F.; Bao, Y.; Chao, Y., Synthesis of water-dispersible photoluminescent silicon nanoparticles and their use in biological fluorescent imaging. *Journal of Nanoparticle Research* **2011,** *13* (1), 405-413.

24. Mekki, A.; Holland, D.; McConville, C. F.; Salim, M., An XPS study of iron sodium silicate glass surfaces. *Journal of Non-Crystalline Solids* **1996,** *208* (3), 267-276.

25. Du, H. H.; Tressler, R. E.; Spear, K. E.; Pantano, C. G., Oxidation Studies Of Crystalline Cvd Silicon-Nitride. *Journal of the Electrochemical Society* **1989,** *136* (5), 1527-1536.

26. Dementjev, A. P.; de Graaf, A.; van de Sanden, M. C. M.; Maslakov, K. I.; Naumkin, A. V.; Serov, A. A., X-ray photoelectron spectroscopy reference data for identification of the C3N4 phase in carbon-nitrogen films. *Diamond and Related Materials* **2000,** *9* (11), 1904-1907.

27. Morales, A. M.; Lieber, C. M., A laser ablation method for the synthesis of crystalline semiconductor nanowires. *Science* **1998,** *279* (5348), 208-211.

28. Wang, Q.; Bao, Y.; Zhang, X.; Coxon, P. R.; Jayasooriya, U. A.; Chao, Y., Uptake and Toxicity Studies of Poly-Acrylic Acid Functionalized Silicon Nanoparticles in Cultured Mammalian Cells. *Advanced Healthcare Materials* **2012,** *1* (2), 189-198.

29. Alkilany, A. M.; Murphy, C. J., Toxicity and cellular uptake of gold nanoparticles: what we have learned so far? *Journal of nanoparticle research* **2010,** *12* (7), 2313-2333.

30. Connor, E. E.; Mwamuka, J.; Gole, A.; Murphy, C. J.; Wyatt, M. D., Gold nanoparticles are taken up by human cells but do not cause acute cytotoxicity. *Small* **2005,** *1* (3), 325-327.

31. Yu, W.; Xu, Y.; Li, H.; Zhan, X.; Lu, W., Synthesis of full-visible-spectrum luminescent silicon nanocrystals and the origin of the luminescence. *Applied Physics A* **2013,** *111* (2), 501-507.

32. Warner, J. H.; Hoshino, A.; Yamamoto, K.; Tilley, R., Water-Soluble Photoluminescent Silicon Quantum Dots. *Angewandte Chemie* **2005,** *117* (29), 4626-4630.

33. Zhou, Z.; Brus, L.; Friesner, R., Electronic structure and luminescence of 1.1-and 1.4-nm silicon nanocrystals: oxide shell versus hydrogen passivation. *Nano Letters* **2003,** *3* (2), 163-167.

34. Zhou, Z.; Friesner, R. A.; Brus, L., Electronic structure of 1 to 2 nm diameter silicon core/shell nanocrystals: surface chemistry, optical spectra, charge transfer, and doping. *Journal of the American Chemical Society* **2003,** *125* (50), 15599-15607.

35. Qiu, T.; Wu, X.; Kong, F.; Ma, H.; Chu, P. K., Solvent effect on light-emitting property of Si nanocrystals. *Physics Letters A* **2005,** *334* (5), 447-452.

36. Williams, A. T. R.; Winfield, S. A.; Miller, J. N., Relative Fluorescence Quantum Yields Using A Computer-Controlled Luminescence Spectrometer. *Analyst* **1983,** *108* (1290), 1067-1071.

37. Dickinson, F.; Alsop, T.; Al-Sharif, N.; Berger, C.; Datta, H.; Šiller, L.; Chao, Y.; Tuite, E.; Houlton, A.; Horrocks, B., Dispersions of alkyl-capped silicon nanocrystals in aqueous media: photoluminescence and ageing. *Analyst* **2008,** *133* (11), 1573-1580.

38. O'Farrell, N., Silicon nanoparticles: applications in cell biology and medicine. *international Journal of Nanomedicine* **2006,** *1* (4), 451-472.

39. John A. Dean, a. F. A. S., Jr.,, *Lange's handbook of chemistry*. McGraw-Hill: New York, **1999.**

40. Chao, Y.; Siller, L.; Krishnamurthy, S.; Coxon, P. R.; Bangert, U.; Gass, M.; Kjeldgaard, L.; PatoleO, S. N.; Lie, L. H.; O'Farrell, N.; Alsop, T. A.; Houlton, A.; Horrocks, B. R., Evaporation and deposition of alkyl-capped silicon nanocrystals in ultrahigh vacuum. *Nature Nanotechnology* **2007,** *2* (8), 486-489.

41. Terry, J.; Linford, M. R.; Wigren, C.; Cao, R. Y.; Pianetta, P.; Chidsey, C. E. D., Alkyl-terminated Si(111) surfaces: A high-resolution, core level photoelectron spectroscopy study. *Journal of Applied Physics* **1999,** *85* (1), 213-221.

42. Ahire, J. H.; Wang, Q.; Coxon, P. R.; Malhotra, G.; Brydson, R.; Chen, R.; Chao, Y., Highly Luminescent and Nontoxic Amine-Capped Nanoparticles from Porous Silicon: Synthesis and Their Use in Biomedical Imaging. *Acs Applied Materials & Interfaces* **2012,** *4* (6), 3285-3292.

43. Lanone, S.; Rogerieux, F.; Geys, J.; Dupont, A.; Maillot-Marechal, E.; Boczkowski, J.; Lacroix, G.; Hoet, P., Comparative toxicity of 24 manufactured nanoparticles in human alveolar epithelial and macrophage cell lines. *Particle and fibre toxicology* **2009,** *6* (1), 1.

44. Rujanapun, N.; Aueviriyavit, S.; Boonrungsiman, S.; Rosena, A.; Phummiratch, D.; Riolueang, S.; Chalaow, N.; Viprakasit, V.; Maniratanachote, R., Human primary erythroid cells as a more sensitive alternative in vitro hematological model for nanotoxicity studies: Toxicological effects of silver nanoparticles. *Toxicology in Vitro* **2015,** *29* (8), 1982-1992.

45. Kou, L.; Sun, J.; Zhai, Y.; He, Z., The endocytosis and intracellular fate of nanomedicines: Implication for rational design. *Asian Journal of Pharmaceutical Sciences* **2013,** *8* (1), 1-10.

46. Zhang, S.; Li, J.; Lykotrafitis, G.; Bao, G.; Suresh, S., Size-Dependent Endocytosis of Nanoparticles. *Advanced Materials* **2009,** *21* (4), 419-424.

47. Fricker, G., Biological Membranes and Drug Transport. *Transporters as Drug Carriers: Structure, Function, Substrates, Volume 44*, 229-262.

48. Bannunah, A. M.; Vllasaliu, D.; Lord, J.; Stolnik, S., Mechanisms of Nanoparticle Internalization and Transport Across an Intestinal Epithelial Cell Model: Effect of Size and Surface Charge. *Molecular Pharmaceutics* **2014,** *11* (12), 4363-4373.

49. Zhang, S.; Gao, H.; Bao, G., Physical principles of nanoparticle cellular endocytosis. *ACS nano* **2015,** *9* (9), 8655-8671.

50. Oh, N.; Park, J.-H., Endocytosis and exocytosis of nanoparticles in mammalian cells. *Int J Nanomedicine* **2014,** *9* (Suppl 1), 51-63.

51. Zhang, L.; Laug, L.; Munchgesang, W.; Pippel, E.; Gösele, U.; Brandsch, M.; Knez, M., Reducing stress on cells with apoferritin-encapsulated platinum nanoparticles. *Nano letters* **2009,** *10* (1), 219-223.

Chapter 5:
Synchrotron-based Fourier Transform Infrared Microspectroscopy:
A Novel Approach For Investigating Nanoparticle Cell Internalisation

5.1. Overview

Biological tissues and cells are extremely complex structures that vary widely in composition. Different cellular components such as proteins, lipids, nucleic acids, and carbohydrates have unique IR spectra. Therefore, variations in their content or structure, can provide important information about the chemistry of cells and tissue states.[1]

Conventional IR microspectroscopy has proven extremely valuable for resolving the chemical components in biological samples, however, the long wavelengths of IR radiation limit the spatial resolution which can be achieved. The resolution of traditional FTIR microspectroscopy is limited to approximately to 75 μm. As individual biological cells are typically between 5 to 30 μm in diameter, they are too small to probe with a conventional thermal (globar) IR source.[1]

Synchrotron-based Fourier Transform Infrared (SR-FTIR) microspectroscopy is a crucial technique that provides fingerprint-like information and is capable of characterising distinct tissue structures. The high brightness of the synchrotron source, which is defined as the photon flux or power emitted per source area and solid angle, allows smaller regions to be probed with an acceptable (S/N).[2, 3] The spatial resolution of a synchrotron IR source is <10 μm (depending on the wavelength) and allows the chemical mapping of single living cells for the first time.[4] In addition, the high brightness of the synchrotron IR source is several hundred times higher than the conventional IR microspectroscopy and has opened the door to cellular and sub-cellular chemical imaging of living cells for further investigation of various components.[1]

In this chapter, SR-FTIR was used to study Caco-2 and CCD-841 cells and to determine the effect of ITC SiNPs on these cells. This method has been used to analyse the internalisation of ITC SiNPs, synthesised as described in Chapter 4, into the cells and to examine how they can affect the cells. First, the measurements were performed on free-standing materials to confirm the expected absorption signals for the relevant functionalities by a synchrotron source. As desired, the spectra obtained from the synchrotron facility showed similar peaks with more details and higher intensity than the normal FTIR facility.

In order to evaluate the effect of ITC SiNPs on cells after uptake, the experiments were carried out by spectral comparison of cells treated by ITC SiNPs and control cells. Individual spectra were collected from both nuclei and cytoplasm of cells and the variations in the protein

and phospholipid contents of the treated cells confirmed the effect of nanoparticle internalisation in the treated cells. The results show that it is possible to establish the vibrational frequencies, corresponding to the specific functional group of cell components, to quantify the changes in cell composition in response to nanoparticle internalisation.

The response of cells to changes in their chemical environment can be evaluated using FPA detector, which provides infrared chemical images. These changes were evaluated via the variations in the distribution of mid-infrared band intensities, and in doing so gives a profile of the biomolecular domains within cells before and after treatment with SiNPs. Such potential changes are due to several factors, including variations in density of various cellular components such as the proteins and phospholipids. This capability will be useful for the study of biological cells, as part of this project to identify and understand the interaction between synchrotron radiation and different cells before and after the nanoparticle internalisation.

5.2. Synchrotron Measurement Studies

5.2.1. Synchroton FTIR Spectroscopy of Free-standing SiNPs

Before analysis, the quality of ITC SiNPs (discussed in Chapter 4) and their precursors was further checked with SR-FTIR. The higher resolution of synchrotron facilitated improved observations of signals related to the expected bonding frequencies occurring in nanoparticles.

Figures 5.1 and 5.2 show the spectra of ITC SiNPs (a) and the starting materials (Br SiNPs and NH_2 SiNPs) used for their synthesis (b). Signals representing the expected functional groups appeared at the anticipated wavenumbers. The C-Si symmetric bending at about 1260 cm^{-1} was clearer compared to that obtained in Chapter 3 by conventional FTIR. The double bond at around 2100 cm^{-1} for both types of ITC SiNPs confirmed the successful synthesis of the isothiocyanate functional group. The overall bonding features obtained by the synchrotron source appeared very sharp and clear compared to the standard laboratory source.

Initially it was decided to use both types of ITC SiNPs for synchrotron studies. This was due to the fact that the double bond was detected in ITC SiNPs (NH_2 SiNPs) with much higher intensity. It was anticipated that detection of these functional groups in cells after nanoparticle internalisation should be possible but, as the peaks related to cellular components were dominant, this double bond was much weaker and not found. Taking this finding in

combination with previous results obtained in Chapter 4, as ITC SiNPs (P Br SiNPs) showed better optical properties, it was decided to use only this type of ITC SiNPs for the biological synchrotron studies.

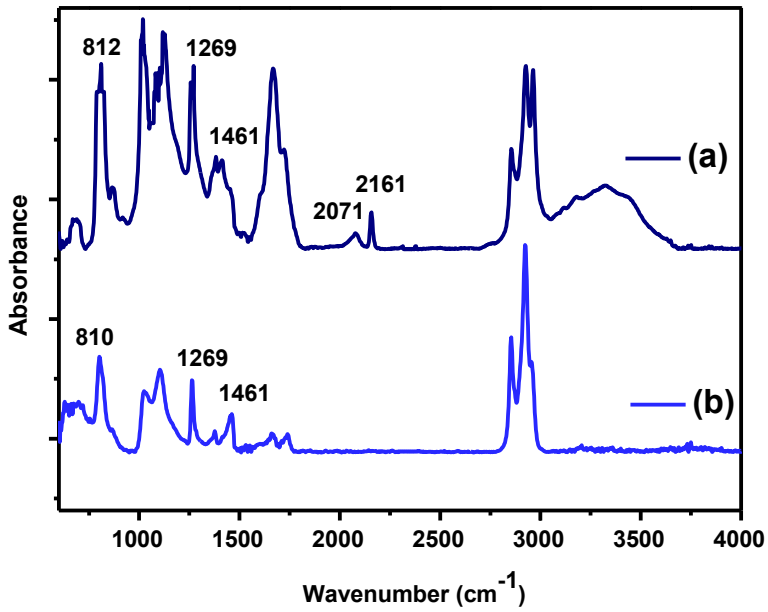

Figure 5.1. SR-FTIR analysis for ITC SiNPs (P Br SiNPs) (a) and Br SiNPs as the precursor (b).

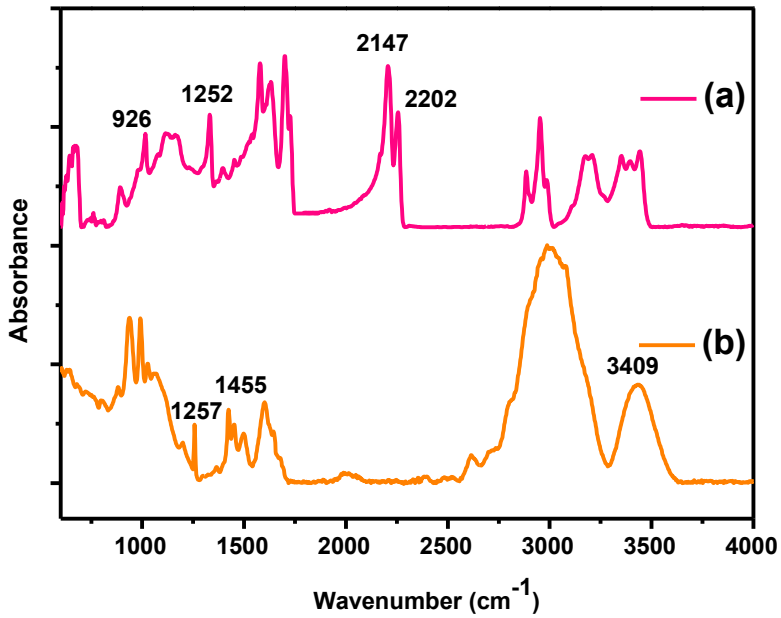

Figure 5.2. SR-FTIR analysis for ITC SiNPs (P NH_2 SiNPs) (a) and NH_2 SiNPs as the precursor (b).

5.2.2. FTIR Spectral Comparison and Analysis of Individual Cells

Figures 5.3 to 5.6 show the visual micrographs of Caco-2 and CCD-841 cells before and after treatment with ITC SiNPs. The presented spectra in the following sections were obtained from these figures.

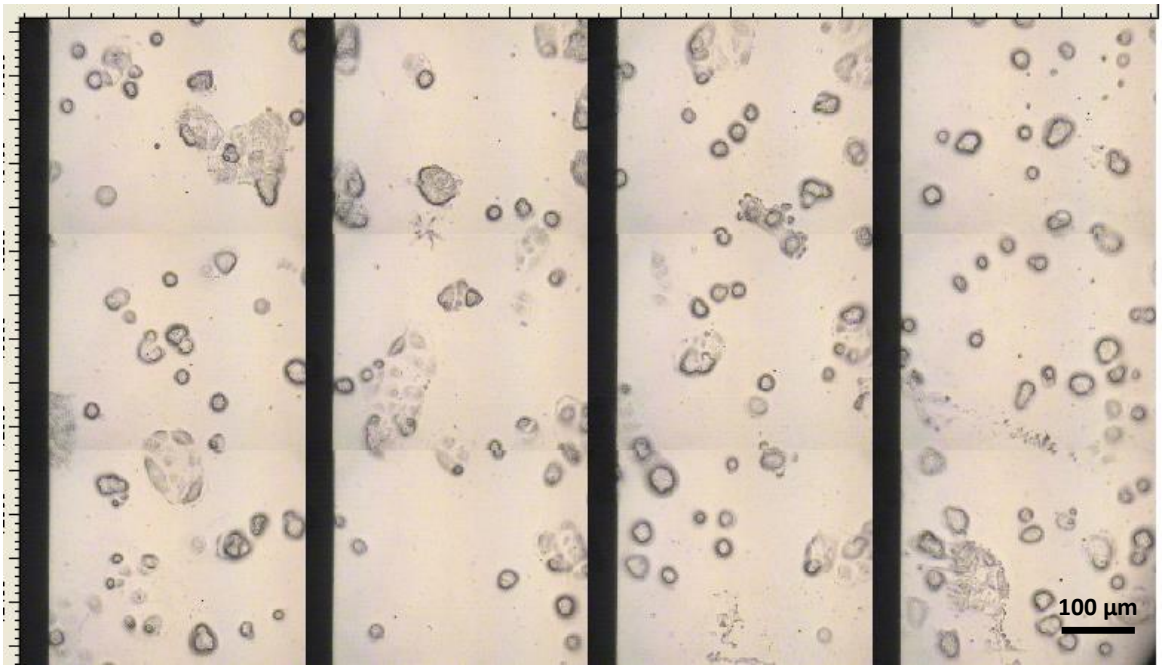

Figure 5.3. Photomicrographs of Caco-2 control cells.

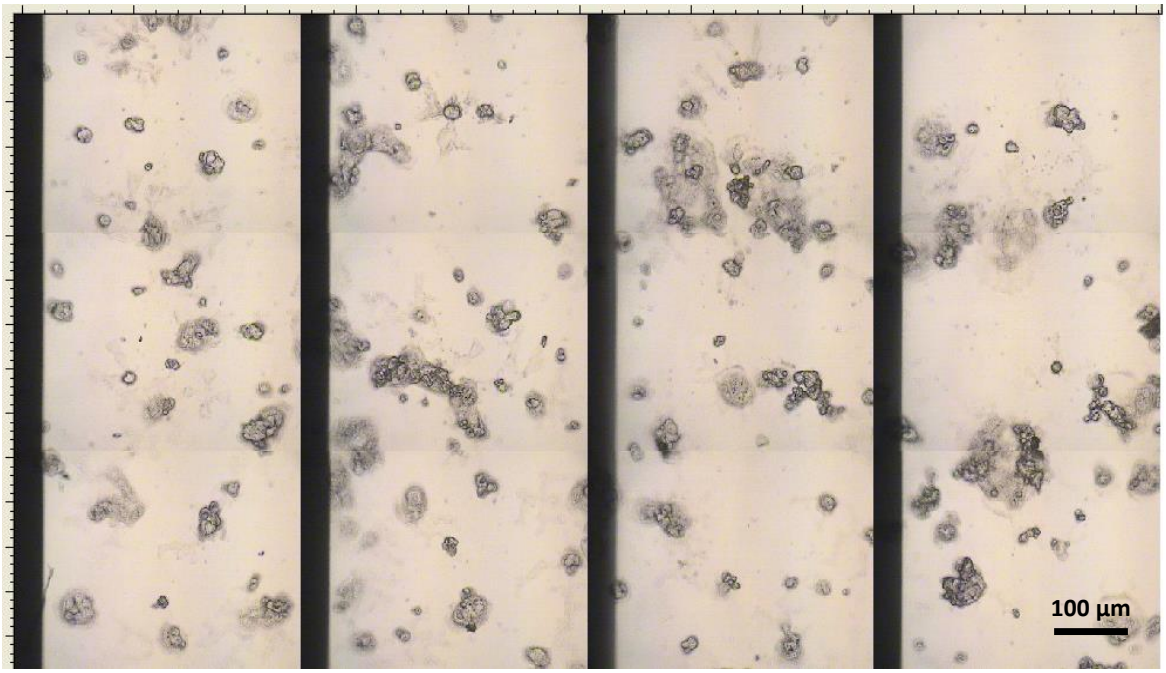

Figure 5.4. Photomicrographs of Caco-2 cells treated with ITC SiNPs.

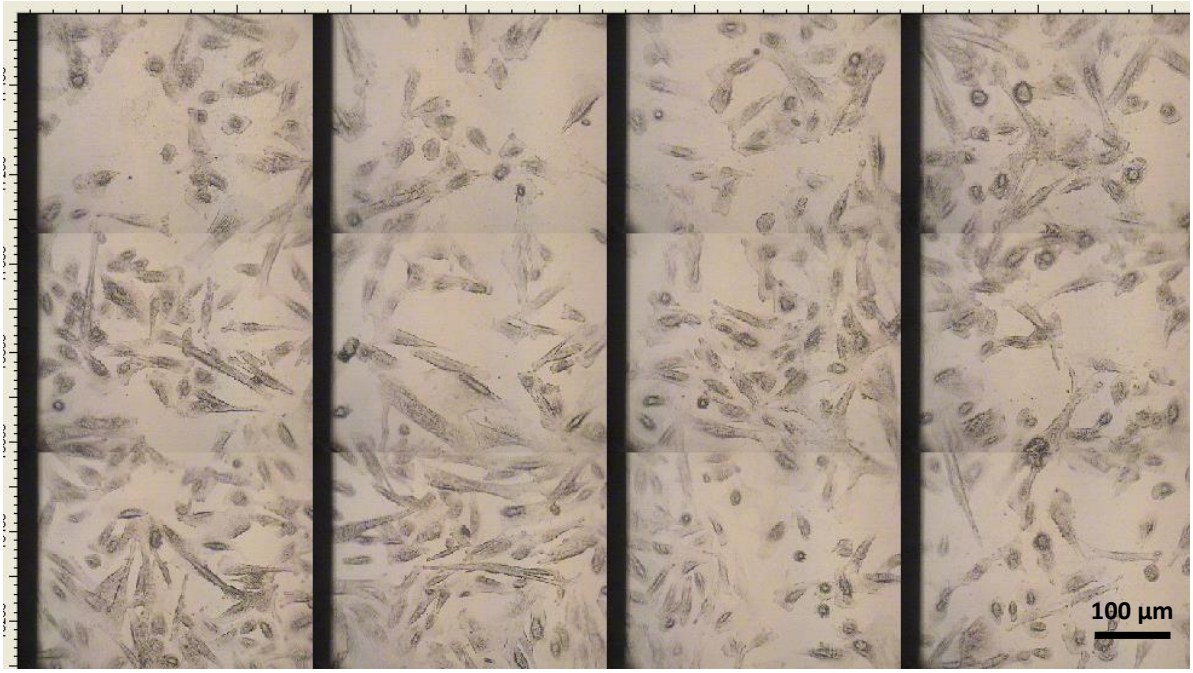

Figure 5.5. Photomicrographs of CCD-841 control cells.

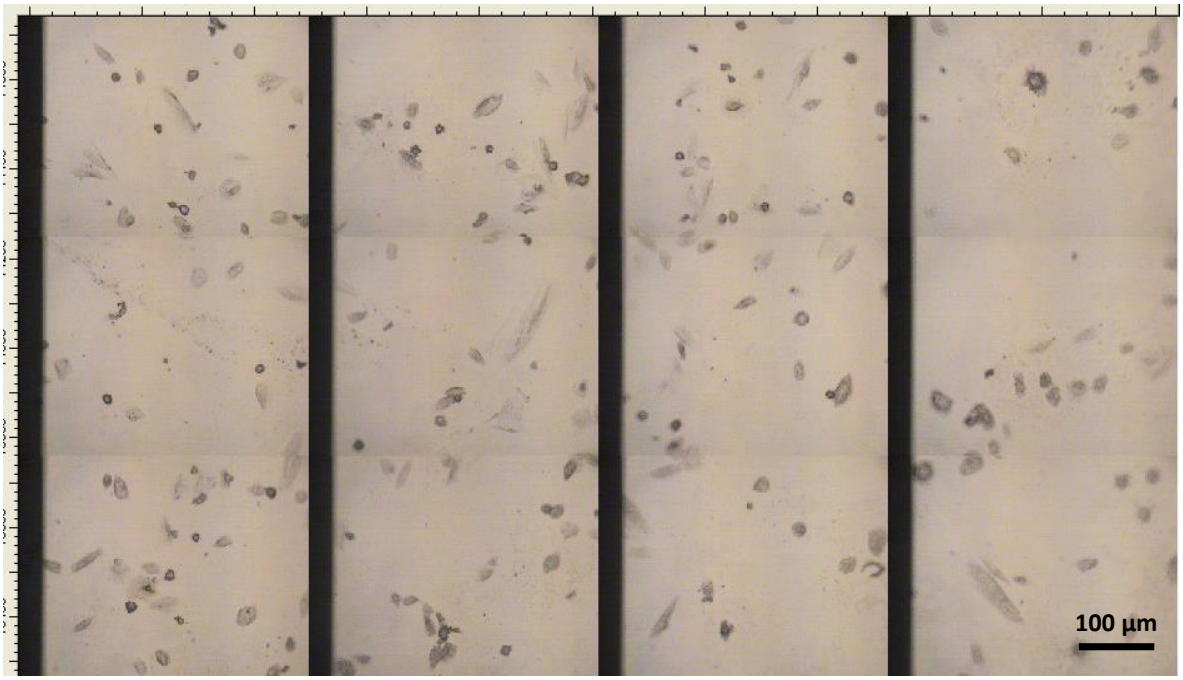

Figure 5.6. Photomicrographs of CCD-841 cells treated with ITC SiNPs.

The ability of IR spectroscopy to distinguish and map various cells and tissues has helped to address the question about the origin of spectral differences between normal and cancer cells. Considering the size of human cells (~5-30 μm), IR microspectroscopy is an ideal method to investigate individual cells. In this project, the differences in spectral quality between the non-treated individual cells and those treated with SiNPs were monitored using IR microspectroscopy.[5] NH_2 SiNPs were used as another type of control material to confirm if the observed effect originates from the isothiocyanate ligand on the surface of NPs being studied.

The spatial resolution of IR microspectroscopy measurements is normally limited by the size of the aperture used, which in turn determines the projected image onto the detector. As a result, to obtain higher quality data in order to resolve individual cells or various components within the cells, apertures as 3-6 μm^2 are desirable.[5] However, in this work we compare spectral data collected at an aperture of 10 μm^2 and it was possible to monitor the differences.

Point spectroscopy gives highly specific data about the material present in cells. Figures 5.7 to 5.12 show a micrograph (a), a chemical map (b) and a number of representative spectra (c) acquired from the positions along a trace shown in sub-figure (a) starting from near the end/edge of cells, going to the cytoplasm, passing the nucleus and then continuing the other side of the cell based on IR characteristics of Caco-2 and CCD-841cells. The image shown in sub-figure (b) was assembled using the integrated absorbance of the amide I band between 1614 cm^{-1} and 1702 cm^{-1} which is contributed to the map showing the protein distribution in the cell.

Both types of cells were treated with 50 μg/mL of ITC SiNPs and NH_2 SiNPs as control for 6 h. The IR spectra were acquired along a line to monitor the nuclei and cytosol IR characteristics of both untreated and treated cells. Each spectrum in sub-figure (c) is an average spectrum obtained from 20 individual cells. Substantial changes were observed in the finger print region (900-1800 cm^{-1}) when comparing treated and control cells.

The most prominent differences were found between the spectra from nuclei and cytosol of both types of cells treated with ITC SiNPs, specifically in ~1653 cm^{-1} which is an important feature of biological IR spectra for the amide I region. Figure 5.7 (c) shows the spectra of non-treated Caco-2 cells, the intensity of signal at 1600 cm^{-1} remained unchanged for the spectra obtained from the cytoplasm and nucleus. However, Caco-2 cells treated with ITC SiNPs (Figure 5.8) showed the largest signal for the amide I region in the nucleus, indicating

considerable protein conformational changes in the nuclei of treated cells with ITC SiNPs. This is in agreement with the hypothesis of the suggested enzymatic process in which isothiocyanates are involved. ITCs are known to induce phase II enzymes. The expression of most phase II genes is mediated through the antioxidant response element (ARE). Nrf2 is a powerful protein and is kept in the cytoplasm under normal conditions. Following the exposure to the oxidative stress such as isothiocyanates, Nrf2 translocates to the nucleus and binds to the DNA at the location of ARE to initiate the transcription of antioxidative genes and their proteins.[6] This will result in the transcriptional activation of a battery of detoxification and antioxidant proteins.[7] Therefore, the increased concentration of proteins in nuclei on cells treated with ITC SiNPs and a higher intensity of the amide I peak is consistent with this.

Similar behaviour was observed in CCD-841cells too; in the spectra of ITC SiNPs treated CCD-841cells, these bands in the amide I region are more pronounced for the nuclei of treated cells (Figure 5.11 (c)). In addition, the spectra obtained from treated cells revealed higher absorption in cytoplasm for C-H stretching region at 2800-3050 cm^{-1} and also a signal at 1737 cm^{-1} which appeared as a small peak on the high frequency side of the amine I band (Figures 5.8 and 5.11). This is related to the non-hydrogen bonded ester carbonyl C=O stretching mode of phospholipids.[8] These differences attributed to variations of phospholipid content, are coming from the cellular membrane. The increased absorption of phospholipids has been previously reported after treatment with various apoptosis inducers which lead to the phospholipid alterations in cellular membrane.[9, 10] This is in agreement with the fact that a large number of isothiocyanates have been shown to induce apoptosis in cells.[11] The fact that both treated cells showed the higher concentration of phospholipids shows this originates from ITC SiNPs because the cells treated with NH_2 SiNPs (Figures 5.9 and 5.12) did not show any increased phospholipid absorbance. This confirms that NH_2 SiNPs are non-toxic control nanoparticles able to be used without inducing significant cytotoxic cellular effects.

A comparison of the spectra of the two cell lines revealed significant spectral differences which indicate that IR spectroscopy can successfully monitor overall cell activity. These spectra display subtle differences between the treated and non-treated cells, and between the nuclei and the cytosol, which is in agreement with the behaviour of ITCs in cells related to the induction of phase II enzymes and apoptotic responses.

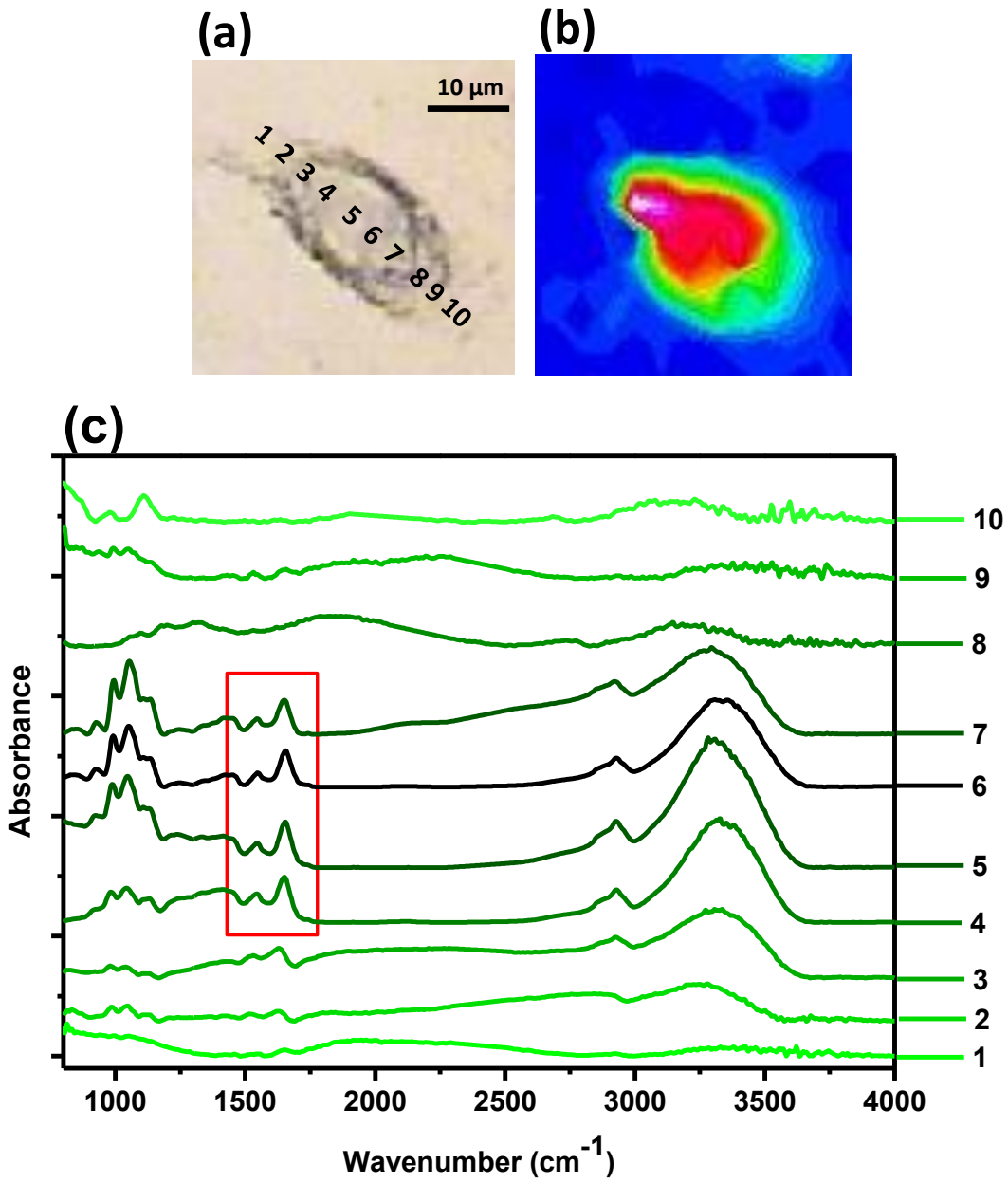

Figure 5.7. Synchrotron infrared imaging of a **control Caco-2** cell showing the visual image (a), protein infrared image (b) and representative infrared spectra (c) acquired along the line in image (a).

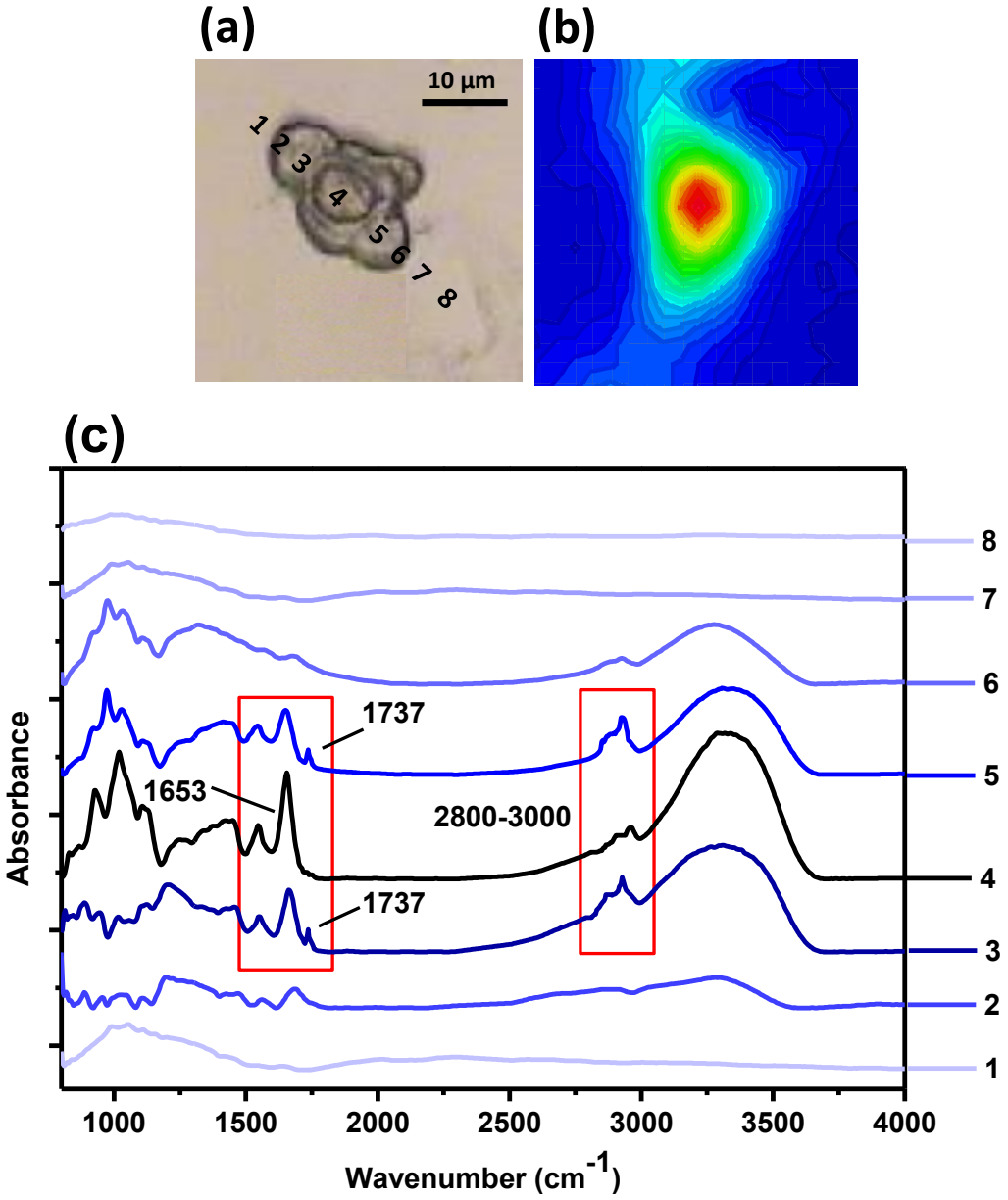

Figure 5.8. Synchrotron infrared imaging of a **Caco-2** cell treated with **ITC SiNPs** showing the visual image (a), protein infrared image (b) and representative infrared spectra (c) acquired along the line in image (a).

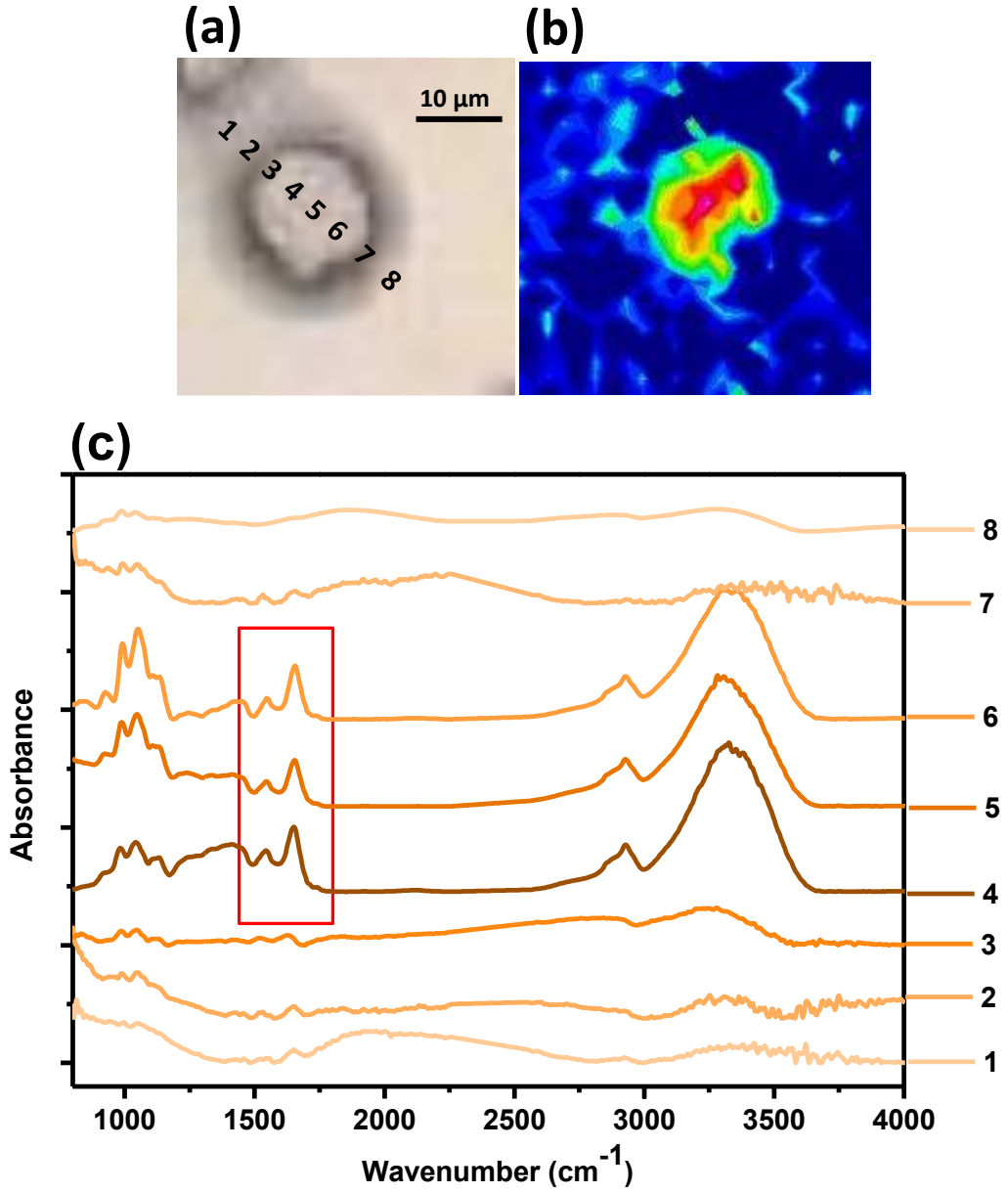

Figure 5.9. Synchrotron infrared imaging of a **Caco-2** cell treated with **NH_2 SiNPs** showing the visual image (a), protein infrared image (b) and representative infrared spectra (c) acquired along the line in image (a).

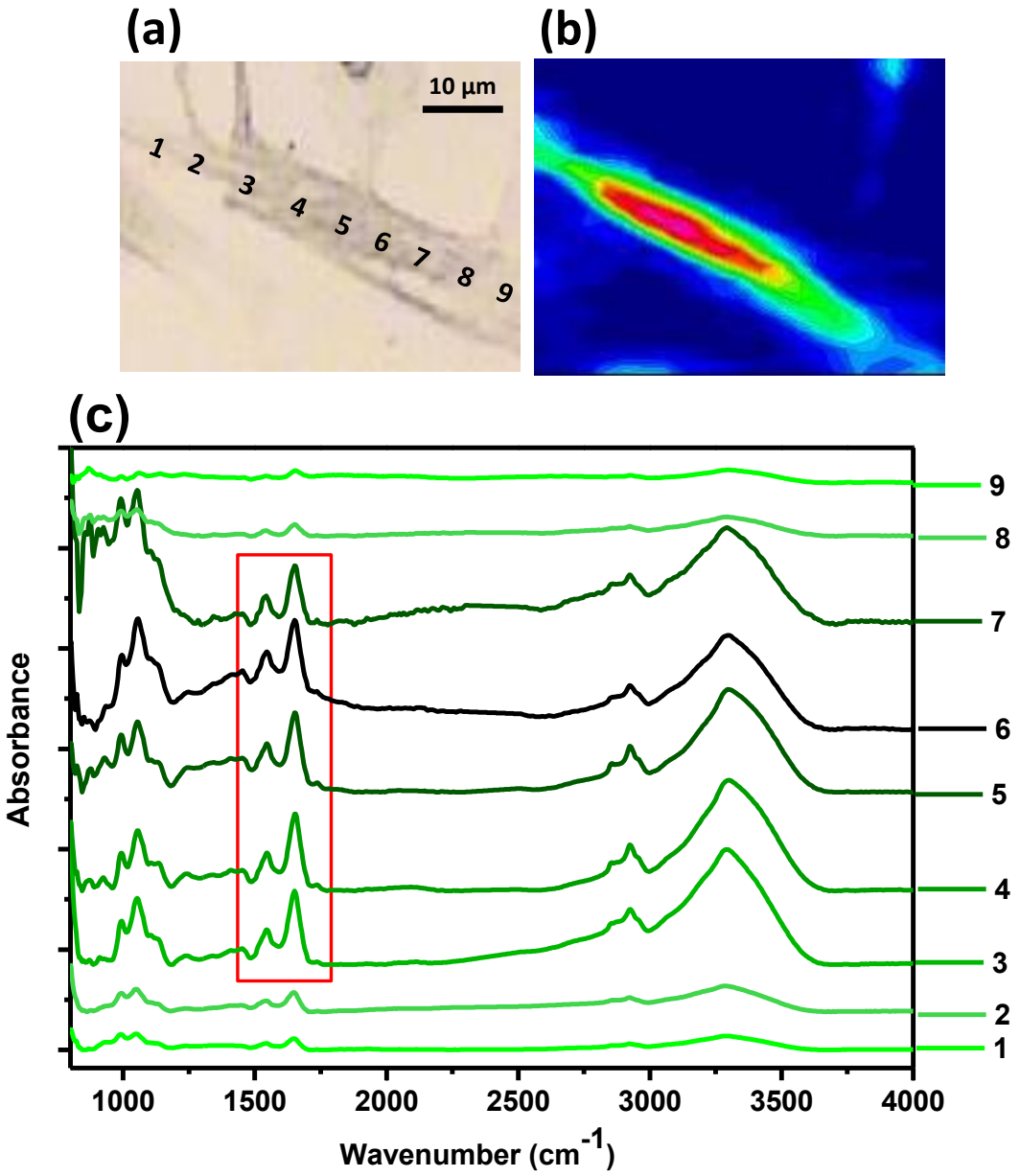

Figure 5.10. Synchrotron infrared imaging of a **control CCD-841** cell showing the visual image (a), protein infrared image (b) and representative infrared spectra (c) acquired along the line in image (a).

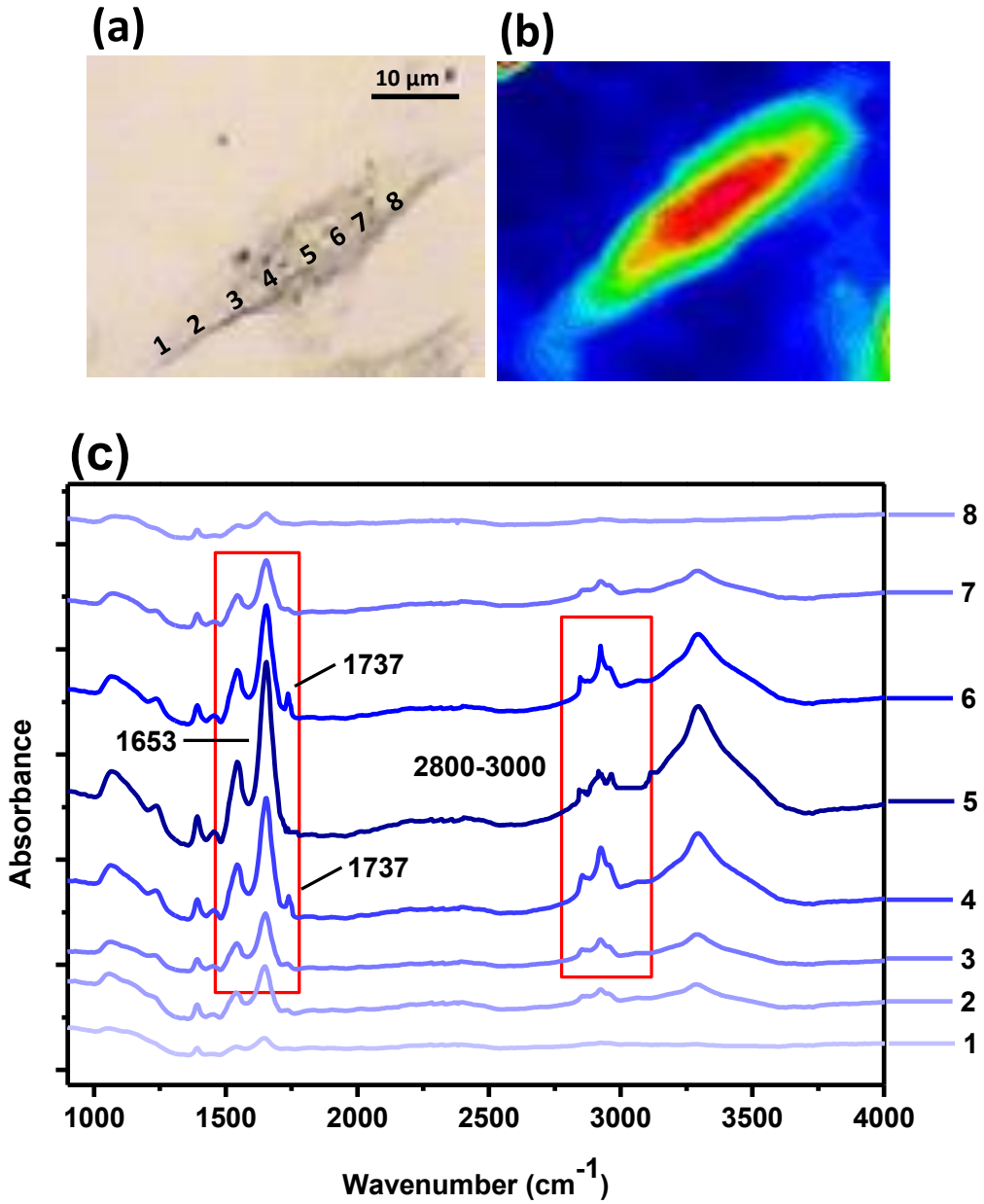

Figure 5.11. Synchrotron infrared imaging of a **CCD-841** cell treated with **ITC SiNPs** showing the visual image (a), protein infrared image (b) and representative infrared spectra (c) acquired along the line in image (a).

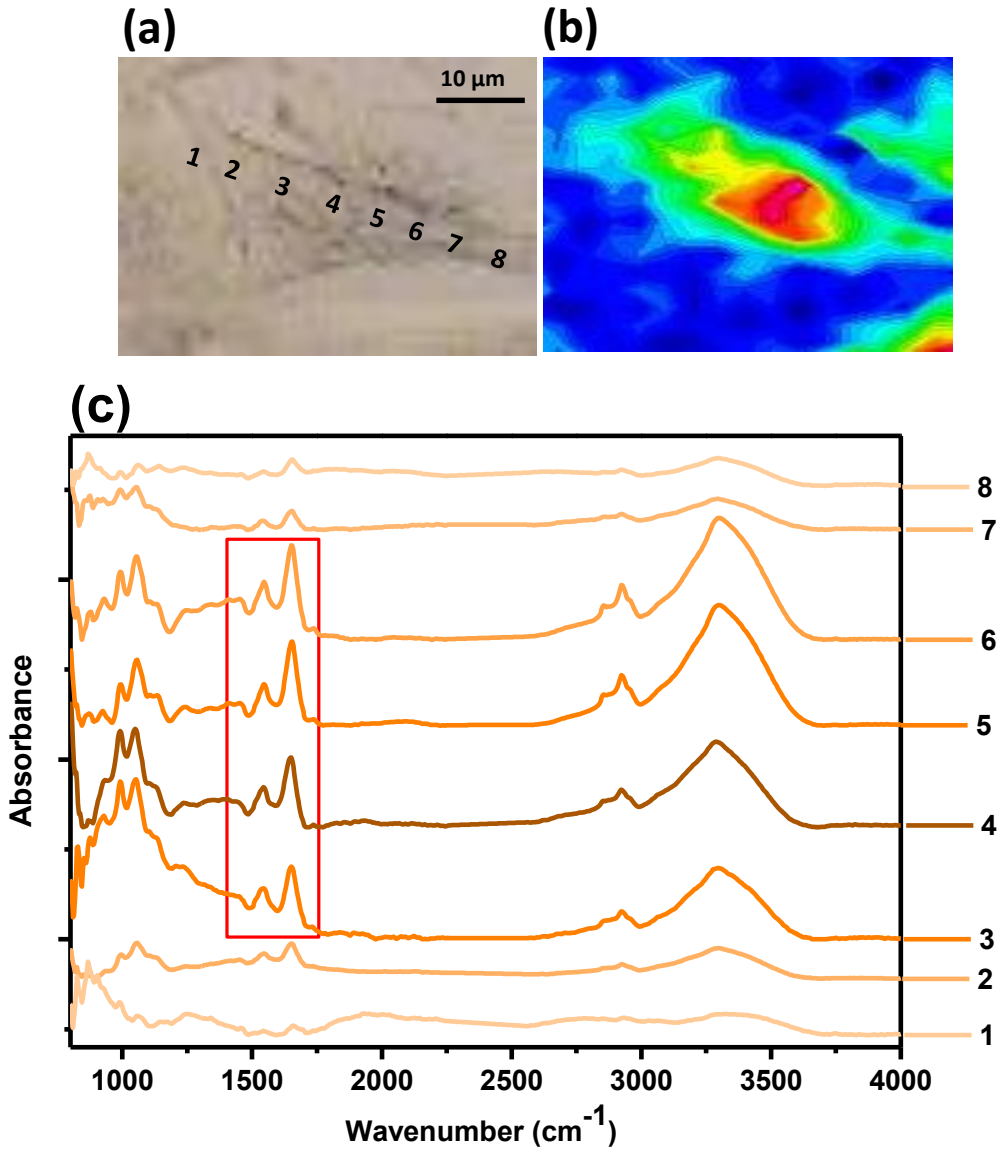

Figure 5.12. Synchrotron infrared imaging of a **CCD-841** cell treated with **NH_2 SiNPs** showing the visual image (a), protein infrared image (b) and representative infrared spectra (c) acquired along the line in image (a).

5.2.3. FTIR Mapping and Chemical Imaging Using Focal Plane Arrays Detector (FPA)

Specific information regarding the spatial distribution of cell components can be obtained by using the approach of functional group mapping. This enables plotting of the absolute intensity of one absorption band within the map. By comparing the maps of different functional groups or their ratios, the information related to relative distribution of different components in the sample can be obtained.[12]

The chemical changes associated with either the treated or control cells were evaluated using FPA mapping. IR imaging was used to evaluate the effect of nanoparticle internalisation on cells and visualise the chemical mapping information from different samples. If nanoparticles are internalised and introduce cytotoxicity or induce apoptosis to the cells, the pattern of chemical absorbance in cells will be different in control and treated cells. Figures 5.13 to 5.18 show the data obtained from FPA analysis, (a) visual micrograph, (b) 2D and (c) 3D chemical imaging of control and treated cells. The images shown in sub-figures (b) and (c) were assembled using the integrated absorbance between 2800 and 3000 cm^{-1} and thus were correlated to the phospholipid distribution of cells. All processed results are displayed on the same false-colour scale showing red (high) through to blue (low) for the given feature.

The data from control cells (Figures 5.13 and 5.16) demonstrated less absorbance when integrated in the same region, which is related to the phospholipid features of cells. The chemical imaging of both Caco-2 (Figure 5.14) and CCD-841 (Figure 5.17) cells when treated with 50 μg/mL ITC SiNPs after 6 h incubation demonstrated considerably higher intensity at this location. This confirms that the spectral data obtained from the individual cells gives a higher distribution of phospholipids for the treated cells, which possibly is as a result of the apoptotic process occurring in the cells due to the effect of isothiocyanate functionality on SiNPs.

The chemical image of cells treated with NH_2 SiNPs was similar to the control cells with no clear observation of phospholipid signal and very low absorption after the integration in the similar region (Figures 5.15 and 5.18). This is in agreement with the MTT data, obtained in Chapter 3, and confirmed that amine-functionalised SiNPs do not change the cell viability at this concentration.

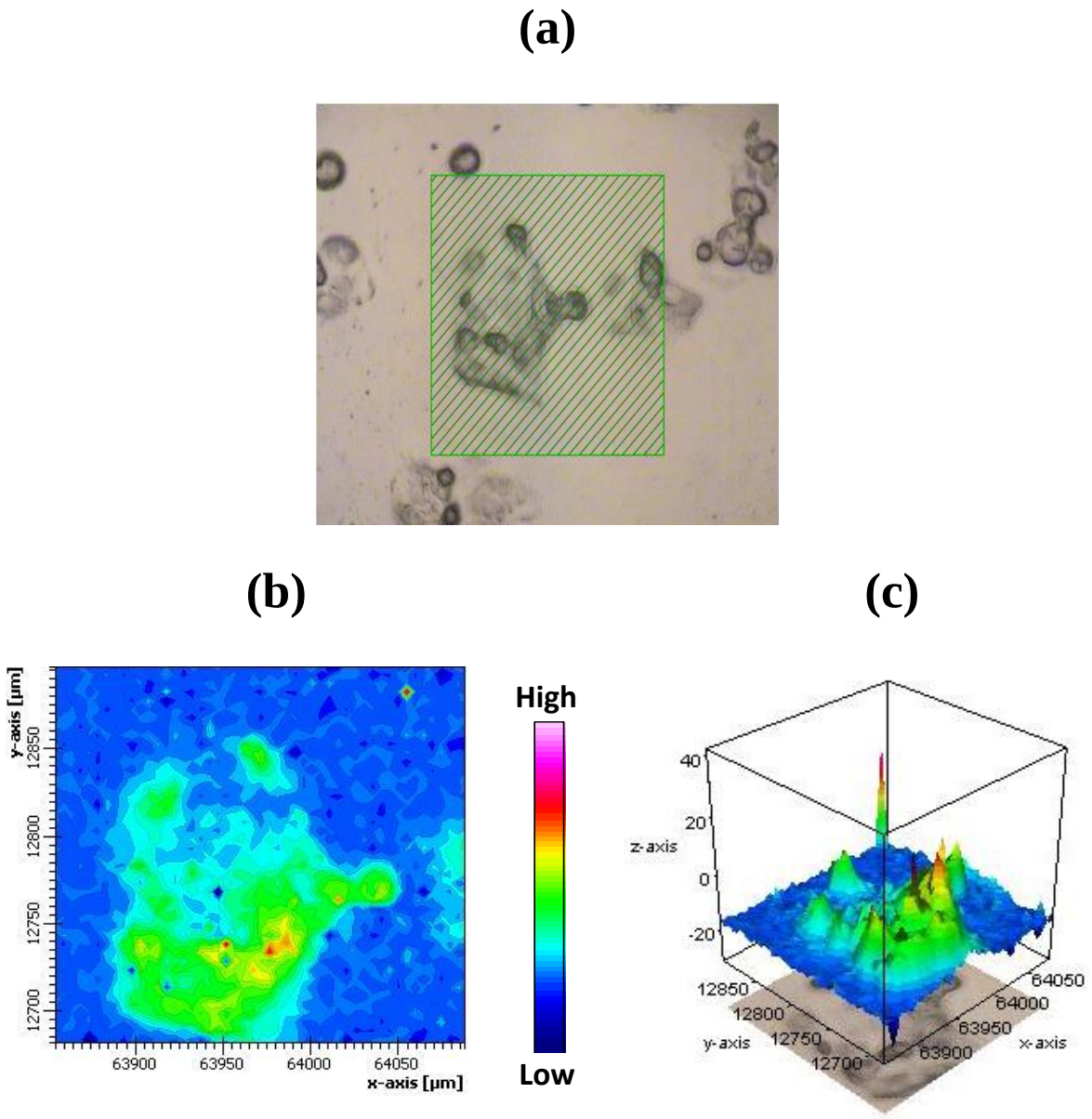

Figure 5.13. Visible and FTIR images of **control Caco-2** cells a microscope image (a), 2D (b) and the 3D (c) chemical images of cells (phospholipid profile). The colour bar indicates low (blue) to high (red) for component imaged.

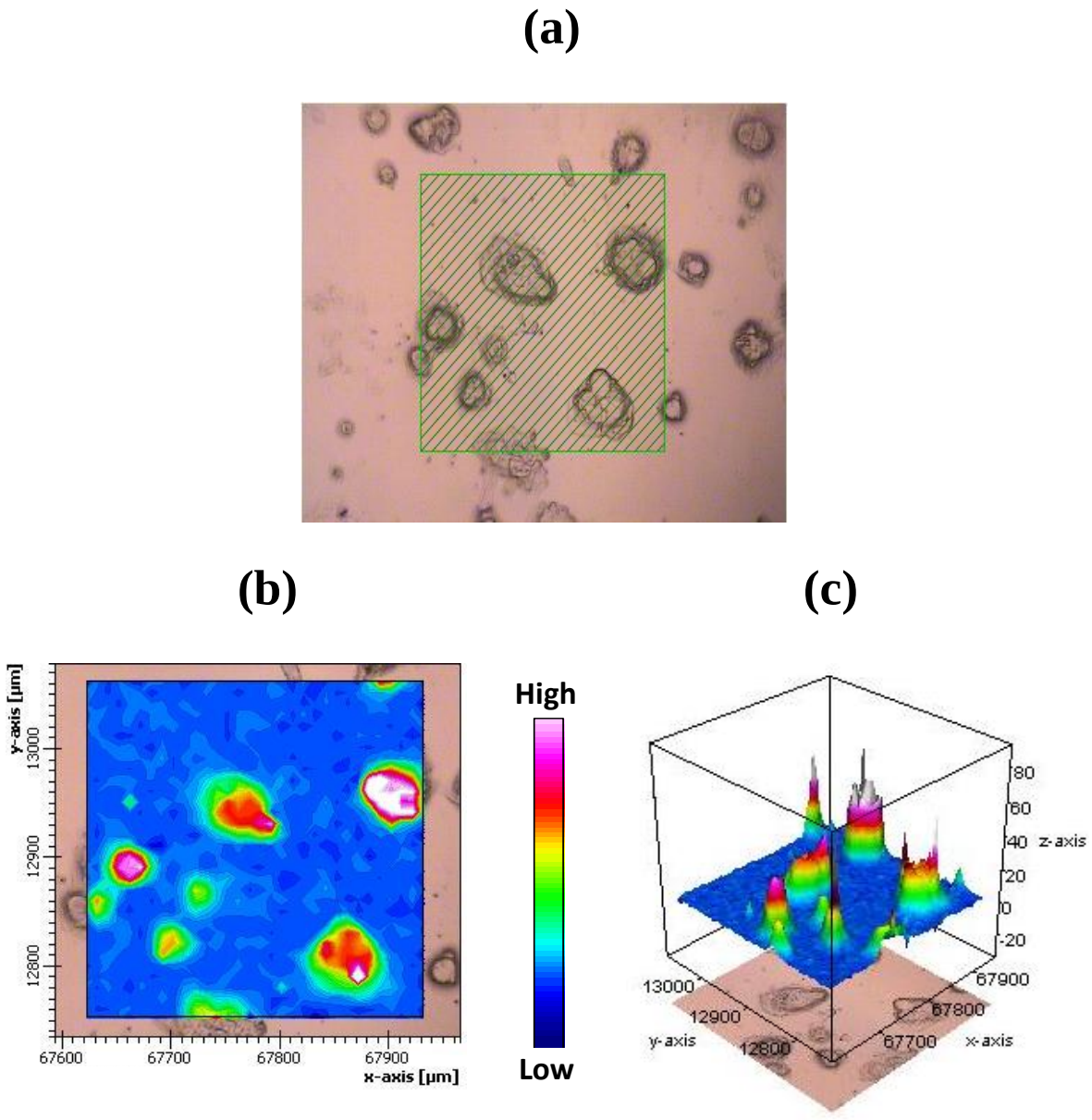

Figure 5.14. Visible and FTIR images of **Caco-2** cells treated with **ITC SiNPs** showing a microscope image (a), 2D (b) and the 3D (c) chemical images of cells (phospholipid profile). The colour bar indicates low (blue) to high (red) for component imaged.

.

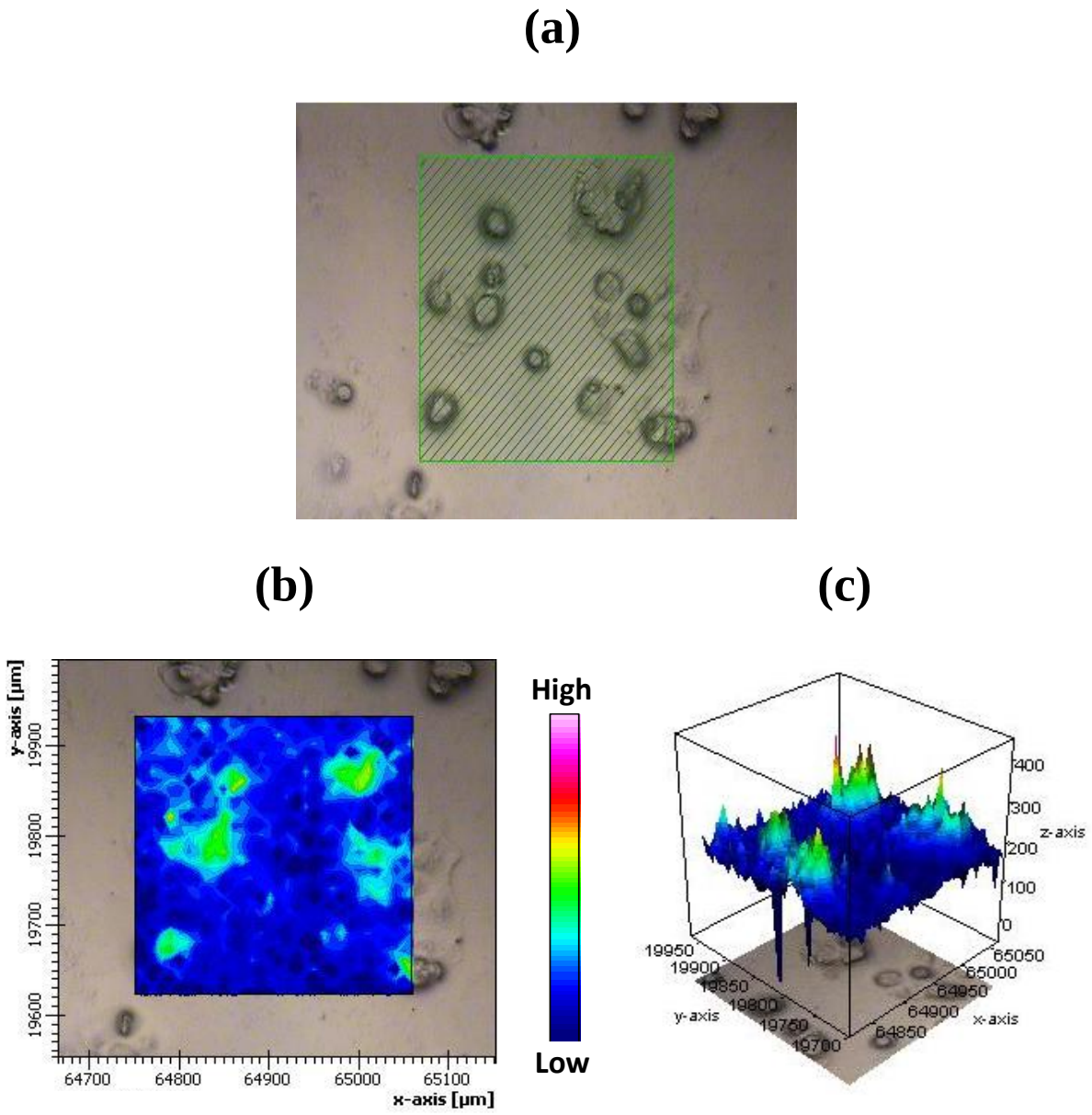

Figure 5.15. Visible and FTIR images of **Caco-2** cells treated with **NH_2 SiNPs** showing a microscope image (a), 2D (b) and the 3D (c) chemical images of cells (phospholipid profile). The colour bar indicates low (blue) to high (red) for component imaged.

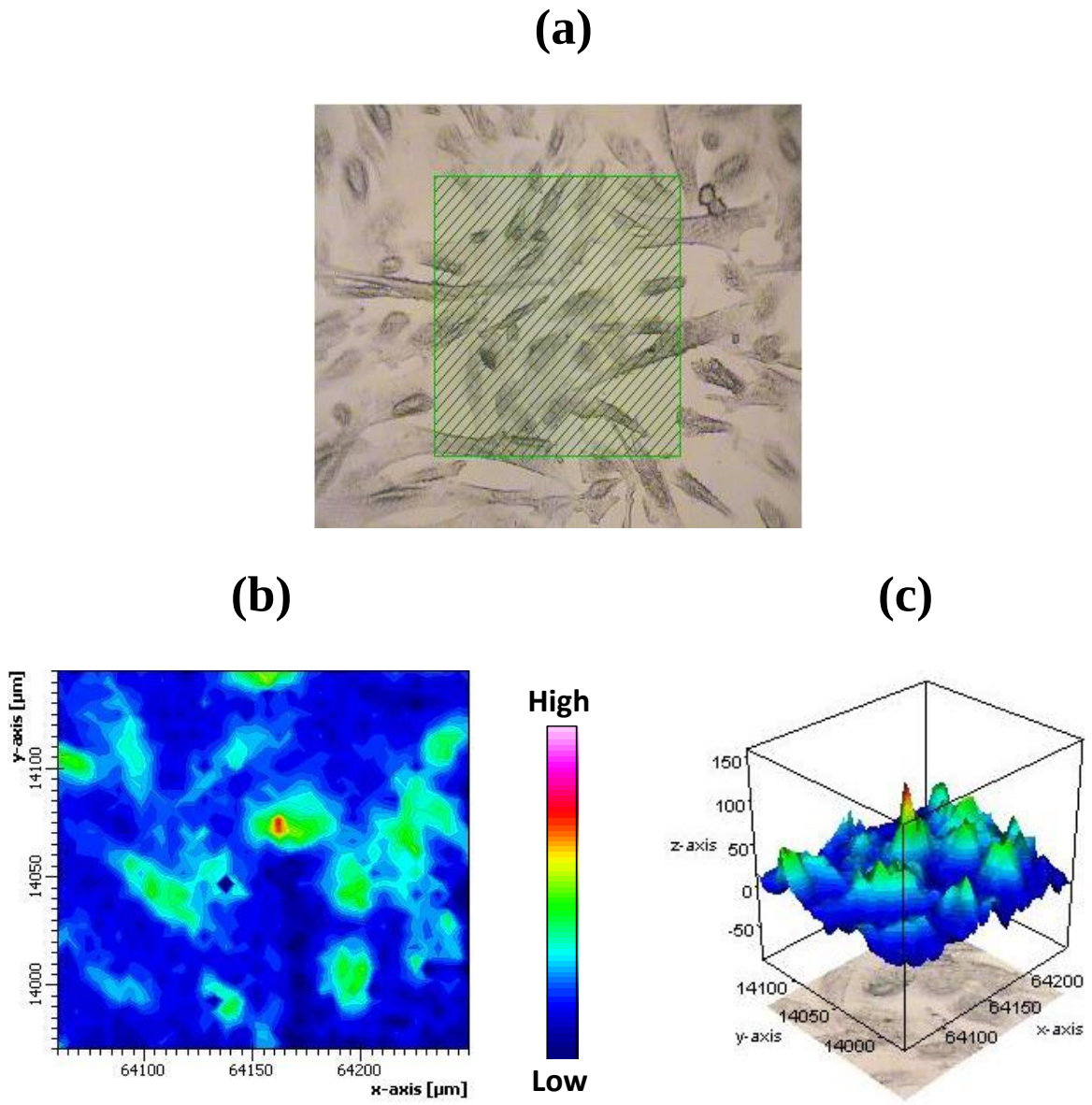

Figure 5.16. Visible and FTIR images of **control CCD-841** cells a microscope image (a), 2D (b) and the 3D (c) chemical images of cells (phospholipid profile). The colour bar indicates low (blue) to high (red) for component imaged.

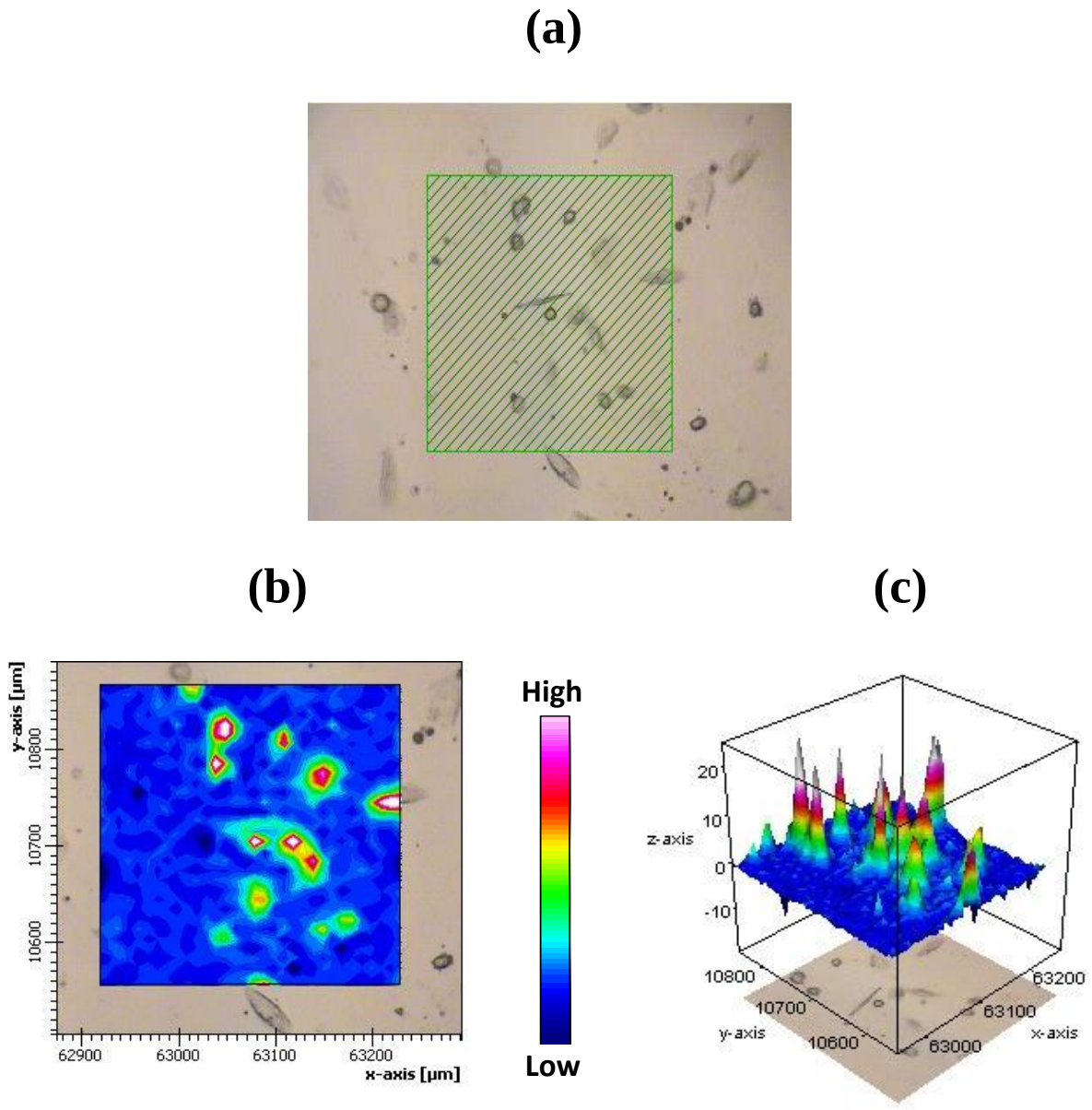

Figure 5.17. Visible and FTIR images of **CCD-841** cells treated with **ITC SiNPs** showing a microscope image (a), 2D (b) and the 3D (c) chemical images of cells (phospholipid profile). The colour bar indicates low (blue) to high (red) for component imaged.

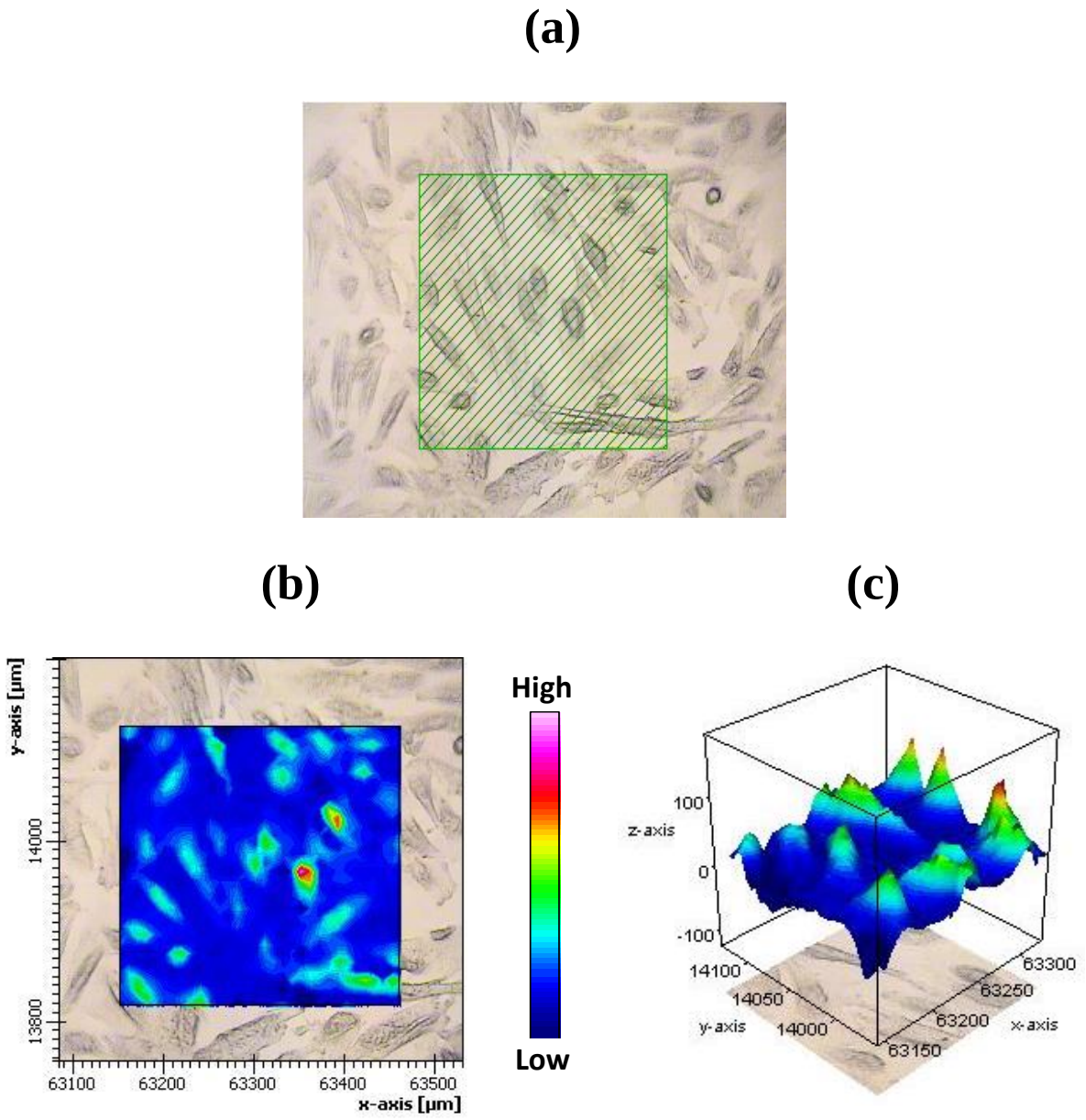

Figure 5.18. Visible and FTIR images of **CCD-841** cells treated with **NH_2 SiNPs** showing a microscope image (a), 2D (b) and the 3D (c) chemical images of cells (phospholipid profile). The colour bar indicates low (blue) to high (red) for component imaged.

5.3. Summary and Conclusions

ITC SiNPs can be successfully internalised into the cells and thus is a promising candidate for further investigation. FTIR microspectroscopy was used as a novel method to investigate the cellular uptake of nanoparticles. This helped in developing an understanding of the effect of these nanoparticles on cells and further investigate the mechanism of their function. This technique also enabled the visualisation of cells and to choose the specific regions to get the spectral data for analysis. 2D and 3D chemical maps were obtained using the FPA detector and revealed the chemical composition of biological cells by raster scanning the sample.

Clear changes were observed in the spectral regions corresponding to the nuclei of cells treated with ITC SiNPs correlated to the protein content and also for the cytoplasm of the treated cells correlated to the phospholipid contents. It is suggested that both of these spectral changes are associated to the mechanism of isothiocyanate when enter cells; they increase the protein level in the nuclei after the migration of enzymes from cytoplasm to the nuclei. ITC SiNPs also increase the chance of apoptosis in the cells which lead to the increase level of phospholipids in the treated cells compared to the non-treated cells and those treated with NH_2 SiNPs as control.

The IR microspectroscopy was capable of monitoring the level of cell activity in detail, and the major advantage of this method over microscopic methods, in the visible/UV spectral region, is its ability to monitor the chemical composition of the sample using the inherent spectral properties of the components. Cells demonstrated large signals for the chemical composition of treated cells when integrated in the phospholipid region.

Although the micron-scale resolution of SR-FITR microspectroscopy may not be the ultimate goal, this technique has significantly improved the resolution compared to alternative conventional sources, which allowed the analysis of various cell components before and after nanoparticle internalisation in this project.

5.4. References

1. Miller, L. M.; Smith, G. D.; Carr, G. L., Synchrotron-based biological microspectroscopy: From the mid-infrared through the far-infrared regimes. *Journal of Biological Physics* **2003,** *29* (2-3), 219-230.

2. Carr, G.; Reffner, J.; Williams, G., Performance of an infrared microspectrometer at the NSLS. *Review of Scientific Instruments* **1995,** *66* (2), 1490-1492.

3. Reffner, J. A.; Martoglio, P. A.; Williams, G. P., Fourier transform infrared microscopical analysis with synchrotron radiation: the microscope optics and system performance. *Review of Scientific Instruments* **1995,** *66* (2), 1298-1302.

4. Holman, H. Y. N.; Martin, M. C.; Blakely, E. A.; Bjornstad, K.; McKinney, W. R., IR spectroscopic characteristics of cell cycle and cell death probed by synchrotron radiation based Fourier transform IR spectromicroscopy. *Biopolymers* **2000,** *57* (6), 329-335.

5. Diem, M.; Romeo, M.; Matthäus, C.; Miljkovic, M.; Miller, L.; Lasch, P., Comparison of Fourier transform infrared (FTIR) spectra of individual cells acquired using synchrotron and conventional sources. *Infrared physics & technology* **2004,** *45* (5), 331-338.

6. Itoh, K.; Wakabayashi, N.; Katoh, Y.; Ishii, T.; Igarashi, K.; Engel, J. D.; Yamamoto, M., Keap1 represses nuclear activation of antioxidant responsive elements by Nrf2 through binding to the amino-terminal Neh2 domain. *Genes & development* **1999,** *13* (1), 76-86.

7. Keum, Y.-S.; Jeong, W.-S.; Kong, A. T., Chemoprevention by isothiocyanates and their underlying molecular signaling mechanisms. *Mutation Research/Fundamental and Molecular Mechanisms of Mutagenesis* **2004,** *555* (1), 191-202.

8. Jamin, N.; Miller, L.; Moncuit, J.; Fridman, W. H.; Dumas, P.; Teillaud, J. L., Chemical heterogeneity in cell death: combined synchrotron IR and fluorescence microscopy studies of single apoptotic and necrotic cells. *Biopolymers* **2003,** *72* (5), 366-373.

9. Liu, K.-Z.; Mantsch, H., Apoptosis-induced structural changes in leukemia cells identified by IR spectroscopy. *Journal of Molecular Structure* **2001,** *565*, 299-304.

10. Liu, K.-Z.; Jia, L.; Kelsey, S. M.; Newland, A.; Mantsch, H., Quantitative determination of apoptosis on leukemia cells by infrared spectroscopy. *Apoptosis* **2001,** *6* (4), 269-278.

11. Wu, B.-B.; Gong, Y.-P.; Wu, X.-H.; Chen, Y.-Y.; Chen, F.-F.; Jin, L.-T.; Cheng, B.-R.; Hu, F.; Xiong, B., Fourier transform infrared spectroscopy for the distinction of MCF-7 cells treated with different concentrations of 5-fluorouracil. *Journal of translational medicine* **2015,** *13* (1), 108.

12. McIntosh, L. M.; Mansfield, J. R.; Crowson, A. N.; Mantsch, H. H.; Jackson, M., Analysis and interpretation of infrared microscopic maps: Visualization and classification of skin components by digital staining and multivariate analysis. *Biospectroscopy* **1999,** *5* (5), 265-275.

Chapter 6: Conclusions and Future Prospects

6.1. Summary and Conclusions

The development of novel new nanotechnologies for biomedical applications, commonly referred to collectively as nanomedicine, has great potential to improve diagnosis and therapeutic methods and thus the overall prognosis for a wide range of diseases. In recent decades, the advancement in nanotechnology and material science has resulted in an increasing number inorganic nanomaterials which have been studied as potential drug delivery carriers, due to their versatile physicochemical properties. SiNPs, in particular, exhibit several unique properties, including conjugation versatility, suitable biocompatibility and very low cytotoxicity levels and therefore offers an excellent drug delivery platform candidate.

Although significant advances have been made in nanomedicine, the largest challenge remains the targeted delivery to a specific cell. The difficulty lies in the recognition of cancerous cells amongst thousands of normal healthy cells as well as providing a suitably stabile nanodelivery system. To date, research efforts have mainly focused on the delivery efficiency in one cell line. However, the cellular delivery system to target specific cell lines in an extremely diverse environment of cell types is required and is not addressed in the majority of studies. SiNPs with multipurpose surface functionalities to target specific receptors with high transfection efficiency are key areas for further development in the next decade, which might lead to breakthroughs for cellular delivery systems.

The work highlighted in this thesis has focused primarily on the synthesis and characterisation of functionalised SiNPs for biomedical applications. Compounds with anticancer properties, such as thiourea and isothiocyanate, were used as capping ligands. These multifunctional systems benefit both from the optical properties of SiNPs for bioimaging purposes and the targeting and therapeutic properties of the conjugate for drug delivery purposes.

The primary objective of the thesis is to develop nanomaterial candidates which are non-toxic, economical with efficient synthesis, for use in biomedical applications. There are three key challenges to realising the potential of such a system:

- A nanodelivery system which exhibits long-term stability.
- The development of a diagnostic approach with efficient targeting of cancer cells.

- Maximally exploiting the therapeutic properties of biomolecules when conjugated on NPs

The first of these three challenges was tackled by utilising a nanosystem which benefits from the central role of the covalent surface Si-C bond, which is inherently stable. For efficient targeting of cancerous cells, the overexpression of EGFR in several common types of cancer was exploited, by using thiourea derivates as the conjugate. On the final challenge, AITC, known as an economical and highly effective anticancer biomolecule, was applied in conjugation with SiNPs for the first time.

In **Chapter 1**, a short history and general introduction to nanomaterials is provided. The properties of semiconductor QDs and in particular SiNPs are discussed, highlighting the origin of SiNP luminescence and influence of the quantum confinement effect in detail. Later, an overview of different methods for synthesis and functionalisation of SiNPs is given with a discussion of the advantages and disadvantages of each method. The possible biomedical applications of SiNPs are also mentioned in addition to the importance of cytotoxicity in the biomedical applications of NPs. The chapter continues by underlining different types of thiourea derivatives as potential inhibitors of EGFR overexpression in cancer cells. Finally, the use of isothiocyanate compounds as potential chemopreventive properties is discussed.

The work in **Chapter 2** describes the general procedures and detailed methods used to synthesise porous SiNPs from electrochemical etching. This is followed by the functionalisation of porous silicon to produce amine-functionalised SiNPs, thiourea-functionalised SiNPs, bromine-functionalised SiNPs, isothiocyanate-functionalised SiNPs in addition to bottom up amine-functionalised SiNPs. Later in this chapter, various apparatus and research techniques used for the physiochemical characterisation of synthesised SiNPs are explained. Finally, biological assays and the synchrotron FTIR microscopy measurements, used in this thesis, are discussed.

In **Chapter 3**, a method for functionalising SiNPs with a thiourea layer over the NP surface is presented. These novel resultant SiNPs offer significant advantages compared to conventional therapeutics. These include the integration of the targeting moiety and therapeutic moiety in the same system, the use of inexpensive materials, and more importantly the production of a highly stable nanosystem.

The synthesised NPs were characterised with a wide selection of techniques such as FTIR, EDX, XPS, TEM, DLS, UV-vis and PL spectroscopy which allowed the chemical composition and physiochemical properties of the materials to be determined. It is shown that the SiNPs produced by this method are silicon rich, crystalline, luminescent, and functionalised with thiourea chains. A quantum yield of approximately 10% was achieved. The PL stability both in the long-term and for a range of different pH values (4-9) confirmed the suitability of these particles for a variety of possible biomedical applications.

The product was examined for *in vitro* cytotoxicity in Caco-2 and CCD-841 cells. The results showed significant toxicity of thiourea SiNPs after 72 h of incubation in Caco-2 cancer cell line, and the toxicity was concentration dependent and became saturated for concentrations above 100 μg/mL. Confocal microscopy confirmed the cell internalisation of SiNPs and flow cytometry data indicated receptor-mediated targeting in cancer cells. Finally, in order to confirm the interaction between the thiourea on the surface of SiNPs and EGFR, Elisa assay was performed on cells.

This nanocomposite takes advantage of the EGFR active targeting of the ligand in addition to the photoluminescence properties of SiNPs for bioimaging purposes.

The work in **Chapter 4** explored the first synthesis and characterisation of SiNPs functionalised with isothiocyanate. This was accomplished by using two different methods with two types of precursors, amine and bromine-functionalised SiNPs. The materials produced in this approach were similar in terms of the chemical characterisation. The surface functionalisation was analysed by FTIR, EDX and XPS studies. However, the optical properties of NPs obtained from the corresponding bromine-functionalised SiNPs as precursor were stronger with a quantum yield of 12.55% which made them more suitable candidates for bioimaging and uptake studies. The highly crystalline structure of NPs was shown by TEM images and DLS measured the hydrodynamic size which was slightly larger than the core size. The *in vitro* toxicity was verified by MTT assay in both cancer and non-cancer cell lines. The synthesised SiNPs were found to reduce the viability of Caco-2 cells to approximately 50% after 24 h treatment with 70 μg/mL NPs. Visualisation imaging of NPs in Caco-2 colorectal cancer cells showed the internal distribution of NPs in the cells. The internalisation of ITC SiNPs (P Br SiNPs) was confirmed by flow cytometry and it is most likely to be based on the receptor mediated endocytosis mechanism since the temperature behaviour was observed in the uptake process of SiNPs.

Finally, a novel approach for investigating the NP cell internalisation is introduced in **Chapter 5**. Synchrotron-based FTIR microspectroscopy was used to determine the effect of isothiocyanate-functionalised SiNPs after the cell internalisation. Individual spectra were collected from both nuclei and cytoplasm of treated and control cells. Spectral comparison of cells treated by NPs and control cells revealed the variations in the protein and phospholipid contents of the treated cells as a result of the effect of NP internalisation. The increased concentration of proteins in the nuclei of treated cells resulted in a higher intensity of the amide I peak, which indicated considerable protein conformational changes in the nuclei. In addition, the spectra obtained from treated cells revealed higher absorption for C-H stretching in the cytoplasm, due to variations of phospholipid content of the cellular membrane. This is assumed to be the result of the apoptosis effect from the isothiocyanate functional group on the treated cells leading to the phospholipid alterations in cellular membrane.

6.2. Discussions and Future Prospects

The methods described in the previous chapters are demonstrated to provide a sound approach to synthesise stable SiNPs, which shows great promise for applications in bioimaging and biomedical fields. They also represent a solid basis with which to develop a further understanding of SiNP properties. However, there are several significant concerns that must be addressed before SiNPs become widely used in the biomedical field.

Despite the fact that there are already numerous researchers working with SiNPs, the nature of certain properties is still unclear. Thus, further investigations are necessary to determine whether the current theories of SiNP optical properties, as explained by quantum confinement and oxide-related defects, are sufficient to fully describe the full range of observed phenomena.[1-3] An example of this issue is in the understanding of photoluminescence quenching when sensing certain chemical molecules, as the competing theories of this are incompatible.

More generally, other possible research avenues include improvements in synthetic strategies to produce stable SiNPs dispersed in a wide range of solvents instead of the given one, and to consistently fabricate controlled particles with an appropriate size and biochemical functional groups for more widespread applications.

It is already established that silicon has a low intrinsic toxicity in cells, in contrast to Cd, for example, which is a significant advantage of SiNPs when considering their biomedical applications. As the number and type of SiNPs in this field continues to increase, studies to characterise their effects after exposure and to address their potential toxicity are relatively few. Therefore, a systematic approach to obtain accurate information on the cytotoxicity of SiNPs (with various additional functionalities) is necessary. It is essential to understand the extent to which NPs impact the specific system or cell line under study. In addition, the *in vivo* cytotoxicity and behaviour of NPs could be completely different as a result of the presence of plasma proteins and the formation of protein corona, which all need to be considered before any wider NP use.

In regard to the two approaches used for the synthesis of amine-functionalised SiNPs, top down methods produce purer and better dispersed NPs in aqueous solvents with no sign of aggregation. The electrochemical etching in general is a straightforward, cost-effective and rapid method. The synthesised particles by this method showed lower cytotoxicity towards cells which indicates that they are more suitable for biomedical applications. However, the resultant SiNPs show a broader size distribution and varied shape compared to the bottom up products. Control of NP size and shape is essential for several reasons, the size of the NPs affects their movement in and out of the vasculature, whereas the margination of particles to vessel wall is impacted by their shape. But most importantly this factor can determine which specific cell uptake mechanism is followed. As a result, utilising batches of NPs with a wide range of sizes will weaken the conclusions of cell internalisation studies, since each size group of NP within a batch will follow different uptake pathways. In addition, Another drawback of top down method, harsh conditions need to be applied for the synthesis; with regard to electrochemical etching, the toxicity of reagents such as hydrofluoric acid used for the preparation of SiNPs.

The key disadvantage of top down methods for the synthesis of SiNPs is scalability. However, there are several examples of such methods being applied on industrial scales, producing particles beyond milligram scales. For instance, the British company, pSiMedica, and a Japanese company, Tokao Yonehara of Canon Inc., have been successful in meeting this challenge by optimising the synthesis of functionalised porous silicon in large quantities leading to the anodization of 10,000 silicon wafers per month. In this technique, layers of pure silicon are deposited onto the porous layer of a silicon wafer. Then, the wafer is bonded to

another silicon wafer with an insulating silicon-oxide surface, in a way that the pure layer of silicon ends up sandwiched in the middle. The porous silicon is selectively dissolved away to leave the desired product which is silicon on top of an oxide layer on top of the silicon wafer.[4]

The bottom up approach offers a better chance to obtain more homogeneous chemical compositions for nanoparticles. In addition, it is low-cost and offers the use of a wide variety of available precursors to synthesise SiNPs. Uniform size distribution and the ability to produce large amounts of material can be considered as the major advantages of this technique. However, the resulting NPs in this method are sometimes less dispersible, possibly due to the high coverage of the particles by the specific functional ligands as they are most of the time originally attached to the core from the beginning in the starting material. In addition, as a result of the solution based synthesis in this approach, the presence of unwanted impurities in the product is normally the drawback of this method which typically requires an extensive purification protocol to be removed. This sometimes leads to a significant degree of oxidation, which subsequently can result in red-tailed broad emission features in the PL spectrum and in some cases causes cytotoxicity in the biological environment.

One of the significant factors when considering the use of NPs more generally, is the high tendency of NPs to form aggregates and their resulting long term stability in specific biological media. Therefore, before any further research applying NPs in biological environments it is crucial to produce well-dispersed and stable batches. The aggregation limits the contact between the NPs and cells, thus reducing the transfection efficiency. Another possible consequence of not having stable NPs is the excretion of NPs and their accumulation in the cell which can harm the cell growth. However, due to the chemical stability of SiNPs, these samples cannot be dissolved easily in the cell, and it is difficult for them to leave cells like ions. Exocytosis can occur due to the osmotic pressure, but this likey has very low rate because their concentration in cells are quite low.

With respect to the synthesis of the thiourea-functionalised SiNPs, the resultant particles showed no obvious sign of agglomeration and NPs were dispersible in a wide range of different solvents. However, a systematic study focusing on the interaction of these particles *in vivo* is still required to predict and avoid any undesired interactions and possibly minimise them by further modification of the particle surface. It would be extremely beneficial to extend the techniques, applied in this thesis, for larger scale production of SiNPs of a wide range of sizes with different photoluminescence colours. Efforts also need to be directed towards improving

the purity of the final product by reducing the use of toxic chemicals such as HF used in electrochemical etching.

The inorganic NPs functionalised with biomolecules are thought to be internalised through the endocytosis process since the particle size is normally less than 500 nm. Although the detailed mechanism of endocytosis has not been well understood, microscopic observations indicate the changes in cell morphology and cytoskeleton structure while endocytosis happens. The endocytosis may be a receptor-mediated, or non-receptor-mediated process.[5] Although considerable advances in the development of SiNPs conjugated with biologically active ligands such as thiourea have been made in this project, with respect to the area of EGFR inhibiting effects of NPs to confirm the receptor mediated endocytosis, there are still significant factors that could be further developed and understood. This project was focused on two cell lines (normal and cancerous) with different levels of receptor expression in order to evaluate any possible interaction between the thiourea-functionalised SiNPs and EGFR. In order to establish the potential of these particles in these regards, and to optimise transfection efficiency of particles, an objective approach is required to cover various types of cell lines with different levels of receptor expression. Obviously this level could vary depending on the passage number of cells and the culture conditions which might affect the exact amount of the EGFR receptor. Therefore, western blotting to determine the accurate level of the EGFR for specific cells before doing any flow cytometry or Elisa test would be highly beneficial, and lead to more robust data. Another possible alternative in this case could be the use of well-known and conventional EGFR inhibitors before any treatment with thiourea-functionalised SiNPs. By following this approach, the fluorescence measured by flow cytometry or the absorbance measured by Elisa test could provide a proper comparison. This would enable the evaluation of whether this inhibition is actually related to the thiourea ligand, and if there is any difference between non-treated or NP treated cells, and those treated first with the inhibitor and then later with the NPs. This would provide a much improved understanding of NP-receptor interactions, and the driving forces in the transfection process which ultimately lead to better cell specific target delivery with high efficiency.

The final precondition for successful treatment of diseases with SiNPs requires an effective bioconjugate. Currently, in this project it was not possible to accurately determine the amount of the therapeutic ligand on the surface of SiNPs obtained by top down approach. This is due to the batch dependent property of the obtained particles which affects the availability and

consistency of active sites on the surface of hydrogen-terminated SiNPs after each synthesis. Any evaluation of therapeutic properties needs to be compared with a control drug of equivalent amount with known properties to determine the drug load in the system under study. Modification of the system towards the synthesis of more homogeneous particles from the top down method in the future could address this issue.

A comparison between the confocal images obtained from the cells treated with ITC SiNPs and those obtained from thiourea SiNPs (Chapter 3, section 3.14.2.1) indicated a clear difference in terms of the internal localisation of these two types of SiNPs. The intensity of thiourea-functionalised SiNPs detected in the cells was brighter than ITC SiNPs and they were mostly distributed within the cytoplasm, whereas ITC SiNPs showed lower brightness with some NPs distributed in different parts of cytoplasm as well as the nuclei. Even though the reason in this regard is not exactly clear, there are several possibilities which may attribute for this different behaviour. First of all, due to the lower viability of cells treated with ITC SiNPs at high concentrations, the amount of SiNPs used for the treatment of cells before imaging was almost half of those used for the thiourea SiNPs (50 µg/mL ITC SiNPs vs 100 µg/mL thiourea SiNPs). This concentration level was optimised to this amount as it was not possible to get enough number of cells for imaging analysis after the treatment with higher concentrations of ITC SiNPs. In addition, those cells which survived and were detected by the microscope did not show any uptake. Therefore, it can be concluded that cell viability correlates with the lack of uptake in the cells and thus lower concentrations of NPs were used for the imaging analysis. In addition, the different ratio of silicon to ligand in these two types of NPs may have led to different proportions of silicon core entering the cells, and therefore may have led to different levels of signal from the particles detected by the confocal microscope. Moreover, size uniformity of NPs should be considered when their interactions with biological systems are examined. Thus, another important factor which may be responsible for this behaviour is the possibility of having more than one endocytosis mechanism in cells treated with ITC SiNPs which would lead to the accumulation of them in different parts of the cells. For example, if particles follow marcrocytosis or clathrine-dependent endocytosis, it is possible that they are sent to lysosomes for degradation[6, 7] whereas if caveolae-dependent endocytosis is the major route of NP endocytosis, it is likely they accumulate in endoplasmic reticulum or nuclear envelope.[8, 9] In addition, clathrin- and caveolae-independent endocytosis which relies on cholesterol and specific lipid compositions, can bypasse the classical endocytic organelles and deliver the NPs via nonendosomal, cytosolic organelles to the endoplasmic reticulum.[10]

In biological solutions such as cell culture media, the surface chemistry of NPs plays a crucial factor in their localisation. Therefore, the higher chemical activity of isothiocyanate functional group could possibly have led to stronger interactions between NPs and various serum proteins in the biological media, causing partial agglomeration. If the NPs are already aggregated or agglomerated prior to binding to the cell membrane, their endocytosis patterns would differ from that of individual NPs.[11]

It should be mentioned that all these parameters need to be well determined and optimised for a better understanding of the behaviour behind the internal localisation of NPs, as it is critical to their intended therapeutic function. Due to the position and amount of NPs within a cell, identification of any degradation of the NPs within intracellular compartments and its impact on cell viability needs to be further addressed. Modifying the loading time and concentration of NPs can promote cell visibility for imaging applications.

Nontoxic SiNPs have created a new chapter in the field of nanoscience. This thesis has demonstrated that it is possible to synthesise SiNPs with high stability, targeted delivery and incorporating the therapeutic properties of conjugated biomolecules. In the future, properly designed materials may expand the use of QDs for biomedical applications, which have been disadvantaged by the presence of toxic elements in many semiconductor QD systems. It is highly likely that interest and research into the field of SiNPs will increase in the coming decades, and it is hoped that a wide range of diseases with a currently poor prognosis will eventually be effectively diagnosed and treated with negligible side-effects. Such developments in the field of nanomedicine will certainly have an immeasurably positive influence on future society.

6.3. References

1. Fuzell, J.; Thibert, A.; Atkins, T. M.; Dasog, M.; Busby, E.; Veinot, J. G.; Kauzlarich, S. M.; Larsen, D. S., Red states versus blue states in colloidal silicon nanocrystals: exciton sequestration into low-density traps. *The Journal of Physical Chemistry Letters* **2013,** *4* (21), 3806-3812.

2. Warner, J. H.; Hoshino, A.; Yamamoto, K.; Tilley, R., Water-Soluble Photoluminescent Silicon Quantum Dots. *Angewandte Chemie* **2005,** *117* (29), 4626-4630.

3. Zhou, Z.; Brus, L.; Friesner, R., Electronic structure and luminescence of 1.1-and 1.4-nm silicon nanocrystals: oxide shell versus hydrogen passivation. *Nano Letters* **2003,** *3* (2), 163-167.

4. Canham, L.; Aston, R., Will a chip every day keep the doctor away? *Physics World* **2001,** *14* (7), 27-31.

5. Rolland, A., *Advanced gene delivery*. CRC Press: **2003;** Vol. 10.

6. Benmerah, A.; Lamaze, C., Clathrin-Coated Pits: Vive La Différence? *Traffic* **2007,** *8* (8), 970-982.

7. Mayor, S.; Pagano, R. E., Pathways of clathrin-independent endocytosis. *Nature reviews Molecular cell biology* **2007,** *8* (8), 603-612.

8. Kou, L.; Sun, J.; Zhai, Y.; He, Z., The endocytosis and intracellular fate of nanomedicines: Implication for rational design. *Asian Journal of Pharmaceutical Sciences* **2013,** *8* (1), 1-10.

9. Pelkmans, L.; Püntener, D.; Helenius, A., Local actin polymerization and dynamin recruitment in SV40-induced internalization of caveolae. *Science* **2002,** *296* (5567), 535-539.

10. Damm, E.-M.; Pelkmans, L.; Kartenbeck, J.; Mezzacasa, A.; Kurzchalia, T.; Helenius, A., Clathrin-and caveolin-1–independent endocytosis entry of simian virus 40 into cells devoid of caveolae. *The Journal of cell biology* **2005,** *168* (3), 477-488.

11. Oh, N.; Park, J.-H., Endocytosis and exocytosis of nanoparticles in mammalian cells. *Int J Nanomedicine* **2014,** *9* (Suppl 1), 51-63.